

University of Nottingham
UK | CHINA | MALAYSIA

Development of three-dimensional spheroid models for the analysis of medulloblastoma drug response and metastatic dissemination

Sophie J. Roper BSc, MSc

Thesis submitted to the University of Nottingham for the degree of Doctor of Philosophy

September 2019

BBSRC Doctoral Training Partnerships

Children's Brain Tumour Research Centre

Abstract

Introduction Medulloblastoma, the most common malignant paediatric brain tumour, is a heterogeneous disease with tumours classified based on their histological and molecular profiles. Studying medulloblastoma *in vitro* is challenging, as traditional two-dimensional (2D) cell culture models fail to recapitulate the multi-dimensional growth, cell-cell interactions, and complex microenvironment that exists *in vivo* and in patient tumours. This project therefore aimed to respond to the need for a robust, reliable, and optimised three-dimensional (3D) *in vitro* culture method for medulloblastoma, which could be applied to study drug response and metastatic dissemination.

Methods A panel of medulloblastoma cell lines representing three of the four molecular subgroups (SHH, Group 3, and Group 4) were tested for use in the 3D spheroid model. Standardised growth conditions, including spheroid size and culture medium, were adopted to allow direct comparisons across cell lines and treatments. Spheroids were characterised by imaging analysis, luminescence-based assays, and immunohistochemical staining. Drug response of 3D spheroids was compared to 2D monolayer culture, with additional long-term and dual-inhibitor studies conducted to exemplify the use of the 3D spheroid model in drug screening approaches. SHH medulloblastoma spheroids were applied to migration and invasion models using basement membrane matrices and hyaluronan (HA) hydrogels containing additional extracellular matrix (ECM) components. Next-generation sequencing (NGS) technologies were adopted to gain an insight into the genes and pathways involved in SHH medulloblastoma leptomeningeal metastatic dissemination using the HA hydrogel model.

Results Medulloblastoma cell lines formed spheroids of different morphologies. The SHH subgroup cell lines (DAOY, ONS76, and UW228-3) formed tight, highly reproducible spheroids, and were therefore chosen as suitable models for

downstream analysis. SHH medulloblastoma spheroids could be maintained for up to 3 weeks in culture, forming physiological gradients within the 3D structure over time. 3D spheroid culture increased resistance to standard-of-care chemotherapeutic drugs compared to 2D monolayer culture and a subpopulation of viable cells was present after treatment. Dual-inhibitor studies with vardenafil, an inhibitor of the multidrug transporter ABCB1, showed synergistic effects which could facilitate the use of lower doses of chemotherapy. The HA hydrogels, containing ECM components highly expressed in SHH patient tumours, were more suitable, physiologically-relevant models of SHH medulloblastoma metastasis than commercially-available basement membrane matrices. NGS revealed the downregulation of cell cycle genes and upregulation of cell movement genes in DAOY and ONS76 spheroids migrating on the HA hydrogel. Overexpression of the insulin pathway, consistent with *in vivo* SHH medulloblastoma metastasis models and patient tumours, was also observed. Thus our model allows us to recapitulate known, and identify novel, mechanisms of cell dissemination from the primary tumour.

Conclusion The 3D spheroid model of medulloblastoma described in this study can be used to analyse drug response and model metastatic dissemination. It is a significant improvement over current *in vitro* techniques and represents an important breakthrough in medulloblastoma research.

Acknowledgements

My PhD journey has been the most challenging, yet rewarding, experience I have ever faced and it would not have been possible without the support that I received from so many people.

First and foremost, I would like to thank my wonderful supervisor, Dr Beth Coyle, for her continued advice and support over the past four years. I am so grateful for your encouragement and kindness which has helped me grow as a researcher and given me confidence in my abilities. It has been an absolute pleasure working with you! I would also like to thank Dr Paul Scotting for his helpful advice and insightful suggestions which were always appreciated and taken on board.

This PhD project would not have been possible without the funding support from the BBSRC Doctoral Training Partnership. I would like to express my thanks to both this research council and the additional funding bodies which supported my attendance at international conferences, experiences which were highlights of my PhD.

I have had the privilege of working with an excellent research group during my time in the Children's Brain Tumour Research Centre. To Dr Franziska Linke, the best postdoc I could have wished for – I am immensely grateful for the helpful discussions and your honest advice (and also for introducing me to the delights of German food and wine!). To my girls, Hannah, Macha, Alice, Christine, and Louisa – I am so happy that I have shared this experience with you all. Thank you for always being there when I needed someone to talk to, for the endless laughter, and for the constant supply of tea and biscuits. A special thank you to Hannah, my best friend of 10 years – I don't know how I would have done this without you.

I would also like to extend my thanks to all other members of the CBTRC who have made my time memorable, from those who were there right the start to those who

joined along the way. A special thank you to Aishah, Whitney, Jasper, Josh, Phoebe, Catherine, and James. I would also like to thank Jane and the whole team at the EACR for making me feel so welcome during my internship.

Finally, I cannot thank my loved ones enough for their continued support throughout this entire journey. To James, my unexpected research finding – thank you for being my never-ending source of love and encouragement. To Lauren and Adam, who both deserve a medal for putting up with me – you have encouraged me every step of the way and have kept me sane (as much as possible) over the last four years. To Lily and Pippa, my constant sources of comfort and companionship – you never failed to put a smile on my face, even on the hardest days. To my grandparents, Gordon, Janet, Nancy, and Tom – thank you for teaching me to always be myself and to try my best in everything that I do. Finally to my parents, Jayne and Ian – I couldn't have done any of this without your endless love, encouragement and support. You have always believed in me and I hope I have made you proud.

Table of Contents

Abstract ..... **i**

Acknowledgements ..... **iii**

Table of Contents ..... **v**

List of Figures ..... **xii**

List of Tables ..... **xvi**

List of Common Abbreviations ..... **xviii**

Chapter 1. Introduction **2**

1.1 Clinical features of medulloblastoma 2

1.1.1 Epidemiology 2

1.1.2 Presentation and diagnosis 2

1.2 Histological classification of medulloblastoma 3

1.2.1 Classic histology 3

1.2.2 Large cell/anaplastic histology 4

1.2.3 Desmoplastic/nodular histology 4

1.2.4 Medulloblastoma with extensive nodularity 4

1.3 Molecular classification of medulloblastoma 6

1.3.1 WNT subgroup 8

1.3.2 SHH subgroup 10

1.3.3 Non-WNT/non-SHH subgroups 14

1.3.3.1 Group 3 14

1.3.3.2 Group 4 16

1.3.4 Further stratification of medulloblastoma molecular subgroups 18

1.4 Medulloblastoma treatment 20

1.4.1 Current treatment regimens 20

1.4.1.1 Surgery 20

1.4.1.2 Treatment for infants 21

1.4.1.3 Treatment for standard risk medulloblastoma 22

1.4.1.4 Treatment for high risk medulloblastoma 23
1.4.2 Improving medulloblastoma treatment 23
1.4.2.1 Redefining medulloblastoma risk groups 24
1.4.2.2 Disrupting the blood-brain barrier 30
1.4.2.3 Targeting cancer stem cells 31
1.4.2.4 Molecularly targeted therapies 33
1.5 Medulloblastoma metastasis 34
1.5.1 Mechanisms of medulloblastoma metastasis 34
1.5.2 Subgroup-specific metastatic behaviours 36
1.5.3 Medulloblastoma metastatic staging 37
1.6 Modelling medulloblastoma 39
1.6.1 Current models of medulloblastoma 39
1.6.1.1 Cell lines 39
1.6.1.2 Patient-derived xenografts 41
1.6.1.3 Organotypic brain slice cultures 41
1.6.1.4 Genetically-engineered mouse models 42
1.6.2 3D *in vitro* culture 44
1.6.3 Spheroid models 45
1.6.3.1 Spheroid morphology 46
1.6.3.2 Methods of spheroid generation 47
1.6.3.3 Applications of spheroid models 49
1.6.4 Modelling the brain extracellular matrix 50
1.7 Hypothesis and aims 51
Chapter 2. Materials and Methods 53
2.1 Standard cell culture 53
2.1.1 Standard culture media 53
2.1.2 Adherent cell culture 53
2.1.3 Semi-adherent cell culture 54
2.1.4 Suspension cell culture 55

2.1.5 Preparation of cell line stocks 55
2.2 Spheroid culture 56
2.2.1 Neurosphere medium 56
2.2.2 Spheroid optimisation 56
2.2.3 Generation and maintenance of spheroids 57
2.3 Spheroid analysis 58
2.3.1 Manual imaging of spheroids 58
2.3.2 Coefficient of variation analysis 58
2.3.3 CellTiter-Glo® 3D cell viability assay 59
2.4 Spheroid sectioning and staining 59
2.4.1 Embedding spheroids in a HistoGel™ block 59
2.4.2 Processing of spheroid blocks 60
2.4.3 Sectioning of spheroid blocks 60
2.4.4 Immunohistochemical staining of spheroid sections 60
2.5 Drug treatments 63
2.5.1 Drugs used in this study 63
2.5.2 2D monolayer and 3D spheroid drug response 63
2.5.3 Fluorescent staining of drug treated spheroids 64
2.5.4 Continual monitoring of drug effects 65
2.5.5 Combination drug treatments 65
2.6 Spheroid migration and invasion assays 66
2.6.1 Collagen IV 66
2.6.2 Basement membrane extract 66
2.6.3 HyStem™ hydrogel 67
2.7 Next-generation sequencing 69
2.7.1 Sample preparation 69
2.7.2 mRNA next-generation sequencing 70
2.7.2.1 Library preparation 70
2.7.2.2 mRNA sequencing 72

2.7.2.3 Quality control of sequencing data 73
2.7.2.4 Alignment and mapping 73
2.7.2.5 Differential expression analysis 75
2.7.3 3' UPX next-generation sequencing 77
2.7.3.1 Library preparation, sequencing and quality control 77
2.7.3.2 Primary sequence analysis 79
2.7.3.3 Secondary differential expression analysis 80
2.7.4 Next-generation sequencing analysis 80
2.7.4.1 Unsupervised analysis 80
2.7.4.2 Differential gene expression analysis 80
2.7.4.3 Gene set enrichment analysis 81
2.8 Patient dataset analysis 81
Chapter 3. Establishing a 3D spheroid model of medulloblastoma 84
3.1 Introduction 84
3.2 Optimisation of medulloblastoma cell lines in the 3D spheroid model . 86
3.2.1 SHH medulloblastoma cell lines form tight spheroids 89
3.2.2 Group 3 medulloblastoma cell lines form aggregates of varying morphology 96
3.2.3 Group 4 medulloblastoma cell lines fail to form suitable spheroids 101
3.2.4 Summary of spheroid optimisation 104
3.3 Validation of 3D spheroid model reproducibility 106
3.4 Characterisation of SHH medulloblastoma spheroids 108
3.4.1 SHH medulloblastoma spheroids are viable for long-term culture .. 109
3.4.2 SHH medulloblastoma spheroids express the stemness marker, SOX2 117
3.5 Summary 119
Chapter 4. Investigating drug response in medulloblastoma spheroids ... 121
4.1 Introduction 121
4.2 Comparison of spheroid drug response analysis methods 122

4.3 Comparison of drug response in 2D monolayer versus 3D spheroid culture 125

4.4 Optimisation of applications to further assess drug response in spheroids 134

4.4.1 Combining fluorescent staining with automated imaging analysis allows high-throughput readouts of spheroid viability 134

4.4.2 Continual monitoring of spheroid volume allows the effects of drugs to be measured over time 137

4.4.3 Combination treatments provide an insight into drug resistance 145

4.5 Summary 152

Chapter 5. Modelling medulloblastoma metastatic dissemination 154

5.1 Introduction 154

5.2 Modelling tumour migration and invasion using 3D spheroids 155

5.3 Modelling spheroid migration across a simple collagen IV basement membrane matrix 156

5.4 Using basement membrane extract to model tumour spread..... 158

5.5 Using hyaluronan hydrogels as brain-specific matrices..... 162

5.5.1 SHH medulloblastoma spheroids express the hyaluronan receptor, CD44 162

5.5.2 Key components of the extracellular matrix are highly expressed in SHH medulloblastoma tumours 164

5.5.3 SHH medulloblastoma spheroids do not effectively invade through hyaluronan hydrogels..... 169

5.5.4 SHH medulloblastoma spheroids actively migrate across the surface of hyaluronan hydrogels..... 174

5.6 Summary 178

Chapter 6. Identifying factors involved in SHH medulloblastoma metastasis using next-generation sequencing technologies 180

6.1 Introduction 180

6.2 *In vitro* modelling of SHH medulloblastoma metastasis..... 180

6.3 NGS of SHH medulloblastoma metastasis models 185

6.3.1 Sample preparation..... 185

6.3.2 Mapping of sequencing data 188
6.3.3 Comparison of NGS techniques 191
6.4 Investigating spheroid-matrix interactions 195
6.4.1 Cell cycle genes are downregulated in spheroids on a HA matrix 197
6.4.2 Cell movement genes are upregulated in spheroids on a HA matrix 200
6.4.3 Laminin has limited effects on spheroid-matrix interactions 205
6.5 Understanding processes involved in SHH medulloblastoma metastasis 208
6.5.1 Cell dissemination is driven by cytoskeletal changes 209
6.5.2 Metastasis-related pathways are upregulated in nodular metastases 212
6.5.3 RhoA-associated pathways are involved in both cell dissemination and nodular formation models of SHH medulloblastoma metastasis 215
6.6 Summary 219
Chapter 7. Discussion 221
7.1 Introduction 221
7.2 Establishment of a 3D *in vitro* model of medulloblastoma 222
7.2.1 Determining the appropriate 3D culture method 223
7.2.2 Cell line differences in the 3D spheroid model 225
7.2.3 Validation of SHH medulloblastoma spheroid reproducibility 229
7.2.4 Characterisation of SHH medulloblastoma spheroids 230
7.3 Assessment of medulloblastoma spheroid drug response 233
7.3.1 Drug response differences in 2D and 3D *in vitro* culture 234
7.3.2 Assessing spheroid drug response over a longer period 237
7.3.3 Overcoming ABCB1-mediated drug resistance 238
7.3.4 Further applications of the medulloblastoma drug screening model 240
7.4 Modelling medulloblastoma metastasis 243
7.4.1 Assessing cell movement on different matrices 243
7.4.2 Optimising sample preparation for NGS 250

7.4.3 Identifying drivers of SHH medulloblastoma metastasis using 3D hydrogel models 251

7.5 Future advances to the medulloblastoma spheroid model 257

7.6 Concluding statement 259

References 261

Appendices 283

Appendix 1. ABCB1 protein expression in DAOY and ONS76 spheroids 283

Appendix 2. Samples excluded from mRNA NGS analysis 284

PhD project outputs 288

Laboratory rotations 288

Research article in preparation 288

Conference papers 288

Presentations 289

Awards and achievements 290

Professional Internship 291

List of Figures

Figure 1.1 Histological subgroups of medulloblastoma 5

Figure 1.2 WNT signalling pathway..... 9

Figure 1.3 SHH signalling pathway 12

Figure 1.4 Intertumoral heterogeneity within medulloblastoma subgroups 19

Figure 1.5 Risk stratification for childhood medulloblastoma according to Schwalbe *et al.*, 2017..... 28

Figure 1.6 Risk-adapted therapy management based on molecular subgrouping according to Northcott et al., 2019..... 30

Figure 1.7 Structure of the leptomeninges in the brain..... 35

Figure 1.8 Medulloblastoma cell lines classified according to molecular subgroup 40

Figure 1.9 Schematic diagram of spheroid zones and physiological gradients 46

Figure 2.1 Library preparation for mRNA next-generation sequencing 72

Figure 2.2 mRNA next-generation sequencing workflow..... 73

Figure 2.3 Alignment and mapping workflow for mRNA next-generation sequencing analysis..... 74

Figure 2.4 Differential expression analysis workflow for mRNA next-generation sequencing analysis..... 76

Figure 2.5 Library preparation for 3' UPX next-generation sequencing 78

Figure 2.6 3' UPX next-generation sequencing primary sequence analysis workflow 79

Figure 3.1 Schematic diagram describing the 3D spheroid model 87

Figure 3.2 SHH medulloblastoma cell lines in standard culture 89

Figure 3.3 Optimisation of spheroid growth conditions for DAOY cells..... 91

Figure 3.4 Optimisation of spheroid growth conditions for ONS76 cells 93

Figure 3.5 Optimisation of spheroid growth conditions for UW228-3 cells..... 95

Figure 3.6 Group 3 medulloblastoma cell lines in standard culture..... 96

Figure 3.7 Optimisation of spheroid growth conditions for HD-MB03 cells 98

Figure 3.8 Assessment of Group 3 medulloblastoma spheroid morphology .. 100

Figure 3.9 Group 4 medulloblastoma cell lines in standard culture 101

Figure 3.10 Assessment of CHLA-01-MED spheroid morphology 102

Figure 3.11 Assessment of CHLA-01R-MED spheroid morphology 103

Figure 3.12 Coefficient of variation analysis for SHH medulloblastoma spheroids 107

Figure 3.13 Long-term growth of DAOY spheroids 110

Figure 3.14 Immunohistochemical staining of DAOY spheroids for markers of proliferation (Ki67) and hypoxia (CA9) 111

Figure 3.15 Long-term growth of ONS76 spheroids 113

Figure 3.16 Immunohistochemical staining of ONS76 spheroids for markers of proliferation (Ki67) and hypoxia (CA9) 114

Figure 3.17 Long-term growth of UW228-3 spheroids 116

Figure 3.18 Immunohistochemical staining of UW228-3 spheroids for markers of proliferation (Ki67) and hypoxia (CA9) 117

Figure 3.19 Immunohistochemical staining of SHH medulloblastoma spheroid sections for SOX2 118

Figure 4.1 Comparison of volume and viability as methods of analysing spheroid drug response 123

Figure 4.2 Comparison of etoposide response in 2D monolayers and 3D spheroids 126

Figure 4.3 Comparison of vincristine response in 2D monolayers and 3D spheroids 128

Figure 4.4 Comparison of cisplatin response in 2D monolayers and 3D spheroids 130

Figure 4.5 Comparison of lomustine response in 2D monolayers and 3D spheroids 132

Figure 4.6 Assessment of spheroid viability after vincristine treatment via Calcein-AM and Propidium Iodide staining 136

Figure 4.7 Schematic diagram describing the continual monitoring of spheroid drug response 138

Figure 4.8 Continual monitoring of the effects of etoposide treatment on DAOY and ONS76 spheroids 140

Figure 4.9 Continual monitoring of the effects of vincristine treatment on DAOY and ONS76 spheroids 142

Figure 4.10 Continual monitoring of the effects of cisplatin treatment on DAOY and ONS76 spheroids 144

Figure 4.11 Assessment of etoposide and vardenafil combination treatments 147

Figure 4.12 Assessment of vincristine and vardenafil combination treatments 149

Figure 4.13 Assessment of cisplatin and vardenafil combination treatments ... 151

Figure 5.1 Schematic diagram describing spheroid migration and invasion models 155

Figure 5.2 SHH medulloblastoma spheroid migration across a collagen IV matrix 157

Figure 5.3 SHH medulloblastoma spheroid invasion within basement membrane extract matrices 159

Figure 5.4 SHH medulloblastoma spheroid migration on a basement membrane extract matrix 161

Figure 5.5 Immunohistochemical staining of SHH medulloblastoma spheroid sections for CD44 163

Figure 5.6 ECM component gene expression across medulloblastoma subgroups 166

Figure 5.7 ECM component gene expression across SHH medulloblastoma subtypes 168

Figure 5.8 DAOY spheroid invasion within hyaluronan hydrogels 171

Figure 5.9 ONS76 spheroid invasion within hyaluronan hydrogels 172

Figure 5.10 UW228-3 spheroid invasion within hyaluronan hydrogels 173

Figure 5.11 DAOY spheroid migration on hyaluronan hydrogels 175

Figure 5.12 ONS76 spheroid migration on hyaluronan hydrogels 176

Figure 5.13 UW228-3 spheroid migration on hyaluronan hydrogels 177

Figure 6.1 Schematic diagram describing the spheroid and single cell models of SHH medulloblastoma metastasis 181

Figure 6.2 *In vitro* modelling of SHH medulloblastoma metastasis using the DAOY cell line 183

Figure 6.3 *In vitro* modelling of SHH medulloblastoma metastasis using the ONS76 cell line..... 184

Figure 6.4 Sample preparation for next-generation sequencing..... 186

Figure 6.5 Comparison of mRNA and 3' UPX NGS workflows..... 191

Figure 6.6 Number of genes identified in samples sequenced by both mRNA and 3' UPX NGS methods..... 192

Figure 6.7 Clustering of “spheroid no matrix” and “spheroid HA matrix” samples 195

Figure 6.8 Genes downregulated in the spheroid-matrix interaction..... 198

Figure 6.9 Genes upregulated in the spheroid-matrix interaction..... 201

Figure 6.10 *IGF2/INS* gene expression in medulloblastoma patient samples.. 204

Figure 6.11 Clustering of “spheroid HA matrix” and “spheroid HA+LAM matrix” samples..... 205

Figure 6.12 Genes upregulated in spheroids on a HA+LAM matrix 206

Figure 6.13 Genes downregulated in spheroids on a HA+LAM matrix..... 207

Figure 6.14 Clustering of spheroid and single cell samples on HA and HA+LAM matrices..... 208

Figure 6.15 Genes upregulated during cell dissemination of SHH medulloblastoma..... 210

Figure 6.16 Genes upregulated during the formation of SHH medulloblastoma nodular metastases..... 213

Figure 6.17 LAM-specific genes shared across SHH medulloblastoma metastatic stages..... 216

Figure 6.18 *RHOA* gene expression in medulloblastoma patient samples 218

Figure 7.1 Comparison of SHH medulloblastoma spheroids in 96-well and 384-well ultra-low attachment plates..... 241

List of Tables

Table 1.1 Summary of the molecular classification of medulloblastoma tumours 7

Table 1.2 Risk stratification for medulloblastoma according to the updated WHO classification 25

Table 1.3 Risk stratification for non-infant childhood medulloblastoma according to Ramaswamy *et al.*, 2016 26

Table 1.4 3D culture techniques 45

Table 2.1 Sodium citrate buffer recipe 61

Table 2.2 Details of primary antibodies used in the study 62

Table 2.3 Drugs used in the study 63

Table 2.4 Patient datasets analysed on the R2 Genomics Analysis and Visualisation Platform 82

Table 3.1 Clinical information for medulloblastoma cell lines used in this study 88

Table 3.2 Summary of medulloblastoma cell lines tested in the 3D spheroid model 105

Table 3.3 Coefficient of variation analysis for SHH medulloblastoma spheroids 108

Table 4.1 Comparison of volume and luminescence as methods of analysing spheroid drug response 124

Table 4.2 Comparison of drug response in 2D monolayers and 3D spheroids for SHH medulloblastoma cell lines 133

Table 6.1 Summary of samples prepared for NGS 187

Table 6.2 Mapping of mRNA NGS sequence data 189

Table 6.3 Mapping of 3' UPX NGS sequence data 190

Table 6.4 Comparison of top 20 gene sets upregulated in spheroids on a HA matrix identified by mRNA and 3' UPX NGS 194

Table 6.5 Top 25 genes most significantly downregulated in the spheroid-matrix interaction 199

Table 6.6 Top 25 genes most significantly upregulated in the spheroid-matrix interaction 202

Table 6.7 Gene set enrichment analysis of genes upregulated during cell dissemination of SHH medulloblastoma 211

Table 6.8 Gene set enrichment analysis of genes upregulated during the formation of SHH medulloblastoma nodular metastases 214

Table 6.9 Gene set enrichment analysis of LAM-specific genes shared across SHH medulloblastoma metastatic stages 217

List of Common Abbreviations

2D	two-dimensional
3D	three-dimensional
ABC	ATP-Binding Cassette
ANOVA	analysis of variance
ATP	adenosine triphosphate
BBB	blood-brain barrier
BME	basement membrane extract
CV	coefficient of variation
CA9	Carbonic Anhydrase 9
CAM	calcein-AM
CNS	central nervous system
COL	collagen I
CSC	cancer stem cell
CSF	cerebrospinal fluid
ECM	extracellular matrix
EGF	epidermal growth factor
EHS	Engelbreth-Holm-Swarm
FDR	false discovery rate
FGF	fibroblast growth factor
FN	fibronectin
FPKM	fragments per kilobase of transcript per million mapped reads
GAG	glycosaminoglycan
GO	gene ontology
GSEA	gene set enrichment analysis
HA	hyaluronan (hyaluronic acid)
HFRT	hyperfractionated radiotherapy
IGF	insulin-like growth factor

IHC	immunohistochemistry
INS	insulin
LAM	laminin-111
LCA	large cell/anaplastic
MBEN	medulloblastoma with extensive nodularity
MRI	magnetic resonance imaging
NGS	next-generation sequencing
PI	propidium iodide
PID	pathway interaction database
PTCH	Patched
QC	quality control
Rho	Ras homolog
RLU	relative luminescence units
ROCK	Rho-associated serine/threonine kinase
SD	standard deviation
SEM	standard error of the mean
SHH	Sonic Hedgehog
SMO	Smoothened
SOX2	SRY (sex determining region Y)-box 2
SUFU	Suppressor of Fused
TME	tumour microenvironment
TP53	Tumour Protein 53
ULA	ultra-low attachment
UMI	unique molecular index
WHO	World Health Organisation
WNT	Wingless-related integration site

Chapter 1

Introduction

Chapter 1. Introduction

Childhood cancer is rare, with only around 1,900 cases diagnosed each year in the UK, accounting for less than 1% of all cancer diagnoses (Cancer Research UK, 2019). Tumours of the central nervous system (CNS) occur in the brain or spinal cord and are the most common solid tumours in children, accounting for approximately 26% of all paediatric cancer cases (Children with Cancer UK, 2019). Not only are brain tumours the leading cause of cancer-related deaths in children, of those who do survive a brain tumour, 62% will be left with life-altering, long-term disabilities (HeadSmart, 2019). There are over 130 different types of brain tumours and each differ in their location, biology, and prognosis. The focus of this project is medulloblastoma, the most common malignant paediatric brain tumour.

1.1 Clinical features of medulloblastoma

1.1.1 Epidemiology

Medulloblastomas account for approximately 20% of all childhood brain tumours (Pui *et al.*, 2011) and around 10% of cancer-related deaths in children (Pizer and Clifford, 2009). Tumours arise in all age groups, but are most prevalent in patients aged between 4 and 9 years (Kool *et al.*, 2012). In addition, children are 10 times more likely to be affected by medulloblastoma than adults (Smoll and Drummond, 2012). Tumours are more common in males than females (Louis *et al.*, 2007); however, there is no difference in age distribution between genders.

1.1.2 Presentation and diagnosis

Medulloblastomas are neuroectodermal tumours which arise in the cerebellum, located in the posterior fossa region of the brain. This area controls balance, posture

and complex motor functions and patients typically present with symptoms including headaches, nausea, diplopia, and hydrocephalus caused by raised intracranial pressure (Polkinghorn and Tarbell, 2007). Patients with a suspected medulloblastoma are diagnosed by computerised tomography (CT) or magnetic resonance imaging (MRI) scanning, revealing a mass in the posterior fossa region. The World Health Organisation (WHO) categorises all medulloblastoma tumours as Grade IV, irrespective of their histological or molecular characteristics, attesting to their malignant and aggressive behaviour (Louis *et al.*, 2016).

1.2 Histological classification of medulloblastoma

Medulloblastoma is a heterogeneous disease consisting of different histological variants. The 2016 WHO classification of CNS tumours defined four histological subtypes of medulloblastoma: classic, large cell/anaplastic, desmoplastic/nodular, and medulloblastoma with extensive nodularity (Louis *et al.*, 2016).

1.2.1 Classic histology

Classic medulloblastoma is the most frequent histological variant, accounting for 72% of all medulloblastoma cases. These tumours occur across all age groups, from infants to adults, but are predominately found in childhood cases. Classic medulloblastomas are characterised by sheets of small cells with rounded nuclei and a high nuclear-cytoplasmic ratio (Ellison, 2010). Rosettes are present in a subset of classic medulloblastoma tumours, representing regions of neuronal differentiation (Ellison, 2002). An example of classic histology is shown in Figure 1.1A.

1.2.2 Large cell/anaplastic histology

Large cell/anaplastic (LCA) medulloblastomas account for around 10% of all cases and occur across all age groups. These tumours are highly aggressive and patients with a LCA tumour are considered to have a significantly poorer prognosis (Eberhart *et al.*, 2002; Ellison, Kocak, *et al.*, 2011). Histologically, these tumours consist of groups of large cells with rounded nuclei and a single nucleolus (Ellison, 2010). LCA tumours are characterised by the presence of nuclear pleomorphism, due to its high nuclear-cytoplasmic ratio, cell wrapping, high mitotic activity, and abundant apoptotic bodies (Figure 1.1B).

1.2.3 Desmoplastic/nodular histology

Desmoplastic/nodular histology is present in around 20% of all medulloblastoma cases, with a higher frequency among infants (approximately 50% of cases). Infants presenting with desmoplastic/nodular medulloblastoma have a significantly better outcome than those diagnosed with classic or large cell/anaplastic tumours (Ellison, Kocak, *et al.*, 2011). Desmoplastic medulloblastoma exhibit nodular, reticulin-free zones of neuronal maturation set in reticulin-rich, densely packed background of undifferentiated embryonal cells (Figure 1.1C). Internodular regions are desmoplastic, consisting of undifferentiated embryonal cells and reticulin-positive collagen strands (Gajjar and Robinson, 2014).

1.2.4 Medulloblastoma with extensive nodularity

Medulloblastoma with extensive nodularity (MBEN) occurs in around 5% of all medulloblastoma cases. These tumours are more common in infants than other age groups, with around 20% of cases arising in patients less than three years of age. MBEN shares similarities with desmoplastic/nodular medulloblastoma as it too is

characterised by the presence of nodular and internodular regions (Figure 1.1D). The nodular regions in MBEN tumours however, are more abundant and are usually large and irregularly shaped, displaying a linear streaming pattern (Louis *et al.*, 2007; Ellison, 2010).

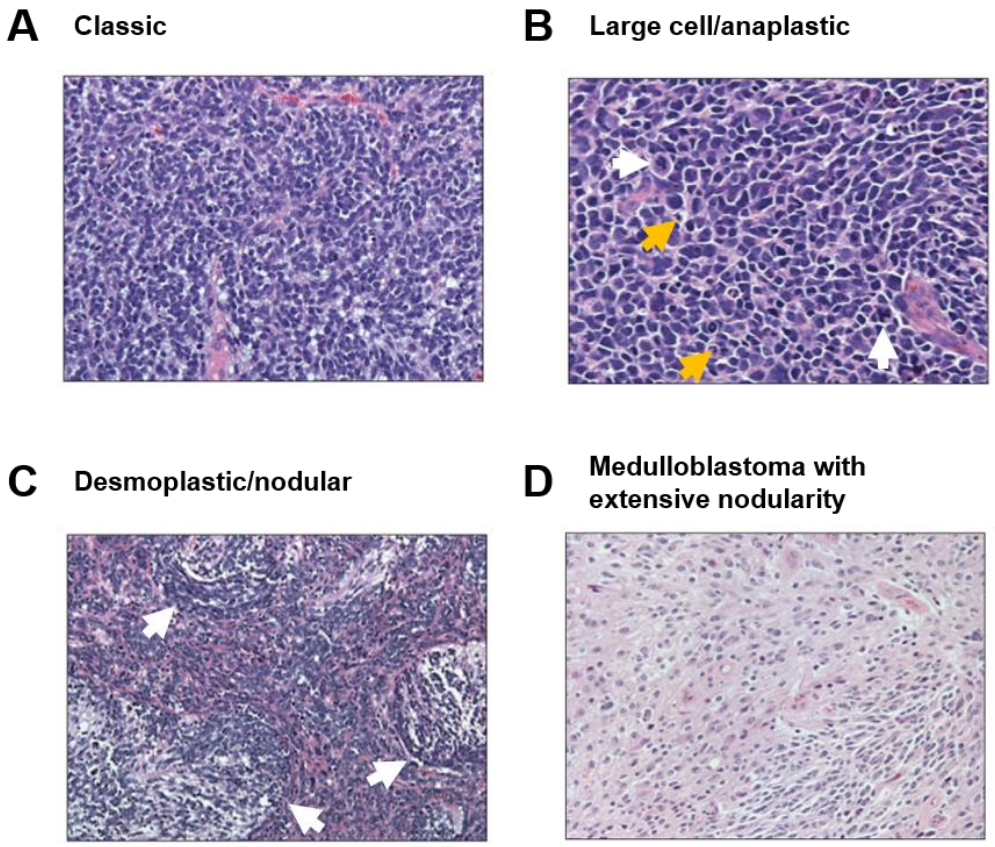


Figure 1.1 Histological subgroups of medulloblastoma
Histological variants of medulloblastoma as shown by haematoxylin and eosin (H&E) staining. (**A**) Classic medulloblastoma exhibits sheet-like proliferation of monotonous small cells with hyperchromatic nuclei and scant cytoplasm. (**B**) Large cell/anaplastic medulloblastoma is characterised by diffuse, marked nuclear pleomorphism, frequent mitotic figures (white arrows), and abundant apoptotic bodies (yellow arrows). (**C**) Desmoplastic medulloblastoma exhibit nodular, reticulin-free zones of neuronal maturation (arrows) set in reticulin-rich, densely packed background of undifferentiated embryonal cells. (**D**) Medulloblastoma with extensive nodularity is characterised by lobular architecture with reticulin-free zones that are rich in neurophil-like tissue and larger than those seen in desmoplastic medulloblastoma. Images and descriptions obtained from Yeom *et al.*, 2013.

1.3 Molecular classification of medulloblastoma

In the fourth edition of the WHO classification of CNS tumours in 2007, only histology was taken into account when classifying medulloblastoma tumours (Louis *et al.*, 2007). More recently, advancements in the molecular understanding of medulloblastoma has revolutionised the way in which tumours are classified.

Gene expression profiling studies from multiple research groups identified numerous molecular subgroups of medulloblastoma (Thompson *et al.*, 2006; Kool *et al.*, 2008; Cho *et al.*, 2011; Northcott, Korshunov, *et al.*, 2011). Following an international consensus on the molecular classification of medulloblastoma, it is now widely accepted that there are four distinct subgroups: WNT, SHH, Group 3, and Group 4 (Northcott, Jones, *et al.*, 2012; Taylor *et al.*, 2012). These subgroups differ in their clinical features, as well as their genetic profiles and pathway signatures, as summarised in Table 1.1. Following on from this, it was demonstrated by Schwalbe *et al.* in 2013 that there was 81% concordance between gene expression and DNA methylation profiling in the identification of medulloblastoma molecular subgroups. Hovestadt *et al.*, 2013 supported this finding and showed that utilising DNA methylation array platforms on either frozen or paraffin-embedded tissue is a reliable method of classifying medulloblastomas based on molecular subgroup. DNA methylation profiling has now superseded gene expression analysis and is considered the go-to method for assessing medulloblastoma subgroup status (Korshunov *et al.*, 2017).

Based on the significance of molecular subgrouping for medulloblastoma tumours, the most recent update of the WHO classification of CNS tumours now classifies medulloblastomas according to both their molecular characteristics as well as histopathological features (Louis *et al.*, 2016). The following section will discuss each of the medulloblastoma molecular subgroups in further detail.

Table 1.1 Summary of the molecular classification of medulloblastoma tumours

Medulloblastoma tumours are classified into four subgroups (WNT, SHH, Group 3, and Group 4) according to their molecular characteristics. Table adapted from Northcott *et al.*, 2012.

	WNT subgroup	SHH subgroup	Group 3	Group 4
Prevalence	10%	30%	25%	35%
Gender ratio (male:female)	1:1	1.5:1	2:1	3:1
Age group	Children	Infants and adults	Infants and young children	Children
Histology	Classic, rarely LCA	Classic > desmoplastic/ Nodular > LCA > MBEN	Classic > LCA	Classic, rarely LCA
Metastatic at diagnosis	~5-10%	~15-20%	~40-45%	~35-40%
Prognosis	Excellent	Intermediate	Poor	Intermediate
Overall survival (5 years)	~95%	~75%	~40-45%	~75%
Expression signature	WNT signalling	SHH signalling	MYC signature	Neuronal signature

1.3.1 WNT subgroup

Epidemiology

Around 10% of medulloblastoma cases belong to the WNT subgroup, named after the signalling pathway dysregulated in these tumours. WNT medulloblastomas are equally distributed between males and females and typically occur in patients over three years of age. WNT tumours are infrequently metastatic (Kool *et al.*, 2012), hence patients have an excellent long-term prognosis (Clifford *et al.*, 2006; Remke *et al.*, 2011), with a 5-year overall survival rate of around 95% (Ellison *et al.*, 2005).

Histology

The majority of WNT tumours are characterised by a classic histology; however, rare cases of large cell/anaplastic histology have been reported (Ellison, Dalton, *et al.*, 2011).

Genetic profile

WNT medulloblastomas are characterised by activation of the WNT signalling pathway (Figure 1.2). In normal WNT signalling, the binding of the WNT ligand to its cell-surface receptor frizzled (FRZ) recruits the dishevelled (DSH) protein to block the phosphorylation-activated degradation of β-catenin by glycogen synthase kinase-3β (GSK3β), which is in a complex with adenomatous polyposis coli (APC) and Axin. β-catenin is then able to translocate to the nucleus where it activates the transcription of target genes. Suppressor of fused (SUFU) represses the pathway by promoting β-catenin export from the nucleus.

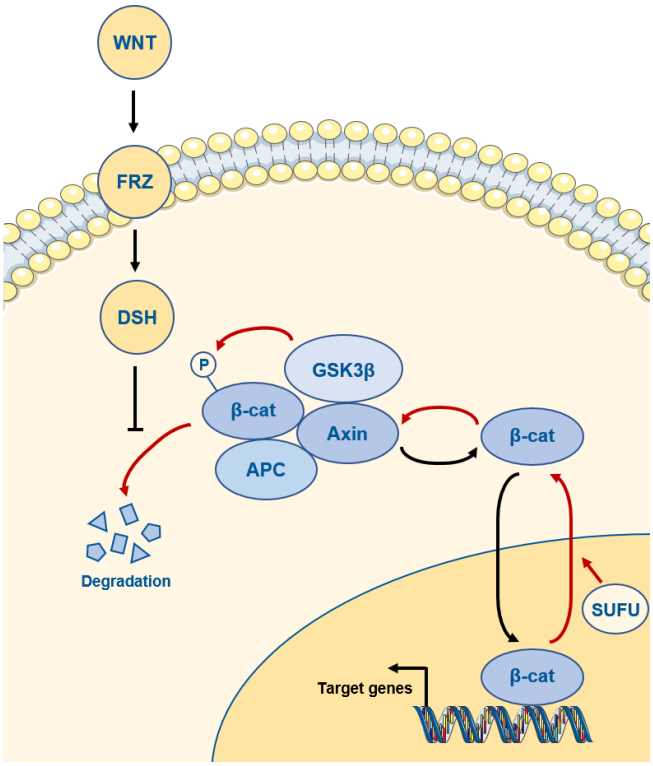


Figure 1.2 WNT signalling pathway
The WNT ligand binds to its cell-surface receptor frizzled (FRZ). FRZ recruits the dishevelled (DSH) protein which blocks the phosphorylation-activated degradation of β-catenin (β-cat) by glycogen synthase kinase-3β (GSK3β), which is in a complex with adenomatous polyposis coli (APC) and Axin. β-catenin is then able to translocate to the nucleus where it activates the transcription of target genes. Suppressor of fused (SUFU) represses the pathway by promoting β-catenin export from the nucleus. Black and red steps represent activation and inhibition of the pathway, respectively. Image adapted from Scotting, Walker and Perilongo, 2005.

Around 90% of WNT subgroup tumours exhibit mutations in *CTNNB1*, encoding β-catenin, resulting in the accumulation of β-catenin in the nucleus and activation of the WNT signalling pathway (Northcott, Shih, *et al.*, 2012). WNT medulloblastomas also commonly exhibit monosomy 6, deletions of one copy of chromosome 6 (Clifford *et al.*, 2006). A study by Zhukova *et al.*, 2013 showed that around 16% of WNT tumours display *TP53* mutations; however, mutational status did not significantly affect 5-year overall survival. A recent international study on genetic predisposition in medulloblastoma revealed that, within their cohort, patients with germline *APC* mutations developed WNT tumours (Waszak *et al.*, 2018). Furthermore, these germline *APC* mutations in WNT medulloblastoma patients were mutually exclusive with somatic *CTNNB1* mutations.

Localisation and cellular origin

Although medulloblastoma tumours typically arise in the cerebellum, Gibson *et al.*, 2010 were the first group to show that the localisation and cellular origin of WNT medulloblastomas differs compared to other subgroups. Examination of MRI scans and intra-operative reports of WNT tumours showed their localisation within the fourth ventricle and infiltration of the dorsal brainstem. They also showed that WNT medulloblastomas arise in the lower rhombic lip progenitors of the dorsal brainstem and can be initiated in mice by transgenic expression of an activated mutant β-catenin (*Ctnnb1*) allele compounded with *Trp53* deletion. Around 15% of mice expressing the activated *Ctnnb1* transgene developed classic medulloblastomas after around 10-12 months. Subsequently, Robinson *et al.*, 2012 added a PI3K catalytic-α polypeptide mutant allele ($Pik3ca^{E545K}$) to the established WNT mouse model, generating mice with WNT tumours with classic histology by 3 months of age.

1.3.2 SHH subgroup

Epidemiology

Tumours classified in the SHH subgroup account for around 30% of medulloblastoma cases. SHH medulloblastomas are slightly more common in males compared to females and there is a bimodal age distribution with peak incidences in infants and adults (Northcott, Jones, *et al.*, 2012). Patients diagnosed with SHH tumours have an intermediate prognosis, with an overall 5-year survival of 60-80% (Kool *et al.*, 2012).

Histology

Almost all desmoplastic/nodular and MBEN tumours are classified in the SHH subgroup; however, other histological variants such as classic and large

cell/anaplastic are also associated with this molecular subtype (Ellison, Dalton, *et al.*, 2011). Infants with desmoplastic/nodular SHH tumours have a better prognosis than those with a classic histology; however, histology is not a prognostic marker in adult cases (Northcott, Hielscher, *et al.*, 2011).

Metastasis

Around 15-20% of patients are metastatic at diagnosis and are considered to be at a higher risk than patients who are non-metastatic (Ramaswamy *et al.*, 2016). SHH tumours typically recur locally in the original resection cavity (Ramaswamy *et al.*, 2013), with leptomeningeal dissemination more common in infant SHH medulloblastoma than adult cases (Northcott, Hielscher, *et al.*, 2011).

Genetic profile

SHH medulloblastomas are characterised by activation of the SHH signalling pathway. In normal SHH signalling, binding of the SHH ligand to its cell-surface receptor patched (PTCH) inhibits its repression on smoothened (SMO), allowing SMO to promote intracellular signalling. SMO represses the cleavage of GLI (the cleaved form has a transcriptional repressor role in the nucleus), allowing its release from a complex with fused (FU) and costal (COS). GLI is subsequently translocated to the nucleus where it activates the transcription of target genes. In addition to suppressing the WNT signalling cascade, SUFU is also able to repress SHH signalling by promoting the export of GLI from the nucleus and by directly repressing the transcriptional activity of GLI.

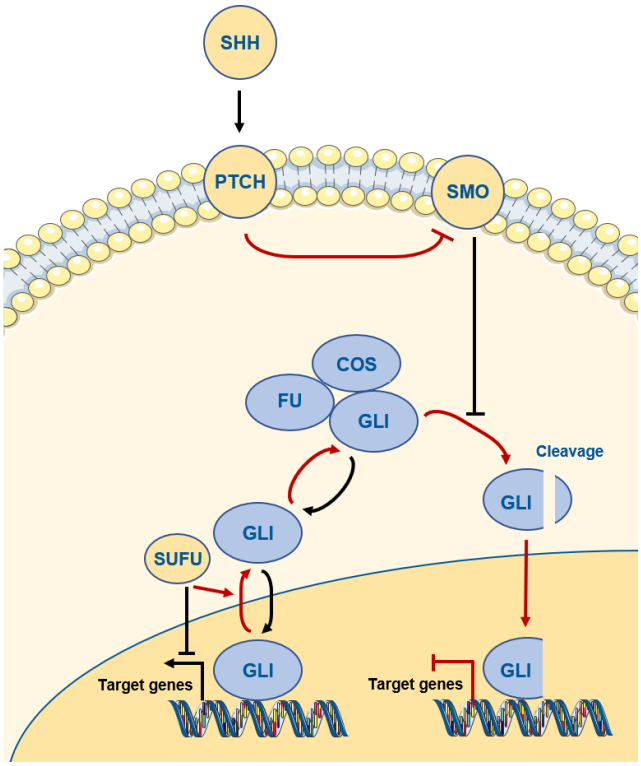


Figure 1.3 SHH signalling pathway
The SHH ligand binds to its cell-surface receptor patched (PTCH), inhibiting its repression on smoothened (SMO), allowing SMO to promote intracellular signalling. SMO represses the cleavage of GLI (the cleaved form has a transcriptional repressor role in the nucleus), allowing its release from a complex with fused (FU) and costal (COS). GLI is then able to translocate to the nucleus where it activates the transcription of target genes. Suppressor of fused (SUFU) represses SHH signalling by promoting the export of GLI from the nucleus and by directly repressing the transcriptional activity of GLI. Black and red steps represent activation and inhibition of the pathway, respectively. Image adapted from Scotting, Walker and Perilongo, 2005.

SHH subgroup tumours commonly exhibit mutations in key components of the SHH signalling pathway including *PTCH1*, *SMO*, and *SUFU* (Kool *et al.*, 2014). Sequencing of SHH medulloblastoma patient cohorts has provided insight into the age-associated genomic differences in SHH medulloblastoma cases (Northcott, Hielscher, *et al.*, 2011). There is an equal frequency of *PTCH1* mutations across all age groups, whereas *SMO* mutations are more common in adult cases and *SUFU* mutations are almost exclusively found in infant patients. Somatic copy number alterations are also present in the SHH subgroup, including *MYCN* and *GLI2* amplifications (Northcott, Korshunov, *et al.*, 2011). Broad genetic aberrations are also frequently associated with this subset of medulloblastomas, including

chromosomal gains (3q and 9p) and losses (9q, 10q, 14q, and 17q) (Kool *et al.*, 2012). Analysis of patient cohorts by Zhukova *et al.*, 2013 found that *TP53* mutations are enriched among patients with SHH medulloblastoma. This genetic abnormality is particularly important as individuals with Li-Fraumeni syndrome, caused by germline mutations in *TP53*, are at a higher risk of developing medulloblastoma (Orr *et al.*, 2019). Ramaswamy *et al.*, 2016 stratified patients with *TP53*-mutated SHH tumours as very high risk due to their poor survival. This risk has also been acknowledged in the most recent WHO classification of CNS tumours, where SHH tumours are now classified into two groups: *TP53*-wildtype and *TP53*-mutated (Louis *et al.*, 2016).

Germline mutations affecting components of the SHH pathway have been reported to predispose to SHH medulloblastoma. *SUFU* germline mutation were reported by Taylor *et al.*, 2002. Recent studies have shown how these mutations strongly predispose to medulloblastoma arising in infancy, and patients have a poorer prognosis than usually observed for SHH medulloblastoma (Guerrini-Rousseau *et al.*, 2018). Patients with Gorlin syndrome are predisposed to medulloblastoma tumours due to germline mutations in *PTCH1* (Garrè *et al.*, 2009) and *SUFU* (Smith *et al.*, 2015).

Localisation and cellular origins

SHH medulloblastomas occur within the cerebellar hemispheres (Gibson *et al.*, 2010) and are known to arise from multiple cellular origins. Mouse models of SHH medulloblastoma show that these tumours can arise from cerebellar granule neuron precursors (Schüller *et al.*, 2008). Yang *et al.*, 2008 also demonstrated that neural stem cells of the subventricular zone respond to SHH signalling and can be regarded as cells of origin for SHH medulloblastoma tumours. Another study by Grammel *et al.*, 2012 demonstrated that the cochlear nuclei of the brainstem are another cellular origin for this subset of tumours.

1.3.3 Non-WNT/non-SHH subgroups

Medulloblastomas which do not belong to the WNT or SHH subgroup are categorised as either Group 3 or Group 4 tumours. These tumours account for around 60% of all medulloblastoma cases yet remain the least understood in respect to their biology and developmental origins.

1.3.3.1 Group 3

Epidemiology

Group 3 tumours account for around 25% of medulloblastoma cases. These tumours are more common in males than females (at a ratio of 2:1) and occur predominantly in infants and young children (Northcott, Jones, *et al.*, 2012). Patients diagnosed with Group 3 tumours have a poor prognosis, with an overall 5-year survival of around 50%.

Histology

Group 3 tumours mostly exhibit a classic histology. This subgroup also harbours a high prevalence of large cell/anaplastic tumours, yet lack cases of desmoplastic/nodular disease (Kool *et al.*, 2012).

Metastasis

Approximately 40-45% of patients with Group 3 medulloblastoma present with metastatic disease at diagnosis. A study of the recurrence patterns across medulloblastoma subgroups by Ramaswamy *et al.*, 2013 highlighted the aggressive metastatic behaviour of Group 3 tumours and found that almost all recurrences were distant, located away from the primary tumour site. Due to their aggressive

nature and extremely poor prognosis, metastatic Group 3 tumours are stratified as very high risk (Ramaswamy *et al.*, 2016).

Genetic profile

The most common genetic signature associated with Group 3 medulloblastomas is aberrant *MYC* expression (Cho *et al.*, 2011). This subgroup demonstrate high levels of chromosome instability with more than 50% of tumours exhibiting structural chromosomal aberrations such as losses of chromosome 10q, 16q, and 17p and gains of chromosome 1q, 7, 17q, and 18 (Northcott, Korshunov, *et al.*, 2011). The presence of an isochromosome 17 may also be a subgroup-specific marker for this set of tumours (Shih *et al.*, 2014). Numerous medulloblastoma sequencing and copy number studies were conducted in 2012 which identified driver genes associated with Group 3 tumours including *MYC* amplification (16.7%), *PVT1* amplification (11.9%), *SMARCA4* (10.5%), *OTX2* amplification (7.7%), *CTDNEP1* (4.6%), *LRP1B* (4.6%), and *KMT2D* (4%) (Jones *et al.*, 2012; Pugh *et al.*, 2012; Robinson *et al.*, 2012).

Localisation and cellular origin

A recent study of the radiological characteristics of medulloblastoma revealed that Group 3 tumours are located within the fourth ventricle (Zapotocky *et al.*, 2018). In addition, more than half of the primary Group 3 tumours analysed in their cohort did not exceed 35 mm in diameter, making them significantly smaller than SHH and Group 4 tumours.

MYC-driven mouse models of Group 3 medulloblastoma have given insights into the cellular origins for this subgroup. When combined with *Trp53* inactivation, these models generated tumours from three cell types: *ATOH1*-positive or *ATOH1*-negative cerebellar granule neuron precursors from the external granule cell layer (Kawauchi *et al.*, 2012), and prominin 1-positive lineage-negative neural stem cells

(Pei *et al.*, 2012). In a more recent study, the comparison of Group 3 medulloblastomas to developmental cerebellar cell clusters showed a resemblance to Nestin-positive cerebellar early stem cells (Vladoiu *et al.*, 2019).

1.3.3.2 Group 4

Epidemiology

Group 4 medulloblastoma is the most prevalent subgroup, accounting for around 35% of cases (Kool *et al.*, 2012). Group 4 tumours are more common in males than females (at a ratio of 3:1) and typically occur in children, with a median age of incidence of 9 years. Patients diagnosed with Group 4 tumours have an intermediate prognosis, with an overall 5-year survival of around 75% (Northcott, Jones, *et al.*, 2012).

Histology

Group 4 medulloblastoma generally exhibit a classic histology. Large cell/anaplastic histology occurs in a minority of cases but at a lower frequency compared to Group 3 tumours (Kool *et al.*, 2012).

Metastasis

Group 4 tumours have a high metastatic rate and around 35-40% of patients present with metastases at diagnosis (Northcott, Jones, *et al.*, 2012). Similarly to Group 3 tumours, distal metastases at recurrence are more common than local disease (Ramaswamy *et al.*, 2013).

Genetic profile

Group 4 medulloblastoma is the least genetically understood medulloblastoma subgroup. Group 4 tumours are associated with a neuronal expression signature

and chromosomal aberrations include losses of chromosomes 8, 10, 11, and 17p and gains of chromosomes 4, 7, 17q, and 18 (Northcott, Korshunov, *et al.*, 2011). Driver genes for Group 4 tumours include *KDM6A* (13%), *SNCAIP* gain (10.4%), *MYCN* amplification (6.3%), *KMT2C* (5.3%), *CDK6* amplification (4.7%), and *ZMYM3* (3.7%) (Jones *et al.*, 2012; Pugh *et al.*, 2012; Robinson *et al.*, 2012). The presence of isochromosome 17q is observed in around 80%, making this abnormality a molecular hallmark of Group 4 tumours (Taylor *et al.*, 2012). In addition, most female Group 4 medulloblastoma patients exhibit loss of one copy of the X chromosome (Northcott, Korshunov, *et al.*, 2011).

Localisation and cellular origin

Group 4 medulloblastomas typically arise in the fourth ventricle; however, some cases arise in the lateral recess (Zapotocky *et al.*, 2018). Unlike the other medulloblastoma subgroups in which mouse models have enabled us to gain insights into cellular origins, the lack of suitable Group 4 *in vivo* models has hindered advances in determining cells of origin for this subset of tumours. However, Lin *et al.*, 2016 provided candidate cells of origin for this medulloblastoma subgroup. They revealed that *LMX1A* is a master regulator of Group 4 transcriptional programs and could be regarded as a subgroup-specific transcription factor. They identified deep cerebellar nuclei of the cerebellar nuclear transitory zone, or their earlier precursors originating from the upper rhombic lip, as putative cells of origin for Group 4 medulloblastoma. Recently, two of the leading medulloblastoma research groups have proposed that Group 4 medulloblastomas arise from cells in the unipolar brush cell (UBC) lineage (Hovestadt *et al.*, 2019; Vladoiu *et al.*, 2019). There are three main regions of the cerebellum where UBCs may be produced: the cerebellar ventricular zone, the rhombic lip, and the external granular layer (Englund *et al.*, 2006). This recent advancement aids our understanding of Group 4 tumours and will allow continued research to elucidate the mechanisms by which these proposed cells form Group 4 tumours.

1.3.4 Further stratification of medulloblastoma molecular subgroups

Although the classification of medulloblastoma tumours into four distinct molecular subgroups has reformed the way in which the tumours are approached in the clinic, it was apparent that there was heterogeneity within each subgroup. Therefore, there have been numerous attempts to further categorise these subgroups in recent years. The most notable study was conducted by Cavalli *et al.*, 2017, who subcategorised the four medulloblastoma molecular subgroups into 12 subtypes with distinct somatic copy-number aberrations, activated pathways, and clinical outcomes (Figure 1.4).

WNT medulloblastomas were divided into two subtypes: WNTα (70%) and WNTβ (30%). Although these subtypes have similar survival rates, they differ in their patient demographics, with WNTα tumours prevalent in children, compared to WNTβ which is enriched in older patients.

The SHH subgroup was divided into four clinically and cytogenetically distinct subtypes: SHHα (29%), SHHβ (16%), SHHγ (21%), and SHHδ (34%). SHHα tumours have the worst prognosis and exhibit mutations in *TP53* and amplification of *MYCN*/*GLI2*. SHHβ medulloblastomas also have a poor prognosis and affect infants with metastatic disease. The SHHγ subtype also affect infants and tumours typically display MBEN histology; however, patients with these tumours have a good outcome. The SHHδ subtype mainly consists of adult cases and tumours are enriched for *TERT* mutations.

Analysis of Group 3 and 4 medulloblastoma tumours showed that they were molecularly distinct entities. Group 3 tumours were classified into three subtypes: Group 3α (47%), Group 3β (26%), and Group 3γ (28%). Both Groups 3α and 3β have a more favourable prognosis than Group 3γ which are characterised by *MYC* amplification. Group 4 tumours were also subcategorised into three subtypes:

Group 4α (30%), Group 4β (33%), and Group 4γ (37%). Unlike other subgroups, there was no significant difference in overall survival or metastatic dissemination rates across the Group 4 subtypes. Instead these tumours were categorised based on genetic aberrations.

This study significantly enhances our understanding of medulloblastoma molecular subgroups. The identification of clinically and biologically relevant subtypes which explains the heterogeneity within subgroups will refine clinical classification and improve preclinical modelling of the disease.

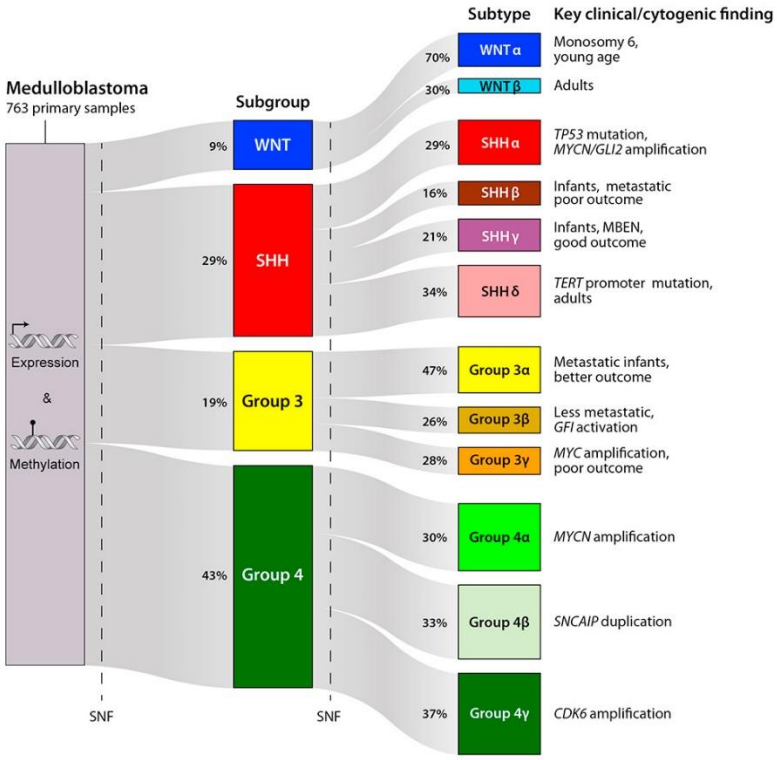


Figure 1.4 Intertumoral heterogeneity within medulloblastoma subgroups
Cavalli *et al.*, 2017 analysed the gene expression and methylation profiles of 763 primary medulloblastoma samples. They identified twelve subtypes within the four molecular subgroups (WNT, SHH, Group 3, and Group 4) with distinct somatic copy-number aberrations, activated pathways, and clinical outcomes. Diagram taken from Cavalli *et al.*, 2017.

1.4 Medulloblastoma treatment

Treatment for medulloblastoma is typically based on patient risk. Risk stratification currently accounts for factors including patient age, metastatic status, and the extent of surgical resection, with patients categorised into one of three risk groups:

(1) Infants: children under three years of age.
(2) Standard risk: patients over three years of age with localised disease and total or near-total surgical resection.
(3) High risk: metastatic patients with large cell/anaplastic tumours and incomplete tumour resection.

1.4.1 Current treatment regimens

1.4.1.1 Surgery

Surgery is a standard-of-care treatment for all medulloblastoma patients. The aim is to remove as much of the tumour as possible (maximal surgical resection) without causing damage to the normal brain tissue, which can cause severe neurological side effects. The extent of resection is dependent upon tumour biology, with more aggressive and invasive tumours proving harder to completely remove. Patients with a residual tumour of >1.5 cm^2 are typically categorised as high risk and subjected to more aggressive therapy regimens. However, a recent systematic review investigating the clinical importance of the extent of surgical resection generated mixed results and the prognostic implications are still unclear (Thompson *et al.*, 2018). This study found that total tumour resection did not confer an overall survival benefit compared to near total resection for most medulloblastoma patients. This clearly demonstrates that the benefits of total resection must be balanced against the survival and quality of life for the patient.

Around 25% of medulloblastoma patients who undergo surgery to remove their tumour develop posterior fossa syndrome, also known as cerebellar mutism, as a side effect of their treatment. This is characterised by loss of speech, hypertonia, extreme irritability, and ataxia. Pre-operative conditions including the size of the tumour (>5 cm diameter) and whether it infiltrates into or compresses the brainstem, are associated with a higher risk of developing posterior fossa syndrome (Pols *et al.*, 2017). Approximately 50% of patients recover from this impairment, whereas the others continue to display residual symptoms (Robertson *et al.*, 2006).

Following surgery, patients are treated with adjuvant chemotherapy with or without radiotherapy, dependent upon their allocated risk group.

1.4.1.2 Treatment for infants

Approximately 25-35% of medulloblastoma cases arise in infants, those under 3 years of age, and have a poor prognosis. Unlike older children, the use of radiotherapy is avoided in infants due to the neurocognitive deficits associated with radiation-induced damage to the developing brain (Pizer and Clifford, 2009). Instead, following maximal surgical resection, infants are treated with chemotherapy regimens including cyclophosphamide, methotrexate, vincristine, carboplatin, and etoposide. Infants treated using these protocols have a 5-year progression free survival of around 80% (if their tumour was completely resected), above 50% (where residual tumour is present), and approximately 30% (for those with macroscopic metastases) (Rutkowski *et al.*, 2005).

The CCG-99703 phase I/II clinical trial tested whether outcome for infants with medulloblastoma could be improved by treatment with higher doses of chemotherapy in combination with peripheral stem cell transplantation (Cohen *et al.*, 2015). This high-dose chemotherapy strategy produced promising overall survival results and patients with SHH medulloblastoma had an excellent outcome

(Lafay-Cousin *et al.*, 2016). The phase II SJYC07 trial aimed to assess whether survival could be improved in young children with risk-adapted therapy. Unfortunately this approach did not improve event-free survival, but methylation subgrouping analyses highlighted that patients with SHH medulloblastoma had an improved progression-free survival outcome compared to Group 3 patients (Robinson *et al.*, 2018). These studies highlight the need for more molecular subgroup driven treatment strategies to improve patient outcomes.

1.4.1.3 Treatment for standard risk medulloblastoma

Following maximal surgical resection, treatment for standard risk medulloblastoma consists of a combination of radiotherapy and adjuvant chemotherapy. Patients with standard risk disease are treated with a reduced dose of craniospinal radiotherapy (with a total dose of 24.3 Gy) plus a localised boost to the posterior fossa of up to 54-55.8 Gy. Radiotherapy is usually combined with weekly concurrent vincristine treatment, followed by a multidrug regimen consisting of cisplatin, vincristine, and lomustine, or cisplatin, vincristine, and cyclophosphamide (Packer *et al.*, 2006). The addition of adjuvant chemotherapy allowed the craniospinal radiotherapy dose to be reduced to 24.3 Gy (from 36.0 Gy), preserving neurocognitive function whilst not affecting patient survival rates. Patients treated using these protocols have a 5-year progression free survival of around 80% (Packer *et al.*, 2012).

The recent SIOP-PNET4 clinical trial aimed to compare two radiotherapy treatment regimens for standard risk patients: standard radiotherapy (as above) versus hyperfractionated radiotherapy (HFRT). HFRT consisted of twice daily 1 Gy doses with total craniospinal and posterior fossa doses of 36 Gy and 60 Gy, respectively, plus a further 68 Gy boost to the tumour bed. Both radiotherapy treatment groups also received identical adjuvant chemotherapy. The study showed that there was no advantage in either event-free or overall survival for patients treated by either

regimen and advised that HFRT should not be adopted as a standard approach due to being more time consuming and resource intensive (Lannering *et al.*, 2012). More recent retrospective analysis of the SIOP-PNET4 cohort aimed to redefine the risk stratification in these standard risk patients to account for molecular biomarkers of the medulloblastoma subgroups (Clifford *et al.*, 2015). More than 50% of the patients analysed were redefined as 'favourable risk' indicating that therapies could have been de-escalated in these patients (Goschzik *et al.*, 2018).

1.4.1.4 Treatment for high risk medulloblastoma

Patients with high risk medulloblastoma require more aggressive treatment including a higher dose of craniospinal radiotherapy (36.0 Gy) with a localised boost to the posterior fossa of up to 54-55.8 Gy. Adjuvant chemotherapy regimens including combinations of cisplatin, lomustine, vincristine, etoposide, cyclophosphamide, carboplatin, and procarbazine have been used. 5-year progression-free survival rates are around 50-60% in high risk patients treated according to these protocols (Packer *et al.*, 2012).

The HIT-2000 trial for patients aged 4-21 with metastatic medulloblastoma aimed to intensify therapy through the addition of neo-adjuvant systemic and intraventricular chemotherapy, craniospinal HFRT, plus the addition of four cycles of maintenance chemotherapy. 5-year overall survival improved in comparison to the HIT-91 trial (Hoff *et al.*, 2009) and the HIT-2000 regimen was considered feasible and conferred an overall favourable survival (Von Bueren *et al.*, 2016).

1.4.2 Improving medulloblastoma treatment

Although medulloblastoma treatment has advanced over the past few decades, challenges still remain. For example, the identification of clinically-relevant

molecular subgroups has changed the way in which medulloblastoma tumours should be risk stratified and therefore, which treatment regimens these patients should receive. As well as this, therapy resistance is a significant problem for many patients and more targeted therapies should be developed to overcome this issue.

1.4.2.1 Redefining medulloblastoma risk groups

Treatment for medulloblastoma is currently based on standard or high risk groups. However, the advances in molecular and genetic profiling has highlighted the intertumoral heterogeneity in medulloblastoma and the need to redefine patient risk groups. There have been numerous proposals as to how patient risk should be stratified. The incorporation of molecular subgroups into the latest WHO classification of CNS tumours allowed the identification of low, standard, and high risk patients based on both their genetic profile and tumour histology (Louis *et al.*, 2016). Table 1.2 summarises the WHO stratification of medulloblastomas based on molecular subgrouping and histological variants. Patients at high risk included those with *TP53*-mutated SHH tumours with classic or LCA histology, and Group 3 LCA tumours.

Table 1.2 Risk stratification for medulloblastoma according to the updated WHO classification

Summary of the WHO classification medulloblastoma risk stratification based on molecular subgrouping and histology. Table adapted from Louis *et al.*, 2016.

Molecular subgroup	Histology	Risk	Frequency of incidence
WNT	Classic	Low-risk	High
	Large cell/anaplastic	Unknown	Very rare
SHH: *TP53* mutant	Classic	High-risk	Low
	Large cell/anaplastic	High-risk tumour	High
	Desmoplastic/nodular	Unknown	Very rare
SHH: *TP53* wildtype	Classic	Standard-risk	Low
	Large cell/anaplastic	Unknown	Low
	Desmoplastic/nodular	Low-risk	High
	MBEN	Low-risk	High
Group 3	Classic	Standard-risk	High
	Large cell/anaplastic	High-risk	Medium
Group 4	Classic	Standard-risk	High
	Large cell/anaplastic	Unknown	Rare

In 2015, an international consensus conference was held with the objective of further refining medulloblastoma risk stratification for non-infant childhood cases in the context of molecular subgrouping (Ramaswamy *et al.*, 2016). The following risk groups were proposed: low, standard, high, and very high risk. A summary of this stratification across subgroups is shown in Table 1.3. Patients diagnosed with low risk medulloblastoma have an excellent prognosis, with a survival rate of more than 90%. Non-metastatic WNT medulloblastoma is categorised as low risk, in addition to non-metastatic Group 4 patients exhibiting loss of chromosome 11. Standard risk patients have an overall survival of 75-90%. SHH medulloblastomas which are either non-metastatic, *TP53* wildtype or non-*MYC* amplified are characterised as standard risk and these patients have an improved outcome compared to patients

with metastatic disease. Non-metastatic Group 3 patients without *MYC* amplification and non-metastatic Group 4 patients without chromosome 11 loss are also stratified as standard risk. High risk patients have an overall survival of 50-75%. Patients with metastatic SHH tumours are stratified as high risk regardless of their *MYCN* amplification status. Metastatic Group 4 patients are also considered to be high risk, with this subset of patients at greatest risk within the high risk subgroup. Patients characterised as very high risk have the worst prognosis, with an overall survival of less than 50%. *TP53*-mutated SHH medulloblastomas are characterised as very high risk irrespective of their metastatic status. Metastatic Group 3 tumours are also characterised as very high risk.

Table 1.3 Risk stratification for non-infant childhood medulloblastoma according to Ramaswamy *et al.*, 2016

Summary of the non-infant childhood medulloblastoma risk stratification based on molecular subgrouping. Table adapted from Ramaswamy *et al.*, 2016.

	WNT subgroup	SHH subgroup	Group 3	Group 4
Low risk (>90% survival)	<16 years	n/a	n/a	Non-metastatic and chr11 loss
Standard risk (75-90% survival)	n/a	*TP53* wildtype, no *MYCN* amplification, or non-metastatic	No *MYC* amplification and non-metastatic	Non-metastatic
High risk (50-75% survival)	n/a	Metastatic or *MYCN* amplification	n/a	Metastatic
Very high risk (<50% survival)	n/a	*TP53* mutation (regardless of metastatic status)	Metastatic	n/a

A recent study by Schwalbe *et al.*, 2017 analysed 428 primary medulloblastoma samples and identified seven distinct molecular subtypes. The WNT subgroup remained unchanged, whilst SHH tumours were divided into two age-dependent groups (SHH-infant and SHH-child). Group 3 and 4 tumours were categorised based on risk (G3-low, G3-high, G4-low, and G4-high). This led to the development of a further model of childhood medulloblastoma risk stratification, assigning patients to one of four groups: favourable, standard, high, and very high risk. These groups were based on both molecular subgrouping and additional risk modifiers including *MYC* amplification, histology, and metastasis (summarised in Figure 1.5). These groups differed in their prognoses with progression-free survivals of 91% (favourable risk), 81% (standard risk), 42% (high risk), and 28% (very high risk).

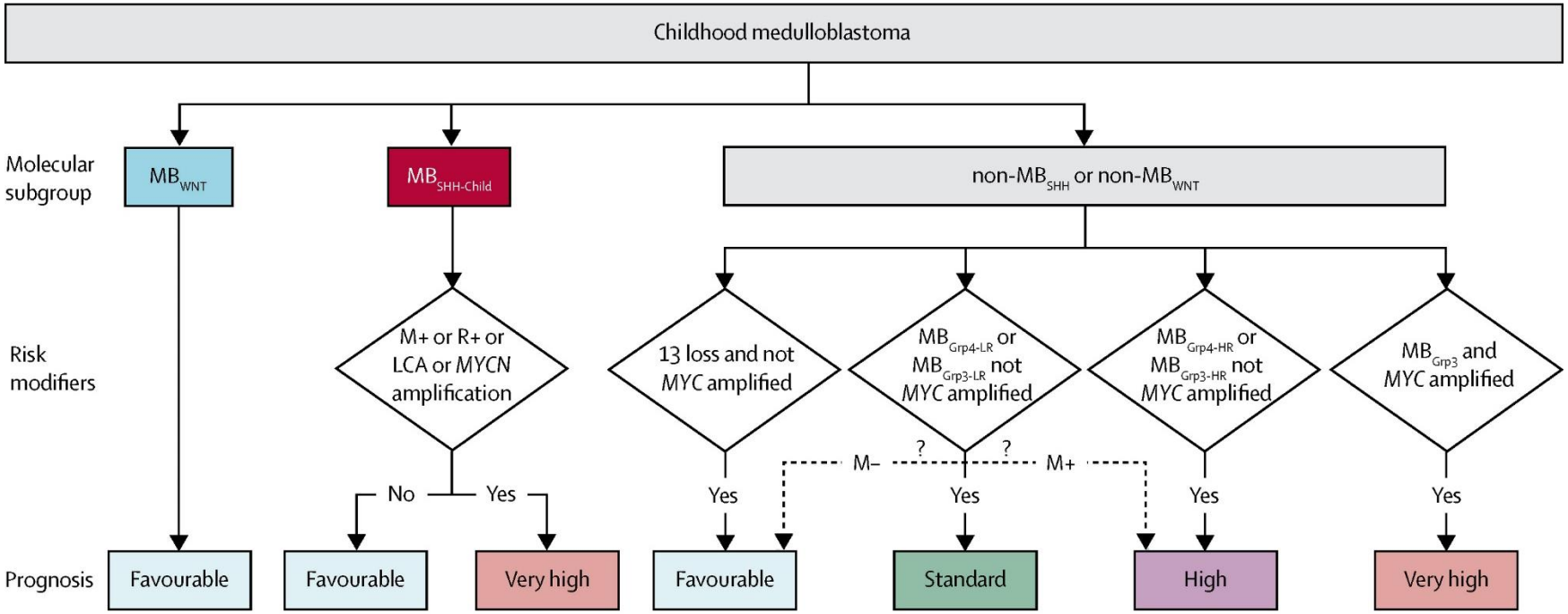


Figure 1.5 Risk stratification for childhood medulloblastoma according to Schwalbe *et al.*, 2017

Summary of the childhood medulloblastoma risk groups (favourable, standard, high, and very high risk) based on molecular subgrouping. Figure taken from Schwalbe *et al.*, 2017.

The three different models described (Louis *et al.*, 2016; Cavalli *et al.*, 2017; Schwalbe *et al.*, 2017) highlight the importance of molecular subgrouping when considering medulloblastoma risk stratification. More recently, Northcott *et al.*, 2019 reviewed these models and described a risk-adapted management algorithm (Figure 1.6). The aim of this model is to ascribe differential therapy to patients on the basis on risk, molecular subgroup, and clinical characteristics. Using this model, patients diagnosed with medulloblastoma are first stratified based on molecular subgroup (WNT, SHH, or non-WNT/non-SHH). Following this, they are assigned to either a standard or high risk group and this designates the type of therapy that they will receive. This model is defining a new era of medulloblastoma management and is allowing dose reduction or escalation of conventional therapy for patients depending upon their apparent risk. This type of approach is already being applied in clinical trials. The actively-recruiting SIOP-PNET5 trial for children (>3-5 years of age) with WNT medulloblastoma is based on the low and standard risk biological profile definitions from the SIOP-PNET4 study. SIOP-PNET5 is testing whether different therapy regimens for low and standard risk patients can improve survival. Low risk patients are treated with radiotherapy and reduced-intensity maintenance chemotherapy, whereas standard risk treatment tests whether carboplatin during radiotherapy followed by maintenance chemotherapy improves patient outcome.

It is evident that directing treatment strategies based on molecular and clinical risk factors has the potential to improve patient outcomes. It is now important that such an approach is adopted internationally and that new clinical trials to assess these risk-adapted models are explored.

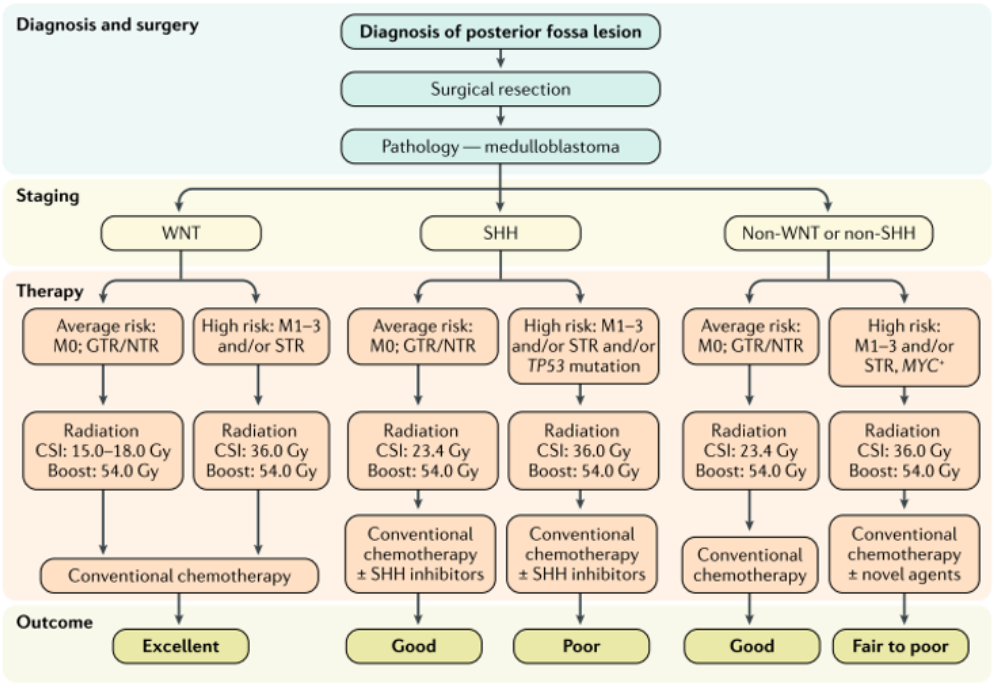


Figure 1.6 Risk-adapted therapy management based on molecular subgrouping according to Northcott et al., 2019

The aim of this model is to ascribe differential therapy to patients on the basis of risk group, molecular subgroup, and clinical characteristics. Patients are stratified based on molecular subgroup (WNT, SHH, or non-WNT/non-SHH) and risk (average or high) to define their treatment regimen. Figure taken from Northcott *et al.*, 2019. GTR: gross total resection, NTR: near-total resection, STR: subtotal resection.

1.4.2.2 Disrupting the blood-brain barrier

The vasculature of the CNS is unique due to its ability to tightly regulate the movement of molecules, cells, and toxins between the blood and the CNS (Daneman and Prat, 2015). This protective layer is called the blood-brain barrier (BBB) and consists of endothelial cells connected by tight junctions and covered in pericytes and basement membrane. The BBB provides a physiological obstacle for cancer treatment as astrocytes surrounding the BBB make it almost 98% impermeable to small molecules and almost 100% to larger molecules (Kumar *et al.*, 2017). A study by Phoenix *et al.*, 2016 described how the response to chemotherapy differed between medulloblastoma subgroups due to the presence or absence of the BBB. They found that WNT tumours lacked a functional BBB due

to the tumours secreting WNT antagonists to block BBB formation. The leaky vasculature of WNT tumours made them vulnerable to treatment and the increased exposure to chemotherapeutics resulted in an improved response to treatment. Therapy response could be improved in non-WNT tumours, where the BBB remains intact, by disruption of the BBB through the inhibition of WNT signalling.

Alternative methods of bypassing the BBB include drug delivery by nanoparticle encapsulation (Oller-Salvia *et al.*, 2016) and local delivery methods such as convection enhanced delivery (Parrish, Sarkaria and Elmquist, 2015). These methods would enable targeted drug delivery to the tumour with the aim of decreasing systemic toxicities.

1.4.2.3 Targeting cancer stem cells

Cancer stem cells (CSCs) are a small subpopulation of cells within a tumour with self-renewal and differentiation capacities. Evidence for CSCs in medulloblastoma was first reported when the stem cell marker CD133 showed an ability for proliferation, self-renewal, and differentiation in human medulloblastoma tissue cultured *in vitro* (Singh *et al.*, 2003) and *in vivo* (Singh *et al.*, 2004). The presence of CSCs within a tumour can contribute to therapy resistance in multiple ways, for example through quiescence, elevated expression of multidrug transporters, enhanced capacity for DNA repair, and decreased entry into apoptosis (Dean, 2009).

A study by Vanner *et al.*, 2014 showed that SHH medulloblastoma growth is driven by rare quiescent Sox2-positive (Sox2+) cells. SOX2, encoded by the SRY (sex determining region Y)-box 2 (*SOX2*) gene, is a transcription factor that plays an important role in the development of the CNS as well as maintaining self-renewal and pluripotency of embryonic and neural stem cells. *SOX2* is amplified and expressed in medulloblastoma, particularly in the SHH subgroup where expression

is required and sufficient to drive proliferation (Ahlfeld *et al.*, 2013). The Vanner study showed that quiescent Sox2+ cells were resistant to antimitotic and SHH-targeted therapies and were likely to be responsible for disease relapse. They also showed that Sox2+ cells could be targeted with the antineoplastic antibiotic mithramycin, a drug known to cross the BBB, blocking tumour growth. Further investigations of mithramycin should be conducted to assess the therapeutic potential of this agent for SHH medulloblastomas in particular.

Cancer stem cells also express members of the adenosine triphosphate (ATP)-binding cassette (ABC) transporter family. ABC transporters are active drug efflux pumps which export drugs back into the systemic circulation and are regarded as major causes of drug resistance (Szakács *et al.*, 2006). Chemotherapy agents including etoposide, vincristine, methotrexate, and doxorubicin are substrates for these drug efflux pumps (Begicevic and Falasca, 2017). Two ABC transporters, ABCB1 (also known as p-glycoprotein) and ABCG2 (breast cancer resistance protein) are highly expressed at the BBB (Uchida *et al.*, 2011). Expression of ABCB1 in medulloblastoma has previously been associated with high risk and a poor patient outcome (Chou *et al.*, 1995; Othman *et al.*, 2014). Targeting ABC transporters is a promising approach for treatment and there are multiple pan-ABC inhibitors and repurposed drugs available (Falasca and Linton, 2012; Bugde *et al.*, 2017). Othman *et al.*, 2014 demonstrated that combination therapy with the ABCB1 inhibitor vardenafil potentiated the effects of etoposide treatment and reduced the clonogenic survival of medulloblastoma cells *in vitro*. ABC transporter inhibition could also be regarded as a mechanism for targeting the CSC subpopulation of therapy-resistant cells present within tumours.

1.4.2.4 Molecularly targeted therapies

The identification of genetic drivers and pathway signatures in medulloblastoma has prompted the development of molecularly targeted therapies. There are numerous targeted approaches currently being tested for medulloblastoma treatment. For example, to target the SHH pathway, SMO inhibitors are proving to be promising candidates to inhibit the activation of downstream SHH target genes (Ransohoff, Sarin and Tang, 2015). The SMO inhibitors vismodegib and sonidegib, approved by the Food and Drug Administration (FDA) for the treatment of basal cell carcinoma, have been tested in paediatric medulloblastoma patients. Phase I and II clinical trials for vismodegib and sonidegib showed that the inhibitors are well tolerated in patients and anti-tumour activity was demonstrated in SHH-driven medulloblastomas (Gajjar *et al.*, 2013; Robinson *et al.*, 2015; Kieran *et al.*, 2017; Li, Song and Day, 2019).

1.5 Medulloblastoma metastasis

Metastasis is the process of tumour spread and involves cell dissemination from the primary tumour and the establishment of secondary disease in a multi-step process termed the invasion-metastasis cascade (Valastyan and Weinberg, 2011). The initiation of metastatic spread involves cell dissemination from the primary tumour. During this process, cells migrate and invade into their surrounding tumour microenvironment (TME), which consists of many different cell types including tumour cells, fibroblasts, immune cells, pericytes, and extracellular matrix (ECM) (Wang *et al.*, 2017). There are numerous different patterns of cell movement including single cell migration and collective migration, where cells migrate as sheets, strands or clusters (as reviewed by Friedl, 2004). Following local invasion, tumour cells enter the blood or lymphatic systems (intravasation) where they circulate and eventually exit the vasculature (extravasation) at distant tissues where they form micrometastases. The propensity of some tumour types to favour particular organs as secondary tumour sites is highlighted through the “seed and soil” hypothesis. This trend was first observed by Stephen Paget in 1889, who suggested that metastasis was not a random event. Instead, it was hypothesised that some tumours (the “seed”) grew preferentially in the microenvironments of specific organs (the “soil”). This hypothesis highlights the importance of the interaction between tumour cells and their TME (Langley and Fidler, 2011).

1.5.1 Mechanisms of medulloblastoma metastasis

The predominant method of metastasis for medulloblastoma tumours is leptomeningeal dissemination, where tumour cells are released into the cerebrospinal fluid (CSF) and transported around the CNS. The leptomeninges is a protective tissue layer which surrounds the brain and spinal cord and consists of two main layers: the arachnoid mater and the pia mater (Figure 1.7). The CSF, a

clear, plasma-like fluid which bathes the CNS, flows between these two structures in the subarachnoid space (Sakka, Coll and Chazal, 2011).

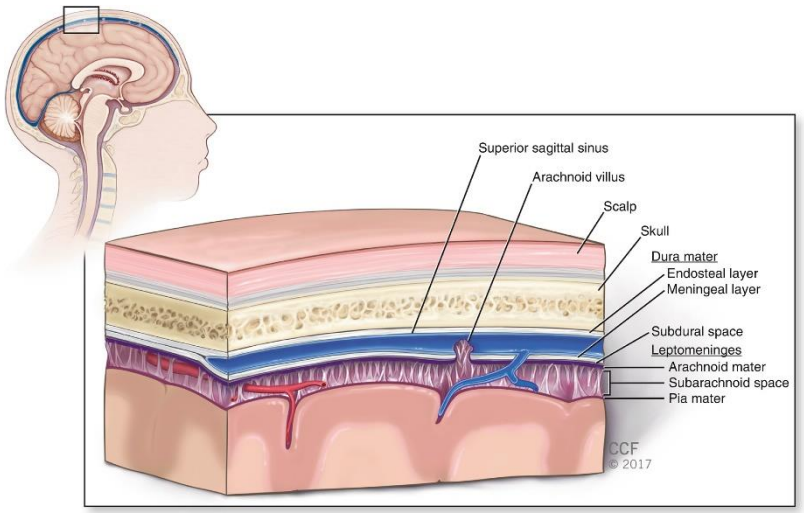


Figure 1.7 Structure of the leptomeninges in the brain
The leptomeninges consists of two main layers: the arachnoid mater and the pia mater, in between which is the subarachnoid space (where the cerebrospinal fluid (CSF) flows). Above the leptomeninges is the subdural space and the dura mater, which is attached to the skull. Image taken from Bellamkonda and Peereboom, 2018.

The mechanisms by which medulloblastoma tumours metastasise via the leptomeninges is still poorly understood. The invasion-metastasis cascade, based on metastatic spread through haematogenous or lymphatic systems, is not an appropriate model to describe leptomeningeal spread. Recently, Fults, Taylor and Garzia, 2019 proposed a leptomeningeal dissemination cascade consisting of three stages:

(1) Initiation: medulloblastoma cells escape from the primary tumour mass in the cerebellum and enter the CSF.
(2) Dispersal: surviving cells spread through the CSF channels.
(3) Colonisation: disseminated cells or cell aggregates implant on a distal surface and establish metastases.

This model more accurately reflects the metastatic process observed in medulloblastomas and serves as an alternative to the standard invasion-metastasis cascade. In addition to leptomeningeal dissemination, it has recently been shown that medulloblastomas do have the capacity to metastasise via a haematogenous route (Garzia *et al.*, 2018). In this study, pairs of mice were surgically joined together to form a parabiosis model, whereby the mice shared a circulatory system but their CSF channels were not connected. Prior to surgery, tumour cells were injected into the donor mice to induce tumour formation. Following parabiosis, spinal leptomeningeal dissemination occurred in both the donor and recipient mice, indicating that the cells which shed from the primary tumour in the donor mice reached the spine of the recipient through a haematogenous route, not via the CSF. Further studies regarding the incidence of haematogenous dissemination and whether there is subgroup specificity should be conducted to further understand this method of metastatic spread.

1.5.2 Subgroup-specific metastatic behaviours

Almost 20-30% of medulloblastoma patients present with metastatic disease at diagnosis and these individuals have a poor outcome (Kool *et al.*, 2012). As previously discussed, the incidence of metastasis differs between the medulloblastoma molecular subgroups, with metastatic disease significantly more common in patients with Group 3 or 4 medulloblastoma (Northcott, Korshunov, *et al.*, 2011). A study by Ramaswamy *et al.*, 2013 aimed to characterise the recurrence patterns across medulloblastoma subgroups and showed that the location of recurrence differs; SHH tumours are more likely to recur locally in the tumour bed whilst Group 3 and 4 tumours predominantly recur with leptomeningeal metastases. In addition, they found that tumours retain the same subgroup at recurrence and this finding was supported by the analysis of paired primary-metastatic patient cohorts (Wang, Dubuc, *et al.*, 2015). However, a study by Wu *et al.*, 2012 showed

that matched primary and metastatic tumours were genetically distinct. They suggested that only rare cells within the primary tumour have the ability to metastasise and this subclone drives clonal selection in the metastases. This study also used a SHH mouse model to investigate the genetic drivers and signalling pathways. Pathway analysis comparing mouse and human medulloblastoma metastases identified only one shared signalling pathway, insulin signalling, which has previously been recognised as essential for medulloblastoma formation (Hahn *et al.*, 2000).

Patterns of medulloblastoma metastasis can be broadly categorised into nodular (the formation of small nodules on the leptomeningeal surface) and diffuse (laminar coatings across the leptomeninges). A study by Dufour *et al.*, 2012 showed that patients with nodular metastases had a significantly better overall survival than patients with diffuse metastases. More recently, Zapotocky *et al.*, 2018 assessed the MRI characteristics of metastatic medulloblastomas and demonstrated that the nodular and diffuse patterns of metastatic dissemination are highly subgroup-specific. In their study, SHH medulloblastomas spread only in a nodular manner whereas Group 3 tumours mainly displayed laminar metastases, with Group 4 tumours exhibiting both of these patterns. These findings further emphasize the heterogenous behaviour of medulloblastoma tumours. In addition, these distinct subgroup preferences for the pattern of metastatic dissemination could allow metastatic tumours to be subgrouped based on MRI characteristics.

1.5.3 Medulloblastoma metastatic staging

Medulloblastomas are categorised according to the Chang staging system, initially developed in 1969 (Chang, Housepian and Herbert, 1969). This system consists of five metastatic (M) stages, with a lower M-stage correlating with prolonged progression-free survival (Ellison, Kocak, *et al.*, 2011). Patients characterised as stage M0 have no evidence of metastases whereas those who are positive for

metastatic spread (M+) are classified in stages M1-M4, dependent upon the extent of metastasis. Stage M1 indicates the presence of tumour cells in the CSF. Seeding in the cerebellar/cerebral subarachnoid space or in the third or lateral ventricles is classified as stage M2, while metastases in the spinal subarachnoid space is classed as stage M3. The highest metastatic stage, M4, involves the presence of metastases outside the cerebrospinal axis.

1.6 Modelling medulloblastoma

Tumour modelling is essential in cancer research to increase our understanding of cancer biology and behaviour, allow drug screening for potential new therapies, and to provide insights into the mechanisms of metastasis. In order to study these processes in a laboratory setting, it is essential to mimic patient tumours as accurately as possible either *in vitro* or *in vivo*. This section aims to summarise the medulloblastoma models currently available, as well as discuss the use of 3D *in vitro* cultures to model cancer.

1.6.1 Current models of medulloblastoma

A review by Neumann, Swartling and Schüller in 2017 described how an ideal medulloblastoma model should reflect the clinical features, histological phenotype, cell of origin, and genetic alterations of a tumour. However, no models are currently available which are capable of encompassing all of these aspects. Instead, each have their own strengths and weaknesses and the choice of which model to use is based on the complexity of the research question being asked. The current models of medulloblastoma can be broadly categorised into the following groups: cell lines (including both established and primary cultures), patient derived xenografts, *ex vivo* organotypic brain slice cultures, and genetically engineered mouse models.

1.6.1.1 Cell lines

The majority of *in vitro* experiments to study medulloblastoma involve the use of established cell lines, well-characterised models which have acquired the ability to proliferate indefinitely. A review of medulloblastoma literature by Ivanov *et al.*, 2016 found that there are around 44 established medulloblastoma cell lines; however, only some of these have their molecular subgroup status confirmed (Figure 1.8).

Experiments using established cell lines are typically performed in two-dimensional (2D) culture, where cells are grown on rigid surfaces such as glass or plastic. Although this method is easily accessible and amenable for high throughput studies, continuous culture can lead to a homogeneous population of cells which do not accurately represent tumour tissue.

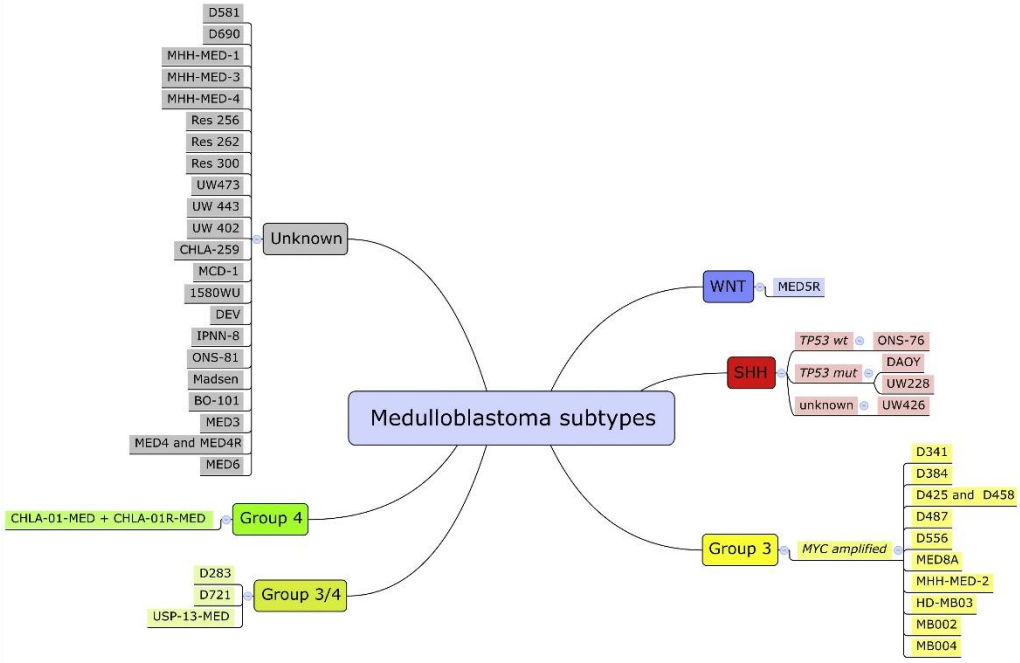


Figure 1.8 Medulloblastoma cell lines classified according to molecular subgroup
There are 44 established medulloblastoma cell lines; however, only a proportion of these have been classified according to molecular subgroup. Figure taken from Ivanov *et al.*, 2016.

Alternatively, cells can be derived directly from patient tissue, a technique known as primary culture. These cell lines more closely resemble tumours; however, their heterogenous nature makes them particularly hard to standardise and results in increased experimental variability. In addition, the generation of primary cultures is particularly difficult and there have been limited successes in creating primary medulloblastoma cell lines. One reason for this may be that, following tumour resection and enzymatic dissociation, cells are normally placed in culture media containing a high percentage of serum to promote growth. For medulloblastoma

cells, this may not be the correct media composition and instead they may require additional growth factors and supplements normally essential for neuronal-like cell growth. Furthermore, the addition of serum to culture media promotes an adherent phenotype which can be unsuitable for some medulloblastoma cell lines which typically grow in suspension.

1.6.1.2 Patient-derived xenografts

Patient-derived xenografts (PDXs) involve the culturing and passaging of patient's tumour cells in immunocompromised mice, preferentially orthotopically (i.e. in the original anatomical location of the tumour). Following the expansion of cells in multiple mice, it is then possible to culture these patient-derived cells *in vitro* and perform functional experiments. However, this whole process is very time-consuming and expensive. In addition, although this method of culture is suitable for more aggressive medulloblastoma tumours which are able to proliferate *in vivo*, it may not be appropriate for the less aggressive WNT subgroup. Successful PDX models have been developed for SHH medulloblastoma tumours, for example Kool *et al.*, 2014 showed how their SHH PDX model could be used to study genotype-related responses to SMO inhibition. In addition, Sandén *et al.*, 2017 established and characterised an orthotopic Group 3 medulloblastoma PDX model for preclinical drug evaluation.

1.6.1.3 Organotypic brain slice cultures

An alternative model of medulloblastoma which bridges the gap between *in vitro* and *in vivo* studies is organotypic brain slice culture. This method involves the culturing and maintenance of cerebellar brain slices *ex vivo* and can be coupled with cell line co-culture to provide a sophisticated model of medulloblastoma growth and spread. This technique has been successfully utilised by multiple

medulloblastoma research groups to study targeted SMO inhibition (Chadwick *et al.*, 2015) and also model the penetration and uptake of nanoparticles (Meng *et al.*, 2016). One of the most informative studies using this *ex vivo* model was performed by Neve *et al.*, 2017 where they modelled cell dissemination and local infiltration of 3D medulloblastoma spheroids co-cultured with cerebellar brain slices. In this study, they used immunofluorescence and advanced imaging techniques to detect tumour cells infiltrating away from the primary tumour spheroid across the brain slice over a 30 day period. Overall, this shows the huge potential of combining both cell line based models with organotypic brain slices to study medulloblastoma growth and progression.

1.6.1.4 Genetically-engineered mouse models

Studying medulloblastoma *in vivo* using genetically-engineered mouse models (GEMMs) has greatly improved our understanding of the genetic pathways dysregulated in tumours, as well as provided insights into the cells of origin for the different molecular subgroups. There are currently mouse models available for WNT, SHH, and Group 3 medulloblastomas; however, no accepted transgenic models of Group 4 have been successfully developed.

As previously discussed in section 1.3.1, mouse models of the WNT subgroup involve targeted expression of mutant *Ctnnb1*. Gibson *et al.*, 2010 developed a transgenic mouse model with constitutively active *Ctnnb1* and mutant *Tp53*. This model was improved by Robinson *et al.*, 2012 by the addition of a constitutively active *Pik3ca* allele, increasing the incidence of murine WNT medulloblastoma from around 15% to 100%. Development of WNT subgroup models with additional gene alterations (e.g. *Ddx3x* and *Smarca4*) is ongoing, with the aim of providing more accurate models of disease (Roussel and Stripay, 2019).

There are several transgenic models of SHH medulloblastoma available. Many of these models, which were developed more than a decade ago, are driven by the deletion of *Ptch1* (Goodrich *et al.*, 1997), constitutive activation of *Smo* (Hatton *et al.*, 2008), *Myc* overexpression (Swartling *et al.*, 2010), or *Sufu* deletion (Lee *et al.*, 2007). However, there are many more SHH medulloblastoma mouse models available, as reviewed by Neumann, Swartling and Schüller, 2017.

The establishment of Group 3 medulloblastoma *in vivo* models has occurred more recently. These models typically utilise targeted *Myc* overexpression, combined with *Trp53* loss-of-function mutations, in neuronal stem cells or progenitor cells (Kawauchi *et al.*, 2012, 2017; Pei *et al.*, 2012). So far, all of the mouse models generated for Group 3 medulloblastoma rely on either *Myc* or *Mycn* overexpression. Group 3 medulloblastoma patients with tumours harbouring *MYC* amplification have a poor outcome (Cavalli *et al.*, 2017); therefore, therapeutic testing using the established mouse models is essential to find ways to improve prognosis. However, Group 3 medulloblastomas are heterogeneous and there should be efforts to develop further *in vivo* models that are based on alternative genetic aberrations within this subgroup.

The main advantages of working with mouse models is the ability to study tumour formation and growth in a living organism which has similarities to human anatomy, physiology, and genetics. In addition, gene editing techniques, for example using the Cre-loxP or Tet-on/Tet-off systems, allow the easy manipulation of the mouse genome to study genetic alterations. *In vivo* systems also model cell-matrix interactions and the blood-brain barrier, a feature commonly missing from *in vitro* studies. However, the generation of GEMMs is very time consuming and expensive. In addition, some aspects of human medulloblastoma biology may not be modelled due to the lack of conservation between mice and humans.

In summary, there are various types of models available to study medulloblastoma. However, there is huge potential to improve current models, as well as develop new

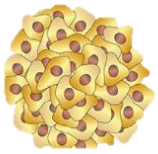
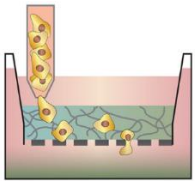
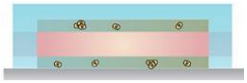
models which recapitulate the intertumoral and intratumoral heterogeneity that exists in the disease.

1.6.2 3D *in vitro* culture

In vitro cell-based experiments performed in 2D culture fail to reflect the multi-dimensional growth of patient tumours and the interactions with their surrounding cellular and extracellular environment. However, over the past few decades, there has been a vast improvements in three-dimensional (3D) culture technologies which aim to recapitulate the characteristics observed in patient tumours to provide a more predictive model of tumour biology (Edmondson *et al.*, 2014). 3D culture models can be broadly categorised into four types: gel/matrix based, spheroids, transwell-based, and tumour-microvessels. A summary of these four approaches is shown in Table 1.4 and reviewed by Katt *et al.*, 2016. Each model has their own advantages and disadvantages depending upon the needs of the researcher. For example, gel/matrix-based models, in which cells are embedded within a gel or ECM to study the interaction of cells in their surrounding matrix, are ideal for studying matrix remodelling as well as cell migration and invasion. Transwell-based and tumour-microvessel models can also be used to assess cell movement; however, neither of these techniques are as high-throughput as spheroid models.

Table 1.4 3D culture techniques

3D culture models can be broadly categorised into four types: gel/matrix-based, spheroids, transwell-based, and tumour-microvessels. A diagram descripting each model and a brief description of the technique is shown. Images adapted from Katt *et al.*, 2016.

3D model	Diagram	Description
Gel/matrix-based models		Cells are embedded within a gel or ECM and the interaction of the cells with the surrounding matrix can be observed.
Spheroid models		Spheroids are aggregates of cells grown in suspension (shown) or embedded within an ECM matrix. This model is suitable for high-throughput growth and drug screening assays.
Transwell-based models		Transwell-based models can be used to assess cell movement across a porous membrane. To assess migration, cells are seeded on top of the membrane and migrate to the bottom chamber. Invasion through an ECM coating on the membrane (shown) can be also be modelled.
Tumour-microvessel models		Microvessel models can be used to study the interactions between tumour cells and ECM, with a cylindrical vessel containing media supplying nutrients.

1.6.3 Spheroid models

3D *in vitro* tumour modelling using spheroids was first pioneered in the early 1970s (Sutherland, McCredie and Rodger, 1971). Spheroids are cell aggregates which can be grown in suspension or embedded within an ECM matrix and have been widely used for drug evaluation and disease modelling (Friedrich *et al.*, 2009; Vinci *et al.*, 2012; Zanoni *et al.*, 2016; Mittler *et al.*, 2017).

1.6.3.1 Spheroid morphology

The spheroid model involves the growth of cancer cells in a spatial conformation, mimicking *in vivo* and patient tumour growth. The influx of oxygen, nutrients, and growth factors and the efflux of carbon dioxide and waste results in different concentration gradients within the 3D structure (Lin and Chang, 2008). These gradients create three zones within the spheroid, as shown in Figure 1.9. The outer layer, which is exposed to the highest concentrations of oxygen, nutrients, and growth factors, consists of proliferating cells. The middle layer contains quiescent, viable cells and the core, in which there is the highest concentration of carbon dioxide and other waste products, is typically hypoxic.

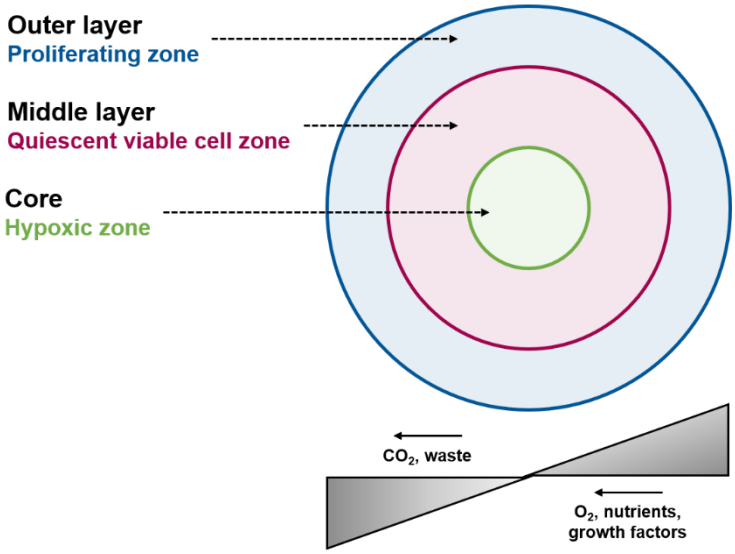


Figure 1.9 Schematic diagram of spheroid zones and physiological gradients
Physiological gradients, caused by the influx of oxygen, nutrients, and growth factors and the efflux of carbon dioxide and waste, result in three zones within the spheroid: an outer layer (consisting of proliferating cells), a middle layer (containing quiescent, viable cells), and a hypoxic core. Figure modified from Lin and Chang, 2008.

1.6.3.2 Methods of spheroid generation

There are numerous methods of spheroid generation. The decision regarding which technique to adopt is typically based on the requirements of the experiment and was reviewed by Hoarau-Véchot *et al.*, 2018. Methods of spheroid generation include:

Spontaneous spheroid formation

This technique utilises non-adherent surfaces to allow the spontaneous formation of spheroids from single cells. Previously, this involved coating cell culture plates with an inert substance to prevent cell attachment, thus forcing the cells to form an aggregate (Kelm *et al.*, 2003). Following on from this, Ivascu and Kubbies, 2006 developed a technique whereby cells seeded in poly(2-hydroxyethyl methacrylate) (poly-HEMA) coated round-bottomed 96-well plates effectively produced spheroids. More recently, the production of ultra-low attachment (ULA) round-bottom plates have modernised the spontaneous spheroid formation technique. These plates have a covalently-bound hydrogel layer that effectively inhibits cellular attachment and promotes the formation of a single spheroid in each well. This method allows spheroid size to be accurately controlled by adjusting the cell seeding density and produces highly reproducible, centrally-located spheroids that are ideal for downstream analysis (Vinci *et al.*, 2012).

Hanging drop method

The hanging drop technique involves placing small drops of cells in suspension (around 15-30 µL) onto the underside of the lid of a tissue culture dish. When the lid is inverted, cells accumulate in the drop and aggregate, forming a spheroid over time. This method of spheroid generation does not rely on matrices or scaffolds, and instead allows the cells to naturally aggregate. More sophisticated, higher-throughput techniques have now been developed using 384-well hanging drop

plates (Tung *et al.*, 2011). These have a tray filled with liquid creating a humidified environment and access holes where cell suspensions are seeded to form the hanging drops. One of the main advantages of the hanging drop method is the ability to generate single, uniform spheroids in each drop, making the approach compatible with drug screening studies. However, although the hanging drop method is simple, long-term culture of spheroids is difficult.

Suspension culture

Suspension culture involves the continual agitation of a cell suspension within a container to promote cell-cell interactions. There are two main approaches to this technique: spinner flasks and bioreactors. Spinner flasks contain a stirrer which continuously moves the cell suspension, generating large yields of spheroids (Lin and Chang, 2008). However due to the forces applied to the cells undergoing this agitation, this method is known for altering spheroid morphology and producing aggregates of differing sizes. The alternative method of suspension culture, bioreactors, was developed by NASA and involves rotating the entire culture container (Schwarz, Goodwin and Wolf, 1992). Similarly to spinner flasks, bioreactors produce a high number of spheroids of different sizes.

Scaffold-based models

Culturing cells in the presence of scaffolds, such as hydrogels, is another method of spheroid generation (Caliari and Burdick, 2016). Cells can be either plated on top or within a matrix and, therefore, this technique is ideal for investigating cell-matrix interactions. However, scaffolds can be expensive and this technique is lower throughput compared to the ULA plate and hanging-drop methods.

Magnetic levitation

An alternative technique of spheroid generation was developed by Souza *et al.*, in 2010. In this method, cells are treated with gold and magnetic iron oxide

nanoparticles with filamentous bacteriophage overnight and then seeded into ULA plates. Immediately after seeding, a magnet-containing lid is placed on top of the plate, prompting cell levitation towards the magnet. Cells aggregate and form spheroids within days. This technique is useful for preparing large spheroids (up to 1 mm^2) and is therefore ideal for users who aim to model hypoxic/necrotic cores. However, this method is not as widely adopted as the beads required are expensive.

1.6.3.3 Applications of spheroid models

The spheroid model can be applied to multiple aspects of cancer research. General spheroid assessments can be informative in terms of their growth kinetics, proliferation, and gene/protein expression profiles. As well as this, they can be applied to numerous functional assays.

One of the most common applications is drug screening, which involves testing the effects of potential chemotherapeutics, small molecule inhibitors, and drug delivery systems. Generally, spheroids are more resistant to treatment than conventional 2D monolayers and their response more accurately reflects the drug concentrations effective *in vivo* (Friedrich *et al.*, 2009).

It is also possible to study cell-cell and cell-ECM interactions *in vitro* using spheroids by modelling their migration on or invasion within different matrices (Vinci, Box and Eccles, 2015). A more detailed description of matrices that can be used to model the ECM is provided in section 1.6.4.

1.6.4 Modelling the brain extracellular matrix

Work by Mina Bissell's group has highlighted the importance of the TME in tumour progression and its effects on neighbouring cells (Bissell and Hines, 2011). As discussed previously, the TME consists of many different cell types including tumour cells, fibroblasts, immune cells, pericytes, and ECM (Wang *et al.*, 2017). The composition of the brain TME differs considerably compared to other tumour types. Most notably, there are unique cell types including microglia, astrocytes, and neurons in the brain (Quail and Joyce, 2017). In addition, the brain ECM has a distinctive composition and is composed primarily of the glycosaminoglycan (GAG) hyaluronan (hyaluronic acid; HA) (Rauch, 2004, 2007). Fibrous glycoproteins including fibronectin, collagens, and laminins are also present in the brain ECM (Novak and Kaye, 2000).

The use of natural or synthetic matrices to study cell-ECM interactions *in vitro* can be coupled with 3D cell culture techniques to provide a more detailed model of tumour biology. Mechanical properties of the ECM, such as architecture and rigidity, influence cell behaviour. Tissue or matrix stiffness is measured by the elastic modulus (E), the amount of force required to deform a substance in Pascals (Pa) (Barnes, Przybyla and Weaver, 2017). The brain is one of the softest organs in the body ($E \leq 4x10^2$ Pa); however, brain tumour stiffness can range between 100-10,000 Pa. Therefore, the use of hydrogels which mimic tissue stiffness are especially informative as they recapitulate the ECM stresses that the tumour would face *in vivo* and in patients (Vanderhooft *et al.*, 2009).

1.7 Hypothesis and aims

Although there are some publications discussing 3D *in vitro* models of medulloblastoma (Zanini *et al.*, 2013; Ivanov *et al.*, 2014; Grotzer, Neve and Baumgartner, 2016), there is a need to develop a robust, reliable, and optimised 3D model for the medulloblastoma research community.

We hypothesised that medulloblastoma growth, drug response, and metastatic dissemination could be modelled in 3D culture.

The aims of this study were to:

(1) Optimise, validate, and characterise a 3D *in vitro* model of medulloblastoma
(2) Apply the established 3D medulloblastoma model to study drug response and metastatic dissemination
(3) Identify factors involved in SHH medulloblastoma metastasis using the 3D *in vitro* model through next-generation sequencing technologies.

Chapter 2

Materials and Methods

Chapter 2. Materials and Methods

2.1 Standard cell culture

2.1.1 Standard culture media

Nine medulloblastoma cell lines were used in this study. Clinical information for each cell line is detailed in Table 3.1. DAOY, D283, D425, and D458 cells were cultured in Dulbecco's Modified Eagle Medium (DMEM; Gibco, 31885) supplemented with 10% foetal bovine serum (FBS; HyClone, SH30541.03). UW228-3 cells were cultured in DMEM/F-12 nutrient mixture (Gibco, 11320) supplemented with 15% FBS and 1% sodium pyruvate (Gibco, 11360070). ONS76 and HD-MB03 cells were cultured in RPMI 1640 (Sigma-Aldrich, R8758) supplemented with 10% FBS. CHLA-01-MED and CHLA-01R-MED were cultured in DMEM/F-12 supplemented with 2% B-27 supplement (Gibco, 17504044), 20ng/mL recombinant human epidermal growth factor (EGF; Gibco, PHG0315), and 20ng/mL recombinant human basic fibroblast growth factor (FGF; Gibco, PHG0266).

2.1.2 Adherent cell culture

The SHH medulloblastoma cell lines DAOY, ONS76, and UW228-3 cell lines grew adherently in standard culture. For these cell lines, stocks were recovered from liquid nitrogen and thawed rapidly in a 37°C water bath. Cells were then transferred into tissue culture treated T75 flasks (Corning, 430641U) containing 10 mL of pre-warmed standard culture medium and incubated at 37°C in 5% CO_2 and high humidity. Medium was replaced after 24 hours and cells were incubated until they reached approximately 70% confluency. To subculture cells, media was discarded and cells were washed with 10 mL Hank's Balanced Salt Solution (HBSS; Gibco,

14170), followed by a 5 minute incubation in pre-warmed Trypsin-EDTA (Sigma-Aldrich, T4174) at 37°C to promote cell detachment. Trypsinisation was inhibited by the addition of media and cells were then seeded into T75 flasks at a ratio of 1:10 and incubated at 37°C in 5% CO_2 and high humidity.

2.1.3 Semi-adherent cell culture

The Group 3 medulloblastoma cell lines HD-MB03, D283, D425, and D458 grew semi-adherently in standard culture, with populations of adherent, semi-adherent, and suspension cells within the flask. For these cell lines, stocks were recovered from liquid nitrogen and thawed rapidly in a 37°C water bath. Cells were then transferred to a 15 mL tube (Greiner Bio-One, 188261), diluted in 5 mL standard culture medium and centrifuged for 5 minutes at 100 x *g*. Following centrifugation, the supernatant was discarded and cells were resuspended in pre-warmed standard culture medium and transferred into tissue culture treated T25 flasks (Eppendorf, 0030710126). Cells were incubated at 37°C in 5% CO_2 and high humidity until they reached approximately 70% confluency. To subculture cells, media was removed and transferred into a 50mL tube. Cells were washed with 10 mL HBSS and the wash was transferred to the same tube. Cells were then incubated in pre-warmed Trypsin-EDTA for 5 minutes at 37°C to promote detachment. Trypsinisation was inhibited by the addition of media and the resulting cell suspension was also transferred to the tube which was then centrifuged at 100 x *g* for 5 minutes. Following centrifugation, the supernatant was discarded and cells were resuspended in their standard culture media then seeded into tissue culture treated T75 flasks at a ratio of 1:5 to 1:10 and incubated at 37°C in 5% CO_2 and high humidity.

2.1.4 Suspension cell culture

The Group 4 medulloblastoma cell lines CHLA-01-MED and CHLA-01R-MED grew as clusters and single cells in suspension in standard culture. These cell lines were recovered in the same way as semi-adherent cell lines (as described in section 2.1.3) but were grown in non-treated T25 flasks (Eppendorf, 0030710029). To maintain cells, fresh medium was added every 3-4 days. To subculture cells, the cell suspension was transferred into a 50 mL tube and centrifuged for 5 minutes at 100 x *g*. Cells were then resuspended in ¼ conditioned medium and ¾ fresh medium and seeded into non-treated T25 flasks at a ratio of 1:2 to 1:4 and incubated at 37°C in 5% CO_2 and high humidity.

2.1.5 Preparation of cell line stocks

Cell suspensions were centrifuged for 5 minutes at 100 x *g* and the supernatant was discarded. Adherent cell lines were resuspended in freezing medium (90% FBS + 10% dimethyl sulfoxide (DMSO; Sigma, D2650)), whereas semi-adherent and suspension cell lines were resuspended in Cellbanker® 2 cryopreservation media (AMS Biotechnology Ltd., 11891). Cells were frozen at a concentration of 1 x 10^6 cells/mL as either 1 mL aliquots in cryovials (Alpha Laboratories, LW3532) or 0.5 mL aliquots in FluidX tubes (Brooks Life Sciences, 68-0703). Aliquots were placed at -80°C in a Mr Frosty™ (Thermo Fisher Scientific, 10110051) overnight before being transferred to liquid nitrogen for long-term storage.

2.2 Spheroid culture

2.2.1 Neurosphere medium

Neurosphere medium for spheroid culture was made using DMEM/F-12, 2% B-27 supplement, 1% N-2 supplement (Gibco, 17502048), 2 µg/mL Heparin (Stem Cell Technologies, 07980), 20 ng/mL EGF, and 10 ng/mL bFGF. Fresh neurosphere medium was made weekly and stored at 4°C.

Some cell lines required the addition of methyl cellulose in the neurosphere medium to promote tighter spheroid formation. To prepare a 1.2% stock, 600 mg of methyl cellulose (Sigma, M7027) was autoclaved and diluted in 50 mL of pre-heated DMEM/F-12. The solution was stirred for 30 minutes at room temperature, then for an additional 2 hours at 4°C. Following this, the solution was centrifuged for 2 hours at 5,000 x *g* and the clear, viscous supernatant was removed. Methyl cellulose was stored at 4°C for up to 3 months and was diluted to a concentration of 0.24% in neurosphere medium for experimental use.

2.2.2 Spheroid optimisation

To determine the optimal growth conditions for medulloblastoma cell lines in the spheroid model, different culture media and seeding densities were tested. Cells were harvested, centrifuged at 100 x *g* for 5 minutes and resuspended in either standard culture medium or neurosphere medium with or without methyl cellulose. Cells were then seeded at increasing densities in ultra-low attachment (ULA) round-bottom 96-well plates (Corning, 7007) in a volume of 200 µL/well. The outer wells of the ULA plate were filled with HBSS to reduce the effects of evaporation. For semi-adherent and suspension cell lines, plates were centrifuged after seeding at 100 x *g* for 5 minutes to encourage spheroid compactness. Plates were incubated

at 37°C in 5% CO_2 and high humidity and spheroids were maintained by performing 50% medium replenishments every 3-4 days. Spheroid formation and growth was assessed on days 1, 4, and 7 post-seeding by manual imaging, as detailed in section 2.3.1. Significant differences in spheroid diameter were calculated using two-way ANOVA analyses with Sidak's multiple comparisons post-hoc test using GraphPad Prism 8.1.2 (GraphPad Software Inc.).

2.2.3 Generation and maintenance of spheroids

Cell lines were grown in their standard culture conditions until they reached approximately 70% confluency. At this point, cells were harvested and dissociated into single cell suspensions for spheroid generation. Cells were seeded in their optimal conditions in a volume of 200 µL/well in a ULA plate. Plates were incubated at 37°C in 5% CO_2 and high humidity. Spheroids were maintained by performing 50% medium replenishments every 3-4 days.

2.3 Spheroid analysis

2.3.1 Manual imaging of spheroids

Spheroid images were taken on a camera (Canon, DS126431) attached to a brightfield microscope (Olympus, CKX41) at 10X magnification. The scale of images was determined using a calibration slide. A macro developed by Ivanov *et al.*, 2014, compatible with the open-access software ImageJ (Fiji), was used for spheroid size analysis. The macro automatically calculated spheroid area and drew a blue outline of the detected spheroid. When the macro failed to detect the correct spheroid circumference, manual outlining was performed. Spheroid area (A) measurements were exported to Microsoft Excel and additional dimensions were calculated, including:

$$\text{Radius (r)} = \sqrt{\frac{A}{\pi}} \qquad \text{Diameter (d)} = 2r \qquad \text{Volume (v)} = \frac{4}{3}\pi r^3$$

2.3.2 Coefficient of variation analysis

Coefficient of variation (CV) analysis was used to determine the uniformity of spheroids both within (intraplate CV) and between (interplate CV) experimental repeats. Spheroids were generated as described in section 2.2.3, imaged on day 4 and variability in spheroid diameter was calculated using the following equation:

$$\text{CV (\%)} = \frac{\text{Standard deviation}}{\text{Mean}} \times 100$$

2.3.3 CellTiter-Glo® 3D cell viability assay

The CellTiter-Glo® 3D cell viability assay (Promega, G9683) was used to assess spheroid viability at multiple time points. This luciferase-based assay lysed the cells and generated a luminescent signal proportional to the amount of adenosine triphosphate (ATP) present, indicative of the number of viable cells within the spheroid. To assess viability, spheroids were transferred in 100 µL medium from the ULA plate in which they were generated into a black-walled 96-well plate (Greiner Bio-One, 655090) for analysis. 100µL of CellTiter-Glo® 3D reagent (thawed to room temperature) was added to each well. The plates were shaken at 250 rpm for 5 minutes in an orbital incubator (Stuart®, SI500) to promote cell lysis, followed by an additional 25 minute incubation at room temperature. Luminescence was measured on a FLUOstar Omega plate reader (BMG Labtech Ltd). Measurements were exported to Microsoft Excel and the data were normalised against a blank (media only) control. The relationship between luminescence signal and time was assessed using Pearson's correlation coefficient (r) using GraphPad Prism 8.1.2.

2.4 Spheroid sectioning and staining

2.4.1 Embedding spheroids in a HistoGel™ block

Spheroids were generated and maintained as described in section 2.2.3. On days 7, 14, and 21, ten spheroids were pooled into a 1.5 mL microcentrifuge tube, medium was removed and spheroids were washed with 1 mL of HBSS. The wash was removed and spheroids were resuspended in 500 µL of HistoGel™ (Thermo Fisher Scientific, HG-4000-012), pre-warmed to 60°C. Spheroids in HistoGel™ were transferred to a Tissue-Tek® cryomold (Agar Scientific, AGG4581) and were rapidly cooled by placing on ice. Spheroid blocks were transferred from the cryomold into tissue processing cassettes (Simport, M490). Blocks were fixed in 4%

paraformaldehyde (PFA) for two hours, washed twice for 10 minutes in phosphate buffered saline (PBS) and then processed.

2.4.2 Processing of spheroid blocks

Spheroid blocks were processed overnight in a tissue processor (Leica, TP1020). Samples were dehydrated by incubating in a series of alcohol solutions with increasing concentrations (one bath of 50%, 70%, 90%, and four baths of 100% methanol; one hour each), cleared with xylene (three baths; one hour each), and infiltrated with molten paraffin (two baths; two hours each; vacuum on). The following day, spheroid blocks were embedded in paraffin using a wax embedding machine (Leica, EG1160).

2.4.3 Sectioning of spheroid blocks

Sectioning of the spheroid blocks was kindly completed by Dawn Dilks (laboratory technician). Spheroid microarray blocks were placed on ice for at least one minute prior to sectioning. Blocks were carefully aligned on a microtome (Leica, RM2235) and 4 µm sections were cut. The resulting ribbons were floated onto a pre-heated 52°C water bath (Leica, HI1210) and separated with forceps. Each section was placed onto an APES-coated slide and left to dry at 60°C on a hot block (Leica, HI1220).

2.4.4 Immunohistochemical staining of spheroid sections

Immunohistochemistry (IHC) was used to visualise the distribution of specific proteins within spheroid sections. Slides were placed in a rack and deparaffinised in xylene for 15 minutes and rehydrated in a series of ethanol baths (100% ethanol for 10 minutes followed by 95%, 80%, and 70% ethanol for 5 minutes each) before

being washed with tap water. Heat-induced antigen retrieval was performed by placing the rack in a pre-heated steamer in sodium citrate buffer (Table 2.1) for 40 minutes. Following antigen retrieval, slides were washed in PBS for 2 minutes and placed in a humidified chamber.

Table 2.1 Sodium citrate buffer recipe

Reagent	Quantity for 1 L
Citric acid monohydrate	2.1 g
Distilled water	1 L
Sodium hydroxide (to pH 6)	~ 13 mL
Tween 20	0.5 mL

Spheroid sections were circled with a hydrophobic pen (Vector Laboratories, H4000) and slides placed in a humidified chamber. Endogenous peroxidase activity was suppressed to reduce background signal by incubating sections in peroxidase suppressor (Thermo Fisher Scientific, 35000) for 30 minutes, followed by two 3 minute washes in PBS. Next, slides were blocked in Universal Blocker™ blocking buffer (Thermo Fisher Scientific, 1859332) for 30 minutes. Slides were then incubated in primary antibody (diluted in blocking buffer) for one hour at room temperature. The details of each primary antibody are shown in Table 2.2. Tissue in which the protein is known to be expressed was included as a positive (with primary antibody) and negative (without primary antibody) control.

Table 2.2 Details of primary antibodies used in the study

Antibody	Species	Dilution	Positive tissue control	Product details
Ki67	Mouse	1:400	Tonsil	Cell Signalling Technology, 9449
CA9	Mouse	1:800	Breast cancer	Absolute Antibody, Ab00414-1.1
SOX2	Mouse	1:200	Foetal brain	Invitrogen, MA1-014
CD44	Rabbit	1:500	Tonsil	Abcam, ab157107

Slides were washed twice for 3 minutes in PBS, before a one hour incubation in a horseradish peroxidase (HRP)-tagged secondary antibody (either goat anti-mouse (Abcam, ab214879) or goat anti-rabbit (Abcam, ab214880)), then washed twice for 3 minutes in PBS. Antibody detection was performed using diaminobenzidine (DAB) chromogen by diluting 30 µL of SignalStain® DAB chromogen concentrate (Cell Signalling Technology, 11725) in 1 mL of SignalStain® DAB diluent (Cell Signalling Technology, 11724) and incubating slides until desired staining was achieved (between 5 and 10 minutes). Slides were washed in water for 5 minutes and counterstained with Harris Modified haematoxylin (Thermo Fisher Scientific, 1859352), then washed in tap water. Slides were dehydrated in ethanol (95%, then 100%) and xylene, before being mounted with medium (Thermo Fisher Scientific, 1859351). Images of stained spheroid sections were taken at 10X and 20X magnification (Brunel Microscopes Ltd., N510).

2.5 Drug treatments

2.5.1 Drugs used in this study

Details of the drugs used in this study are included in Table 2.3.

Table 2.3 Drugs used in the study

Drug	Stock concentration	Vehicle	Product details
Etoposide	10 mM	DMSO	Selleckchem, S1225
Vincristine	100 µM	DMSO	Sigma, V8388
Cisplatin	10 mM	DMF	Selleckchem, S1166
Lomustine	50 mM	DMSO	Selleckchem, S1840
Vardenafil	10 mM	DMSO	Selleckchem, S2515

2.5.2 2D monolayer and 3D spheroid drug response

Drug response was assessed in cell lines grown as 2D monolayers and 3D spheroids. For 2D monolayer drug response analysis, cells were harvested when they reached approximately 70% confluence and seeded at a density of 1,000 cells/well in black-walled 96-well plates. Cells were left to adhere overnight before drug treatment. For 3D spheroid drug response analysis, spheroids were generated as described in section 2.2.3 in black-walled 96-well ULA plates (Corning, 4520) to avoid transfer after treatment. Spheroids were drug treated on day 4.

At the point of drug treatment, 50% of medium was removed from each well and replaced with drug at 2X concentration. 2D monolayers and 3D spheroids were

treated with increasing concentrations of four chemotherapy drugs: etoposide, vincristine, cisplatin, and lomustine (details of these drugs are shown in Table 2.3).

Following 72 hours of drug treatment, CellTiter-Glo® 3D reagent (thawed to room temperature) was added to each well at a 1:1 ratio. The plates were shaken at 250 rpm for 5 minutes in an orbital incubator to promote cell lysis, followed by an additional 25 minute incubation at room temperature. Luminescence was measured on a FLUOstar Omega plate reader. Measurements were exported to Microsoft Excel and the data were normalised against a blank (media only) control. Drug response was calculated as a percentage of the vehicle-treated control and dose-response curves and IC_{50} values were generated by non-linear regression analysis using GraphPad Prism 8.1.2. Fold changes in IC_{50} values between 2D monolayers to 3D spheroids were calculated using the following equation:

$$\text{Fold change} = \frac{(B - A)}{A}$$

(where A and B correspond to the IC_{50} values of 2D monolayers and 3D spheroids, respectively).

2.5.3 Fluorescent staining of drug treated spheroids

Fluorescent staining of drug treated spheroids was combined with automated imaging analysis to provide readouts of spheroid viability. Spheroids were generated as described in section 2.2.3. On day 4, 50% of medium was removed from each well and replaced with three concentrations of vincristine (1, 5, and 10 nM) at 2X concentration. Following 72 hours of treatment, the fluorescent dyes Calcein-AM (CAM; Nexcelom Bioscience, CS1-0119) and Propidium Iodide (PI; Nexcelom Bioscience, CS1-0109) were added to the spheroid wells at a final concentration of 1 µg/mL and incubated for 1 hour. Automated imaging analysis was performed using the Celigo® cytometer (Nexcelom Bioscience) to measure the

relative intensity of CAM and PI signals. Images were acquired of each well in 4 fields of view at a resolution of 1 µm/pixel using the brightfield, red, and green channels. Data were exported to Microsoft Excel where CAM/PI ratios were calculated to provide an indication of spheroid health and viability with a ratio of >1 representing high viability and <1 indicating low viability. Significant differences in CAM/PI ratios were calculated using one-way ANOVA analyses with Dunnett's multiple comparisons post-hoc test using GraphPad Prism 8.1.2.

2.5.4 Continual monitoring of drug effects

Continual monitoring of spheroid volume was used to assess the effects of drugs over time. Spheroids were generated as described in section 2.2.3 and were drug treated on day 4 for 72 hours. Following treatment, a 50% medium replenishment was performed on days 7 and 10. Images were taken on day 4 (pre-treatment) and day 7 (post-treatment), as well as additional monitoring on days 10 and 13. Spheroid size measurements were determined as described in section 2.3.1 and changes in spheroid volume were calculated as a percentage of day 4. Significant differences in volume between the vehicle- and drug-treated spheroids were calculated using repeated measures two-way ANOVA analyses with Dunnett's multiple comparisons post-hoc test using GraphPad Prism 8.1.2.

2.5.5 Combination drug treatments

Spheroids were generated as described in section 2.2.3 and were treated with either etoposide, vincristine, or cisplatin in combination with 10 µM vardenafil (details shown in Table 2.3) for 72 hours. Images were taken after treatment and spheroid sizes were measured as described in section 2.3.1. Changes in spheroid volume were calculated as a percentage of the vehicle-treated controls.

Significance was calculated using one-way ANOVA analyses with Sidak's multiple comparisons post-hoc test using GraphPad Prism 8.1.2.

2.6 Spheroid migration and invasion assays

2.6.1 Collagen IV

Collagen IV (Cultrex®, 3410-010) was thawed on ice for 2 hours and diluted in cold, sterile water to a concentration of 10 µg/mL. 50 µL of diluted collagen IV was added to each well of a tissue-culture treated 96-well plate (Eppendorf, 0030730119) and the solution was spread evenly over the well's surface. The collagen IV-coated plates were left to dry for 2 hours at room temperature, before wells were rinsed with culture medium. Day 4 spheroids were then transferred from the 96-well ULA plate in which they were generated to the collagen IV-coated plate in 100 µL of neurosphere medium. An additional 100 µL of fresh neurosphere medium was added to each well and plates were incubated at 37°C for 1 hour to allow the spheroids to settle on the collagen IV matrix. Spheroid migration across collagen IV was assessed by manual imaging over a 72 hour period.

2.6.2 Basement membrane extract

Basement Membrane Extract (BME; Cultrex®, 3432-001) was thawed overnight at 4°C. The batch used in this study (#33645G15) had a concentration of 16.15 mg/mL.

For spheroid migration experiments, BME was diluted to a concentration of 10 mg/mL in cold neurosphere medium. 50 µL of diluted BME was added to each well of a tissue-culture treated 96-well plate and the solution was spread evenly over the well's surface. The BME-coated plates were incubated at 37°C for 1 hour to allow

the BME layer to set. Day 4 spheroids were then transferred from the 96-well ULA plate in which they were generated, to the BME-coated plate in 100 µL of neurosphere medium. An additional 100 µL of fresh neurosphere medium was added to each well and plates were incubated at 37°C for 1 hour to allow the spheroids to settle on the BME matrix. Spheroid migration across BME was assessed by manual imaging over a 72 hour period.

For BME invasion experiments, spheroids were generated as described in section 2.2.3. On day 4, 100 µL of medium was removed from each well and BME was added to make a final concentration of either 3 mg/mL or 10 mg/mL. Plates were incubated at 37°C for 1 hour to allow the BME to set. An additional 50 µL of fresh neurosphere medium was then added to each well. Spheroid invasion in BME was assessed by manual imaging over a 72 hour period.

2.6.3 HyStem™ hydrogel

The HyStem™ hydrogel kit (ESI-BIO™, GS311) was used as a brain-specific matrix for spheroid migration and invasion assays. The HyStem™ kit consisted of Glycosil® (thiol-modified HA), ExtraLink®-Lite (PEGDA; polyethylene glycol diacrylate), and water. Glycosil®, ExtraLink®-Lite, and water were thawed at room temperature. 1mL of water was added to the thawed Glycosil® and the vial was placed on a rocker (Stuart®, SRT6) for 40 minutes to allow the solution to dissolve. ExtraLink®-Lite was prepared by adding 250 µL of water to the thawed vial. Hydrogels were prepared at 1% Glycosil® and 2% ExtraLink®-Lite concentrations to achieve a matrix stiffness around 1.5-2 kPa. The ECM components laminin-111 (Cultrex®, 3400-010-03), collagen I (Cultrex®, 3447-020-01), and fibronectin (Cultrex®, 3420-001-03) were incorporated in some hydrogel conditions at a concentration of 50 µg/mL (optimised by Dr Franziska Linke, Postdoctoral Research Fellow in Dr Beth Coyle's group).

For HyStem™ invasion experiments, spheroids were generated as described in section 2.2.3. On day 4, as much media as possible was removed from each well of the spheroid plate (around 180 µL). Spheroids were then embedded in 50 µL of hydrogel and incubated at 37°C for 30 minutes to allow the gel to set. An additional 100 µL of fresh neurosphere medium was then added to each well. Spheroid invasion in HyStem™ was assessed by manual imaging over a 72 hour period.

For HyStem™ migration experiments, 50 µL of diluted hydrogel was added to each well of a tissue-culture treated 96-well plate and the solution was spread evenly over the well's surface. The hydrogel-coated plates were incubated at 37°C for 30 minutes to allow the gel layer to set. Day 4 spheroids were then transferred from the 96-well ULA plate in which they were generated, to the hydrogel-coated plate in 100 µL of neurosphere medium. An additional 100 µL of fresh neurosphere medium was added to each well and plates were incubated at 37°C for 1 hour to allow the spheroids to settle on the matrix. Spheroid migration across HyStem™ hydrogels was assessed by manual imaging over a 72 hour period.

Assessment of the migratory patterns of single cells seeded on hydrogel matrices was performed by Dr Franziska Linke. HyStem™ hydrogel-coated 96-well plates were prepared as described above and single cells were seeded at a density of 10,000 cells/well on top of the matrices. The plate was transferred to a 37°C incubator and was not moved for the following 4 hours to allow cell attachment. Cell movement on HyStem™ hydrogels was assessed by manual imaging every 3-4 days.

2.7 Next-generation sequencing

2.7.1 Sample preparation

Five conditions were selected for next-generation sequencing (NGS). Spheroid samples were harvested after 48 hours of migration and single cell samples were harvested on day 12. Ten wells per condition were pooled into a 1.5 mL microcentrifuge tube and snap-frozen in liquid nitrogen and stored at -80°C. RNA isolation was performed using the NucleoSpin® RNA Plus kit (Macherey-Nagel, 740984). Samples were transferred to tubes containing lysing Matrix D beads (MP Biomedicals™, 11412420), 1.4mm ceramic spheres used for grinding matrices. 350 µL of lysis buffer was added to each tube and samples were homogenised for 30 seconds using a Fast-Prep^{24} tissue homogeniser (MP Biomedicals™, 12079310). Samples were then transferred to a new 1.5 mL microcentrifuge tube and centrifuged at 11,000 x *g* for 5 minutes to pellet the hydrogel at the bottom of the tube. The homogenised lysate was transferred to a NucleoSpin® gDNA removal column and centrifuged at 11,000 x *g* for 30 seconds. Following centrifugation, the column was discarded and 100 µL of binding solution was added to the flow-through to adjust the RNA binding conditions. The lysate was transferred to a NucleoSpin® RNA Plus column and centrifuged at 11,000 x *g* for 15 seconds. The membrane was washed with 200 µL of wash buffer 1, followed by 600 µL of wash buffer 2, both centrifuged at 11,000 x *g* for 15 seconds. A final wash with 250 µL of wash buffer 2 was performed and samples were centrifuged at 11,000 x *g* for 2 minutes to dry the membrane completely. RNA was eluted in 30 µL of RNase-free water and centrifuged at 11,000 x *g* for 1 minute. RNA was stored at -80°C and samples were shipped on dry ice to QIAGEN Genomic Services (Hilden, Germany), where the subsequent steps of NGS were performed.

Quality control of the RNA was performed using the Qubit RNA high sensitivity assay (Invitrogen™, Q32852) which quantified the amount of RNA in each sample. Samples with 100 ng or more of RNA in total were suitable for mRNA NGS. Samples with lower RNA yields were lyophilised and resuspended in a smaller volume of RNase-free water. Another quality control step was performed to quantify the RNA. Samples with an RNA concentration above 1.4 ng/mL were appropriate for 3' UPX NGS. However, samples with a lower RNA concentration were unsuitable for either method of NGS.

2.7.2 mRNA next-generation sequencing

2.7.2.1 Library preparation

Library preparation was carried out using the TruSeq® Stranded mRNA library preparation kit (Illumina, 20020594) according to manufacturer's instructions. A schematic diagram describing the workflow for this kit is shown in Figure 2.1. The process involved the following steps, as described in the TruSeq Stranded mRNA protocol:

(1) Purification and fragmentation of mRNA:

The poly-A containing mRNA molecules were purified using poly-T oligo attached magnetic beads. Following purification, the mRNA molecules were fragmented into small pieces and primed for cDNA synthesis.

(2) First strand cDNA synthesis:

The cleaved RNA fragments were copied into first strand cDNA using reverse transcriptase and random primers.

(3) Second strand cDNA synthesis:

This process removed the RNA template, synthesised a replacement strand, and incorporated dUTP in place of dTTP to generate double-stranded cDNA. The incorporation of dUTP quenched the second strand during amplification

and magnetic beads separated the double-stranded cDNA from the second strand reaction mix, resulting in blunt-ended cDNA.

(4) Adenylation of 3' ends:

A single ‘A’ nucleotide was added to the 3' ends of the blunt fragments to prevent them from ligating to each other during the adapter ligation reaction. A corresponding single ‘T’ nucleotide on the 3' end of the adapter provided a complementary overhang for ligating the adapter to the fragment.

(5) Ligation of adapters:

Multiple indexing adapters were ligated to the ends of the double-stranded cDNA fragments, to prepare them for hybridisation onto a flow cell.

(6) Enrichment of DNA fragments:

This process used PCR to selectively enrich DNA fragments that had adaptor molecules on both ends and amplified the amount of DNA in the library.

(7) Final library:

The final library was prepared and underwent quality control (QC) before sequencing.

(8) Library QC:

The libraries size distribution was validated and quality inspected on a 4200 TapeStation (Agilent Technologies).

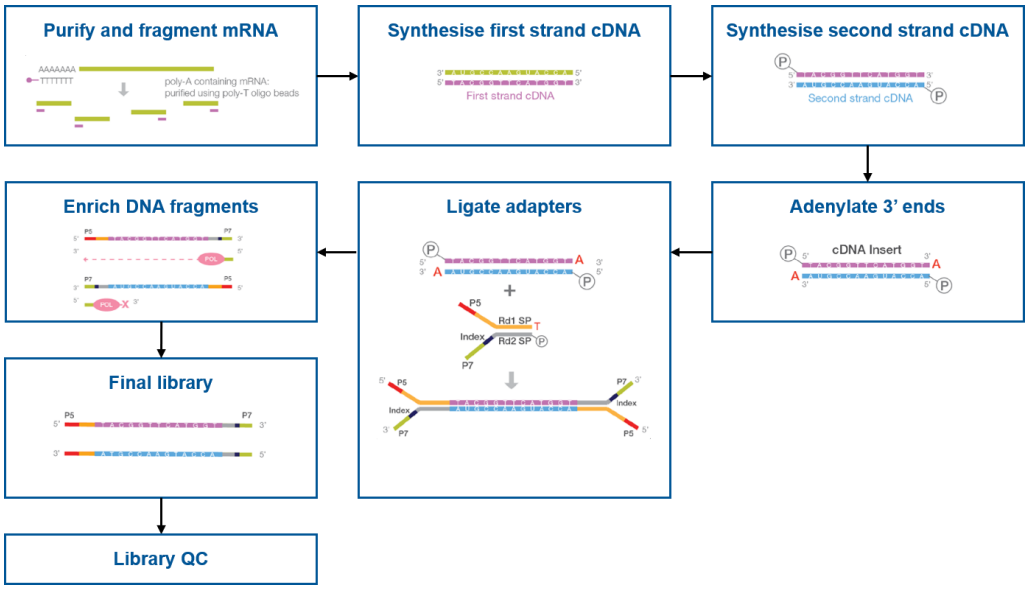


Figure 2.1 Library preparation for mRNA next-generation sequencing
The workflow for the TruSeq Stranded mRNA library preparation kit. Figure adapted from the TruSeq Stranded mRNA protocol (Illumina, 2017b).

2.7.2.2 mRNA sequencing

Sequencing of the generated libraries was performed on a NextSeq 500 desktop sequencer (Illumina; SY-415-1002). A schematic diagram summarising the two main aspects of mRNA NGS, cluster amplification and sequencing, is shown in Figure 2.2. Following preparation, the library was loaded into a flow cell where fragments were captured on a lawn of surface-bound oligos complementary to the library adapters. Each fragment was then amplified into distinct, clonal clusters through bridge amplification. Following cluster generation, sequencing was performed using a technique called sequencing by synthesis (SBS). During a sequencing cycle, the flow cell bound cDNA templates were read by the incorporation of a single fluorescently-labelled deoxyribonucleotide triphosphate (dNTP) to the growing chain. Imaging of the flow cell recorded the emission wavelength and intensity to enable the identification of the incorporated base (called

a ‘base call’). This cycle was repeated 75 times to create a sequence of base calls, known as a ‘read’.

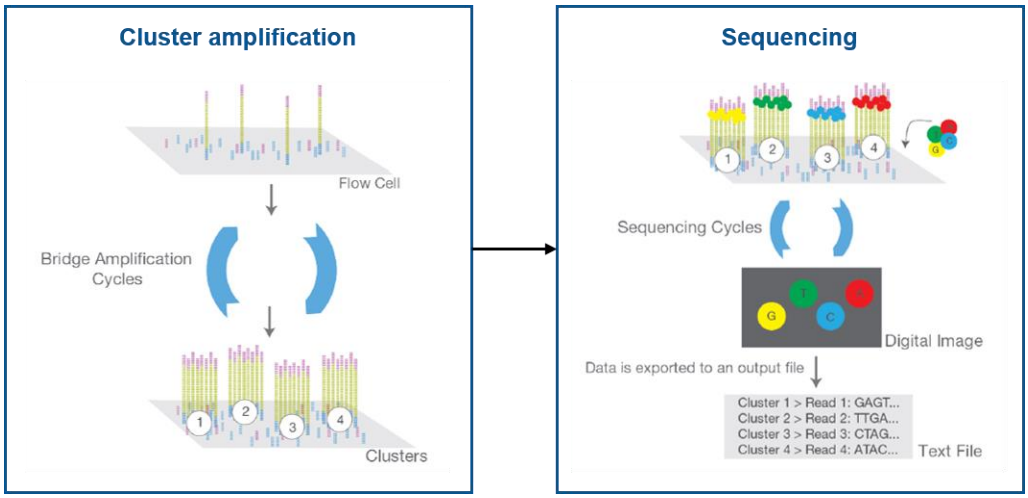


Figure 2.2 mRNA next-generation sequencing workflow
The workflow for mRNA next-generation sequencing including the cluster amplification and sequencing steps. Images were obtained from ‘Introduction to Next-Generation Sequencing Technology’ (Illumina, 2017a).

2.7.2.3 Quality control of sequencing data

Following mRNA sequencing, FASTQ files were generated. These were text-based files containing the sequence data. Quality control of the sequencing data was performed using FASTQC analyses and provided an overview of any problems with the data before conducting further analysis (Andrews, 2010).

2.7.2.4 Alignment and mapping

The alignment and mapping workflow for mRNA next-generation sequencing analysis is shown in Figure 2.3. QIAGEN’s mRNA NGS data analysis pipeline was based on the Tuxedo software package, which is a combination of open-source software and implements peer-reviewed statistical methods. Abundant reads were

removed from the FASTQ files using Bowtie2 (v.2.2.2; Langmead and Salzberg, 2012). These filtered FASTQ files were aligned to a reference genome (GRCh38.p13) using TopHat (v.2.0.11; Trapnell, Pachter and Salzberg, 2009), a fast splice junction mapper for RNA sequencing reads. It used the sequence alignments to identify splice junctions for both known and novel transcripts as well as identification of insertions and deletions. The mapping results obtained underwent quality control and classified the reads into the following classes: mappable reads, outmapped reads or high abundance reds, and unmapped reads.

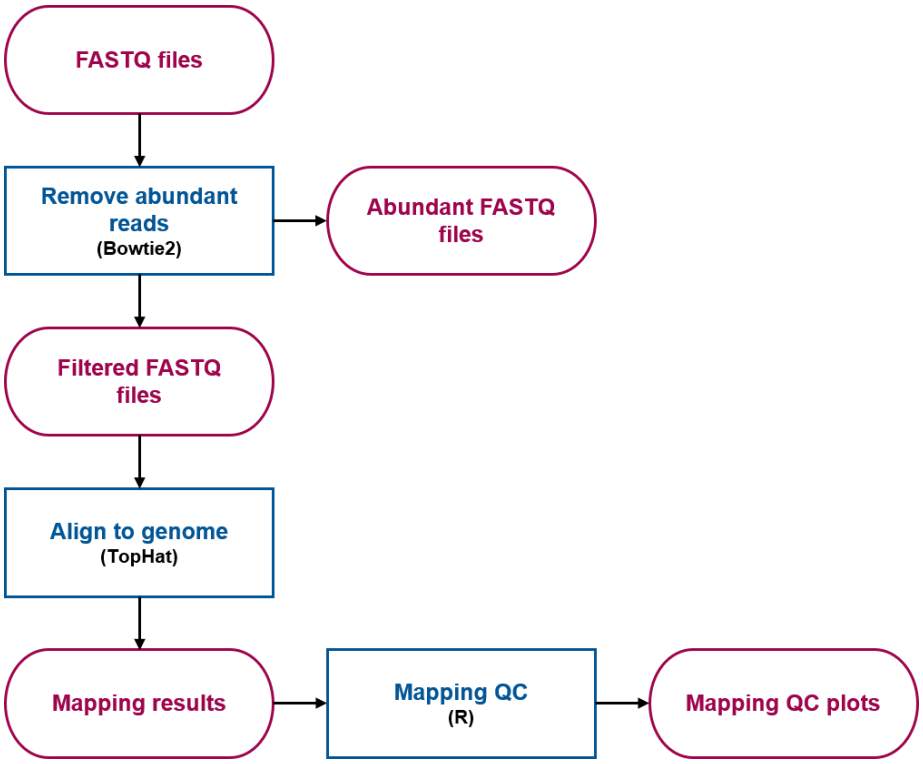


Figure 2.3 Alignment and mapping workflow for mRNA next-generation sequencing analysis

The workflow for alignment and mapping for mRNA next-generation sequencing (NGS) analysis is shown as processes (blue) and outputs (red).

2.7.2.5 Differential expression analysis

A workflow for differential expression analysis for mRNA next-generation sequencing is shown in Figure 2.4. To identify differentially expressed genes between two sample sets, Cufflinks (v2.2.1; Trapnell *et al.*, 2010; Trapnell *et* al., 2012) took the alignment results from TopHat and assembled the aligned sequences into transcripts, thereby constructing a map or a snapshot of the transcriptome. The assembled transcripts of both comparison groups were merged using Cuffmerge to produce a master transcriptome. Expression levels were quantified using Cuffquant before differential expression analysis was conducted with Cuffdiff (Trapnell *et al.*, 2013). When comparing groups, Cuffdiff calculated the FPKM (number of fragments per kilobase of transcript per million mapped fragments) and tested for differential expression and regulation among the assembled transcripts.

Tab delimited files containing the results of differential expression testing between samples were imported into Microsoft Excel. Gene-level pairwise differential regulation analysis was performed by analysing the differences in the FPKM values of transcripts sharing the same Gene ID. Log2 fold changes between the sample comparisons were calculated and significance was determined by an uncorrected p-value and a q-value (a p-value adjusted using the Benjamini-Hochberg False Discovery Rate (FDR) approach) to correct for multiple testing.

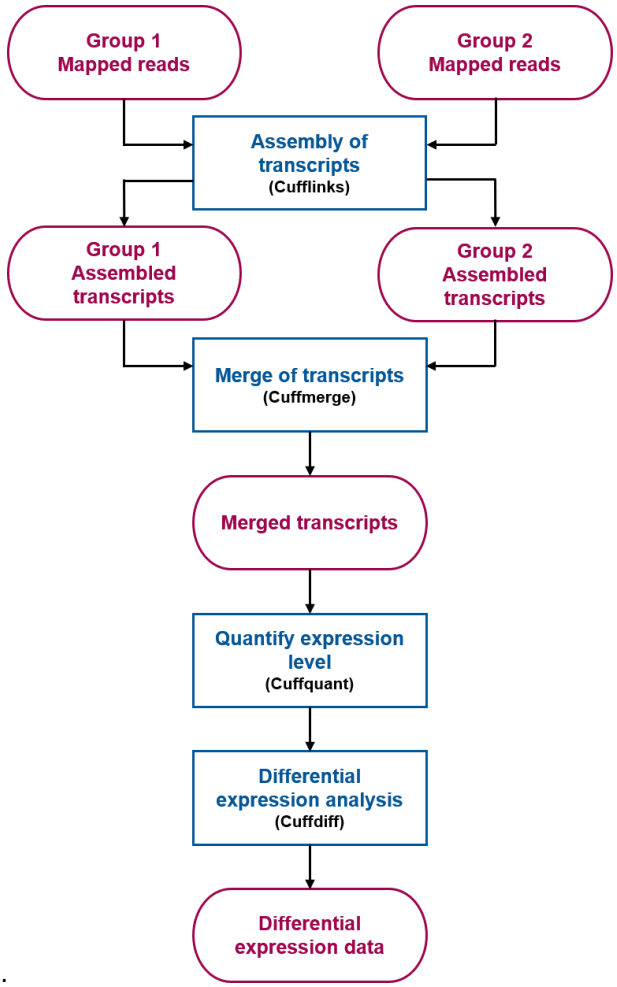


Figure 2.4 Differential expression analysis workflow for mRNA next-generation sequencing analysis

The workflow for differential expressions analysis for mRNA next-generation sequencing (NGS) analysis is shown as processes (blue) and outputs (red).

2.7.3 3' UPX next-generation sequencing

3' UPX sequencing is a method of NGS used for low input samples that sequences the 3' end of RNA near the poly-A tail.

2.7.3.1 Library preparation, sequencing and quality control

The library preparation for 3' UPX NGS was performed using the QIAseq® UPX 3' Transcriptome kit (QIAGEN, 333088). The process involved the following steps, as described in the QIAseq® UPX 3' Transcriptome handbook:

(1) Purified RNA:

A total of 10 ng of purified RNA was converted into cDNA NGS libraries.

(2) Reverse transcription with template switching and UMI and Cell ID assignment:

During reverse transcription, each cell was tagged with a unique ID and each RNA molecule was tagged with a unique molecular index (UMI). Following reverse transcription with integrated template switching, all individually tagged cDNAs were combined. During subsequent amplification and library construction, up to 48 different Sample IDs were assigned.

(3) Template switching amplification:

Amplification of the template switching reaction was performed to ensure cDNA containing UMIs were significantly enriched for subsequent library preparation.

(4) Fragmentation, end-repair, A-addition and adaptor ligation:

Amplified DNA was first fragmented, end-repaired and A-tailed. The prepared DNA fragments were then ligated at their 5’ ends with a sequencing platform-specific adapter.

(5) Universal amplification of 3' end and sample index assignment:

Universal amplification was performed to ensure that the DNA fragments containing the Cell ID and UMIs were sufficiently amplified for NGS.

(6) Library quantification:

Library preparation QC was performed using TapeStation 4200 (Agilent Technologies).

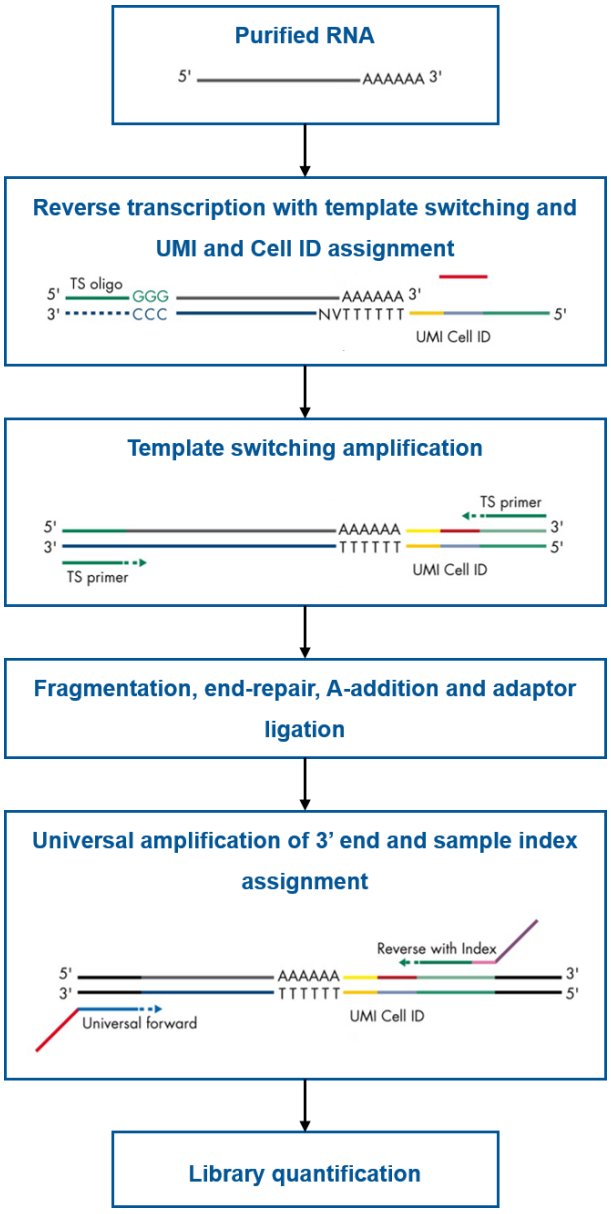


Figure 2.5 Library preparation for 3' UPX next-generation sequencing
The workflow for the QIAseq® UPX 3' Transcriptome kit. Figure adapted from the 3' UPX protocol handbook (QIAGEN, 2019).

Sequencing of the generated libraries was performed on a NextSeq 500 desktop sequencer (Illumina; SY-415-1002) according to manufacturer's instructions. Following sequencing, raw data was de-multiplexed and FASTQ files for each sample were generated and were checked using the FASTQC tool.

2.7.3.2 Primary sequence analysis

Data analysis was performed using the QIAGEN GeneGlobe bioinformatics tool. The first stage of analysis for 3' UPX sequenced samples involved extracting the UMI and cell index sequences from the R2 reads. A specific read structure was expected from the R2 reads (<cell_index><UPX><ACG><poly-T>) as a custom sequencing primer was bound directly before the cell index. If present, any 3' poly-A region was trimmed off the 3' end of the R1 reads. R1 reads with less than 25 base pairs were dropped. The poly-A trimmed R1 reads were aligned to the reference genome (GRCh38.p13) using the splice-aware aligner STAR (Dobin *et al.*, 2013). The aligned reads were annotated to gene regions and the UMIs were then counted for each gene.

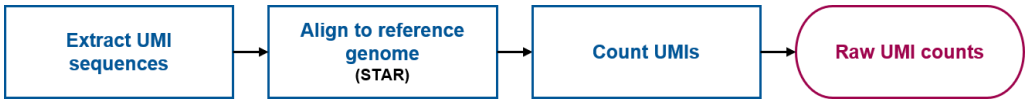


Figure 2.6 3' UPX next-generation sequencing primary sequence analysis workflow
The workflow for primary sequence analysis for 3' UPX next-generation sequencing (NGS) is shown as processes (blue) and outputs (red).

2.7.3.3 Secondary differential expression analysis

The R/Bioconductor package DEseq2 (Love, Huber and Anders, 2014) was used for differentially expression analysis of the UMI count data. DESeq2, a method for differential analysis of count data (raw UMI counts), used shrinkage estimation for dispersions and fold changes to improve stability and interpretability of estimates. This enabled a more quantitative analysis focused on the strength rather than the mere presence of differential expression. DESeq2 created an artificial reference sample by taking the geometric means of counts of all genes and calculated a ratio of the raw counts all genes to their respective geometric means. Then, a normalisation factor was calculated (the median of all ratios per sample) and the raw counts were divided by the corresponding normalisation factor of that sample.

2.7.4 Next-generation sequencing analysis

2.7.4.1 Unsupervised analysis

QIAGEN performed unsupervised analysis of the mRNA sequencing results for each sample. Heatmaps were generated to show the hierarchical clustering of samples using the top 500 most significantly differentially expressed genes. Within heatmaps, each row represented one gene and individual samples were displayed in columns. The colour scale signified the relative expression level of a transcript across all samples. Expression levels above and below the mean were depicted by the colours red and green, respectively.

2.7.4.2 Differential gene expression analysis

Differential gene expression analysis was conducted to identify significantly up- and down-regulated genes within specified comparisons. Significant genes were filtered

based on their fold change (Log2) and FPKM (mRNA) or UMI (3' UPX) values. Lists of significantly differentially regulated genes between comparison groups were compared using GeneVenn (bioinformatics.org/gvenn) to identify shared gene lists.

2.7.4.3 Gene set enrichment analysis

Gene Set Enrichment Analysis (GSEA) was performed using publicly-available software from the University of California San Diego and the Broad Institute (software.broadinstitute.org/gsea). GSEA was used to determine whether sets of genes identified through differential gene expression analysis overlapped with defined gene sets on a Molecular Signatures Database (Subramanian *et al.*, 2005; Liberzon *et al.*, 2011). Gene sets used in this study included the Pathway Interaction Database (PID) gene sets (Schaefer *et al.*, 2009) and Gene Ontology biological processes gene sets (The Gene Ontology Consortium, 2000, 2019). Significance in overlap with the GO gene set was determined using an uncorrected p-value and a q-value (a p-value adjusted using the Benjamini-Hochberg False Discovery Rate (FDR) approach) to correct for multiple testing.

2.8 Patient dataset analysis

The R2 Genomics Analysis and Visualization Platform (r2platform.com) was used to analyse gene expression in publicly-available patient datasets. The datasets used in this study are detailed in Table 2.4. Significant differences in gene expression between groups were calculated using the Kruskal-Wallis test with Dunn's multiple comparisons post-hoc test using GraphPad Prism 8.1.2.

Table 2.4 Patient datasets analysed on the R2 Genomics Analysis and Visualisation Platform

Dataset	Number of samples	Sample type	Reference
Roth	9	Normal cerebellum	Roth et al., 2006
Pfister	223	Medulloblastoma	Northcott et al., 2017
Cavalli	763	Medulloblastoma	Cavalli et al., 2017

Chapter 3

Establishing a 3D spheroid model of medulloblastoma

Chapter 3. Establishing a 3D spheroid model of medulloblastoma

3.1 Introduction

Studying medulloblastoma *in vitro* is challenging, as traditional 2D cell culture models fail to recapitulate the multi-dimensional growth, cell-cell interactions, and complex microenvironment that exists *in vivo* and in patient tumours. The development of a 3D *in vitro* culture technique that can mimic such characteristics would provide a more predictive model of tumour biology, drug response, and metastatic behaviour, thus filling the gap between standard 2D monolayer cultures and animal models.

The first stage in the establishment of a 3D model of medulloblastoma was to determine which culture method to adopt. There are various approaches to 3D culture, including gel/matrix-based models, spheroids, transwell-based models, and tumour-microvessels. Each of these models have advantages and disadvantages, depending on the purpose of the study (discussed in section 1.6.2). We compiled a set of requirements desired for our model, which included: (1) the formation of single, uniform 3D structures, (2) standardised growth conditions across cell lines, and (3) applicable to different methods of assessing viability. A review of 3D *in vitro* modelling literature over the past few decades highlighted that spheroids fulfilled the requirements for our desired model for the following reasons:

(1) Ability to form single, uniform 3D structures:

One of the main advantages of spheroid culture is the easy generation and monitoring of individual spheroids in a multi-well plate format. For this project, we chose to use ultra-low attachment (ULA) plates for the generation and manipulation of single, uniform spheroids. Unlike older techniques that require manually coating

of flat-bottomed 96-well plates with agarose or agar, ULA plates are rounded and have a covalently bound hydrogel layer to effectively inhibit cellular attachment. This surface and rounded shape promotes the formation of a single, highly reproducible spheroid in each well.

(2) Standardised growth conditions across cell lines:

Growth conditions, such as spheroid size, incubation periods, and culture medium, need to be standardised for the spheroid model to allow direct comparisons across cell lines and different experimental models. Spheroid size is an important consideration for this model as spheroids that are too small (e.g. <200 µm diameter) do not have well established pH and oxygen gradients, whereas overly large spheroids (e.g. 500-600 µm diameter) may develop necrotic cores. One of the main advantages of the spheroid model is that the cell seeding density is modifiable to ensure that different cell lines form spheroids that fall within the same size range by a chosen time point. The innovative Nature Protocols publication by Friedrich *et al.*, 2009, recommended a four day formation period for the establishment of identical spheroids with clear pathophysiological gradients. Therefore, we chose to establish spheroids with an intermediate diameter of 250-350 µm by day 4.

In addition, Friedrich *et al.*, 2009 recommended that spheroids used in a screening approach should be grown under identical conditions. The medulloblastoma cell lines used in this study are grown in different serum-containing media in standard culture. To allow direct comparison, we decided to assess spheroid formation and growth in the cell's standard medium as well as serum-free neurosphere medium, containing supplements and growth factors routinely used in the culture and maintenance of neural stem cells.

(3) Different methods of assessing viability:

Quantitative methods of measuring spheroid growth kinetics include size analysis (either using manual or automated imaging systems) and specialised 3D viability

assays. There is also the potential to harvest, process, and section spheroids for immunohistochemical staining, providing an alternative method of assessing cell viability within the spheroid.

The aims of this chapter were therefore to:

(1) Optimise a panel of medulloblastoma cell lines in the 3D spheroid model
(2) Validate the reproducibility of the model
(3) Characterise medulloblastoma spheroids in further detail.

3.2 Optimisation of medulloblastoma cell lines in the 3D spheroid model

The first stage in the establishment of a 3D spheroid model of medulloblastoma was to optimise spheroid growth conditions for a panel of cell lines. For the cell lines to be considered optimised, the spheroids should satisfy the following requirements:

(1) Formation of a tight spheroid or compact aggregate
(2) 250-350 µm diameter in size on day 4
(3) Continuous growth for a minimum of seven days

A schematic diagram summarising the approach we adopted for the 3D spheroid model of medulloblastoma is shown in Figure 3.1. On day 0, cell lines grown in standard culture were harvested to generate a single-cell suspension and were then seeded into 96-well ULA plates. By day 1, the cells formed an aggregate in the centre of the well and were incubated for a further 72 hours until day 4, by which point they reached the optimal size of 250-350 µm in diameter. Following this, spheroids were ready to be used in numerous functional assays, including growth and drug response analysis, as well as migration and invasion assays.

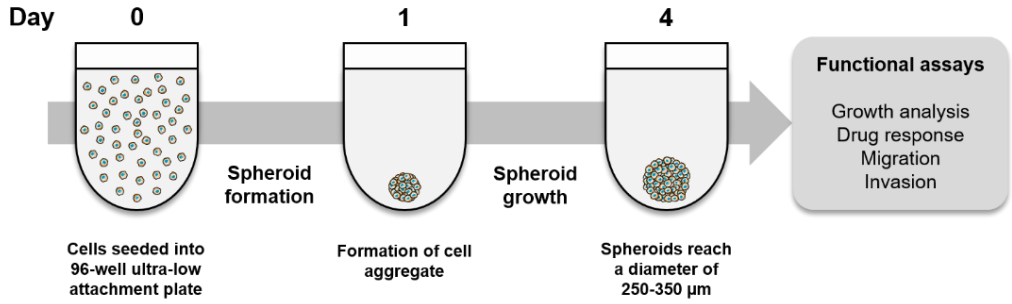


Figure 3.1 Schematic diagram describing the 3D spheroid model
On day 0, cells are harvested and seeded at their optimal seeding density into 96-well ultra-low attachment, round-bottom plates. Cells form an aggregate after 24 hours and are left to grow until day 4, at which point they have reached a diameter of 250-350 µm. The spheroids can then be used in numerous functional assays, including growth and drug response analysis, as well as migration and invasion assays.

Nine medulloblastoma cell lines representing three of the four molecular subgroups (SHH, Group 3, and Group 4) were tested for use in the 3D spheroid model. Clinical information for each cell line is detailed in Table 3.1.

Table 3.1 Clinical information for medulloblastoma cell lines used in this study

Nine medulloblastoma cell lines representing three of the four molecular subgroups (SHH, Group 3, and Group 4) were used in this study. Clinical information, including patient demographics and metastatic stage are shown, alongside the source of each cell line and associated references. *◊ Cell lines with matched primary and metastatic pairs.

	Cell line	Patient demographics	Clinical information	Metastatic stage	Source	References
SHH subgroup	DAOY	4 year old male	Cerebellar medulloblastoma of the posterior fossa with a C242F *TP53* mutation	Non-metastatic (M0)	ATCC® HTB-186™	Jacobsen, Jenkyn and Papadimitriou, 1985; Raffel *et al.*, 1993
	ONS76	2 year old female	Large (3cm) midline cerebellar tumour	Metastatic tumours at the right prepontine cistern (M2)	Annette Künkele (Charité Universitätsmedizin, Berlin)	Tamura *et al.*, 1989; Shimizu *et al.*, 1991
	UW228-3	9 year old female	Midline posterior fossa mass with a T155N *TP53* mutation	Non-metastatic (M0)	John R. Silber (University of Washington, Seattle)	Keles *et al.*, 1995; Künkele *et al.*, 2012
Group 3	HD-MB03	3 year old male	Large cell medulloblastoma in the midline (fourth ventricle and vermis)	Spinal metastases at diagnosis (M3)	Till Milde (DKFZ, Heidelberg)	Milde *et al.*, 2012
	D283	6 year old male	Mass (3cm) in the cerebellar vermis	Peritoneal metastasis and malignant ascites (M2)	ATCC® HTB-185™	Friedman *et al.*, 1985
	D425*	5 year old male	Primary cerebellar tumour	Non-metastatic (M0)	Marcel Kool (DKFZ, Heidelberg)	He *et al.*, 1991
	D458*		Matched metastatic recurrence	Metastatic (M+)	John R. Silber (University of Washington, Seattle)	
Group 4	CHLA-01-MED◊	8 year old male	Primary tumour: cerebellar mass with diffuse leptomeningeal enhancement	Leptomeningeal metastases at diagnosis (M3)	ATCC® CRL-3021™	Xu *et al.*, 2015
	CHLA-01R-MED◊		Metastatic recurrence (8 months after diagnosis): tumour cells from the pleural fluid	Recurrent metastatic cells from pleural fluid (M2)	ATCC® CRL-3034™	

3.2.1 SHH medulloblastoma cell lines form tight spheroids

The SHH medulloblastoma cell lines DAOY, ONS76, and UW228-3 were optimised for use in the 3D spheroid model. These cell lines grow adherently in standard culture, as shown in Figure 3.2.

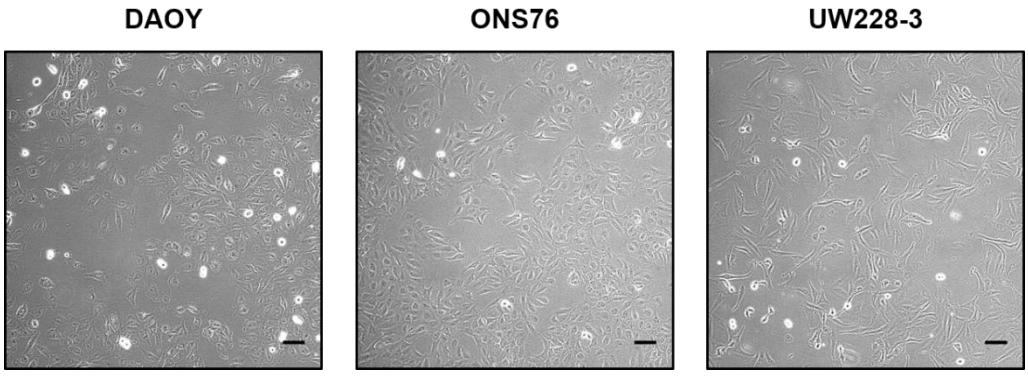


Figure 3.2 SHH medulloblastoma cell lines in standard culture
Brightfield images of the SHH medulloblastoma cell lines DAOY, ONS76, and UW228-3 growing adherently in standard culture (scale bar: 100 µm).

To determine the optimal 3D growth conditions for these cell lines, cells were seeded in 96-well ULA round-bottom plates at increasing densities in either their standard culture medium or neurosphere medium. After four days growth, image analysis was performed to determine the average spheroid diameter for each seeding density. Significant differences in spheroid diameter between standard and neurosphere medium were calculated at each density using two-way ANOVA analyses which determined how the response (in this case, spheroid diameter) was affected by two factors (seeding density and culture medium). A Sidak's post-hoc test was also performed to correct for multiple comparisons. This test compared the mean spheroid diameter in both media compositions at each seeding density to calculate statistical significance.

DAOY cells formed compact spheroids after four days in culture that increased in size relative to the seeding density in both media types (Figure 3.3A). Spheroid diameter analysis showed that spheroids generated in neurosphere medium were significantly larger than those cultured in standard medium at higher seeding densities (Figure 3.3B). The optimal seeding density was determined to be 500 cells/well to produce spheroids around 320 µm in diameter in neurosphere medium. To further assess whether neurosphere medium enhanced spheroid growth, DAOY cells were seeded at 500 cells/well in either standard or neurosphere medium to allow direct comparison of the media types. Growth was assessed over a seven-day period and spheroid diameter was analysed on days 1, 4, and 7 post-seeding. DAOY spheroid growth was significantly enhanced (*$p \leq 0.05$) in neurosphere medium compared to standard medium on day 4 (Figure 3.3C) and this increased further by day 7 (***$p \leq 0.001$).

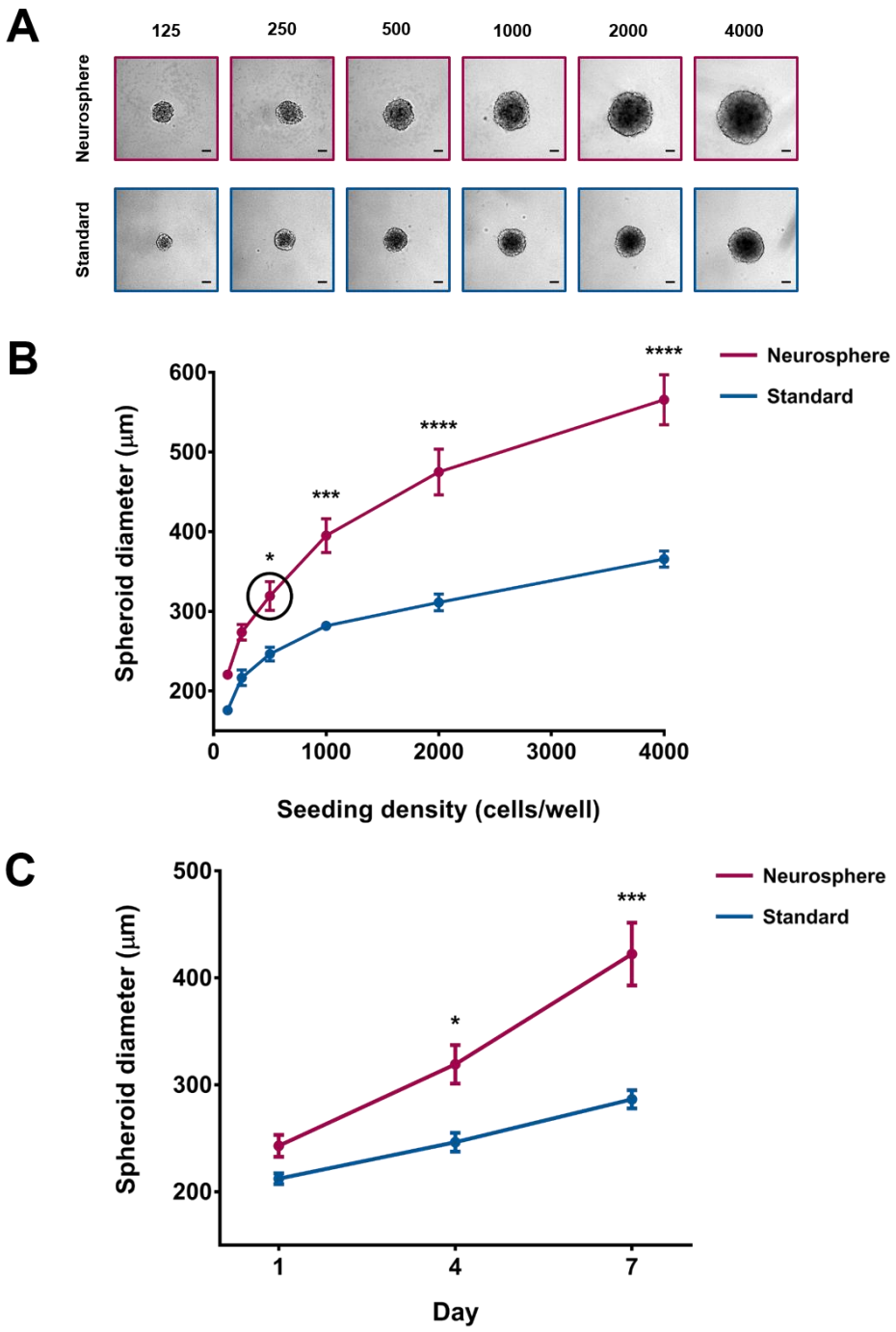


Figure 3.3 Optimisation of spheroid growth conditions for DAOY cells

(**A**) Representative images of spheroids seeded at increasing densities (125, 250, 500, 1000, 2000, and 4000 cells/well) in neurosphere or standard medium after four days growth (scale bar: 100 µm). (**B**) Relationship between cell seeding density (cells/well) and spheroid diameter (µm) after four days growth in neurosphere medium (red) or standard medium (blue). Spheroids generated in neurosphere medium were significantly larger than those cultured in standard medium at selected seeding densities. 500 cells/well in neurosphere medium were chosen as the optimal conditions for spheroid growth (circled). (**C**) Growth of DAOY spheroids seeded at 500 cells/well in either neurosphere or standard medium was assessed over a seven-day period. Spheroid diameter (µm) was significantly enhanced in neurosphere medium. Error bars represent the mean ± SEM of 3 independent experiments each containing ≥3 replicates. Significance was calculated using two-way ANOVA analyses with Sidak's multiple comparisons post-hoc test (*p≤0.05, ***p≤0.001, ****p≤0.0001).

ONS76 cells also formed tight spheroids by day 4 (Figure 3.4A). Again, the spheroids generated in neurosphere medium were significantly larger than those in standard culture medium (Figure 3.4B). 250 cells/well was determined to be the optimal seeding density for ONS76 cells, generating spheroids with an average diameter of 330 µm. Growth analysis of ONS76 spheroids seeded at their optimal seeding density in either standard or neurosphere medium was performed over a seven-day period. Neurosphere medium significantly enhanced spheroid growth (Figure 3.4C) by day 4 (***$p \leq 0.001$) and day 7 (****$p \leq 0.0001$). Interestingly, cells seeded in standard medium formed a small, tight spheroid within 24 hours but they failed to grow over the course of the assay.

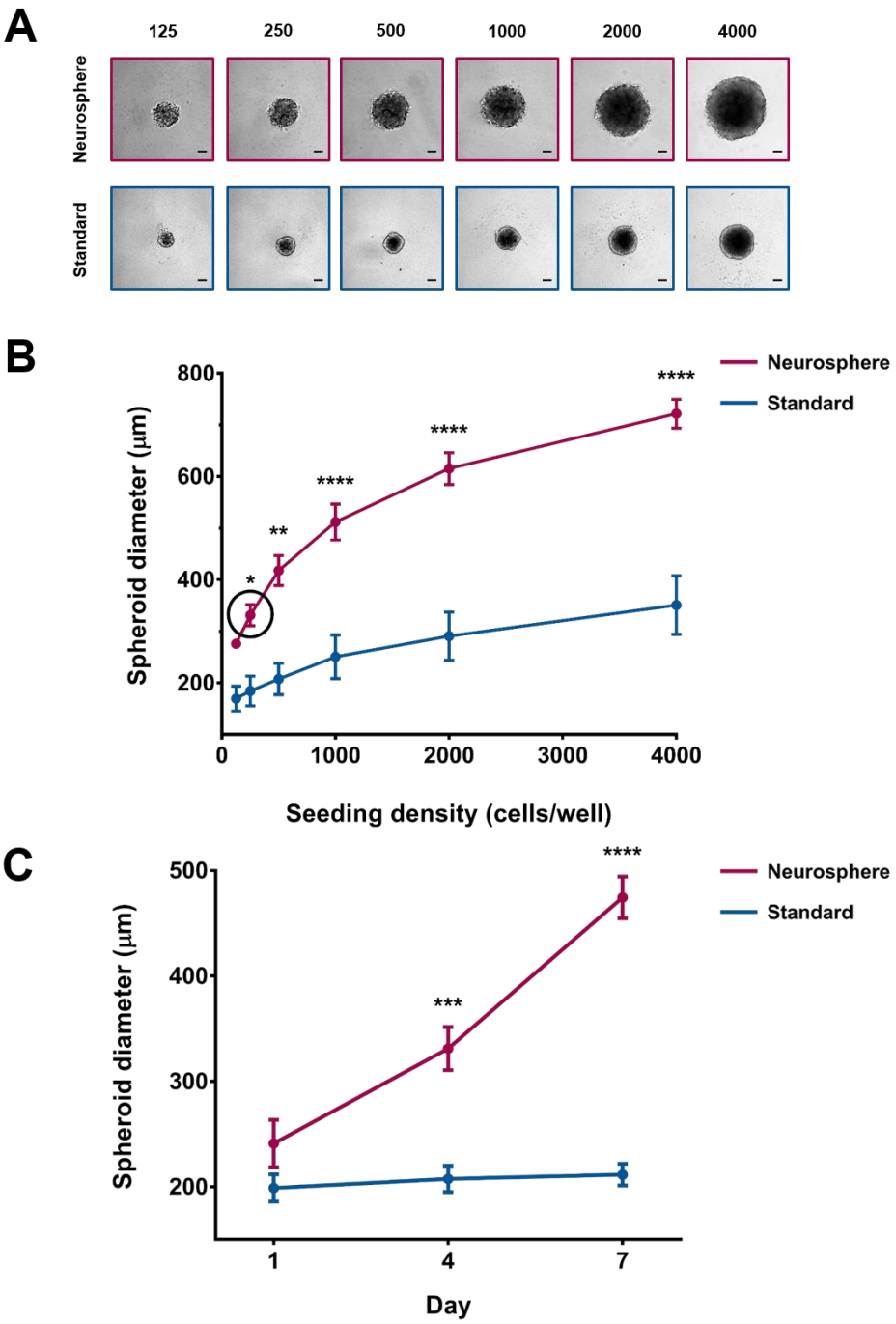


Figure 3.4 Optimisation of spheroid growth conditions for ONS76 cells

(**A**) Representative images of spheroids seeded at increasing densities (125, 250, 500, 1000, 2000, and 4000 cells/well) in neurosphere or standard medium after four days growth (scale bar: 100 µm). (**B**) Relationship between cell seeding density (cells/well) and spheroid diameter (µm) after four days growth in neurosphere medium (red) or standard medium (blue). Spheroids generated in neurosphere medium were significantly larger than those cultured in standard medium at selected seeding densities. 250 cells/well in neurosphere medium were chosen as the optimal conditions for spheroid growth (circled). (**C**) Growth of ONS76 spheroids seeded at 250 cells/well in either neurosphere or standard medium was assessed over a seven-day period. Spheroid diameter (µm) was significantly enhanced in neurosphere medium. Error bars represent the mean ± SEM of 3 independent experiments each containing ≥3 replicates. Significance was calculated using two-way ANOVA analyses with Sidak's multiple comparisons post-hoc test (*p≤0.05, **p≤0.01, ****p≤0.0001).

Imaging analysis revealed that the UW228-3 cell line generated smaller, tighter spheroids than DAOY and ONS76 cells, with a clearly defined edge in both neurosphere and standard media after four days in culture (Figure 3.5A). However, at higher seeding densities in standard medium, this cell line formed an irregular ovoid shape. UW228-3 spheroids formed in neurosphere medium were significantly larger than those cultured in standard medium at higher seeding densities (Figure 3.5B). The optimal seeding density was determined to be 1500 cells/well to produce spheroids over 300 µm in diameter. To confirm whether neurosphere medium also enhanced spheroid growth for this cell line, UW228-3 cells were seeded at their optimal density in either standard or neurosphere medium and spheroid growth was assessed over a seven-day period. Neurosphere medium significantly enhanced spheroid growth (Figure 3.5C) by day 4 (*$p \leq 0.05$) and day 7 (***$p \leq 0.001$). However, the size of spheroids seeded in standard medium remained static over the course of the assay. Like the ONS76 cell line, they failed to grow under standard conditions.

In summary, all three SHH medulloblastoma cell lines tested in the model formed tight spheroids with clearly defined edges. In contrast to other tumour types where the cell's standard culture medium is sufficient for spheroid growth, we have shown that medulloblastoma cell line derived spheroids fail to thrive in these culture conditions. Instead, neurosphere medium was required for the continual growth of SHH medulloblastoma spheroids.

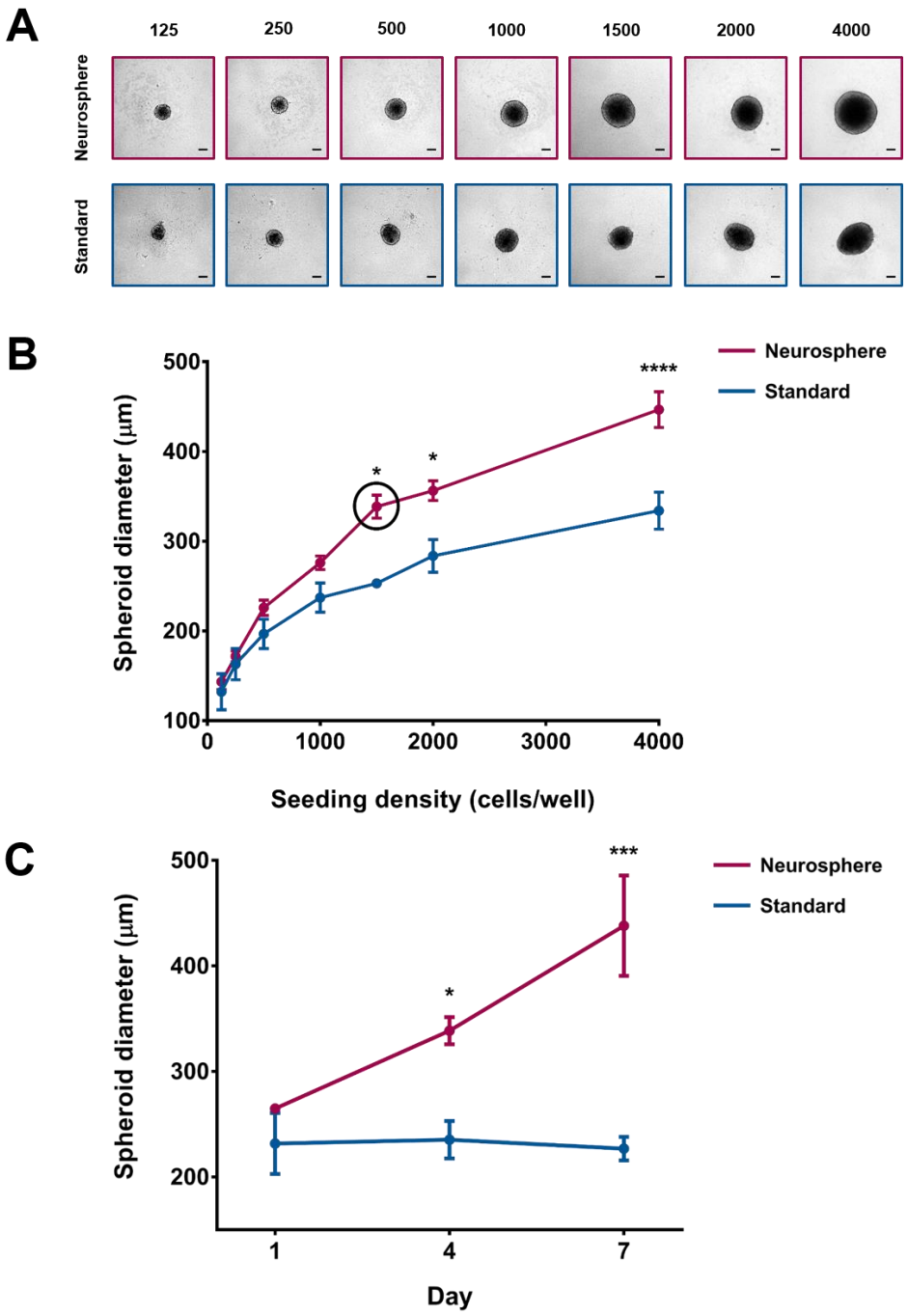


Figure 3.5 Optimisation of spheroid growth conditions for UW228-3 cells

(**A**) Representative images of spheroids seeded at increasing densities (125, 250, 500, 1000, 1500, 2000, and 4000 cells/well) in neurosphere or standard medium after four days growth (scale bar: 100 µm). (**B**) Relationship between cell seeding density (cells/well) and spheroid diameter (µm) after four days growth in neurosphere medium (red) or standard medium (blue). Spheroids generated in neurosphere medium were significantly larger than those cultured in standard medium at selected seeding densities. 1500 cells/well in neurosphere medium were chosen as the optimal conditions for spheroid growth (circled). (**C**) Growth of DAOY spheroids seeded at 1500 cells/well in either neurosphere or standard medium was assessed over a seven-day period. Spheroid diameter (µm) was significantly enhanced in neurosphere medium. Error bars represent the mean ± SEM of 3 independent experiments each containing ≥3 replicates. Significance was calculated using two-way ANOVA analyses with Sidak's multiple comparisons post-hoc test (*p≤0.05, ***p≤0.001, ****p≤0.0001).

3.2.2 Group 3 medulloblastoma cell lines form aggregates of varying morphology

The Group 3 medulloblastoma cell lines HD-MB03, D283, D425, and D458 were next tested for use in the spheroid model. All four of these cell lines grow semi-adherently in standard culture, with populations of adherent, semi-adherent, and suspension cells within the flask (Figure 3.6). The HD-MB03 cell line grows mainly adherently with around 20% of semi-adherent or suspension cells. D283 cells grow around 50% adherently and 50% semi-adherently. The D425 and D458 cell lines grow mostly in suspension, with D425 cells growing in clusters but D458 as single cells.

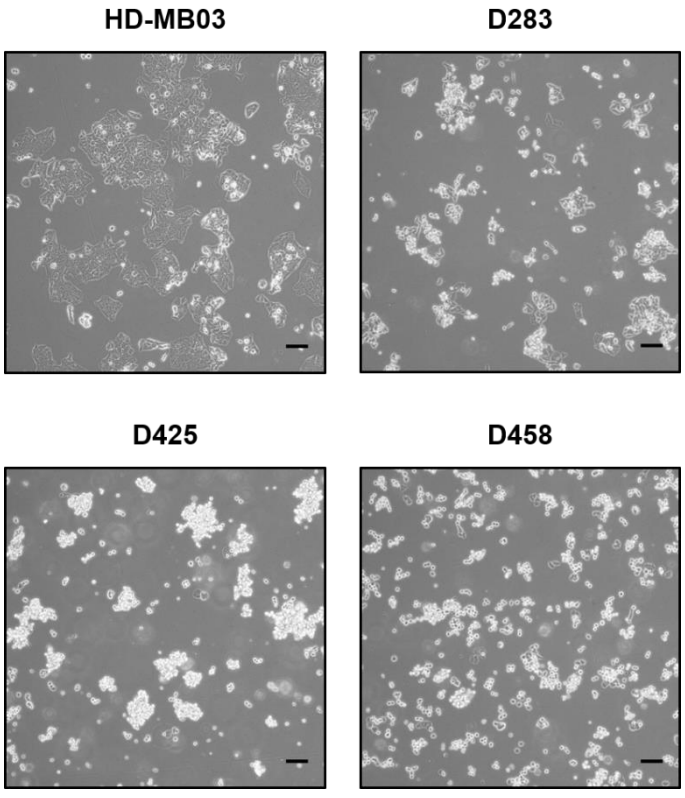


Figure 3.6 Group 3 medulloblastoma cell lines in standard culture
Brightfield images of the Group 3 medulloblastoma cell lines HD-MB03, D283, D425, and D458 growing semi-adherently in standard culture (scale bar: 100 µm).

HD-MB03 cells formed aggregates in neurosphere medium after four days in culture that increased in size relative to the seeding density. However, cells failed to form a 3D structure when seeded in their standard medium, instead forming a sheet-like surface along the bottom of the plate (Figure 3.7A). Spheroid diameter analysis was therefore only completed for spheroids seeded in neurosphere medium. The optimal seeding density was determined to be 250 cells/well to produce spheroids of around 370 µm in diameter by day 4 (Figure 3.7B). Modifications to the spheroid model were introduced to promote the formation of a tighter 3D structure. These included seeding cells in neurosphere medium supplemented with methyl cellulose, a media supplement previously shown to encourage spheroid compactness (Leung *et al.*, 2015). Although other additives, such as collagen, can be used to promote compaction, methyl cellulose was chosen as a more appropriate supplement as it is an inert, adhesive substance which can increase media viscosity and improve spheroid morphology without altering cellular signalling. We also included a post-seeding centrifugation step (5 minutes at 100 x *g*) to encourage the formation of a tighter 3D structure. As shown in Figure 3.7C, these two modifications altered spheroid morphology, resulting in a more compact aggregate of the correct size by day 4.

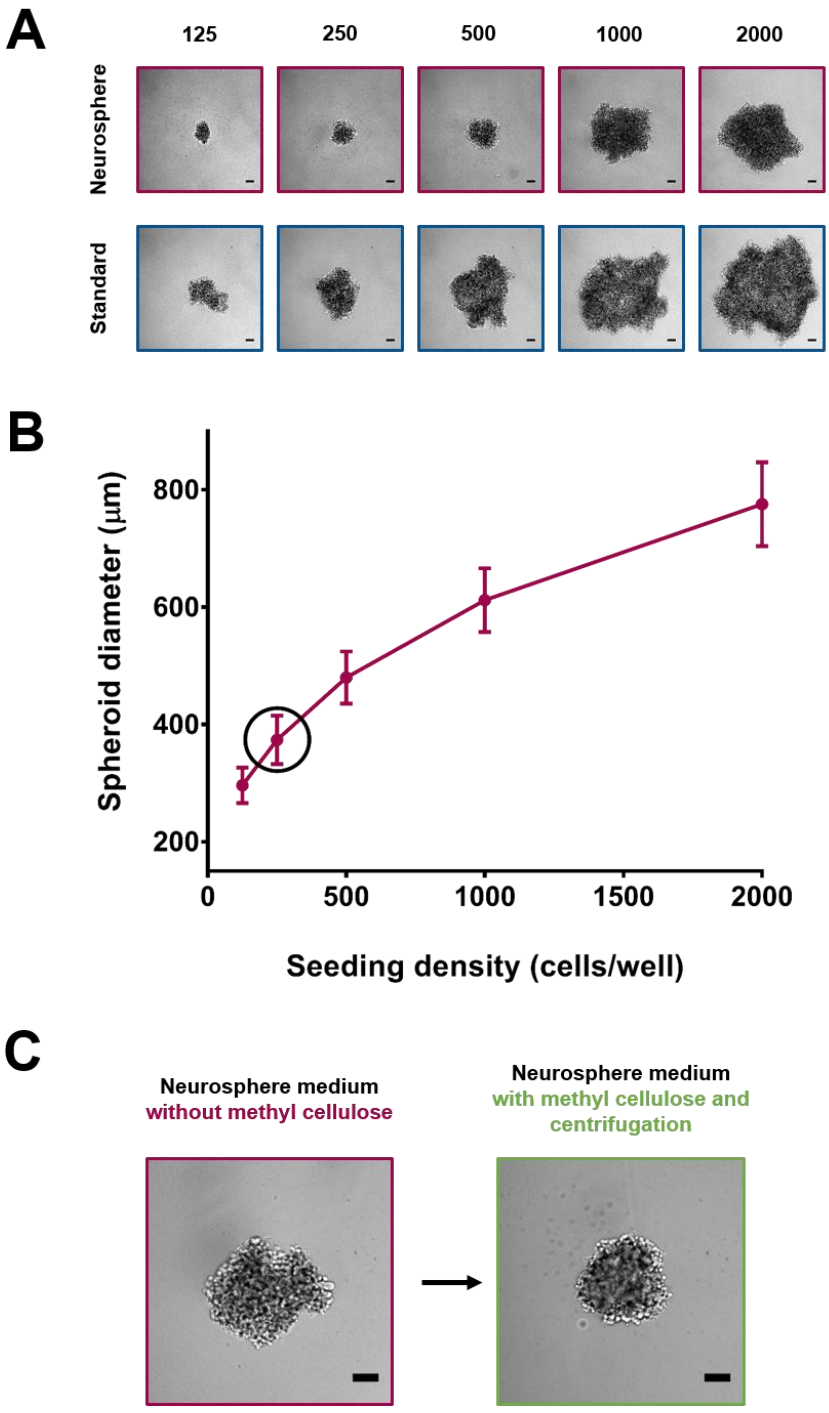


Figure 3.7 Optimisation of spheroid growth conditions for HD-MB03 cells
(**A**) Representative images of spheroids seeded at increasing densities (125, 250, 500, 1000, 1500, and 2000 cells/well) in neurosphere or standard medium after four days growth (scale bar: 100 µm). HD-MB03 cells formed aggregates in neurosphere medium but failed to form a 3D structure in standard medium. (**B**) Relationship between cell seeding density (cells/well) and spheroid diameter (µm) after four days growth in neurosphere medium. 250 cells/well was chosen as the optimal seeding density for spheroid growth (circled). Error bars represent the mean ± SEM of 3 independent experiments each containing ≥3 replicates. (**C**) Addition of methyl cellulose to neurosphere medium and centrifugation after seeding resulted in the formation of a more compact aggregate by day 4 (scale bar: 100 µm).

Following the optimisation of the HD-MB03 cell line, an additional three Group 3 cell lines (D283, D425, and D458) were tested in the spheroid model. As standard medium was shown to be unsuitable for spheroid culture for both SHH and HD-MB03 cell lines, testing was limited to neurosphere medium. Each cell line was seeded at the optimal density determined for the HD-MB03 cell line (250 cells/well) in neurosphere medium alone or neurosphere medium supplemented with methyl cellulose. Plates were centrifuged at the time of seeding to help promote spheroid formation. D283, D425, and D458 cell lines failed to form a 3D structure after four days growth in neurosphere medium (Figure 3.8). However, the addition of methyl cellulose promoted the formation of a tighter aggregate for the D458 cell line, measuring approximately 400 µm in diameter by day 4. The D283 and D425 aggregates remained too loose for continued culture as they fell apart easily during manipulation, for example routine media changes.

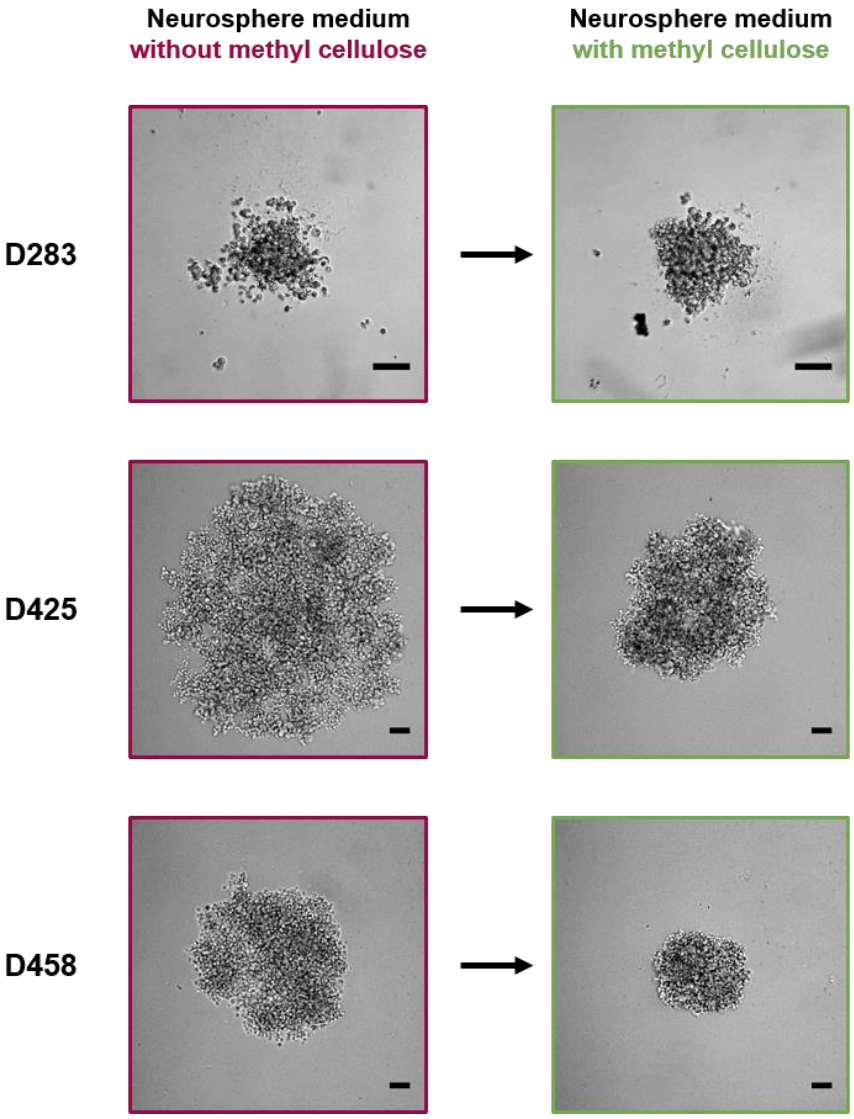


Figure 3.8 Assessment of Group 3 medulloblastoma spheroid morphology
Representative images of D283, D425, and D458 spheroids seeded at 250 cells/well in neurosphere medium without and with methyl cellulose after four days growth (scale bar: 100 µm). All three cell lines failed to form a compact aggregate in neurosphere medium. The addition of methyl cellulose promoted a tighter spheroid morphology for the D458 cell line; however, D283 and D425 aggregates remained loose.

3.2.3 Group 4 medulloblastoma cell lines fail to form suitable spheroids

The Group 4 medulloblastoma cell lines CHLA-01-MED and CHLA-01R-MED grow as clusters and single cells in suspension in standard culture in serum-free medium with the addition of growth factors (Figure 3.9).

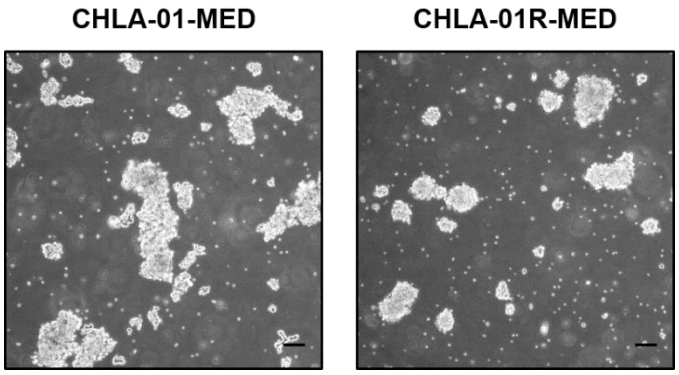


Figure 3.9 Group 4 medulloblastoma cell lines in standard culture
Brightfield images of the Group 4 medulloblastoma cell lines CHLA-01-MED and CHLA-01R-MED growing as clusters in suspension in standard culture (scale bar: 100 µm).

CHLA-01-MED (Figure 3.10) and CHLA-01R-MED (Figure 3.11) were seeded at increasing cell densities in neurosphere medium with or without methyl cellulose and spheroid formation was assessed after four days in culture. Both cell lines were able to form small, singular, albeit loose, clusters at the lower seeding densities (500 and 1000 cells/well) in both media types. However, at higher densities the cell lines struggled to form a single structure, instead displaying multiple clusters and single cells within one well.

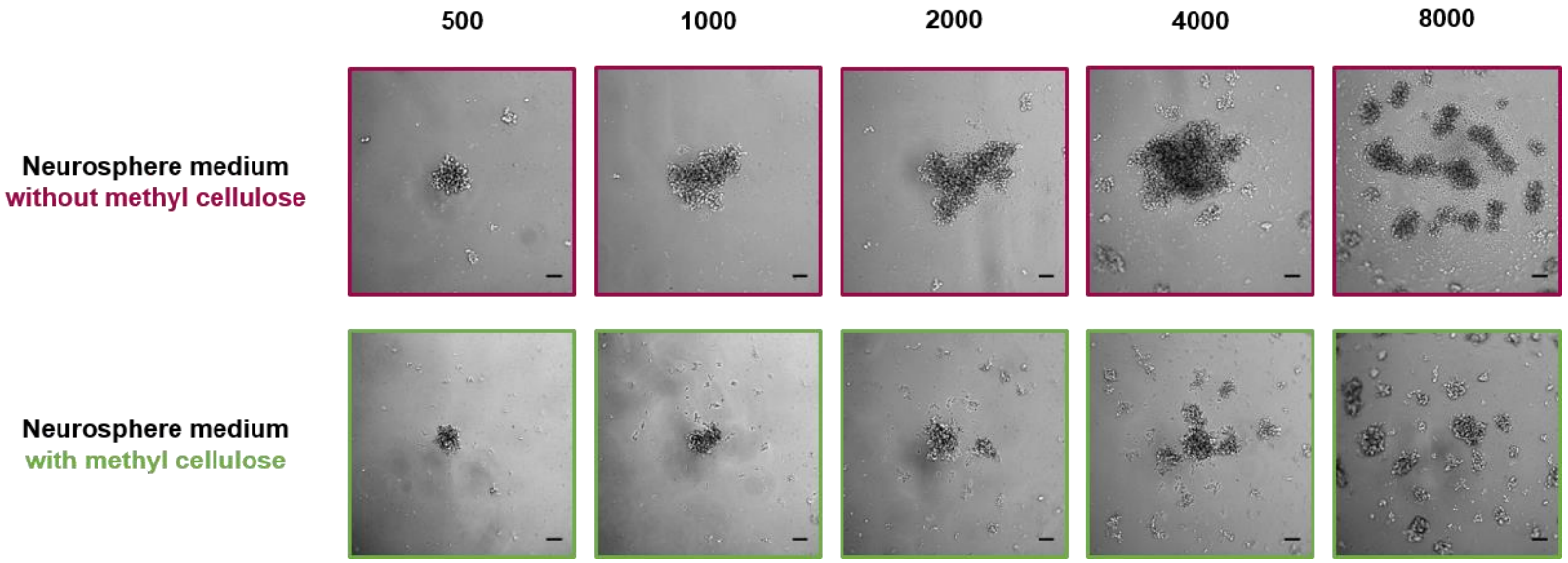


Figure 3.10 Assessment of CHLA-01-MED spheroid morphology

Representative images of the Group 4 medulloblastoma cell line CHLA-01-MED seeded at increasing densities (500, 1000, 2000, 4000, and 8000 cells/well) in neurosphere medium with or without methyl cellulose after four days growth (scale bar: 100 µm). This cell line failed to form a satisfactory spheroid, instead forming multiple clusters within each well at higher densities.

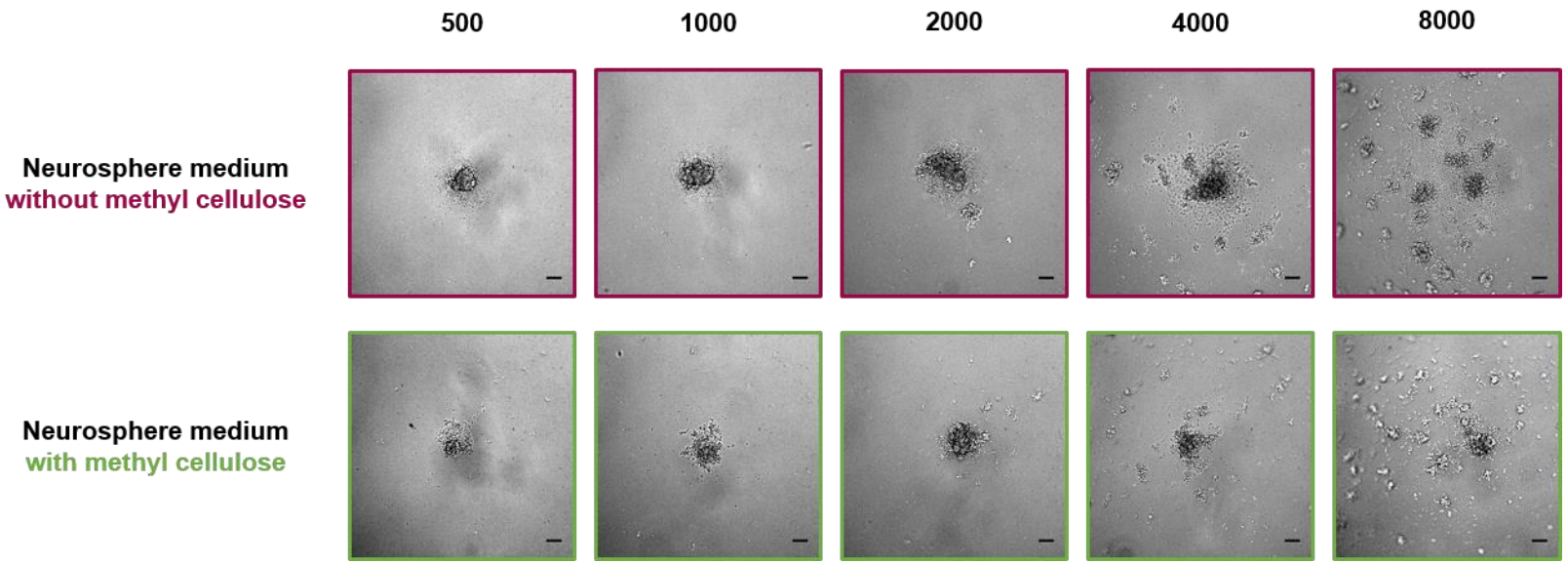


Figure 3.11 Assessment of CHLA-01R-MED spheroid morphology

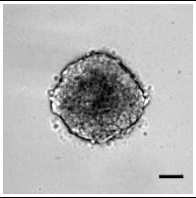
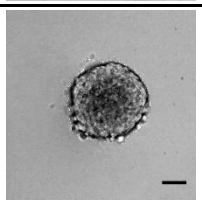
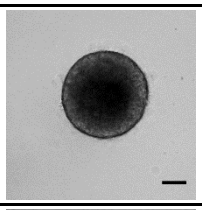
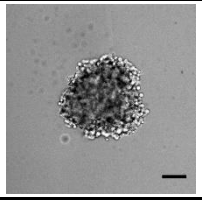
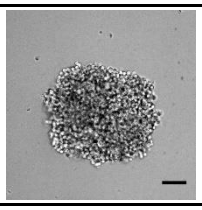
Representative images of the Group 4 medulloblastoma cell line CHLA-01R-MED seeded at increasing densities (500, 1000, 2000, 4000, and 8000 cells/well) in neurosphere medium with or without methyl cellulose after four days growth (scale bar: 100 µm). This cell line failed to form a satisfactory spheroid, instead forming multiple clusters within each well at higher densities.

3.2.4 Summary of spheroid optimisation

A summary of the panel of medulloblastoma cell lines tested for their use in the 3D spheroid model is shown in Table 3.2. SHH medulloblastoma cell lines readily produced tight spheroids which displayed continual growth when cultured in neurosphere medium. Group 3 medulloblastoma cell lines formed looser aggregates; however, a tighter structure could be promoted in two cell lines (HD-MB03 and D458) with the addition of methyl cellulose to neurosphere medium and a centrifugation step after seeding. Group 4 medulloblastoma cell lines failed to form spheroids.

We chose to focus on the SHH medulloblastoma cell lines in this project. A review by Ivanov *et al.*, 2016 regarding the use of medulloblastoma cell lines in research showed that the DAOY, ONS76, and UW228-3 cell lines were all commonly used and highly cited in the literature. This highlighted the urgent need to develop a suitable 3D culture system for these cell lines which could be easily adopted in the medulloblastoma research community. As well as this, we showed that the SHH medulloblastoma cell lines formed ideal spheroids as they exhibited a tighter morphology and were considered suitable for downstream validation and functional assays. Therefore, the rest of this thesis will focus on the DAOY, ONS76, and UW228-3 cell lines. Unless otherwise stated, these cell lines were cultured as spheroids in neurosphere medium throughout the remainder of this study.

Table 3.2 Summary of medulloblastoma cell lines tested in the 3D spheroid model
Nine medulloblastoma cell lines representing three of the four molecular subgroups (SHH, Group 3, and Group 4) were tested for use in the 3D spheroid model. Optimised seeding densities and any necessary modifications required for spheroid culture are shown. For cell lines which formed suitable spheroids, examples of their morphology on day 4 are shown.

	Cell line	Optimised seeding density	Necessary modifications	Example of day 4 spheroid (scale bar: 100 µm)
SHH subgroup	DAOY	500 cells/well	None	
	ONS76	250 cells/well	None	
	UW228-3	1500 cells/well	None	
Group 3	HD-MB03	250 cells/well	+ 0.24% methyl cellulose + centrifugation	
	D283	Not applicable – unsuitable for spheroid culture		
	D425	Not applicable – unsuitable for spheroid culture		
	D458	250 cells/well	+ 0.24% methyl cellulose + centrifugation	
Group 4	CHLA-01-MED	Not applicable – unsuitable for spheroid culture		
	CHLA-01R-MED	Not applicable – unsuitable for spheroid culture		

3.3 Validation of 3D spheroid model reproducibility

In section 3.2.1, the seeding densities of SHH medulloblastoma cell lines were optimised to produce spheroids of 250-350 µm in diameter after four days growth. In addition to this, we found that culture in neurosphere medium was essential for maintained spheroid growth. To validate the use of the three SHH medulloblastoma cell lines in the spheroid model, it was important to demonstrate that the spheroids generated were highly reproducible. Coefficient of variation (CV) analysis was used to determine the uniformity of spheroids both within (intraplate CV) and between (interplate CV) experimental repeats. This unit of measurement has been routinely used to assess the reproducibility of spheroids and Sittampalam *et al.*, 2004 suggested that less than 20% variation in spheroid size was acceptable. To assess both intraplate and interplate CV, at least 20 SHH medulloblastoma spheroids were seeded per plate in their optimal growth conditions and their diameter was calculated on day 4. Scatter plots showed little variation in spheroid diameter across three independent experimental repeats for all three cell lines (Figure 3.12). As shown in Table 3.3, the CV values calculated are all within the acceptable range of less than 20%, with UW228-3 cells showing the least variation.

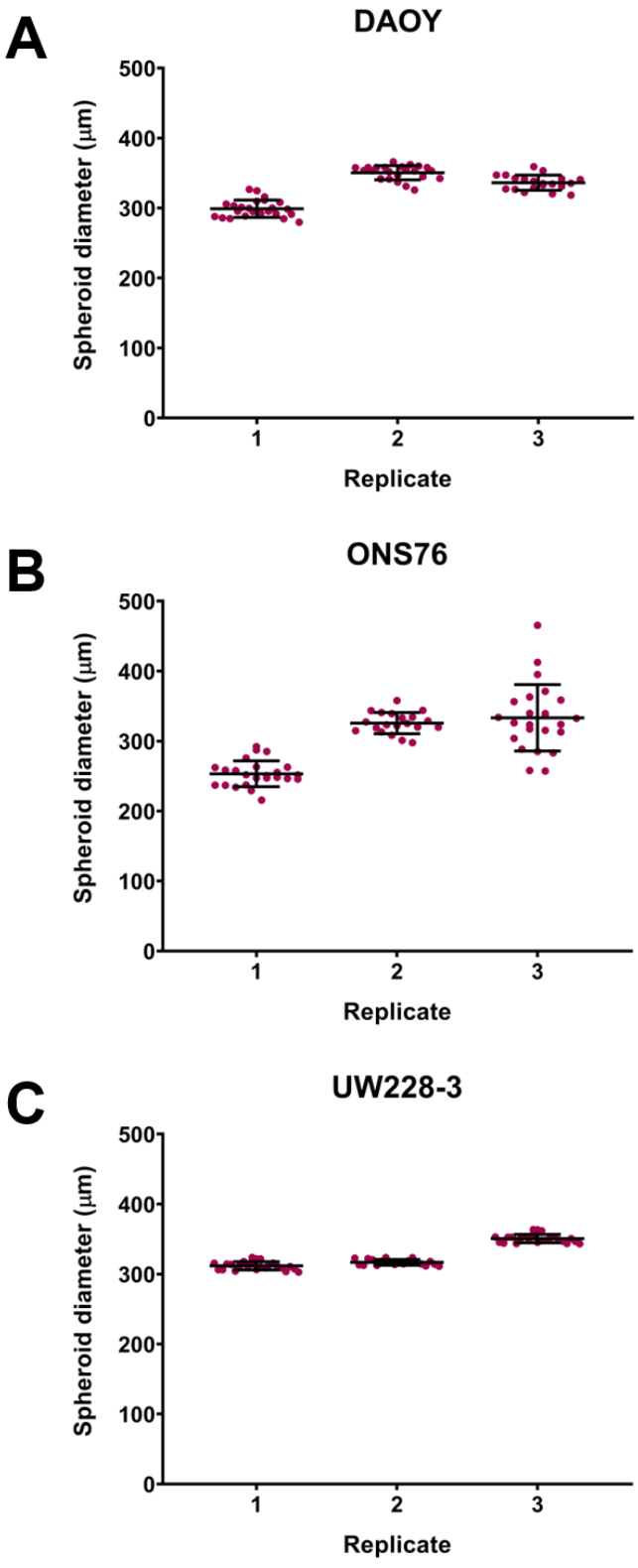


Figure 3.12 Coefficient of variation analysis for SHH medulloblastoma spheroids
Scatter plots displaying variation in spheroid diameter for DAOY (**A**), ONS76 (**B**), and UW228-3 (**C**) cell lines on day 4 over three independent experimental repeats (replicates 1, 2, and 3). Error bars represent the mean ± standard deviation for each experimental repeat containing ≥20 replicates.

Table 3.3 Coefficient of variation analysis for SHH medulloblastoma spheroids
Spheroid diameter variation was calculated using coefficient of variation (CV) analysis for DAOY, ONS76, and UW228-3 spheroids on day 4 over three independent experimental repeats (replicates 1, 2, and 3). Variation within each plate (intraplate CV) and across three plates (interplate CV) is shown. CV values <20% are considered acceptable (Sittampalam *et al.*, 2004).

Cell line	Intraplate CV (%)			Interplate CV (%)
	Replicate 1	Replicate 2	Replicate 3	
DAOY	4.13	2.91	3.21	7.60
ONS76	7.31	4.64	14.21	15.91
UW228-3	1.88	1.28	1.70	5.67

3.4 Characterisation of SHH medulloblastoma spheroids

So far, it has been shown that SHH medulloblastoma cell lines form tight, highly reproducible spheroids that continually grow for a week when cultured in neurosphere medium. Although this time frame is suitable for shorter studies, maintaining spheroids in culture for a longer time period would be a significant advantage over standard 2D culture techniques where cells need to be passaged every 3-4 days to maintain viability. SHH medulloblastoma spheroids were maintained for up to three weeks in culture in order to characterise their long-term growth patterns. Spheroid growth was assessed on days 1, 4, 7, 10, 14, 18, and 21, with two different analysis techniques: imaging to determine spheroid volume and CellTiter-Glo® 3D cell viability assay, a commercially-available luminescence assay. The relationship between either spheroid volume or luminescence signal and time was assessed using Pearson's correlation coefficient (r), a measure of the direction and magnitude of correlation, where values range from -1 (negative correlation) to +1 (positive correlation). In addition to this, spheroids were harvested and sectioned for immunohistochemical staining to assess how the expression of key markers of proliferation (Ki67) and hypoxia (CA9) changed over time.

3.4.1 SHH medulloblastoma spheroids are viable for long-term culture

As shown in Figure 3.13A, DAOY cells formed a tight spheroid after just 24 hours in culture and increased greatly in size over a three week period. Growth analysis revealed an increase in spheroid volume correlated with the length of time (Figure 3.13B; r = 0.9893; ****p≤0.0001) with spheroids reaching an average volume of $2.6x10^8$ μm^3 after 21 days in culture, equivalent to around 790 µm in diameter. Although the luminescence readout of the CellTiter-Glo® 3D cell viability assay also showed a significant correlation between relative luminescence units (RLU) and time (Figure 3.13C; r = 0.9891; ****p≤0.0001), the growth curve does not appear as linear as volume analysis.

Immunohistochemical staining of sectioned DAOY spheroids on days 7, 14, and 21 revealed an interesting pattern of expression (Figure 3.14). After seven days growth, expression of the proliferation marker Ki67 was visible throughout the spheroid section, with no expression of CA9 (a hypoxia marker) present. However, by day 14, positive CA9 staining in the centre of the spheroid section indicates the presence of a hypoxic core, despite there being positive Ki67 expression throughout the spheroid. By day 21, proliferation was restricted to the outer perimeter of the spheroid, with well-defined CA9 expression in a greater proportion of the spheroid core.

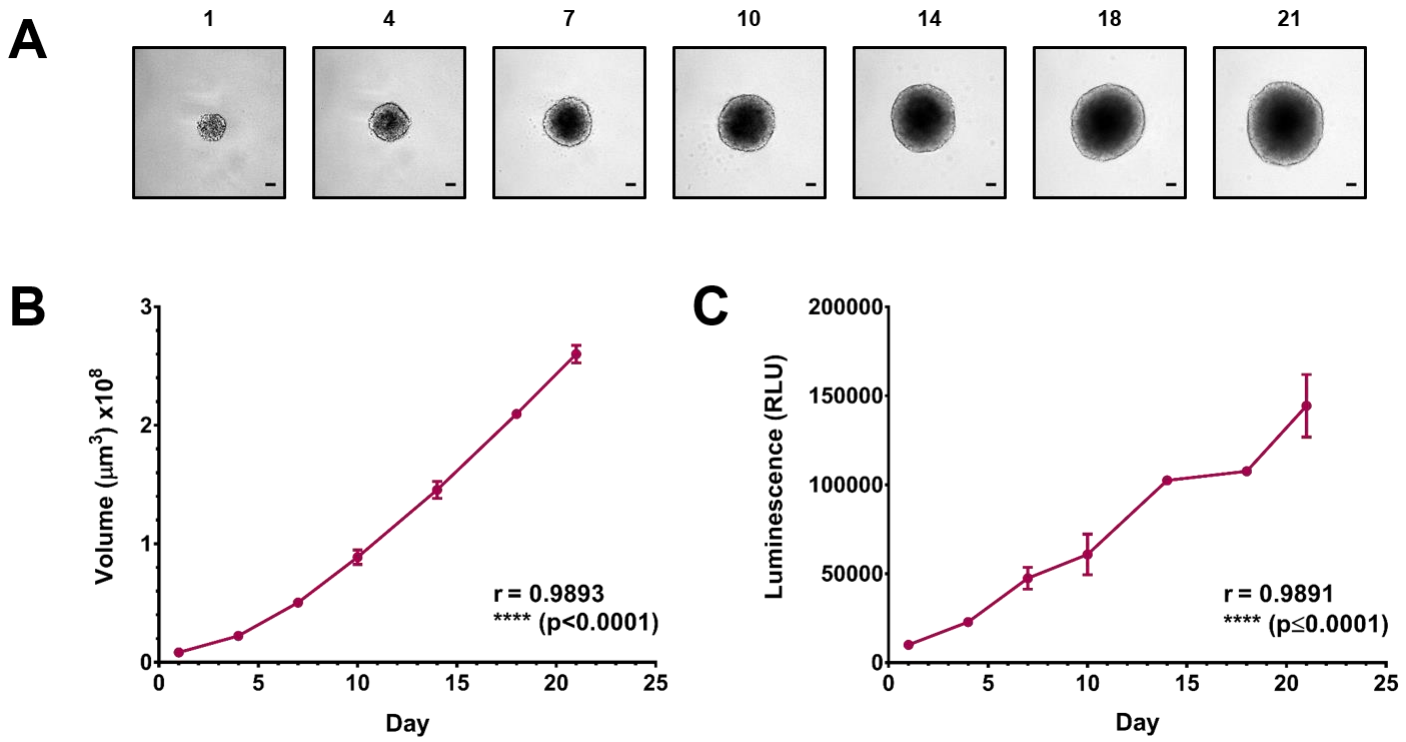


Figure 3.13 Long-term growth of DAOY spheroids

(**A**) Representative images of DAOY spheroids on days 1, 4, 7, 10, 14, 18, and 21 (scale bar: 100 µm). (**B**) Growth analysis revealed a significant increase in spheroid volume (µm^3) over the course of the assay (Pearson's correlation: r = 0.9893; ****p≤0.0001). (**C**) CellTiter-Glo® 3D cell viability assay also showed a significant increase in luminescence (RLU; relative luminescence units) over a three-week period (Pearson's correlation: r = 0.9891; ****p≤0.0001). Error bars represent the mean ± SEM of 4 independent experiments each containing ≥6 replicates at each time point.

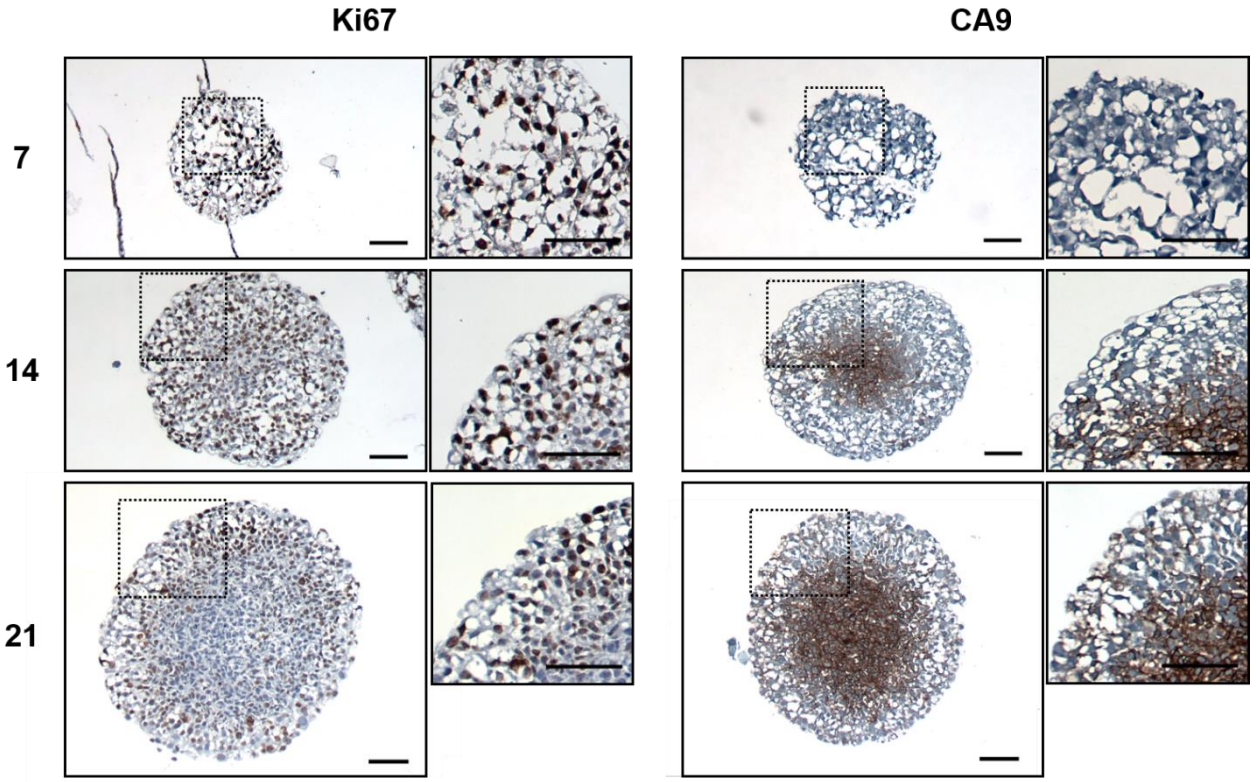


Figure 3.14 Immunohistochemical staining of DAOY spheroids for markers of proliferation (Ki67) and hypoxia (CA9)

DAOY spheroids were harvested on days 7, 14, and 21 and sections were stained with markers of proliferation (Ki67) and hypoxia (CA9). Ki67 expression was visible throughout the spheroid on days 7 and 14, but expression was restricted to the spheroid periphery by day 21. CA9 expression was present by day 14 and became more extensive by day 21. Representative images are shown (scale bar: 100 µm).

ONS76 cells formed a tight spheroid by day 4 and increased in size over a three week period (Figure 3.15A). Spheroid volume analysis showed a significant increase in size, correlating with longer culture time (Figure 3.15B; r = 0.9751; ***p=0.0002). Interestingly, ONS76 spheroid growth accelerated after seven days in culture, reaching an average volume of $3.5x10^8$ μm^3 on day 21 (around 870 µm in diameter). However, this acceleration was not as well observed in the luminescence analysis, where there was greater variability in the results, although the correlation was still apparent (Figure 3.15C; r = 0.9816; ****p≤0.0001).

ONS76 spheroid sections were stained for Ki67 and CA9 on days 7, 14, and 21 (Figure 3.16). As was the case with DAOY spheroids, ONS76 sections also showed expression of Ki67 throughout the entire section on days 7 and 14, with the expression restricted to the outer edge of the spheroid by day 21. This correlated with the expression of CA9, which was not visible by day 7 but became visible in the spheroid core by day 14 and more extensive on day 21.

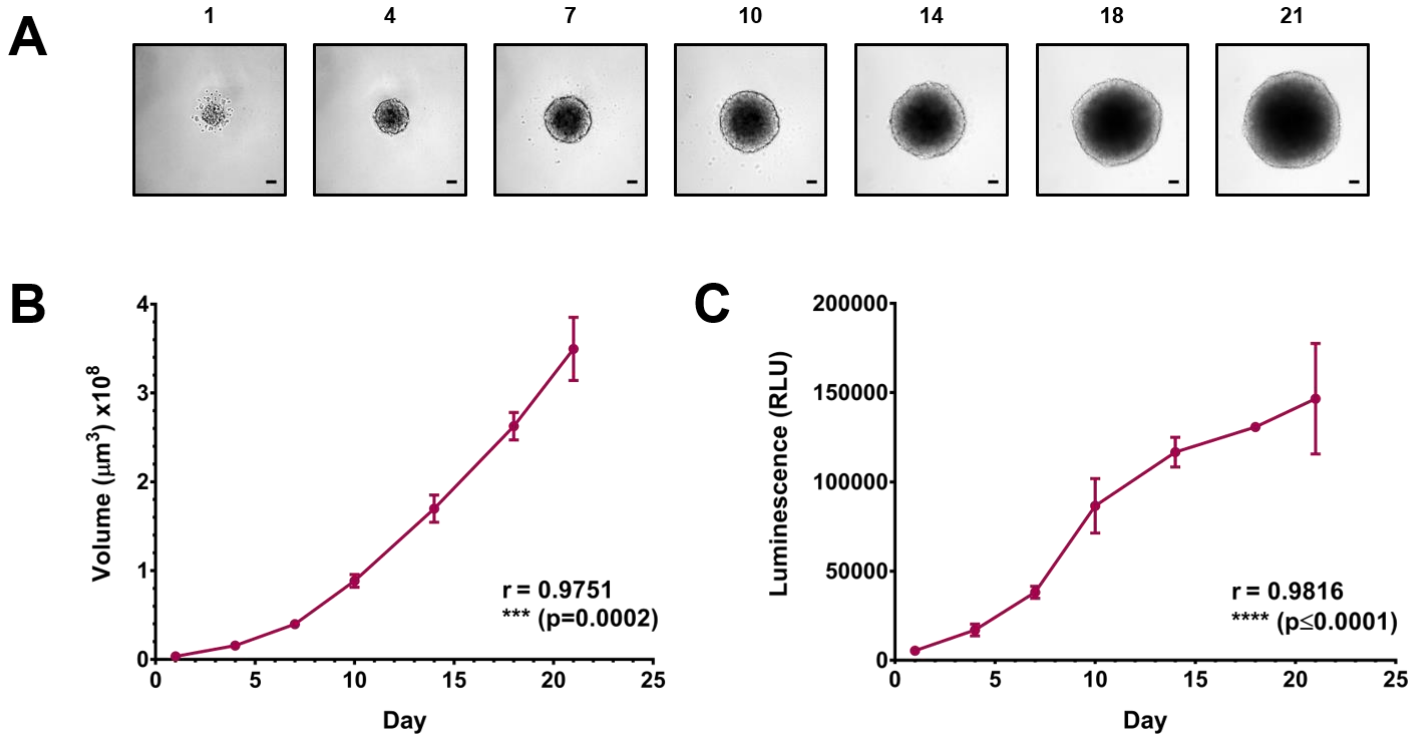


Figure 3.15 Long-term growth of ONS76 spheroids

(**A**) Representative images of ONS76 spheroids on days 1, 4, 7, 10, 14, 18, and 21 (scale bar: 100 µm). (**B**) Growth analysis revealed a significant increase in spheroid volume (µm^3) over the course of the assay (Pearson's correlation: r = 0.9751; ***p=0.0002). (**C**) CellTiter-Glo® 3D cell viability assay also showed a significant increase in luminescence (RLU; relative luminescence units) over a three-week period (Pearson's correlation: r = 0.9816; ****p≤0.0001). Error bars represent the mean ± SEM of 4 independent experiments each containing ≥6 replicates at each time point.

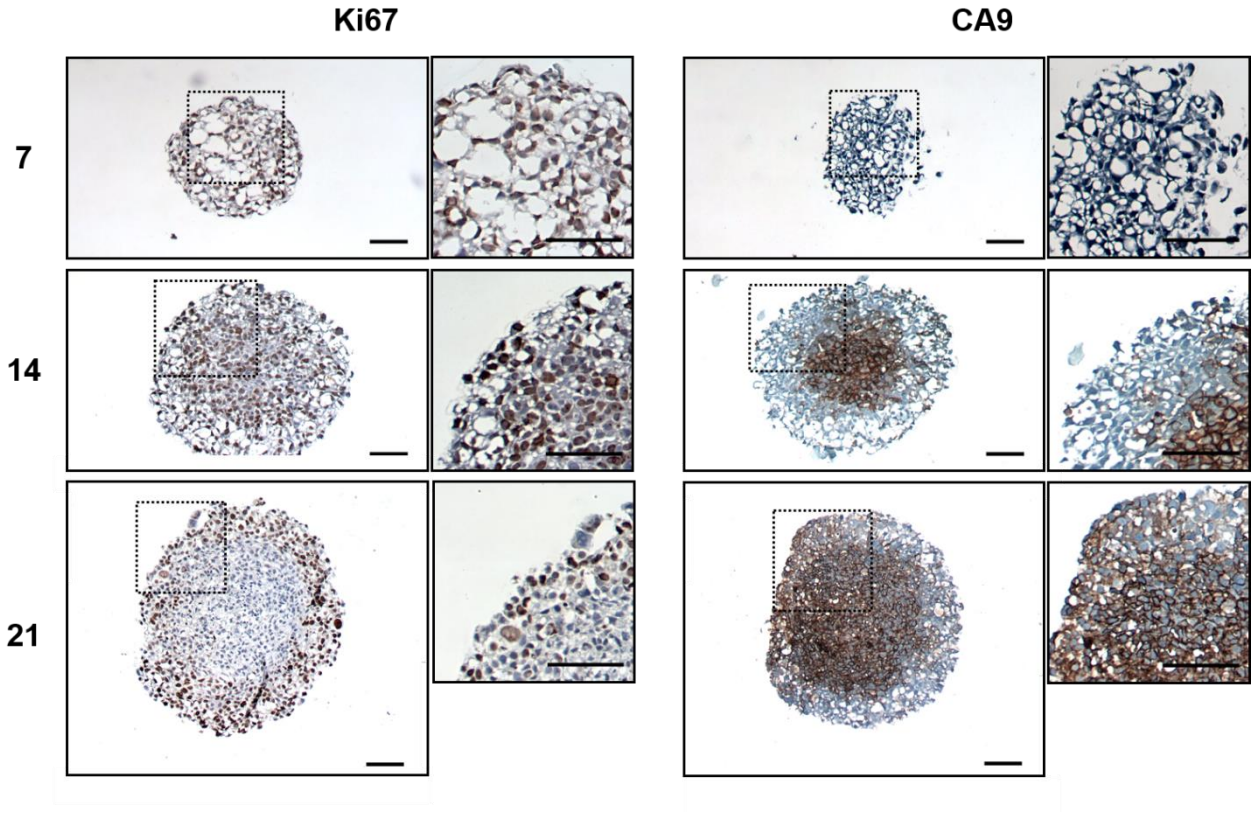


Figure 3.16 Immunohistochemical staining of ONS76 spheroids for markers of proliferation (Ki67) and hypoxia (CA9)

ONS76 spheroids were harvested on days 7, 14, and 21 and sections were stained with markers of proliferation (Ki67) and hypoxia (CA9). Ki67 expression was visible throughout the spheroid on days 7 and 14, but expression was restricted to the spheroid periphery by day 21. CA9 expression was present by day 14 and became more extensive by day 21. Representative images are shown (scale bar: 100 µm).

UW228-3 cells formed much smaller, denser spheroids than the other two cell lines and became ovoid shape by day 7, with an apparent dying population of cells around the spheroid edge as the course of the assay continued (Figure 3.17A). In addition, although spheroid volume did increase significantly (Figure 3.17B; r = 0.8406; *p=0.0361), growth plateaued at day 10. This was mirrored in the luminescence readouts over the same time period, where the results became more variable and showed a decrease in spheroid viability (Figure 3.17C; r = -0.2472; p=0.6368).

Immunohistochemical staining of sectioned UW228-3 spheroids was only performed for day 7 sections due to day 14 and 21 spheroids falling apart during manipulation. Expression of Ki67 was visible throughout the spheroid, with no evidence of CA9 expression (Figure 3.18).

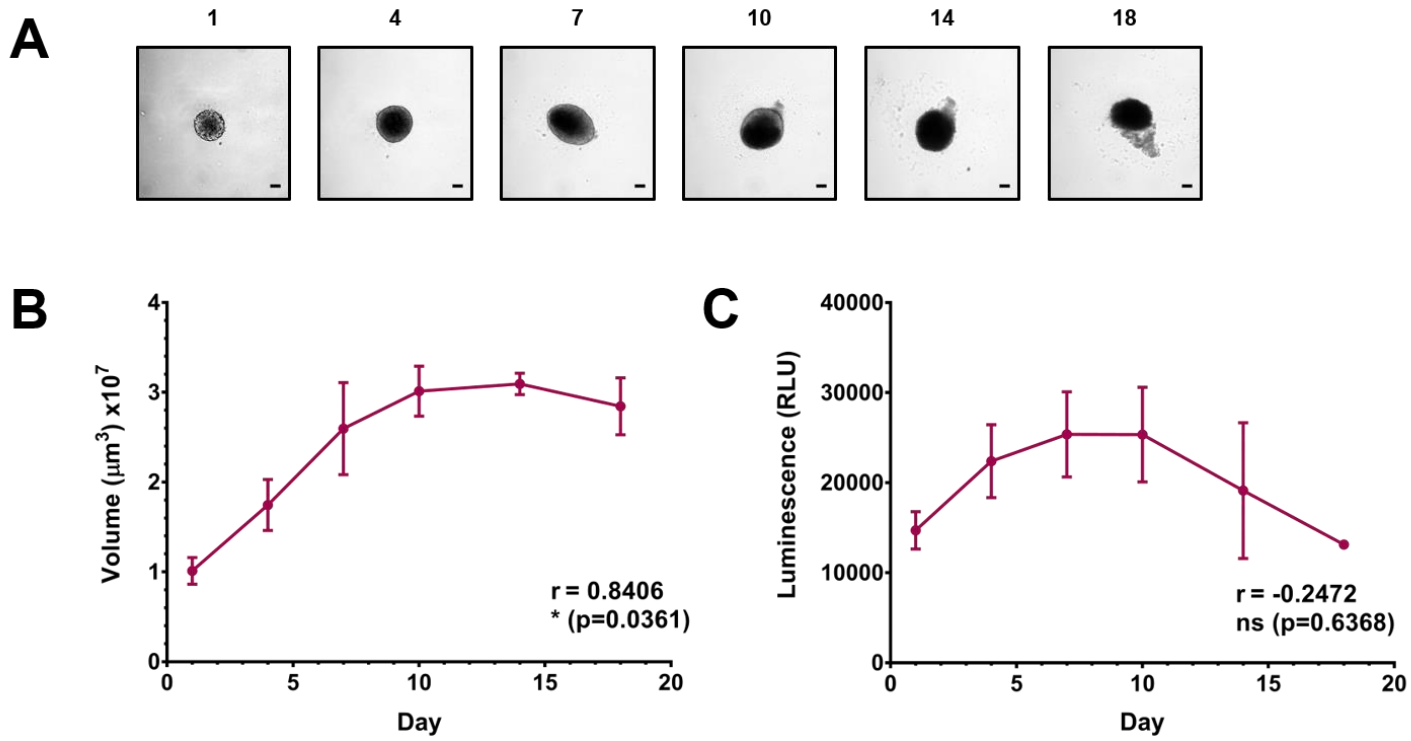


Figure 3.17 Long-term growth of UW228-3 spheroids

(**A**) Representative images of UW228-3 spheroids on days 1, 4, 7, 10, 14, and 18 (scale bar: 100 µm). (**B**) Growth analysis revealed a significant increase in spheroid volume (μm^3) over the course of the assay (Pearson's correlation: r = 0.8406; *p=0.0361), with size plateauing after 10 days in culture. (**C**) CellTiter-Glo® 3D cell viability assay did not show a significant increase in luminescence (RLU; relative luminescence units) over a three-week period (Pearson's correlation: r = -0.2472; p=0.6368), with viability decreasing after 10 days. Error bars represent the mean ± SEM of 4 independent experiments each containing ≥6 replicates at each time point.

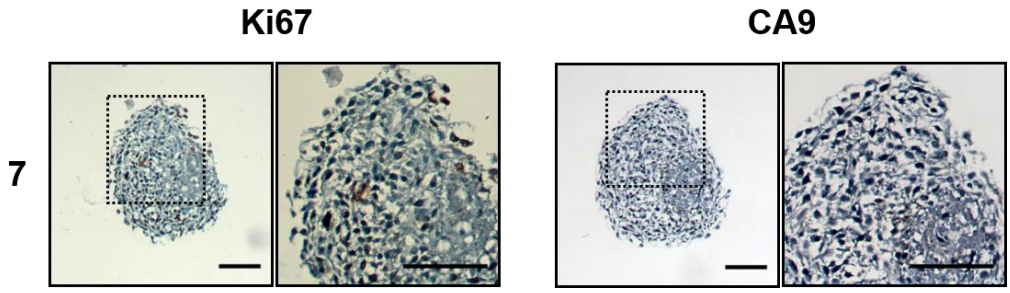


Figure 3.18 Immunohistochemical staining of UW228-3 spheroids for markers of proliferation (Ki67) and hypoxia (CA9)
UW228-3 spheroids were harvested on days 7 and sections were stained with markers of proliferation (Ki67) and hypoxia (CA9). Ki67 expression was visible throughout the spheroid section; however, CA9 expression was not present. Representative images are shown (scale bar: 100 µm).

3.4.2 SHH medulloblastoma spheroids express the stemness marker, SOX2

As shown in section 3.2.1, SHH medulloblastoma cell lines require neurosphere medium, not their standard culture medium, for sustained spheroid growth. As neurosphere medium contains supplements and growth factors routinely used in the culture and maintenance of neural stem cells, it was important to assess whether the spheroids produced in this model were enriched for markers of 'stemness'. SOX2 was chosen as this marker as it plays a crucial role in the maintenance of embryonic and neural stem cells. In addition, SOX2 expression was also shown to be higher in SHH medulloblastoma tumours, compared to the other three molecular subgroups (Ahlfeld *et al.*, 2013).

Immunohistochemical staining of sectioned DAOY, ONS76, and UW228-3 spheroids on day 7 showed SOX2 staining throughout the spheroid section and this was repeated on day 14 for DAOY and ONS76 sections (Figure 3.19). By day 21, SOX2 expression was limited to cells towards the spheroid edge.

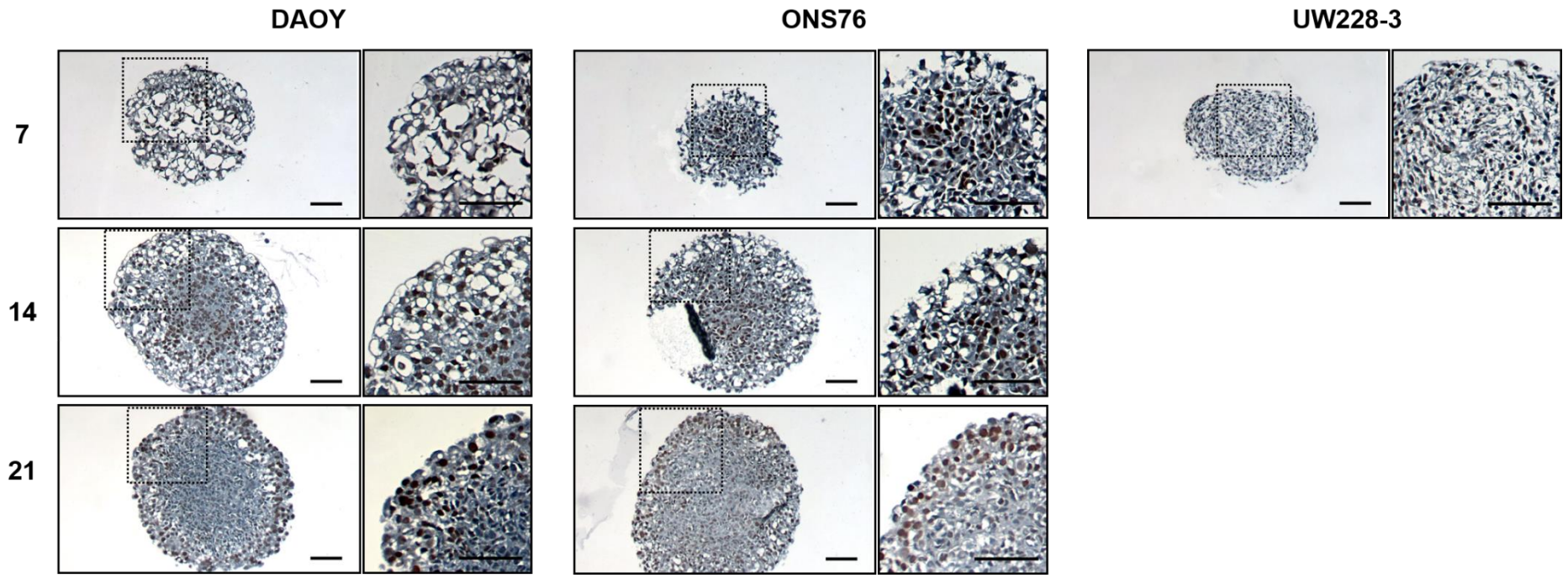


Figure 3.19 Immunohistochemical staining of SHH medulloblastoma spheroid sections for SOX2

SHH medulloblastoma spheroids were stained for the stemness marker SOX2. DAOY and ONS76 spheroid sections were stained for SOX2 on days 7, 14, and 21. However, UW228-3 spheroids fell apart during manipulation on days 14 and 21; therefore, staining for was only performed for day 7. SOX2 expression was visible throughout the spheroid on day 7 for all cell lines and on day 14 for DAOY and ONS76 spheroid. By day 21, expression was restricted to the spheroid periphery in DAOY and ONS76 sections. Representative images are shown (scale bar: 100 µm).

3.5 Summary

- Medulloblastoma cell lines representing three of the four molecular subgroups (SHH, Group 3, and Group 4) were tested in the spheroid model, forming different morphologies:
    - → SHH medulloblastoma cell lines (DAOY, ONS76, and UW228-3) formed tight, highly reproducible spheroids
    - → Group 3 medulloblastoma cell lines produced looser spheroids. However, HD-MB03 and D458 formed tighter spheroids with the addition of methyl cellulose and a centrifugation step. D283 and D425 spheroids were slightly more compact with these modifications but fell apart when undergoing manipulation
    - → Group 4 medulloblastoma cell lines failed to form suitable spheroids.
- Medulloblastoma cell line derived spheroids failed to thrive in the cell's standard culture medium. Instead, serum-free growth factor-enriched neurosphere was required for the continual growth of SHH medulloblastoma spheroids.
- Cell line differences in the 3D spheroid model correlate with subgroup-specific behaviours. The less aggressive adherent SHH cell lines readily form spheroids. However, the more invasive and aggressive Group 3 and Group 4 cell lines either form spheroids with a looser morphology or are unable to form suitable 3D structures.
- SHH medulloblastoma spheroids DAOY and ONS76 were viable in long-term culture (up to 21 days), with the expression of key markers of proliferation (Ki67) and hypoxia (CA9) reflecting the culture time. UW228-3 spheroids are not viable in long-term culture, with growth plateauing by day 10.
- SHH medulloblastoma cell lines express the 'stemness' marker SOX2 throughout the spheroid structures until day 14, following which expression is restricted to the spheroid periphery.

Chapter 4

Investigating drug response in medulloblastoma spheroids

Chapter 4. Investigating drug response in medulloblastoma spheroids

4.1 Introduction

Pre-clinical testing of potential therapeutic agents for cancer treatment typically involves *in vitro* screening of hundreds of drugs, with the most successful taken forward for *in vivo* testing. However, a significant number of drugs which pass *in vitro* tests later fail in animal models. Additionally, more than 90% of potential anticancer drugs that enter human trials fail to translate to the clinic (Dimasi *et al.*, 2010). The development of more appropriate cellular models that recapitulate tumour biology could positively influence pre-clinical testing by providing a more accurate prediction of drug response at the earliest stage. By taking forward only the most promising drug candidates from *in vitro* screening into *in vivo* tests, more therapeutic agents may be successful when progressing to the later trial stages. In turn, this would reduce the number of animals required for testing. The spheroid model would be a highly suitable and robust method for the screening of potential drugs. As shown in chapter 3, we have established a highly reproducible spheroid model for SHH medulloblastoma cell lines in which they are grown in the same growth-promoting medium, forming the same size by day 4. These identical conditions of growth make this model ideal for drug screening by allowing direct comparisons between cell lines (Friedrich *et al.*, 2009).

The aims of this chapter were therefore to:

(1) Compare spheroid drug response analysis methods
(2) Determine whether there was a difference in drug response in 2D monolayer versus 3D spheroid culture
(3) Optimise applications to further assess drug response in spheroids.

4.2 Comparison of spheroid drug response analysis methods

The first stage in the investigation of drug response in medulloblastoma spheroids was to determine an appropriate method of analysis. In section 3.4, two different techniques were used to assess spheroid growth: imaging to determine spheroid volume and the endpoint luminescence-based CellTiter-Glo® 3D cell viability assay. To assess whether changes in volume and viability were appropriate readouts for measuring drug response, SHH medulloblastoma spheroids were treated with increasing concentrations of etoposide, a chemotherapy drug currently used for the treatment of paediatric medulloblastoma. After 72 hours of treatment, spheroids were imaged before the CellTiter-Glo® 3D cell viability assay was performed. Viability was calculated as a percentage of the vehicle-treated controls and dose response curves were generated using non-linear regression analyses.

Both volume (Figure 4.1A) and viability (Figure 4.1B) analysis produced comparable dose response curves for all three cell lines. In order to assess the methods further, two additional parameters of non-linear regression analyses were compared for each cell line (Table 4.1). The first readout compared the fit of the drug response curve by measuring the hill slope (steepness of the curve). There was no significant difference in the hill slope values for either method of analysis for DAOY ($p=0.8057$), ONS76 ($p=0.8698$), and UW228-3 ($p=0.8482$) cell lines. There was also no significant difference in the IC_{50} values (the concentration required to inhibit cell viability by 50%) obtained for each method of analysis across all three cell lines (DAOY: $p=0.9811$; ONS76: $p=0.8075$; UW228-3: $p=0.3304$).

These results showed that both volume and viability were comparable methods of measuring spheroid drug response. The CellTiter-Glo® 3D cell viability assay is however an endpoint measurement, whereas volume can be continually assessed. Therefore, the decision regarding which method to use should be based on the needs of each individual experiment.

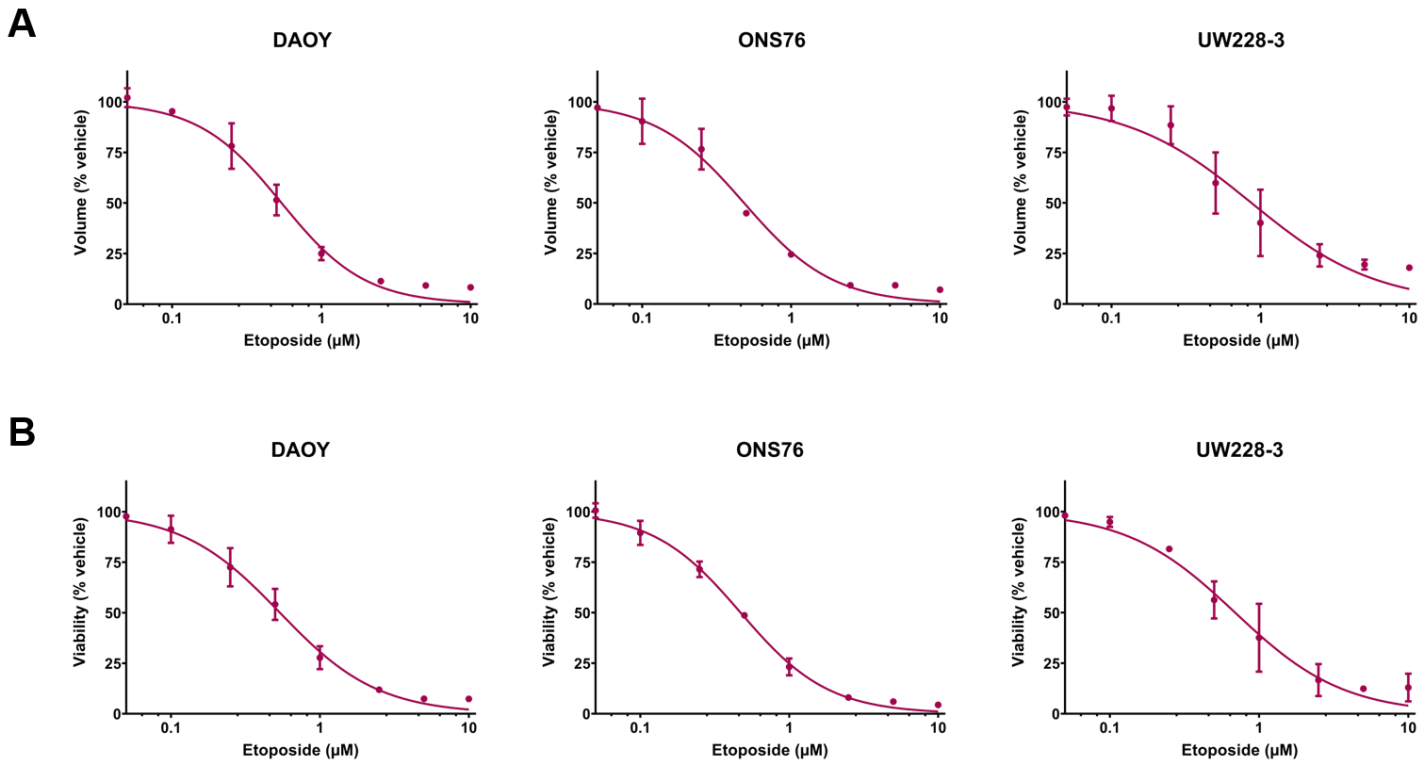


Figure 4.1 Comparison of volume and viability as methods of analysing spheroid drug response

DAOY, ONS76, and UW228-3 spheroids were treated with increasing concentrations of etoposide for 72 hours. Spheroids were imaged after treatment before the CellTiter-Glo® 3D cell viability assay was performed. Viability was calculated as a percentage of the vehicle-treated controls and dose response curves were generated using non-linear regression analyses. Both spheroid imaging (**A**; volume μm^3) and CellTiter-Glo® 3D cell viability assay (**B**; viability) produced comparable dose response curves. Error bars represent the mean ± SEM of at least 2 independent experiments each containing ≥3 replicates.

Table 4.1 Comparison of volume and luminescence as methods of analysing spheroid drug response

DAOY, ONS76, and UW228-3 spheroids were treated with increasing concentrations of etoposide for 72 hours. Non-linear regression analyses compared the fit of the drug response curve (hill slope) and IC_{50} concentrations generated by both spheroid imaging analysis (volume) and the CellTiter-Glo® 3D cell viability assay (luminescence). There was no significant difference in either method of analysis for the two comparisons made.

Cell line	Method of analysis	Comparison 1: curve		Comparison 2: IC_{50}	
		Hill slope	Significantly different?	IC_{50} concentration	Significantly different?
DAOY	Volume	1.879	No (p=0.8057)	0.541 µM	No (p=0.9811)
	Luminescence	1.500		0.539 µM	
ONS76	Volume	1.841	No (p=0.8698)	0.483 µM	No (p=0.8075)
	Luminescence	1.560		0.472 µM	
UW228-3	Volume	1.865	No (p=0.8482)	0.870 µM	No (p=0.3304)
	Luminescence	1.581		0.692 µM	

4.3 Comparison of drug response in 2D monolayer versus 3D spheroid culture

Measuring drug efficacy *in vitro* typically relies on testing potential therapeutic agents on cells grown as 2D monolayers. However, these assays fail to consider the multi-dimensional growth of tumours and therefore do not provide an accurate prediction of drug response. We hypothesised that drug efficacy would differ in 3D spheroids compared to 2D monolayer culture.

To test this hypothesis, SHH medulloblastoma cell lines were treated with increasing concentrations of four standard-of-care chemotherapy drugs (etoposide, vincristine, cisplatin, and lomustine) for 72 hours in both 2D monolayer and 3D spheroid culture. The CellTiter-Glo® 3D cell viability assay was chosen as the most suitable method of analysing the difference between conditions as it is an appropriate endpoint assay for both 2D and 3D culture. Viability was calculated as a percentage of the vehicle-treated controls and non-linear regression analyses were performed to normalise the data and produce dose-response curves from 100% to 0% viability.

Etoposide treatment revealed a significant difference in response in 2D monolayers versus 3D spheroids for all cell lines (Figure 4.2; $p \leq 0.0001$). IC_{50} values for DAOY cells (2D: 0.06 µM; 3D: 0.48 µM) and ONS76 cells (2D: 0.03 µM; 3D: 0.39 µM) showed the most apparent differences, with fold changes of x7 and x12, respectively. There was also a smaller, yet still significant, difference in response for UW228-3 cells (2D: 0.24 µM; 3D: 0.66 µM) with a fold change of x1.75. Interestingly, around 5-10% of cells remained viable at the highest dose of etoposide (10 µM), indicating the possible presence of a drug resistant subpopulation of cells.

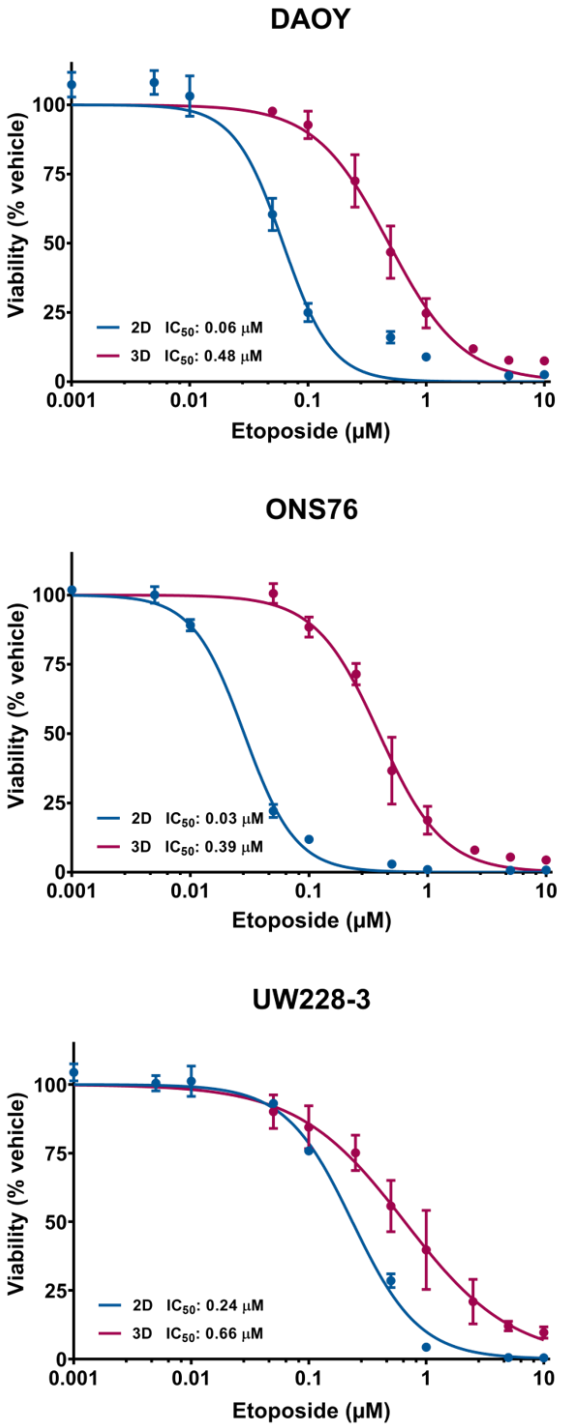


Figure 4.2 Comparison of etoposide response in 2D monolayers and 3D spheroids
DAOY, ONS76, and UW228-3 cell lines were treated with increasing concentrations of etoposide in both 2D monolayer (blue) and 3D spheroid (red) culture for 72 hours. CellTiter-Glo® 3D cell viability assay was performed to compare the responses and viability was calculated as a percentage of the vehicle-treated controls. Dose response curves were generated using non-linear regression analyses and IC_{50} values were calculated for both culture conditions. All three cell lines were more resistant to etoposide treatment in 3D spheroid culture as shown by the shift in the drug response curves and significantly higher IC_{50} values ($p \leq 0.0001$). Error bars represent the mean ± SEM of at least 3 independent experiments each containing ≥3 replicates.

Comparison of vincristine response showed that all three SHH medulloblastoma cell lines were more resistant to treatment in 3D spheroid culture compared to 2D monolayers (Figure 4.3; $p \leq 0.0001$). The fold changes in IC_{50} values for the DAOY (x1.68; 2D: 1.47 nM; 3D: 3.94 nM) and ONS76 (x1.88; 2D: 2.30 nM; 3D: 6.63 nM) cell lines were relatively similar. However, the response to vincristine treatment from the UW228-3 cell line was particularly interesting. Non-linear regression analysis failed to fit a sigmoidal dose-response curve for UW228-3 spheroids due to viability plateauing at around 50% at concentrations of 1 nM and higher. Subsequently, the IC_{50} values and fold change generated from this analysis were ambiguous (x56.39; 2D: 0.90; 3D: 51.65). However, the plateauing response of UW228-3 spheroids to vincristine indicated again that there could be a subpopulation of therapy-resistant cells after treatment. A similar population was also observed in the DAOY and ONS76 spheroids, where around 10% of cells were viable after higher doses of vincristine, with no remaining viable cells present in 2D monolayer culture.

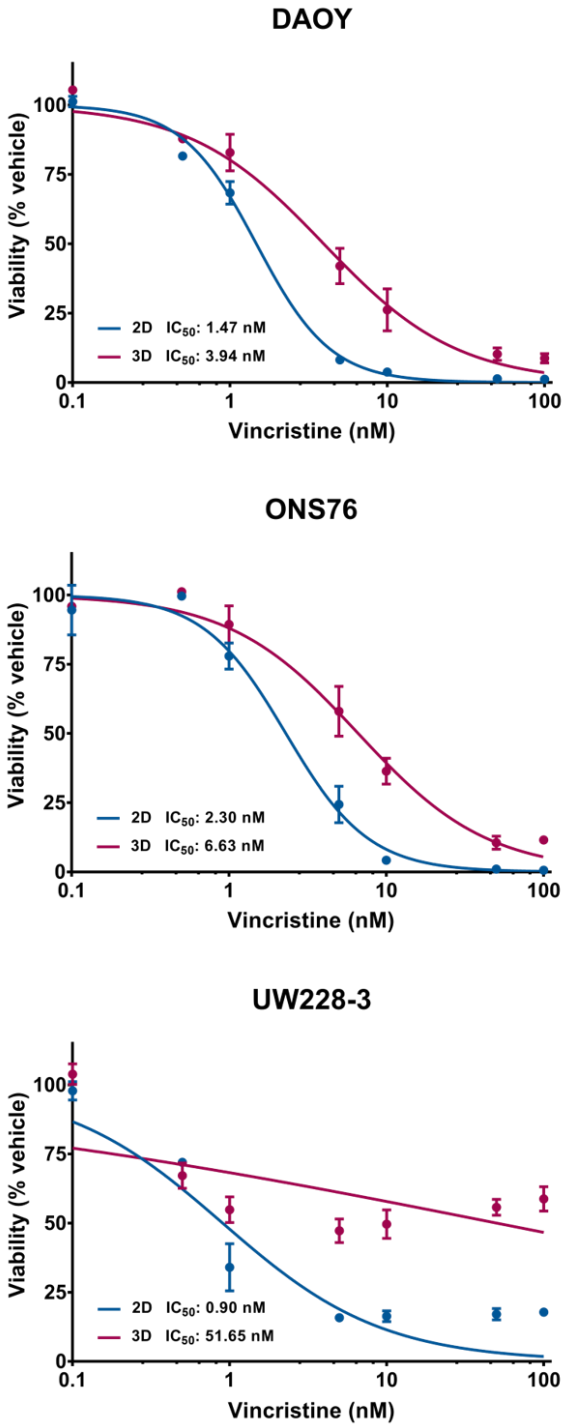


Figure 4.3 Comparison of vincristine response in 2D monolayers and 3D spheroids
DAOY, ONS76, and UW228-3 cell lines were treated with increasing concentrations of vincristine in both 2D monolayer (blue) and 3D spheroid (red) culture for 72 hours. CellTiter-Glo® 3D cell viability assay was performed to compare the responses and viability was calculated as a percentage of the vehicle-treated controls. Dose response curves were generated using non-linear regression analyses and IC_{50} values were calculated for both culture conditions. All three cell lines were more resistant to vincristine treatment in 3D spheroid culture as shown by the shift in the drug response curves and significantly higher IC_{50} values ($p \leq 0.0001$). Error bars represent the mean ± SEM of at least 3 independent experiments each containing ≥3 replicates.

All three SHH medulloblastoma cell lines displayed a shift in response and were more resistant to cisplatin treatment in 3D spheroid culture compared to 2D monolayers (Figure 4.4; $p \leq 0.0001$). Fold changes in IC_{50} values of x10.38 were observed for DAOY cells (2D: 0.08 µM; 3D: 0.91 µM), x24.2 for ONS76 cells (2D: 0.05 µM; 3D: 1.26 µM), and x1.05 for the UW228-3 cell line (2D: 0.59 µM; 3D: 1.21 µM). The highest concentration of cisplatin (10 µM) was sufficient to reduce spheroid viability to less than 4% across all three cell lines.

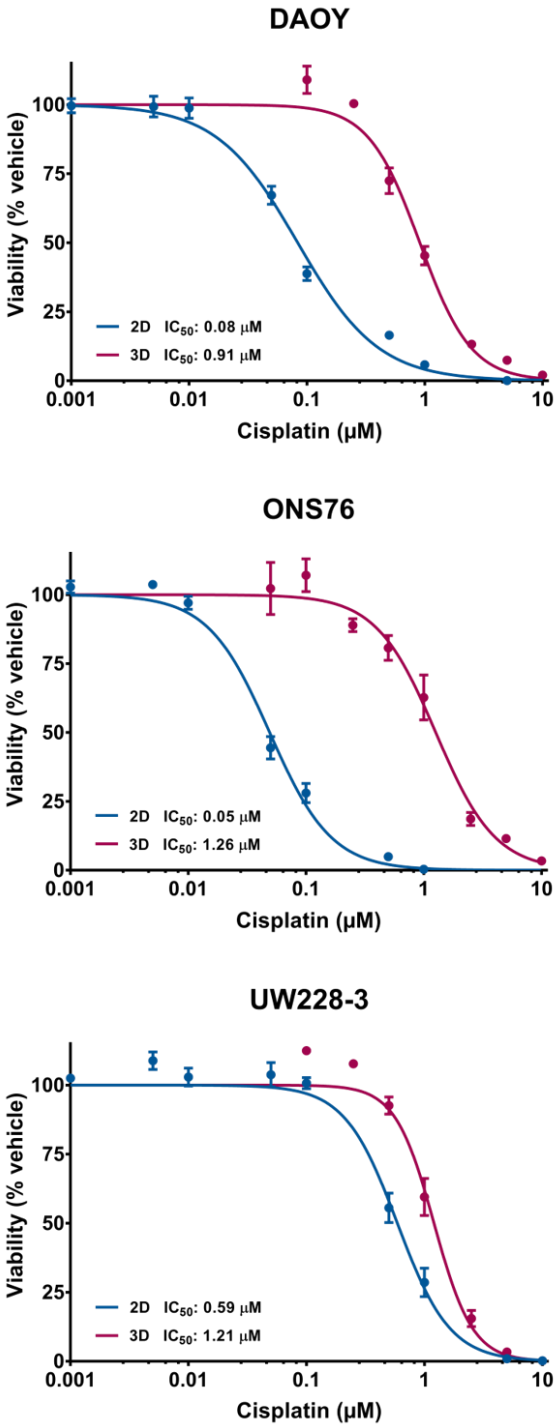


Figure 4.4 Comparison of cisplatin response in 2D monolayers and 3D spheroids
DAOY, ONS76, and UW228-3 cell lines were treated with increasing concentrations of cisplatin in both 2D monolayer (blue) and 3D spheroid (red) culture for 72 hours. CellTiter-Glo® 3D cell viability assay was performed to compare the responses and viability was calculated as a percentage of the vehicle-treated controls. Dose response curves were generated using non-linear regression analyses and IC_{50} values were calculated for both culture conditions. All three cell lines were more resistant to cisplatin treatment in 3D spheroid culture as shown by the shift in the drug response curves and significantly higher IC_{50} values ($p \leq 0.0001$). Error bars represent the mean ± SEM of at least 3 independent experiments each containing ≥3 replicates.

Comparison of lomustine response in 2D monolayers and 3D spheroids showed that only the highest concentrations tested were effective in both culture conditions (Figure 4.5). DAOY and ONS76 cell lines were more resistant to treatment in 3D spheroid culture at these higher concentrations and had significantly higher IC_{50} values than 2D monolayer culture ($p \leq 0.0001$). However, the fold change was smaller than the other chemotherapy agents tested with values of x1.43 for DAOY cells (2D: 35.80 µM; 3D: 86.85 µM) and x1.63 for ONS76 cells (2D: 31.13 µM; 3D: 81.97 µM). There was no significant difference in IC_{50} concentrations for the UW228-3 cell line (2D: 80.28 µM; 3D: 87.39 µM; $p=0.6027$).

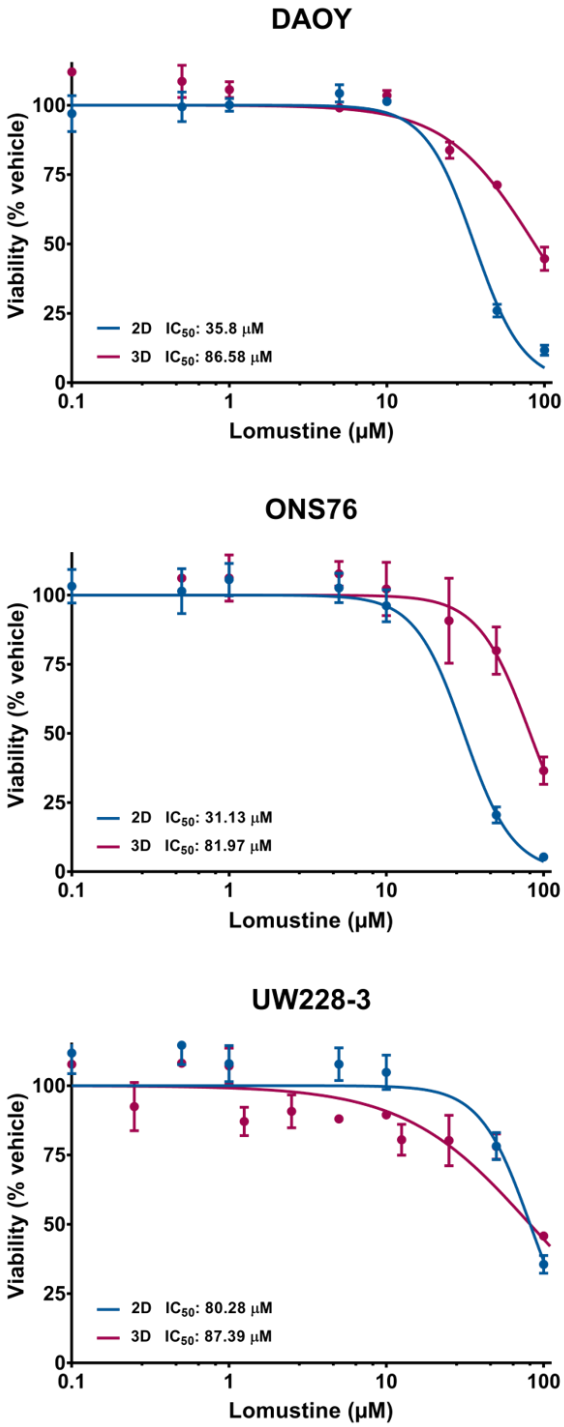


Figure 4.5 Comparison of lomustine response in 2D monolayers and 3D spheroids
DAOY, ONS76, and UW228-3 cell lines were treated with increasing concentrations of lomustine in both 2D monolayer (blue) and 3D spheroid (red) culture for 72 hours. CellTiter-Glo® 3D cell viability assay was performed to compare the responses and viability was calculated as a percentage of the vehicle-treated controls. Dose response curves were generated using non-linear regression analyses and IC_{50} values were calculated for both culture conditions. Only the highest concentrations of lomustine were effective for all cell lines in both conditions. DAOY and ONS76 cell lines were more resistant to lomustine treatment in 3D spheroid culture at these higher concentrations and had significantly higher IC_{50} values than 2D monolayer culture ($p \leq 0.0001$). There was no difference in response for the UW228-3 cell line ($p=0.6027$). Error bars represent the mean ± SEM of at least 3 independent experiments each containing ≥3 replicates.

Overall, there was a significant shift in drug response with 3D spheroids being more resistant to treatment compared to 2D monolayer culture in almost all cell lines and drugs tested (11 out of the 12 combinations). Details of the comparisons are summarised in Table 4.2, including significant differences and fold changes in IC_{50} concentrations.

Table 4.2 Comparison of drug response in 2D monolayers and 3D spheroids for SHH medulloblastoma cell lines

DAOY, ONS76, and UW228-3 cell lines were treated with increasing concentrations of etoposide, vincristine, cisplatin or lomustine in both 2D monolayer and 3D spheroid culture for 72 hours. CellTiter-Glo® 3D cell viability assay was performed to compare the responses and viability was calculated as a percentage of the vehicle-treated controls. Non-linear regression analysis was used to compare the response of cell lines to each drug in both conditions and IC_{50} values (mean ± SEM) were calculated. Significant differences in IC_{50} concentrations and fold changes from 2D monolayer to 3D spheroid culture are shown.

Drug	Cell line	IC_{50} concentrations		Significant difference in IC_{50} concentrations?	IC_{50} fold change (2D → 3D)
		2D monolayers	3D spheroids		
Etoposide (µM)	DAOY	0.06 ± 0.005	0.48 ± 0.042	Yes (p≤0.0001)	x7
	ONS76	0.03 ± 0.001	0.39 ± 0.032	Yes (p≤0.0001)	x12
	UW228-3	0.24 ± 0.015	0.66 ± 0.104	Yes (p≤0.0001)	x1.75
Vincristine (nM)	DAOY	1.47 ± 0.06	3.94 ± 0.50	Yes (p≤0.0001)	x1.68
	ONS76	2.30 ± 0.24	6.63 ± 0.79	Yes (p≤0.0001)	x1.88
	UW228-3	0.90 ± 0.05	51.65 ± 30.95	Yes (p≤0.0001)	x56.39
Cisplatin (µM)	DAOY	0.08 ± 0.005	0.91 ± 0.071	Yes (p≤0.0001)	x10.38
	ONS76	0.05 ± 0.003	1.26 ± 0.101	Yes (p≤0.0001)	x24.2
	UW228-3	0.59 ± 0.035	1.21 ± 0.086	Yes (p≤0.0001)	x1.05
Lomustine (µM)	DAOY	35.80 ± 3.69	86.85 ± 8.91	Yes (p≤0.0001)	x1.43
	ONS76	31.13 ± 4.01	81.97 ± 9.06	Yes (p≤0.0001)	x1.63
	UW228-3	80.28 ± 7.69	87.39 ± 11.02	No (p=0.6027)	x0.09

4.4 Optimisation of applications to further assess drug response in spheroids

So far in this chapter, it has been shown that volume and luminescence can be used as comparable measurements of spheroid drug response. As well as this, we have shown that there is a significant difference in response to chemotherapeutic drugs in spheroids compared to standard 2D monolayer culture. The following sections of this chapter aim to extend this analysis by demonstrating ways in which the spheroid model can be applied to further investigate drug response.

4.4.1 Combining fluorescent staining with automated imaging analysis allows high-throughput readouts of spheroid viability

Drug response analyses performed in section 4.3 indicated the presence of viable cells within the spheroids after exposure to high doses of chemotherapeutic agents. To further investigate this subpopulation of cells and the positioning of viable cells within the spheroid, fluorescent staining was combined with automated imaging analysis to provide additional readouts of spheroid viability.

DAOY, ONS76, and UW228-3 spheroids were treated with three concentrations of vincristine (1, 5, and 10 nM) for 72 hours. After treatment, the fluorescent dyes Calcein-AM (CAM) and Propidium Iodide (PI) were added to the spheroid wells as markers of live and dead cells, respectively. Following this, automated imaging analysis was performed using the Celigo® cytometer to measure the relative intensity of CAM and PI signals. A CAM/PI ratio was calculated to provide an indication of spheroid health and viability with a ratio of >1 representing high viability and <1 indicating low viability. Significant differences in CAM/PI ratios were calculated using one-way ANOVA analyses which compared the differences in means of at least two independent groups. A Dunnett's post-hot test was also

performed to correct for multiple comparisons. This test compared every mean to the control (vehicle-treated) mean to calculate statistical significance.

As shown in Figure 4.6, there was a decrease in the CAM/PI ratio at increasing concentrations of vincristine compared to the vehicle-treated controls. For each cell line, the PI staining of dead cells appeared to be localised to the centre of the spheroid, with CAM-positive cells present at the spheroid periphery even in spheroids treated at the highest vincristine concentration (10 nM).

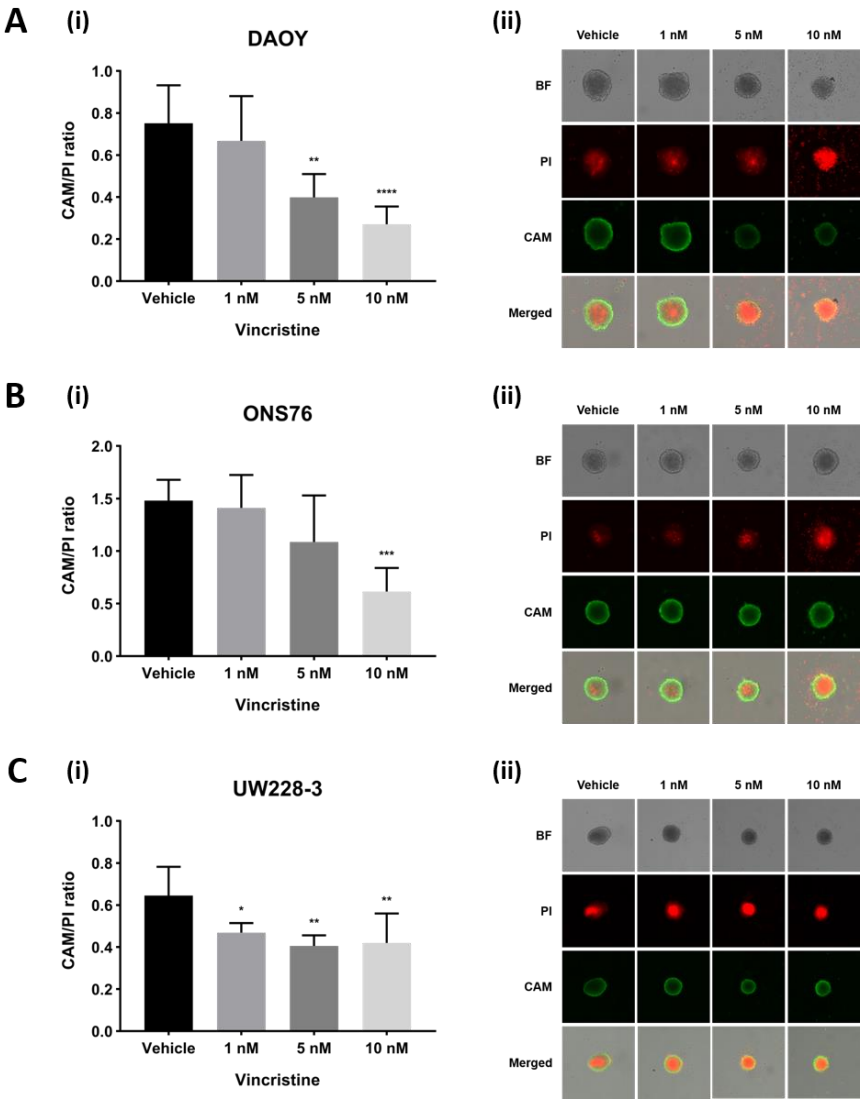


Figure 4.6 Assessment of spheroid viability after vincristine treatment via Calcein-AM and Propidium Iodide staining

DAOY (**A**), ONS76 (**B**), and UW228-3 (**C**) spheroids were treated with three concentrations of vincristine (1, 5, and 10 nM) for 72 hours and stained with the viability markers Calcein-AM (CAM; live cells) and Propidium Iodide (PI; dead cells). (**i**) Automated imaging analysis using the Celigo® cytometer showed a decrease in CAM/PI ratio at increasing concentrations of vincristine, representing a decrease in viability. Error bars represent the mean ± SD of one experiment containing 6 replicates. Significance differences in CAM/PI ratios in comparison to vehicle-treated controls was calculated using one-way ANOVA analyses with Dunnett's multiple comparisons post-hoc test (*p≤0.05, **p≤0.01, ***p≤0.001, ****p≤0.0001). (**ii**) Representative brightfield (BF), PI, CAM, and merged images of treated spheroids are shown.

4.4.2 Continual monitoring of spheroid volume allows the effects of drugs to be measured over time

One of the main disadvantages of chemotherapeutic screening in standard 2D monolayer culture is that the effects of drugs can only be assessed over a short period of time, typically 24 to 72 hours. We have already shown in this chapter that there appears to be a subpopulation of therapy-resistant cells remaining after treatment. We hypothesised that by monitoring the effects of drug treatment over a longer period of time, it would reveal differences in drug response typically missed in endpoint experiments.

Continual monitoring of spheroid volume to assess the effects of drugs over time was carried out with the DAOY and ONS76 cell lines as these spheroids proved the most suitable for long-term culture (see section 3.4.1). A schematic diagram summarising the approach for the continual monitoring of drug response is shown in Figure 4.7. Cells were seeded on day 0 and a spheroid of optimal size was produced by day 4. At this point, spheroids were treated for 72 hours (the same treatment duration tested previously in sections 4.2 and 4.3) with three doses of a chemotherapeutic drug (either low dose, the IC_{50} dose (calculated in section 4.3) or high dose) and a vehicle control. Etoposide, vincristine, and cisplatin were chosen as suitable drugs to test, with lomustine excluded due to lack of potency. Following treatment, a 50% medium replenishment was performed on days 7 and 10. A complete medium replacement could not be performed as manipulation to the spheroids could result in cell loss or disruption, instead 50% medium replenishment (resulting in a 1:2 dilution of the remaining drug and residual drug activity) is considered acceptable in spheroid-based drug assays (Friedrich *et al.*, 2009).

Imaging to measure spheroid volume was chosen as the most suitable method of drug response analysis as it is a continual, not endpoint, measurement. Images were taken on day 4 (pre-treatment) and day 7 (post-treatment), as well as

additional monitoring on days 10 and 13. Changes in spheroid volume were calculated as a percentage of day 4. Significant differences in volume between the vehicle- and drug-treated spheroids were calculated using repeated measures two-way ANOVA analyses which determined how the response (in this case, spheroid volume) was affected by two factors (treatment and time point). A Dunnett's post-hoc test was also performed to correct for multiple comparisons. This test compared, at each time point, every mean to the control (vehicle-treated) mean to calculate statistical significance.

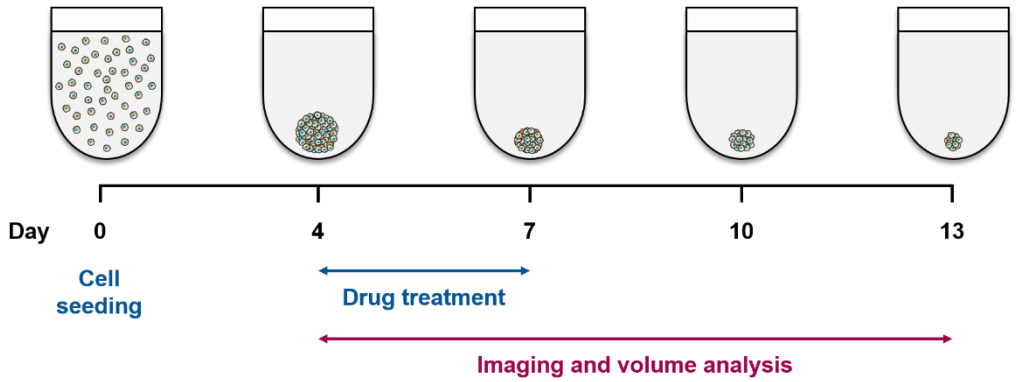


Figure 4.7 Schematic diagram describing the continual monitoring of spheroid drug response

Cells were seeded on day 0 and a spheroid of optimal size was produced by day 4. At this point, spheroids were drug treated for 72 hours, followed by 50% medium replenishment on days 7 and 10. To measure changes in spheroid volume, images were taken on day 4 (pre-treatment) and day 7 (post-treatment), as well as additional monitoring on days 10 and 13.

Continual monitoring of the effects of etoposide treatment on DAOY and ONS76 spheroids is shown in Figure 4.8. Long-term drug response analysis revealed that when treated with a low dose of etoposide (0.1 µM), similar to the peak CSF concentration measured in patients (Kiya *et al.*, 1992; Relling *et al.*, 2016), spheroid volume failed to decrease both during and after treatment. By day 13, spheroids of both cell lines treated with the low dose had more than doubled in size relative to day 4, to approximately 220% in volume; however, this growth was still significantly slower than the vehicle-treated controls. Spheroids treated with either the IC_{50} dose (DAOY: 0.48 µM; ONS76: 0.39 µM) or high dose (1 µM) of etoposide showed continual regression in volume over the course of the experiment.

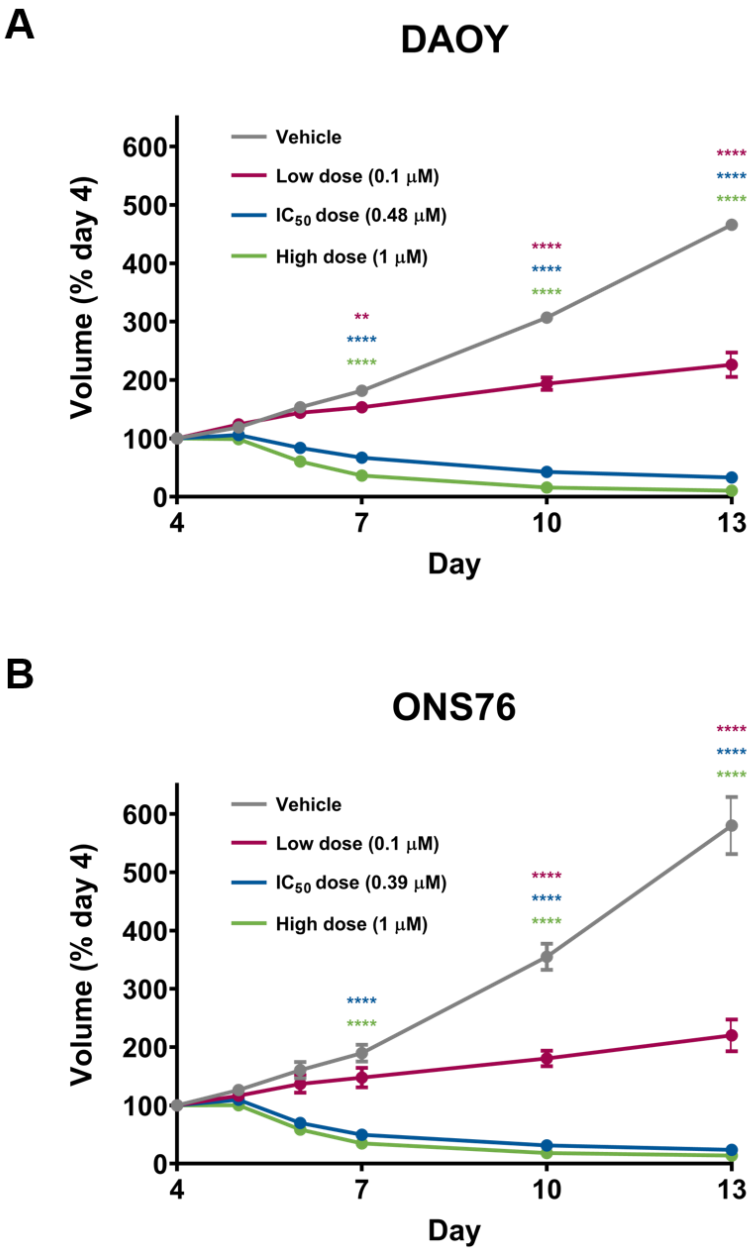


Figure 4.8 Continual monitoring of the effects of etoposide treatment on DAOY and ONS76 spheroids

DAOY (**A**) and ONS76 (**B**) spheroids were treated with a DMSO vehicle (grey) and three concentrations of etoposide: low dose (red; 0.1 µM), IC_{50} dose (blue; DAOY: 0.48 µM, ONS76: 0.39 µM), and high dose (green; 1 µM) for 72 hours. Images were taken on days 4, 7, 10, and 13 to measure changes in spheroid volume (as a percentage of day 4). Treatment with a low dose of etoposide failed to reduce spheroid volume both during and after treatment, but spheroids were significantly smaller than vehicle-treated controls. Spheroids treated with either the IC_{50} or high dose of etoposide showed continual regression in volume. Error bars represent the mean ± SEM of 3 independent experiments each containing 4 replicates. Significance was calculated using repeated measures two-way ANOVA analyses with Dunnett's multiple comparisons post-hoc test. Differences in response between the vehicle and etoposide treatments are represented by coloured asterisks of the corresponding dosage (**p≤0.01, ****p≤0.0001).

The effects of different vincristine dosages were also measured over time (Figure 4.9). A low dose of 1 nM was chosen as this was reported to be the measurable concentration in patient CSF (Jackson *et al.*, 1981). However, treatment with this low dose in spheroids allowed continual growth over the course of the assay, with no significant difference in response compared to the vehicle-treated control for the ONS76 cell line at any time point. Spheroids treated with either the IC_{50} dose (DAOY: 3.94 nM; ONS76: 6.63 nM) or high dose (10 nM) of vincristine showed a significant reduction in volume at each time point measured.

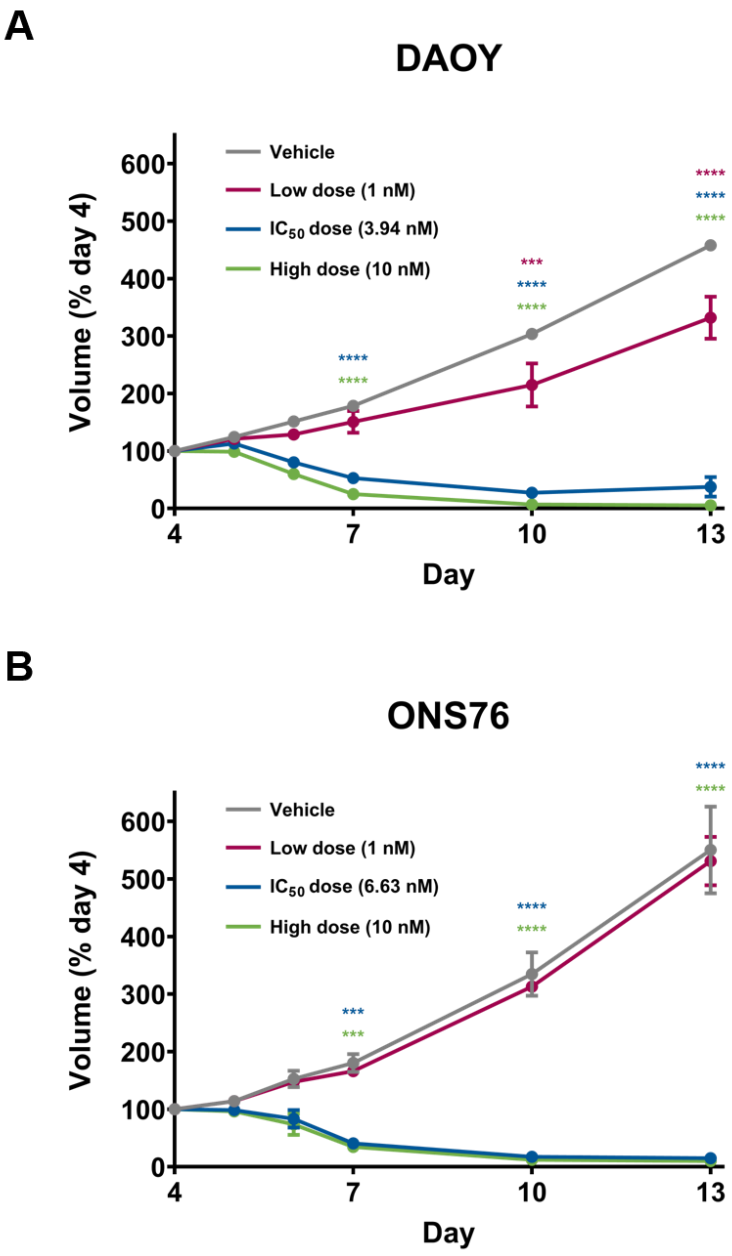


Figure 4.9 Continual monitoring of the effects of vincristine treatment on DAOY and ONS76 spheroids

DAOY (**A**) and ONS76 (**B**) spheroids were treated with a DMSO vehicle (grey) and three concentrations of vincristine: low dose (red; 1 nM), IC_{50} dose (blue; DAOY: 3.94 nM, ONS76: 6.63 nM), and high dose (green; 10 nM) for 72 hours. Images were taken on days 4, 7, 10, and 13 to measure changes in spheroid volume (as a percentage of day 4). Treatment with a low dose of vincristine allowed continual growth of the spheroids over the course of the assay. However, IC_{50} and high dose treatments were effective in reducing spheroid volume. Error bars represent the mean ± SEM of 3 independent experiments each containing 4 replicates. Significance was calculated using repeated measures two-way ANOVA analyses with Dunnett's multiple comparisons post-hoc test. Differences in response between the vehicle and etoposide treatments are represented by coloured asterisks of the corresponding dosage (***p≤0.001, ****p≤0.0001).

DAOY and ONS76 spheroids were also continually monitored after low dose (0.5 µM), IC_{50} dose (DAOY: 0.91 µM; ONS76: 1.26 µM), and high dose (5 µM) cisplatin treatment. These concentrations represented both the minimum measurable level of cisplatin in the CSF (low dose) and the peak CSF concentration (high dose) (Nakagawa *et al.*, 1996). For DAOY spheroids, all three doses of cisplatin reduced volume in comparison to the vehicle-treated control and by day 13, spheroid volume was below 100% for all treatment conditions. For the ONS76 cell line, low dose cisplatin treatment was less effective and spheroids continued to grow over the course of the assay. However, IC_{50} and high dose treatments were successful in reducing spheroid volume.

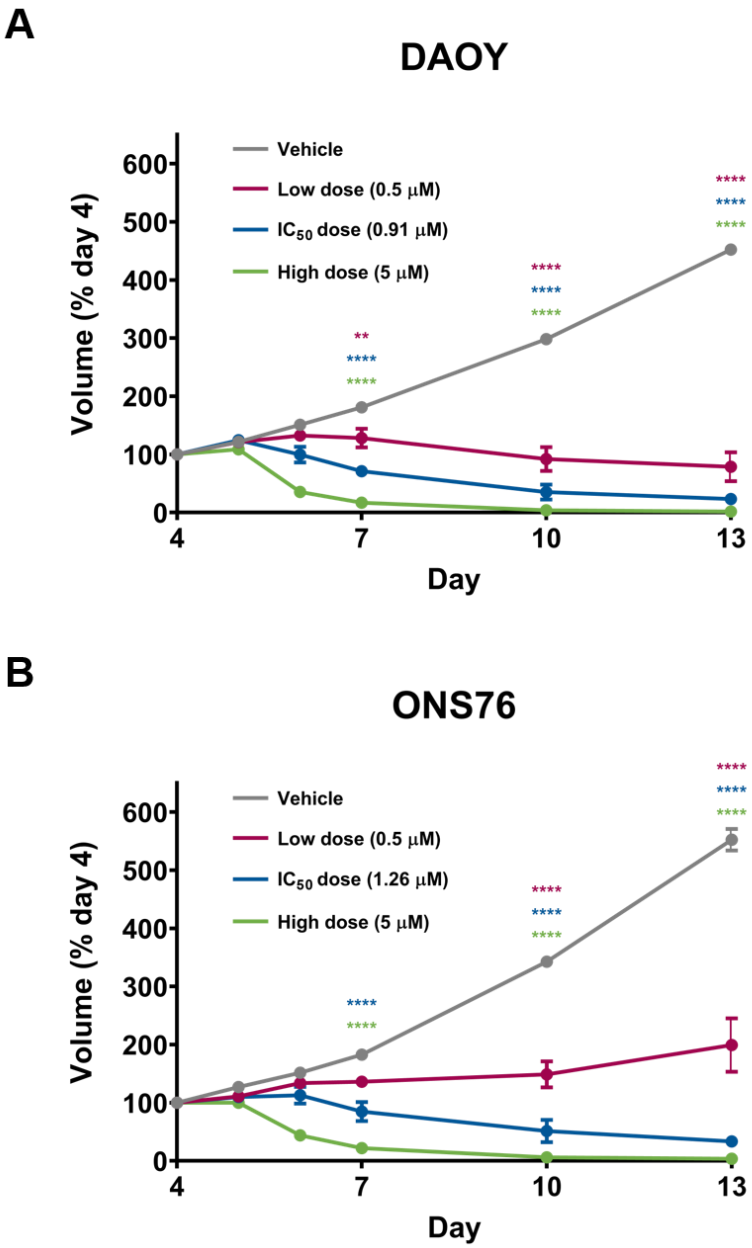


Figure 4.10 Continual monitoring of the effects of cisplatin treatment on DAOY and ONS76 spheroids

DAOY (**A**) and ONS76 (**B**) spheroids were treated with a DMF vehicle (grey) and three concentrations of cisplatin: low dose (red; 0.5 μM), IC_{50} dose (blue; DAOY: 0.91μM, ONS76: 1.26 μM), and high dose (green; 5 μM) for 72 hours. Images were taken on days 4, 7, 10, and 13 to measure changes in spheroid volume (as a percentage of day 4). For DAOY spheroids, low dose cisplatin treatment reduced spheroid volume to approximately 80% by day 13; however, ONS76 spheroids treated at the same dose continued to grow over the course of the assay. IC_{50} and high dose treatments successfully reduced spheroid volume for both cell lines. Error bars represent the mean ± SEM of 3 independent experiments each containing 4 replicates. Significance was calculated using repeated measures two-way ANOVA analyses with Dunnett's multiple comparisons post-hoc test. Differences in response between the vehicle and etoposide treatment are represented by coloured asterisks of the corresponding dosage (**p≤0.01, ****p≤0.0001).

4.4.3 Combination treatments provide an insight into drug resistance

In section 4.4.2, we showed that it was possible to assess the long-term effects of drugs on DAOY and ONS76 spheroids by continually monitoring their volume post-treatment. We were also able to show that when treated at a low dose of either etoposide, vincristine or cisplatin, the spheroids grew in size or maintained a steady volume over the course of the assay. We therefore wanted to assess whether we could potentiate the effects of low dose treatments (the concentrations that typically are achievable in patients) with combination therapy.

Expression of the multi-drug transporter ABCB1 contributes to drug resistance in various cancer types, and is of particular importance as many chemotherapy agents are substrates for ABCB1, including etoposide, vincristine, methotrexate, and irinotecan (Szakács *et al.*, 2006). Previous work within our research group has highlighted ABCB1 as a mechanism of drug resistance in medulloblastoma tumours. Combined treatment with the ABCB1 inhibitor vardenafil (5 or 10 μM) significantly reduced the clonogenic survival of medulloblastoma cell lines treated in combination with etoposide (Othman *et al.*, 2014). We aimed to extend this study to investigate whether ABCB1 could be a driver of the observed resistance in our spheroid model and confirmed that DAOY and ONS76 spheroids expressed the ABCB1 protein (see Appendix 1). We hypothesised that the effects of vincristine or etoposide treatment could be enhanced in combination with vardenafil. However, we anticipated that the same effect would not be observed with cisplatin, a chemotherapy agent which is not a substrate for ABCB1.

To test this hypothesis, DAOY and ONS76 spheroids were treated with either etoposide, vincristine or cisplatin in combination with 10 μM vardenafil (the effective concentration shown by Othman *et al.*, 2014) for 72 hours. Images were taken immediately after treatment to measure changes in spheroid volume and viability was calculated as a percentage of the vehicle-treated controls. Significance was

calculated using one-way ANOVA analyses with Sidak's multiple comparisons post-hoc test.

In addition, we also continually monitored the effects of combination treatment on spheroid volume as described in Figure 4.7. Significance differences between single and combination treatment were calculated using repeated measures two-way ANOVA analyses which determined how the response (in this case, spheroid volume) was affected by two factors (treatment and time point). A Tukey's post-hoc test was also performed to correct for multiple comparisons. This test compared, at each time point, every mean to every other mean to calculate statistical significance.

There was no difference in spheroid volume after vardenafil-only treatment in comparison to the vehicle-treated control for both cell lines (Figure 4.11A, Figure 4.12A, and Figure 4.13A), therefore showing that vardenafil itself does not affect spheroid viability.

The assessment of etoposide and vardenafil combination treatments is shown in Figure 4.11A. Following 72 hour drug treatment, there was no difference in volume between single etoposide treatment and combination treatment with vardenafil for DAOY spheroids at both a low dose (0.1 μM; $p=0.4106$) or high dose (1 μM; $p=0.9926$). The same conclusion was also made for the ONS76 cell line (low dose: $p=0.5448$; high dose: $p=0.9034$). Continual monitoring of the effects of combined low dose etoposide and vardenafil after 72 hours treatment revealed significant differences in volume by day 10 for DAOY spheroids and day 13 for ONS76 spheroids (Figure 4.11B). Combination treatment for both cell lines prevented growth and maintained the original spheroid volume, unlike single etoposide treatment which, although it reduced growth compared to the vehicle-treated control, failed to cause a regression in spheroid size.

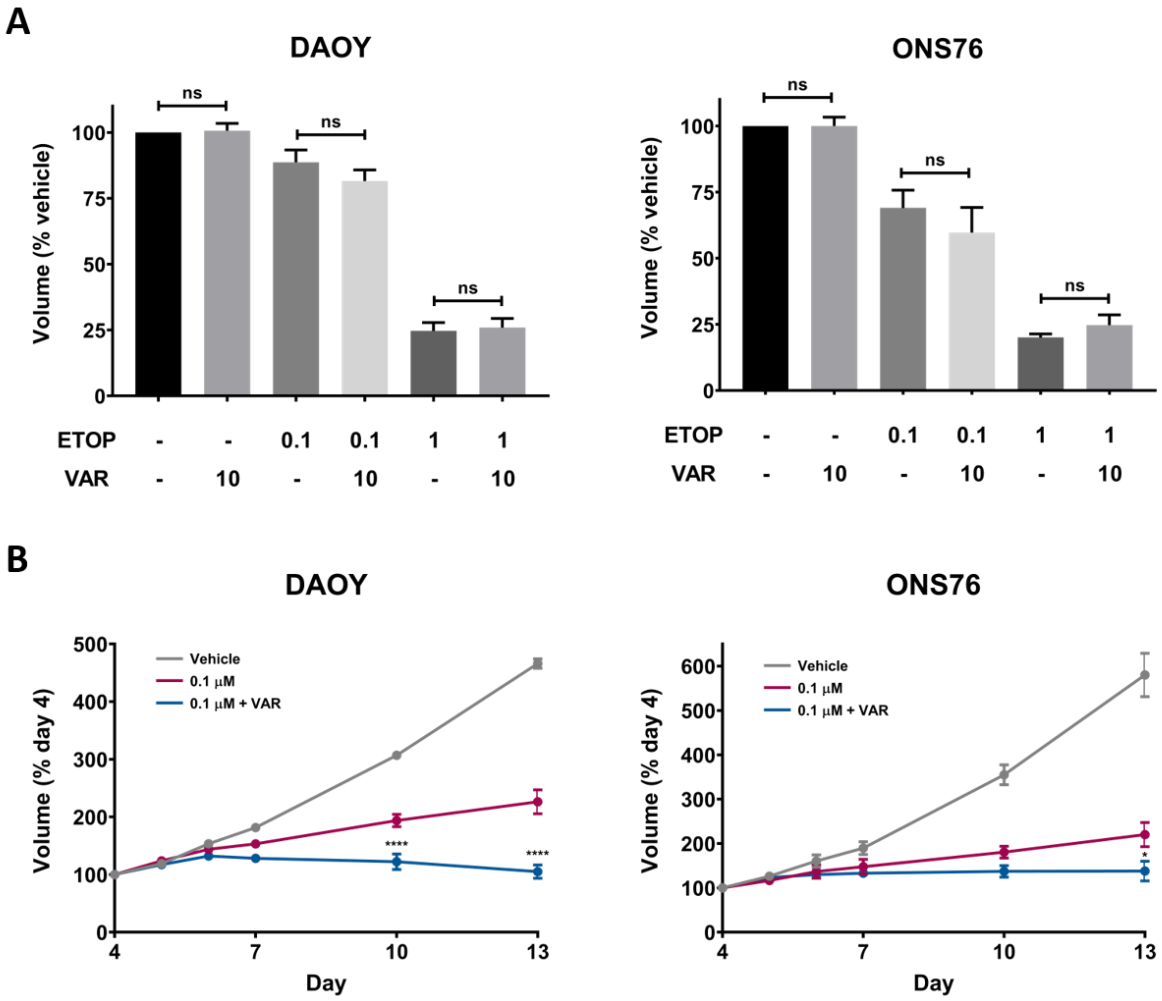


Figure 4.11 Assessment of etoposide and vardenafil combination treatments

DAOY and ONS76 spheroids were treated with etoposide (ETOP) in combination with vardenafil (VAR; 10 μM) for 72 hours. (**A**) Images were taken immediately after treatment to measure changes in spheroid volume relative to the vehicle-treated control. There was no difference in volume after vardenafil-only treatment. In addition, there was no difference in volume between single etoposide treatment (either low dose (0.1 μM) or high dose (1 μM)) and combination treatments with vardenafil. Error bars represent the mean ± SEM of 3 independent experiments each containing 3 replicates. Significance was calculated using one-way ANOVA analyses with Sidak's multiple comparisons post-hoc test (ns=not significant). (**B**) Continual monitoring of the effects of combined low dose etoposide and vardenafil treatment (blue) revealed significant difference in volume by day 10 for DAOY spheroids and day 13 for ONS76 spheroids compared to etoposide alone (red). Error bars represent the mean ± SEM of 3 independent experiments each containing 3 replicates. Significance differences between single and combination treatment were calculated using repeated measures two-way ANOVA analyses with Tukey's multiple comparisons post-hoc test (*p≤0.05, ****p≤0.0001).

Vincristine and vardenafil combination treatments are shown in Figure 4.12A. DAOY spheroids showed a decrease in spheroid volume from 87% after low dose (1 nM) vincristine treatment, down to 33% in combination with vardenafil ($p \leq 0.0001$). A similar effect was seen with ONS76 spheroids at the same dosage where low dose vincristine only decreased volume to 99%; however, vardenafil combination therapy significantly enhanced this regression down to 53% ($p \leq 0.0001$). There was no significant difference in spheroid volume for both cell lines at high dose (10 nM) vincristine and vardenafil combination treatments (DAOY: $p=0.7852$; ONS76 $p=0.9726$). Continual monitoring of the effects of combined low dose vincristine and vardenafil treatment showed that the decrease in spheroid volume observed was further enhanced over a longer period of time (Figure 4.12B). By day 13, spheroid volume had significantly reduced to only 10% of day 4 for DAOY spheroids and below 30% for ONS76 spheroids ($p \leq 0.0001$).

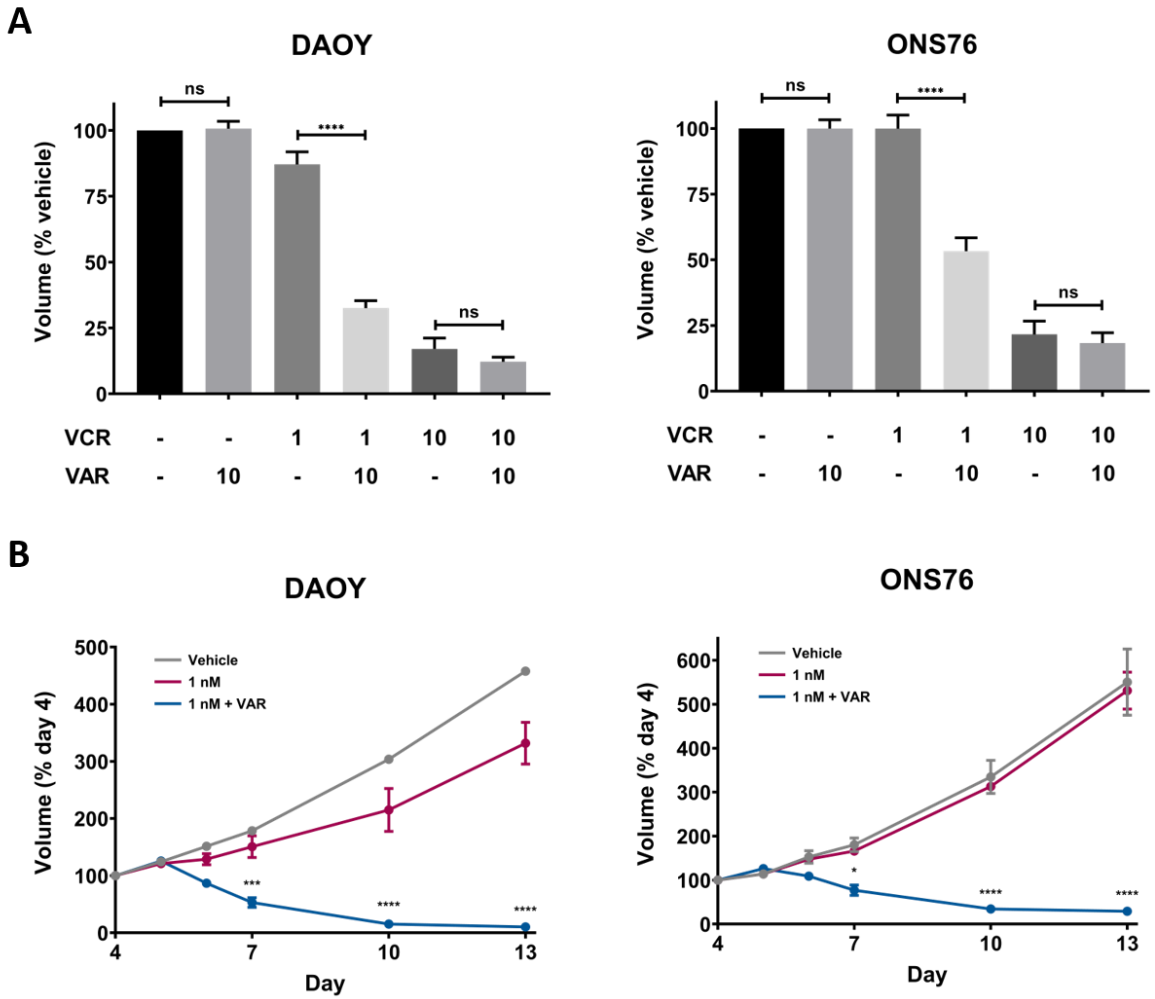


Figure 4.12 Assessment of vincristine and vardenafil combination treatments

DAOY and ONS76 spheroids were treated with vincristine (VCR) in combination with vardenafil (VAR; 10 µM) for 72 hours. (**A**) Images were taken immediately after treatment to measure changes in spheroid volume relative to the vehicle-treated control. There was no difference in volume after vardenafil-only treatment. Low dose (1 nM) vincristine treatment could be potentiated with the addition of vardenafil, however the same effect was not observed at a higher dose (10 nM). Error bars represent the mean ± SEM of 3 independent experiments each containing 3 replicates. Significance was calculated using one-way ANOVA analyses with Sidak's multiple comparisons post-hoc test (ns=not significant, ****p≤0.0001). (**B**) Continual monitoring of the effects of combined low dose vincristine and vardenafil treatment (blue) revealed a continual significant decrease in spheroid volume following treatment compared to vincristine alone (red). Error bars represent the mean ± SEM of 3 independent experiments each containing 3 replicates. Significance differences between single and combination treatment were calculated using repeated measures two-way ANOVA analyses with Tukey's multiple comparisons post-hoc test (*p≤0.05, ***p≤0.01, ****p≤0.0001).

Combination treatments with cisplatin and vardenafil are shown in Figure 4.13. Following 72 hour treatment, there was no difference in spheroid volume between single cisplatin treatment at either a low dose (0.5 µM) or high dose (1 µM) and combination treatments with vardenafil (Figure 4.13A). Interestingly, spheroid volume was higher after combination therapy for both DAOY and ONS76 spheroids. Continual monitoring of the effects of combined low dose cisplatin and vardenafil treatment compared to cisplatin alone showed no difference in response up to day 10. However, by day 13, spheroids treated with only cisplatin were significantly smaller than combination therapy for both cell lines.

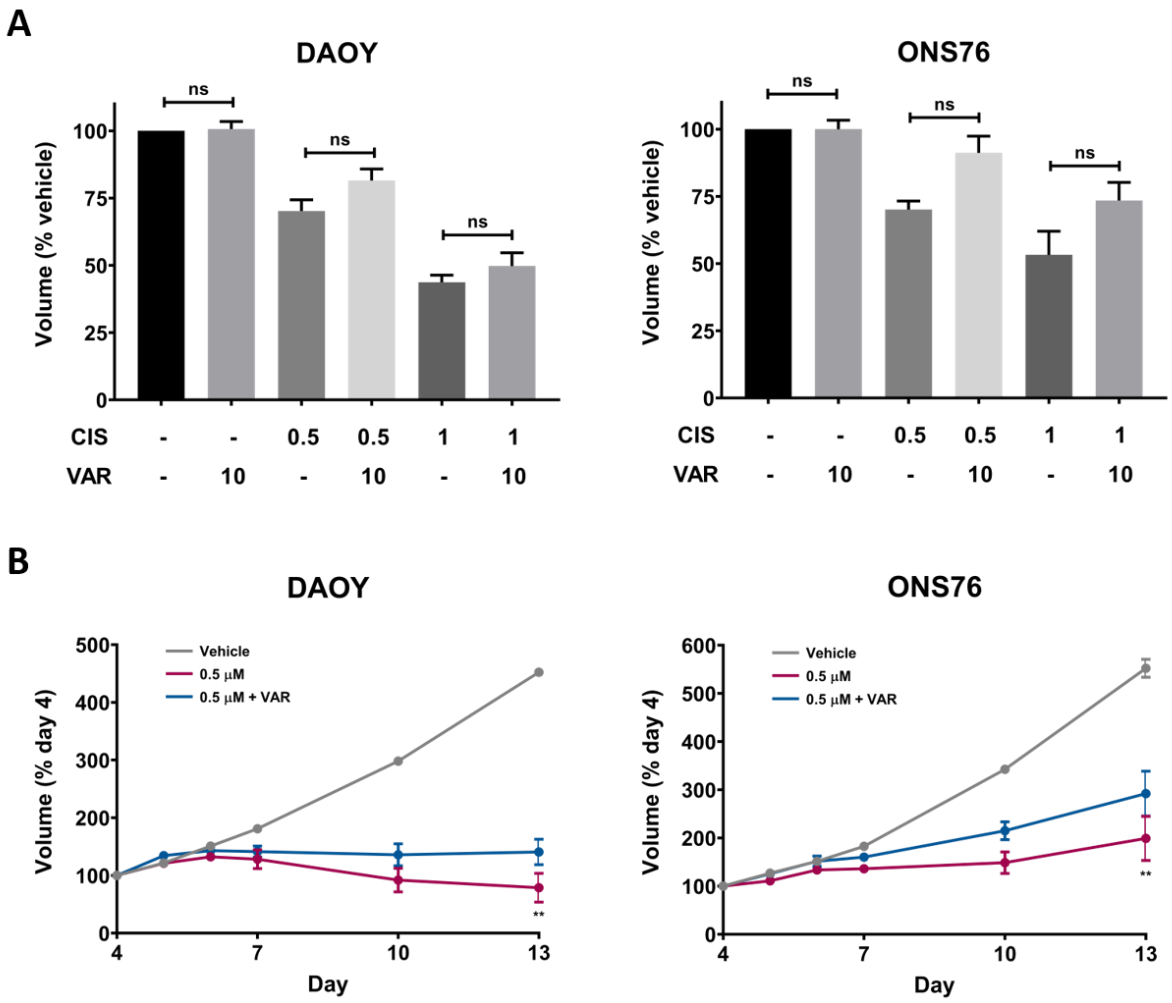


Figure 4.13 Assessment of cisplatin and vardenafil combination treatments

DAOY and ONS76 spheroids were treated with cisplatin (CIS) in combination with vardenafil (VAR; 10 μM) for 72 hours. (**A**) Images were taken immediately after treatment to measure changes in spheroid volume relative to the vehicle-treated control. There was no difference in volume after vardenafil-only treatment. In addition, there was no difference in volume between single cisplatin treatment (either low dose (0.5 μM) or high dose (1 μM)) and combination treatments with vardenafil. Error bars represent the mean ± SEM of 3 independent experiments each containing 3 replicates. Significance was calculated using one-way ANOVA analyses with Sidak's multiple comparisons post-hoc test (ns=not significant). (**B**) Continual monitoring of the effects of combined low dose cisplatin and vardenafil treatment (blue) compared to cisplatin alone (red) showed no difference in response up to day 10. However, by day 13 single treatment was significantly lower than combination therapy for both cell lines. Error bars represent the mean ± SEM of 3 independent experiments each containing 3 replicates. Significance differences between single and combination treatment were calculated using repeated measures two-way ANOVA analyses with Tukey's multiple comparisons post-hoc test (**p≤0.01).

4.5 Summary

- Comparison of two methods of assessing spheroid drug treatment (imaging to measure changes in spheroid volume and the commercially-available luminescence-based CellTiter-Glo® cell viability assay) showed that both are suitable and equivalent readouts of response.
- 3D spheroids were more resistant to drug treatment compared to 2D monolayer culture, with significant differences in response observed after treatment with four currently used standard-of-care chemotherapy drugs.
- Fluorescent labelling of cells using Calcein-AM (CAM; live cells) and Propidium Iodide (PI; dead cells) revealed a decrease in the CAM/PI ratio after higher doses of vincristine, with a subpopulation of viable cells remaining around the spheroid periphery after treatment.
- Long-term analysis of the effects of chemotherapeutics showed differences in outcomes which would be missed in standard drug response assays.
- Dual-inhibitor studies with the ABCB1 inhibitor vardenafil showed synergistic effects which could facilitate the use of lower doses of the chemotherapy when treated in combination with vardenafil.

Chapter 5

Modelling medulloblastoma metastatic dissemination

Chapter 5. Modelling medulloblastoma metastatic dissemination

5.1 Introduction

One of the major clinical problems associated with medulloblastoma is metastasis, with around 20-30% of patients presenting with metastatic disease at diagnosis (Kool *et al.*, 2012). The characteristic mode of metastatic spread is to the leptomeninges of the brain and spinal cord. This occurs through the dissemination of tumour cells to the leptomeningeal space (between the pia mater and the arachnoid mater) and the circulation of tumour cells to the rest of the CNS via the CSF. Zapotocky *et al.*, 2018 recently showed that patterns of metastatic dissemination are highly subgroup-specific. SHH medulloblastoma tumours spread in a nodular fashion whereas Group 3 tumours mainly display laminar metastases, with Group 4 tumours exhibiting both of these patterns. Although we now have a better understanding of the differential patterns of tumour spread across medulloblastoma subgroups, the mechanisms by which metastatic dissemination occurs is still poorly understood. The initial stages of tumour spread involves the alteration of the cell's cytoskeleton, increased cell motility, and interaction with the surrounding extracellular matrix (ECM). It is possible to study these cell-cell and cell-ECM interactions *in vitro* using 3D spheroids by modelling their migration on or invasion within different matrices.

Our objective was to develop a 3D spheroid model of medulloblastoma metastatic dissemination. The aims of this chapter were therefore to:

(1) Test simple and established basement membrane models of spheroid migration and invasion
(2) Model medulloblastoma metastatic dissemination using brain-specific matrices containing key components of the ECM.

5.2 Modelling tumour migration and invasion using 3D spheroids

A schematic diagram describing the spheroid migration and invasion models adopted in this study is shown in Figure 5.1. Spheroids are generated in 96-well ultra-low attachment, round-bottom plates and reach their optimal size of 250-350 µm in diameter on day 4, as described in chapter 3. At this stage, spheroids could be used in migration and invasion assays. To model migration, day 4 spheroids were transferred to an ECM-coated, flat-bottom, 96-well plate. Cell migration across the ECM surface can then be measured over time. To model invasion, day 4 spheroids were embedded within an ECM in the same plate in which they were generated. Invasion into the surrounding matrix could be assessed over time.

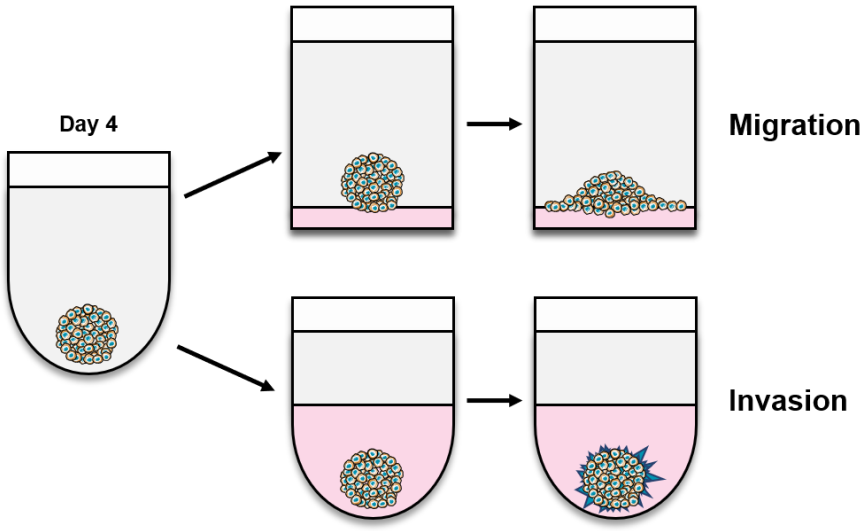


Figure 5.1 Schematic diagram describing spheroid migration and invasion models
Spheroids are generated in 96-well ultra-low attachment, round-bottom plates and reach their optimal size of 250-350 µm in diameter on day 4. To model migration, day 4 spheroids are transferred to a 96-well flat-bottom plate coated with an extracellular matrix (ECM). Cell migration across the ECM surface is then assessed over time. To model invasion, day 4 spheroids are embedded within ECM and invasion into the surrounding matrix can be visualised.

5.3 Modelling spheroid migration across a simple collagen IV basement membrane matrix

The first spheroid migration assay tested in this study was a simple basement membrane model. The basement membrane is a specialised self-assembled ECM that surrounds all tissues (Jayadev and Sherwood, 2017). There are four major components of basement membranes: collagen IV, laminin, nidogen, and perlecan (LeBleu, MacDonald and Kalluri, 2007). As collagen IV can be used as a thin coating on tissue culture surfaces, we chose to model spheroid migration across this simplified basement membrane matrix.

Four days post-generation, spheroids were transferred to a collagen IV coated 96-well flat-bottom plate. Spheroid migration across collagen IV was then assessed over a 72 hour period. Figure 5.2 shows representative images of the differential patterns of SHH medulloblastoma spheroid migration over time. DAOY spheroids displayed single cell dissemination over the collagen IV surface after 24 hours. By 48 and 72 hours, these single cells had formed small nodules on the matrix. The main spheroid body continued to grow at the expected rate over the course of the assay. ONS76 spheroids exhibited a substantially different pattern of migration compared to DAOY spheroids, with a “bursting effect” at two ends of the spheroid body after 24 hours. Cells collectively migrated over the collagen IV matrix over the following 48 hours, with elongated protrusions at the outer migratory edge. UW228-3 spheroids failed to display any form of migration across the matrix and remained static in size over the course of the experiment.

It is important to note that this simplified collagen IV basement membrane model showed different levels of migration both within and between experiments. This may have been due to uneven coatings of collagen IV across the surface of the plates. However, it indicated that this model was not an ideal candidate for modelling the initial stages of tumour spread due to its lack of reproducibility.

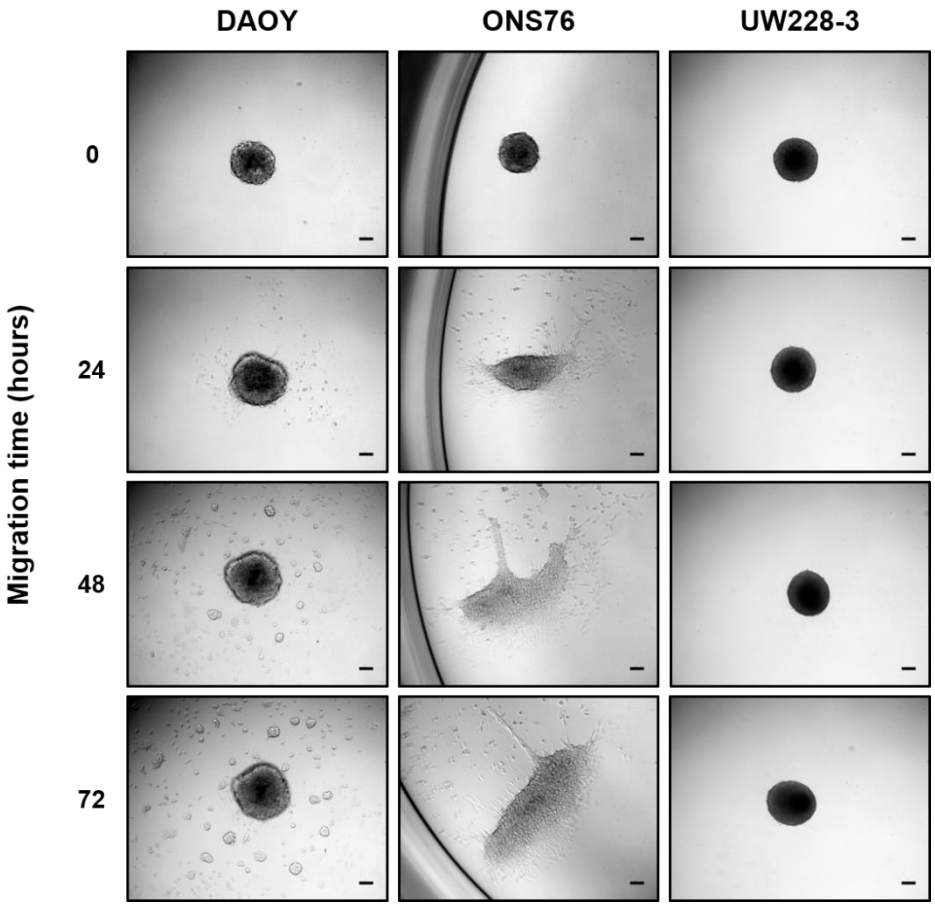


Figure 5.2 SHH medulloblastoma spheroid migration across a collagen IV matrix
DAOY, ONS76, and UW228-3 spheroids were transferred to a collagen IV coated 96-well flat-bottom plate on day 4 (0 hours). Spheroid migration across collagen IV was assessed over a 72 hour period. DAOY spheroids displayed single cell migration by 24 hours and the formation of small nodules on the collagen IV surface at 48 and 72 hours. ONS76 spheroids showed collective cell migration by 24 hours on two sides which spread further by 48 and 72 hours. UW228-3 spheroids failed to migrate across the collagen IV surface at any time point. Images of the same spheroid at different time points are shown (scale bar: 100 µm).

5.4 Using basement membrane extract to model tumour spread

Following on from the simple collagen IV basement membrane model, we chose to test whether SHH medulloblastoma spheroids were capable of invading through and migrating on Basement Membrane Extract (BME) matrices. BME is a commercially-available matrix that is widely used in 3D *in vitro* invasion and migration assays. This soluble form of basement membrane is purified from Engelbreth-Holm-Swarm (EHS) murine chondrosarcoma tumours (Orkin *et al.*, 1977). ECM components within BME include laminin, collagen IV, entactin, and heparin sulfate proteoglycans. To model spheroid invasion through BME matrices, two concentrations were chosen: 3 and 10 mg/mL. The lower concentration has been previously used in 3D spheroid invasion assays (Onion *et al.*, 2016; Sabnis *et al.*, 2019) but a higher gelling concentration, recommended by the manufacturer, was also included to provide a stiffer matrix for cell movement.

Four days after the generation of spheroids, media was removed from each well and spheroids were embedded in either a low or high concentration of BME. Control wells containing no matrix were included to model typical spheroid growth. Spheroid invasion into the surrounding matrix was then assessed over a 72 hour period.

Figure 5.3 shows the invasion of SHH medulloblastoma spheroids into BME matrices. For DAOY spheroids, embedding in 10 mg/mL of BME promoted the formation of small protrusions into the matrix by 72 hours, whereas 3 mg/mL BME supported spheroid growth, not invasion. A similar growth supporting role was observed in ONS76 spheroids embedded in 3 mg/mL; however, there was visible blebbing around the spheroid edge over the course of the experiment. Embedding in 10 mg/mL BME did not have an extensive effect on ONS76 spheroids and their size was similar to growth without matrix. UW228-3 spheroids failed to invade through either BME matrix concentration.

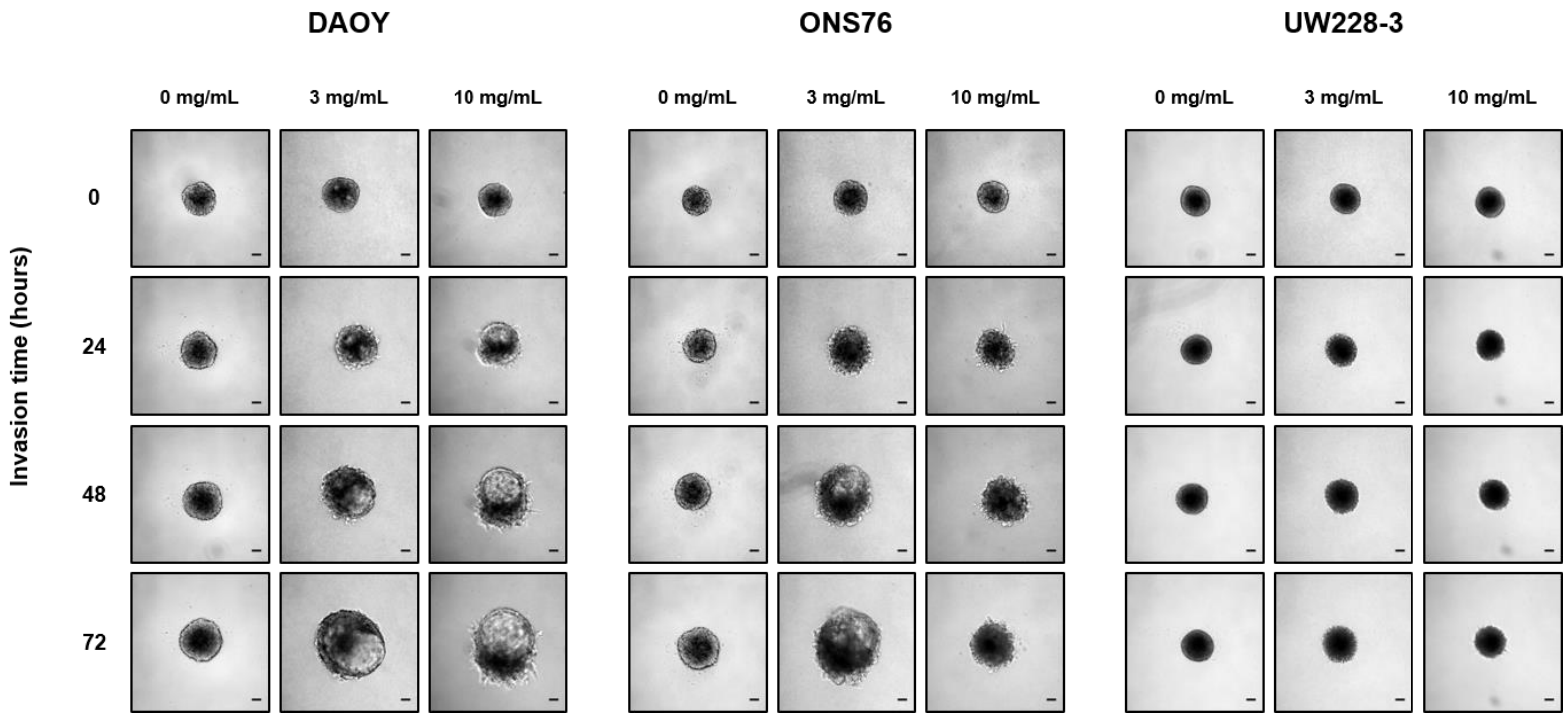


Figure 5.3 SHH medulloblastoma spheroid invasion within basement membrane extract matrices

DAOY, ONS76, and UW228-3 spheroids were embedded in 0, 3, or 10 mg/mL basement membrane extract (BME) on day 4 (0 hours) and invasion into the surrounding matrix was monitored over 72 hours. For DAOY spheroids, embedding in the highest concentration of BME (10 mg/mL) allowed the formation of protrusions into the matrix by 72 hours, whereas 3 mg/mL BME supported spheroid growth, not invasion. ONS76 spheroids embedded in 3 mg/mL BME grew substantially larger than spheroids in no matrix, with blebbing visible around the spheroid edge. 10 mg/mL BME did not have an extensive effect on ONS76 spheroids. UW228-3 spheroids failed to invade through the BME matrix. Images of the same spheroid at different time points are shown (scale bar: 100 μm) and are representative of 3 independent experiments each containing 3 replicates.

To model spheroid migration on BME, 10 mg/mL was chosen as an appropriate concentration as it provided a stiffer matrix. Four days post-generation, spheroids were transferred to a BME coated 96-well flat-bottom plate. Spheroid migration across the BME matrix was then assessed over a 72 hour period. DAOY spheroids displayed a bursting effect on one edge of the spheroid after 24 hours and this directionality continued for the following 48 hours. By 72 hours, there were elongated protrusions from the spheroid edge. ONS76 spheroids showed similar, albeit less substantial, migratory behaviour, with cells migrating more from one edge. UW228-3 spheroids failed to migrate substantially but displayed slight protrusions from the outer edge at 72 hours.

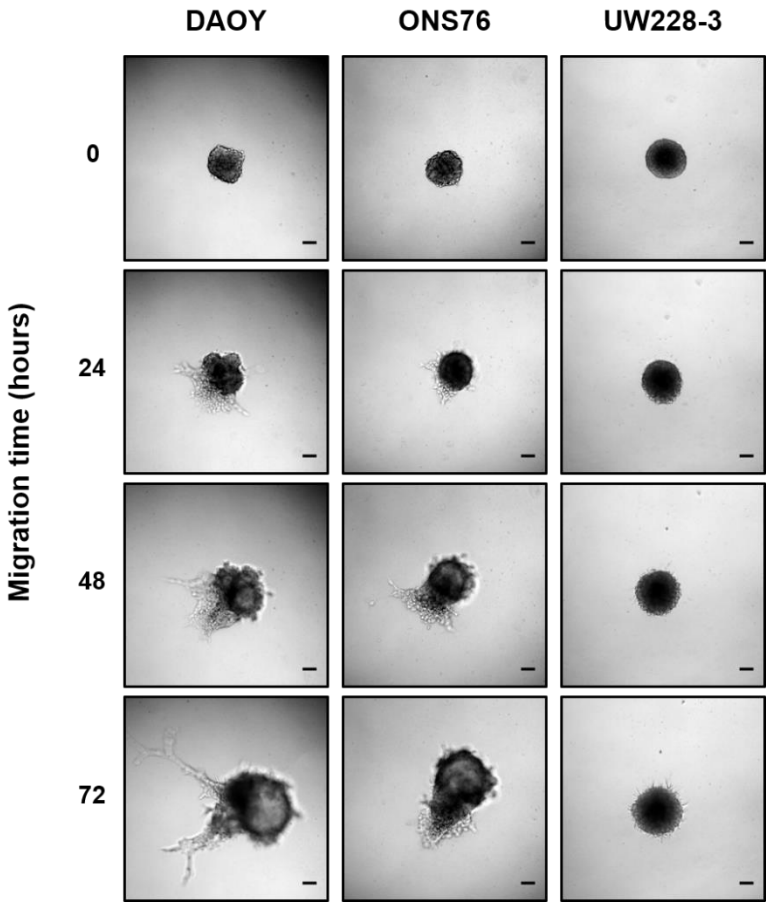


Figure 5.4 SHH medulloblastoma spheroid migration on a basement membrane extract matrix

DAOY, ONS76, and UW228-3 spheroids were transferred to a 10 mg/mL basement membrane extract (BME) coated 96-well flat-bottom plate on day 4 (0 hours). Spheroid migration across BME was assessed over a 72 hour period. DAOY spheroids displayed a “bursting” effect on one edge of the spheroid after 24 hours and this directionality was visible over the course of the assay with elongated protrusions at 72 hours. ONS76 spheroids showed similar, but less substantial, migratory behaviour. UW228-3 spheroids displayed slight projections from the outer edge at 72 hours. Images of the same spheroid at different time points are shown (scale bar: 100 µm) and are representative of 3 independent experiments each containing 3 replicates.

5.5 Using hyaluronan hydrogels as brain-specific matrices

So far in this chapter, collagen IV and BME have been used as matrices for spheroid migration and invasion modelling. Although these models have been commonly used in the past for many cancer types, the use of organ-specific matrices would be more appropriate for studying metastatic dissemination of tumours. Hyaluronan (HA) is a major constituent of the brain ECM (Rauch, 2004; Rauch, 2007) and therefore was considered the most appropriate component for the basis of a brain-specific model. For this study, we chose to use the HyStem™ hydrogel kit, a semi-synthetic 3D hydrogel platform which consisted of Glycosil® (thiol-modified HA), ExtraLink®-Lite (PEGDA; polyethylene glycol diacrylate), and water. One of the main advantages of HyStem™ was that the matrix could be modified to mimic the brain's stiffness, thus making is a more physiologically relevant model (Vanderhooft *et al.*, 2009). A hydrogel with a stiffness around 1.5-2 kPa, within the range of normal brain tumour stiffness (Barnes, Przybyla and Weaver, 2017), could be produced by making a 1% Glycosil® and 2% ExtraLink®-Lite solution. As well as this, the hydrogels could be customised by adding ECM proteins, growth factors, and cell attachment factors, allowing flexibility for the user. There was also the possibility to encapsulate cells within or place them on top of the matrix, making the hydrogels suitable for migration and invasion studies.

5.5.1 SHH medulloblastoma spheroids express the hyaluronan receptor, CD44

We firstly wanted to test whether SHH medulloblastoma spheroids were capable of interacting with a HA matrix. CD44, a cell surface glycoprotein, is a receptor for HA and its expression in a HA-rich microenvironment has been shown to maximise 3D cell invasion (Kim and Kumar, 2014). To assess the expression of CD44, spheroids were harvested, processed, and sectioned for immunohistochemical staining.

DAOY and ONS76 spheroid sections were stained for CD44 on days 7, 14, and 21. However, UW228-3 spheroids fell apart during manipulation on days 14 and 21; therefore, staining for was only performed for day 7. As shown in Figure 5.5, CD44 expression was visible throughout spheroid sections across multiple time points for the SHH medulloblastoma cell lines, indicating that they were suitable for use within HA matrices.

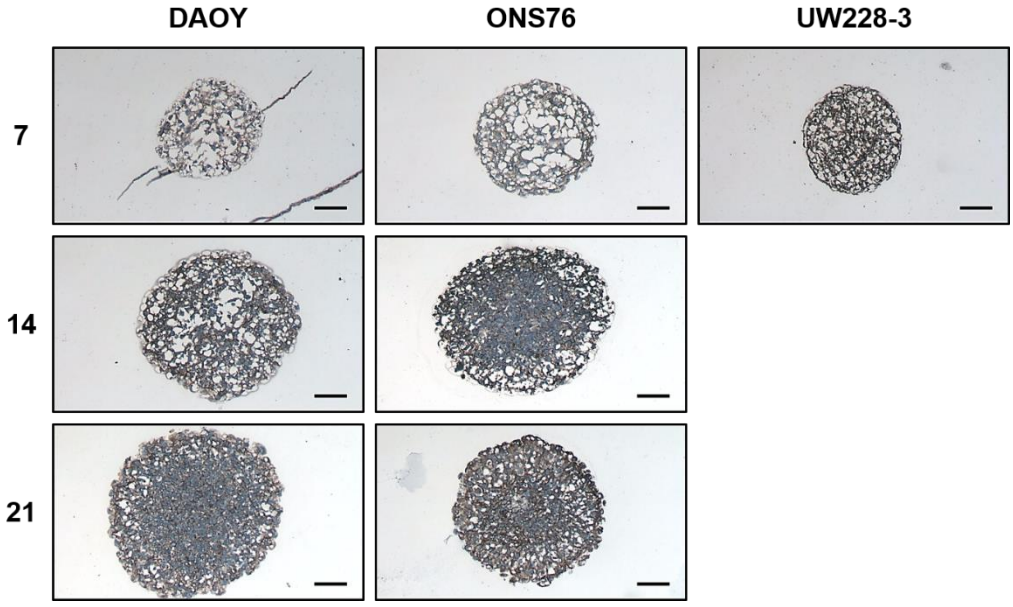


Figure 5.5 Immunohistochemical staining of SHH medulloblastoma spheroid sections for CD44

SHH medulloblastoma spheroids were stained for the hyaluronan receptor CD44. DAOY and ONS76 spheroid sections were stained for CD44 on days 7, 14, and 21. However, UW228-3 spheroids fell apart during manipulation on days 14 and 21; therefore, staining for was only performed for day 7. CD44 expression was visible throughout all spheroid sections. Representative images are shown (scale bar: 100 µm).

5.5.2 Key components of the extracellular matrix are highly expressed in SHH medulloblastoma tumours

As already indicated, one of the main benefits of the HyStem™ HA hydrogel system is its ability to be customised with additional ECM components. It is well established that fibrous proteins such as laminins, collagens, and fibronectin are present in the brain ECM (Novak and Kaye, 2000). The laminin isoforms present in the brain basement membrane include laminin-111 and -211, encoded by the subunits α1, α2, β1 and γ1 (Yousif, Di Russo and Sorokin, 2013). It has also been shown that collagen I is overexpressed in medulloblastoma (Liang *et al.*, 2008) and that medulloblastoma cells migrate in the presence of fibronectin (Mohan *et al.*, 2012).

To assess the gene expression of these brain-specific laminin, collagen I, and fibronectin subunits in medulloblastoma patient tumours, the R2 Genomics Analysis and Visualization Platform was used to analyse the largest publicly-available medulloblastoma patient dataset (Cavalli *et al.*, 2017). The Cavalli dataset consisted of 763 patient samples from the four medulloblastoma molecular subgroups (WNT: n=70; SHH: n=223; Group 3: n=144; Group 4: n=326). Significant differences in gene expression between the WNT, Group 3, and Group 4 subgroups compared to the SHH subgroup (the focus of this study) were calculated using the Kruskal-Wallis test, a non-parametric test which compared at least three unmatched groups which are ranked in value from low to high. A Dunn's post-hoc test was also performed to correct for multiple comparisons. This test compared the difference in the sum of ranks between groups to calculate statistical significance.

Gene expression of the laminin subunits α1 (*LAMA1*), α2 (*LAMA2*), and γ1 (*LAMC1*) was significantly higher in the SHH subgroup compared to the other three molecular subgroups (Figure 5.6; ****p≤0.0001). Although laminin-β1 (*LAMB1*) expression was highest in the WNT subgroup, expression in SHH tumours was significantly higher than in Group 3 and 4 tumours (Group 3: ***p≤0.001; Group 4; ****p≤0.0001).

Expression of the *COL1A1* and *COL1A2* genes, encoding the collagen I α1 and α2 subunits, respectively, was also significantly higher in the SHH subgroup. This pattern was also observed for *FN1*, encoding fibronectin, although there was no significant difference between SHH and Group 3 tumours. This analysis shows that these ECM components are relevant for addition to a HA hydrogel for modelling SHH medulloblastoma metastatic dissemination in particular.

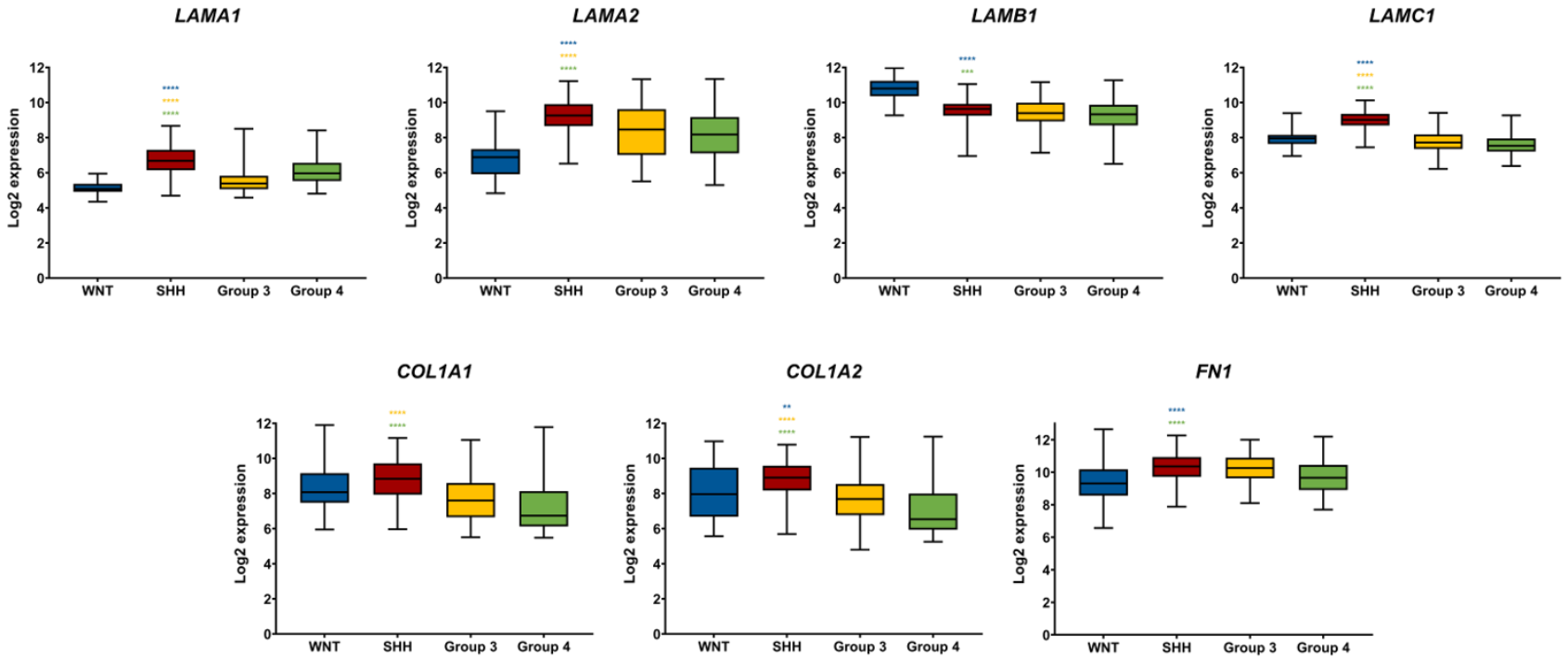


Figure 5.6 ECM component gene expression across medulloblastoma subgroups

Gene expression (Log2) of ECM components was assessed on the R2 Genomics Analysis and Visualization Platform using the Cavalli dataset which consisted of patient samples from the four medulloblastoma subgroups (WNT: n=70; SHH: n=223; Group 3: n=144; Group 4: n=326). Box and whisker plots display the median and interquartile range (25th and 75th percentiles) and the error bars represent the minimum and maximum values in each dataset. Significant differences in gene expression compared to the SHH subgroup were calculated using the Kruskal-Wallis test with Dunn's multiple comparisons post-hoc test. Differences are represented by coloured asterisks of the corresponding subgroup (WNT: blue; Group 3: yellow; Group 4: green; ***p≤0.001, ****p≤0.0001).

It was recently shown that medulloblastoma molecular subgroups could be further categorised into subtypes, with SHH tumours divided into four additional groups: α, β, γ, and δ, as discussed previously in section 1.3.4. Of these four subtypes, SHHβ have the poorest prognosis and are associated with the presence of metastatic disease. We therefore performed further analysis using only the SHH samples in the Cavalli dataset to assess gene expression differences in the same ECM components across the SHH subtypes (α: n=65; β: n=35; γ: n=47; δ: n=76). Significant differences in gene expression between the α, γ, and δ subtypes compared to the β subtype were calculated using the Kruskal-Wallis test with Dunn's multiple comparisons post-hoc test.

LAMA1, *LAMB1*, *COLA1*, *COLA2*, and *FN1* expression was significantly higher in SHHβ compared to at least one other subtype (Figure 5.7; ****p≤0.0001). However, *LAMA2* and *LAMC1* expression was not significantly higher than other subtypes. These analyses indicate that elevated expression of certain ECM components could play a role in the highly aggressive, metastatic medulloblastoma cases.

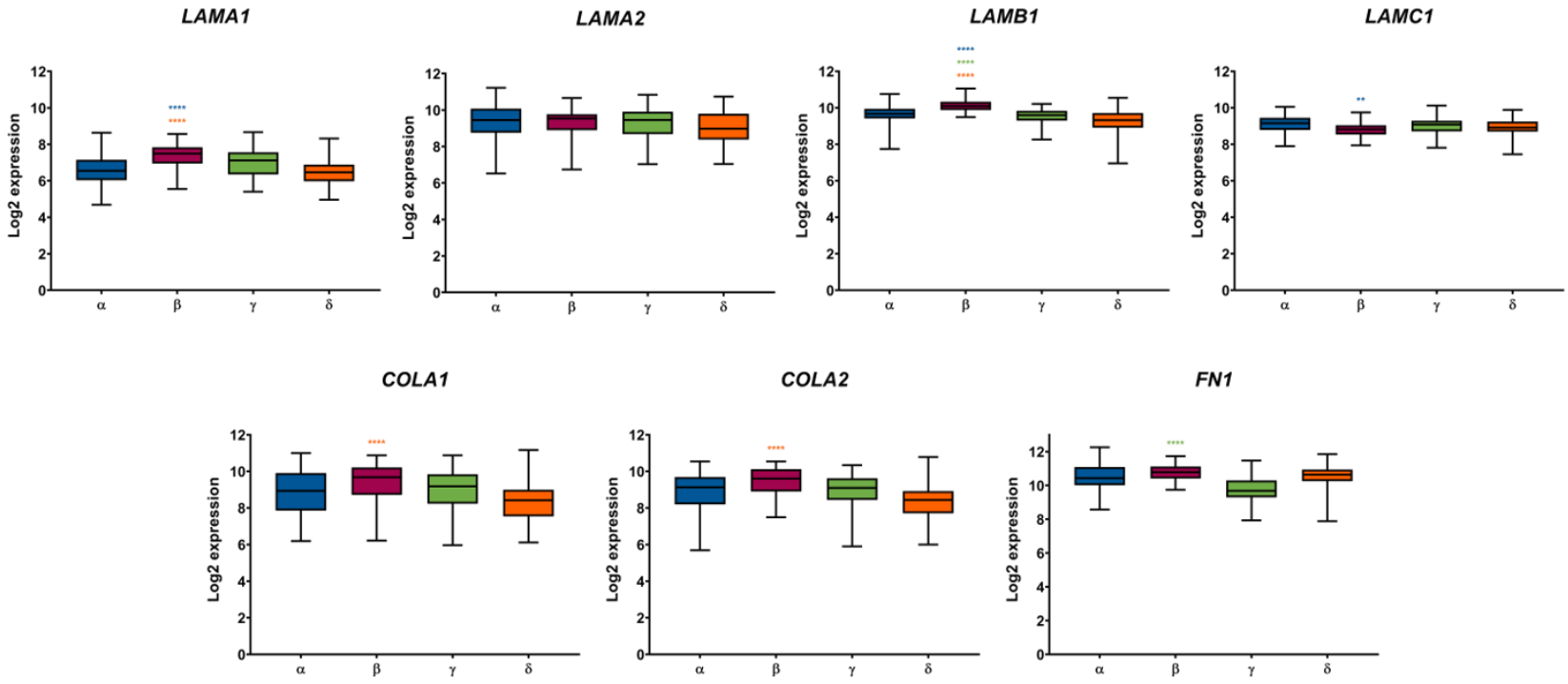


Figure 5.7 ECM component gene expression across SHH medulloblastoma subtypes

Gene expression (Log2) of ECM components was assessed on the R2 Genomics Analysis and Visualization Platform using the Cavalli dataset. SHH patients were categorised into four subtypes (α: n=65; β: n=35; γ: n=47; δ: n=76). Box and whisker plots display the median and interquartile range (25th and 75th percentiles) and the error bars represent the minimum and maximum values in each dataset. Significant differences in gene expression between the α, γ, and δ subtypes compared to the β subtype were calculated using the Kruskal-Wallis test with Dunn's multiple comparisons post-hoc test. Differences are represented by coloured asterisks of the corresponding subtype (α: blue; γ: green; δ: orange; ****p≤0.0001).

5.5.3 SHH medulloblastoma spheroids do not effectively invade through hyaluronan hydrogels

So far, we have shown that the SHH medulloblastoma spheroids express the HA receptor, CD44. As well as this, we have investigated gene expression of ECM components and their relevance in SHH medulloblastoma. For our brain-specific HA model, we chose to add each of the ECM factors (laminin, collagen I, and fibronectin) individually to the gels to assess spheroid invasion and migration.

Four days after the generation of spheroids, media was removed from each well and spheroids were embedded in HA hydrogels containing either laminin-111 (LAM), collagen I (COL), or fibronectin (FN). A final concentration of 50 µg/mL of ECM factors was optimised by Dr Franziska Linke (Postdoctoral Research Fellow in Dr Beth Coyle's group) to promote cell movement in other medulloblastoma *in vitro* hydrogel models and was therefore chosen as an appropriate concentration for this study. Control wells containing no matrix were included to model typical spheroid growth. Spheroid invasion into the surrounding matrices was then assessed over a 72 hour period.

For the DAOY cell line, spheroid size did not substantially change in any of the hydrogel solutions compared to the matrix-free control (Figure 5.8). There was an obvious lack of invasion across all conditions, with spheroid morphology altering around the outer edge, indicating that the hydrogels were supporting growth and not invasion into the matrix. An exception was the HA+FN hydrogel, where there was some evidence of cell shedding on one edge after 72 hours. As shown in Figure 5.9, ONS76 spheroids also did not invade into the surrounding matrices, although the morphology of the spheroids did slightly change when grown in the hydrogels. Spheroids embedded in HA+LAM appeared less rounded, with blebbing structures around the edge at 48 and 72 hours. UW228-3 spheroids failed to invade any HA

matrix composition over the 72 hour period and appeared similar to the control spheroids across the course of the experiment (Figure 5.10).

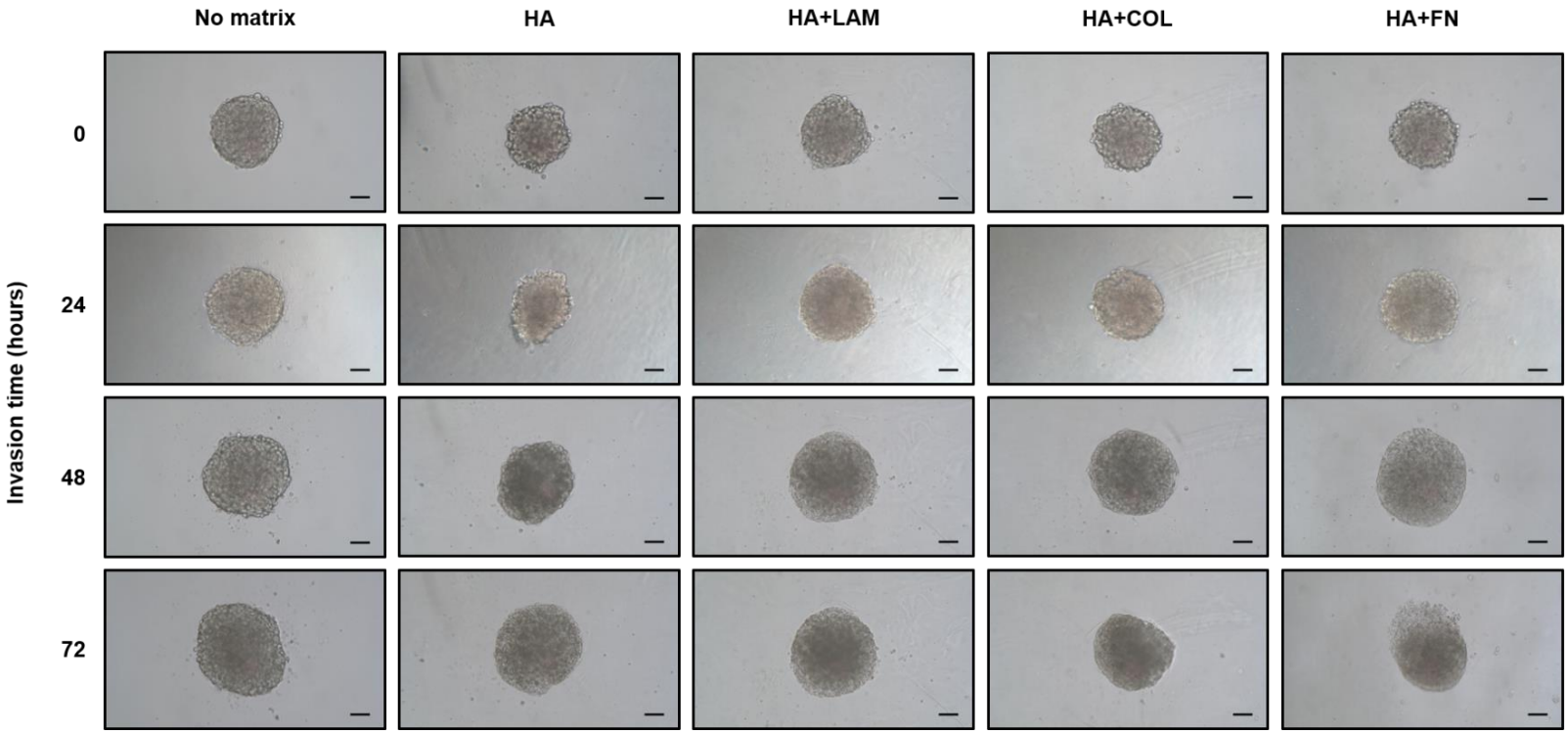


Figure 5.8 DAOY spheroid invasion within hyaluronan hydrogels

DAOY spheroids were embedded in hyaluronan (HA) matrices with or without the extracellular matrix components laminin-111 (LAM), collagen I (COL), and fibronectin (FN) on day 4 (0 hours) and invasion into the surrounding matrix was monitored over 72 hours. A no matrix control was included to assess normal spheroid growth. DAOY spheroids did not invade into the surrounding matrices, although the morphology of the spheroids did change when grown in the hydrogels. After 72 hours, there appeared to be some cell shedding from the spheroid edge in the HA+FN condition Images of the same spheroid at different time points are shown (scale bar: 100 µm) and are representative of 3 independent experiments each containing 3 replicates.

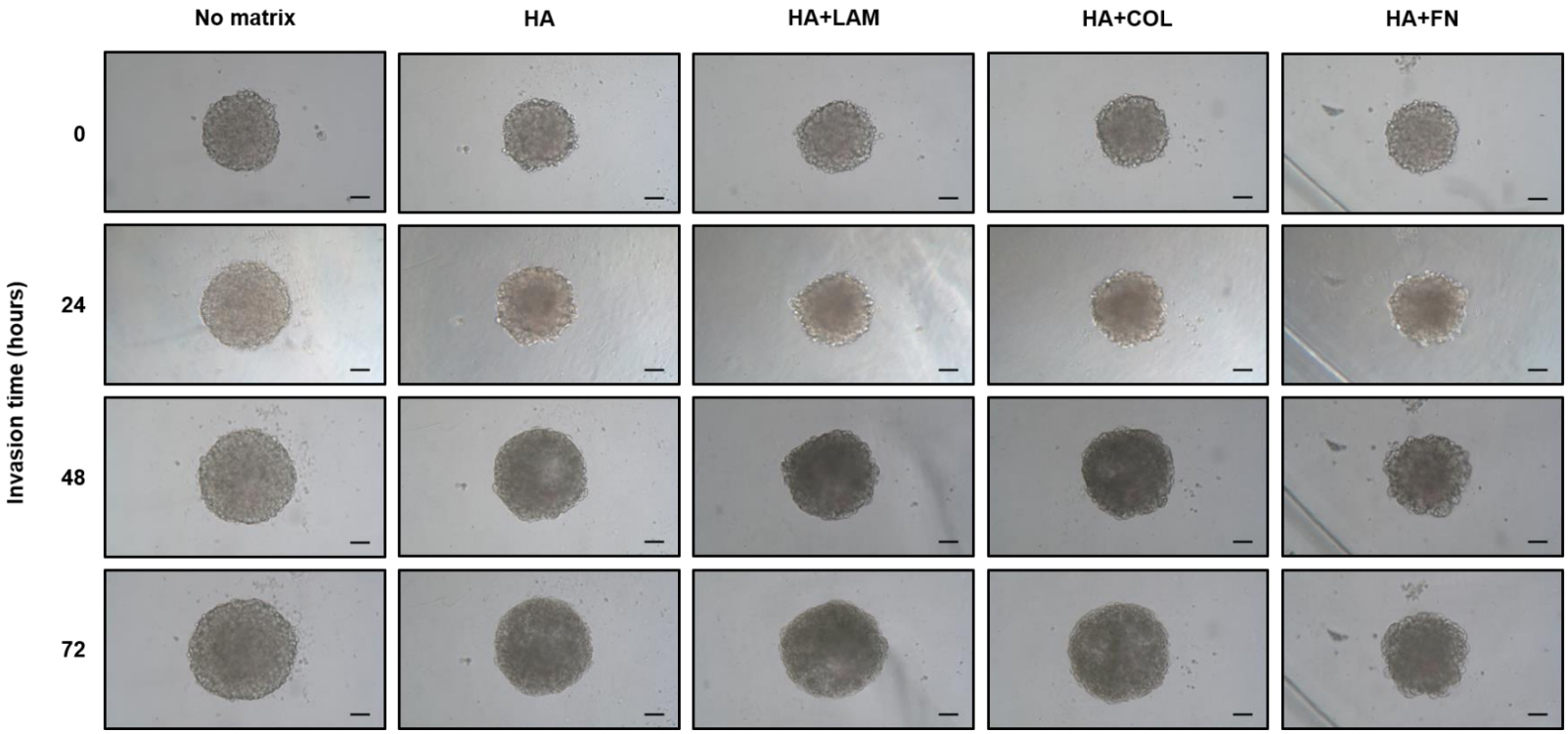


Figure 5.9 ONS76 spheroid invasion within hyaluronan hydrogels

ONS76 spheroids were embedded in hyaluronan (HA) matrices with or without the extracellular matrix components laminin-111 (LAM), collagen I (COL), and fibronectin (FN) on day 4 (0 hours) and invasion into the surrounding matrix was monitored over 72 hours. A no matrix control was included to assess normal spheroid growth. ONS76 spheroids did not invade into the surrounding matrices, although the morphology of the spheroids did change when grown in the hydrogels, with spheroids embedded in HA+LAM appearing less rounded. Images of the same spheroid at different time points are shown (scale bar: 100 µm) and are representative of 3 independent experiments each containing 3 replicates.

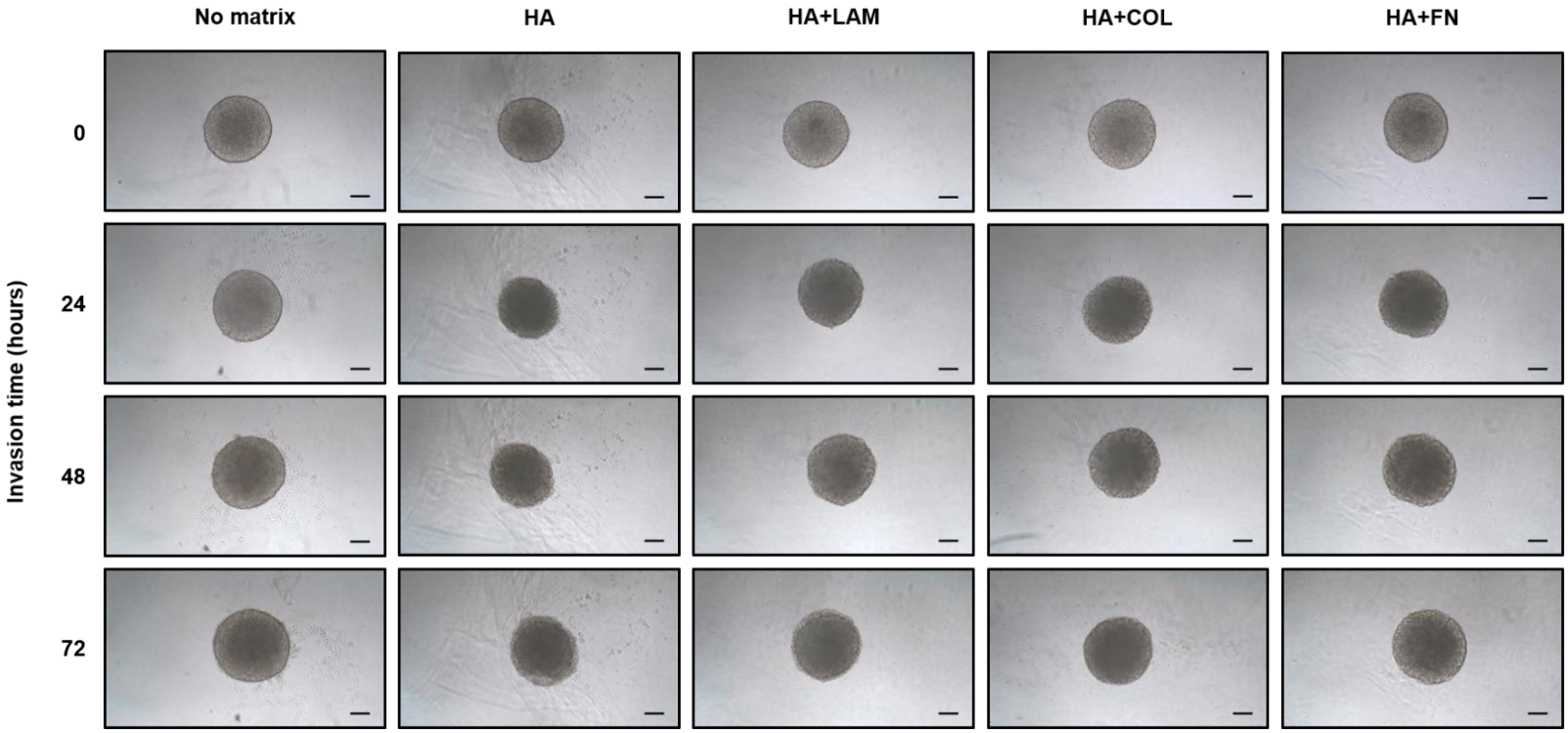


Figure 5.10 UW228-3 spheroid invasion within hyaluronan hydrogels

UW228-3 spheroids were embedded in hyaluronan (HA) matrices with or without the extracellular matrix components laminin-111 (LAM), collagen I (COL), and fibronectin (FN) on day 4 (0 hours) and invasion into the surrounding matrix was monitored over 72 hours. A no matrix control was included to assess normal spheroid growth. UW228-3 spheroids grown in HA+COL and HA+FN appeared similar to the control spheroids across the course of the experiment. However, after 72 hours, HA and HA+LAM matrices seemed to cause slight infiltration into the surrounding matrices. Images of the same spheroid at different time points are shown (scale bar: 100 µm) and are representative of 3 independent experiments each containing 3 replicates.

5.5.4 SHH medulloblastoma spheroids actively migrate across the surface of hyaluronan hydrogels

To assess the migration of SHH medulloblastoma spheroids across the surface of brain-specific hyaluronan matrices, day 4 spheroids were transferred to 96-well, flat-bottom plates coated with HA hydrogels containing 50 µg/mL of LAM, COL, or FN. Control wells containing no matrix were included to model typical spheroid growth. Spheroid migration across the matrices was then assessed over a 72 hour period.

DAOY spheroids readily migrated across all matrices over 72 hours, with cells disseminating from around the whole spheroid edge in a collective manner (Figure 5.11). A similar level of migration was observed across the HA, HA+LAM, and HA+COL matrices after 72 hours; however, spheroids on the HA+FN matrix appeared to migrate further within the first 24 hours and over the course of the experimental period than spheroids on any other matrix.

Similar to DAOY cells, ONS76 spheroids also displayed collective cell migration from the spheroid body across all four HA matrix conditions (Figure 5.12). Again, HA+FN matrices encouraged the most migration out of the hydrogel matrix compositions. A similar level of migration was observed across the HA, HA+LAM, and HA+COL matrices for ONS76 spheroids over the course of the assay.

So far, the UW228-3 cell line has shown very little invasive or migratory capacity in the other matrices tested. However, UW228-3 spheroids migrated especially well over the HA+FN matrix, with extensive cell dissemination within 24 hours (Figure 5.13). Conversely, there was very little migration on HA, HA+LAM, and HA+COL matrices.

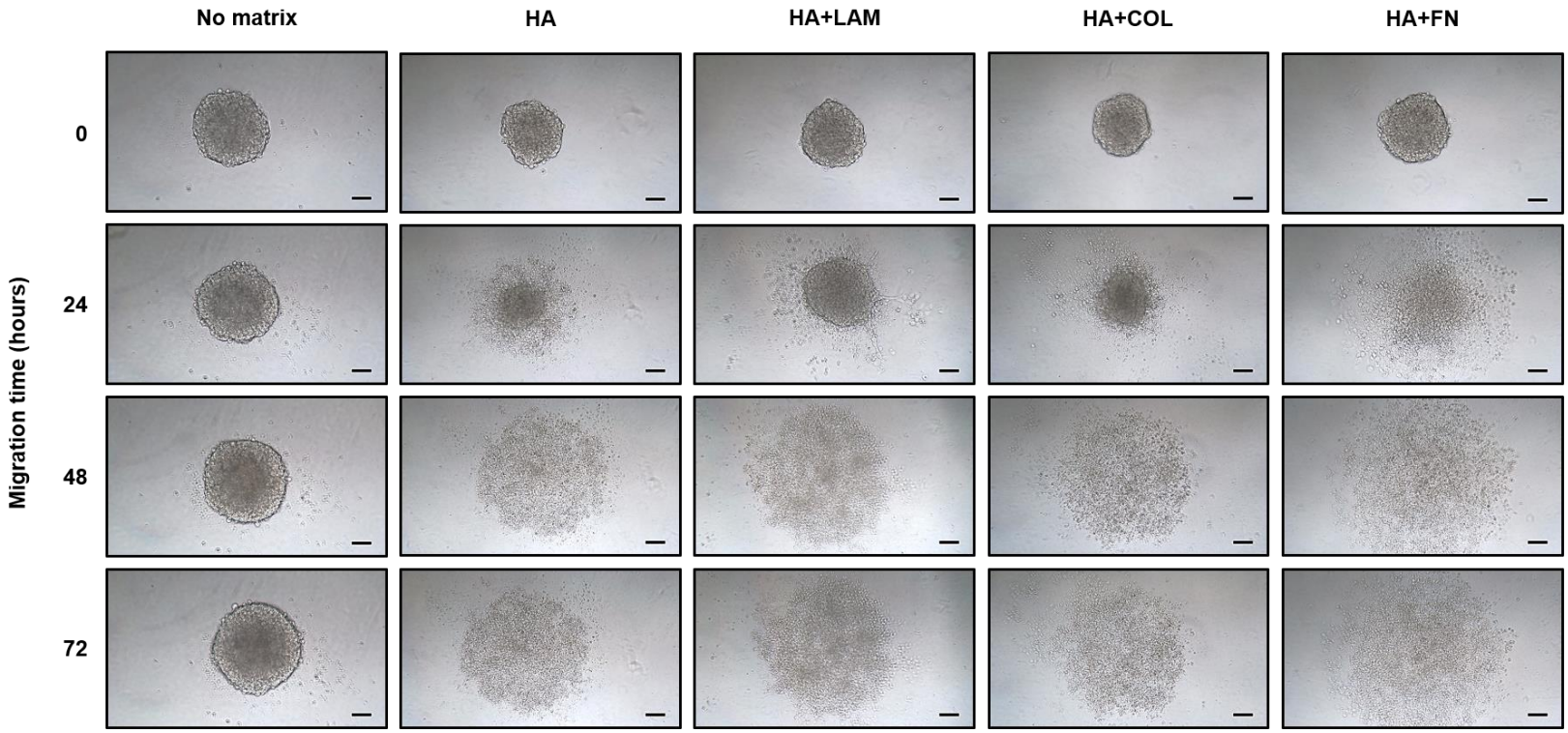


Figure 5.11 DAOY spheroid migration on hyaluronan hydrogels

DAOY spheroids were transferred to a 96-well flat-bottom plate coated with hyaluronan (HA) matrices with or without the extracellular matrix components laminin-111 (LAM), collagen I (COL), and fibronectin (FN) on day 4 (0 hours). A no matrix control was included to assess normal spheroid growth. Spheroid migration across the matrices was assessed over a 72 hour period. DAOY spheroids readily migrated across all matrices. Images of the same spheroid at different time points are shown (scale bar: 100 µm) and are representative of 3 independent experiments each containing 3 replicates.

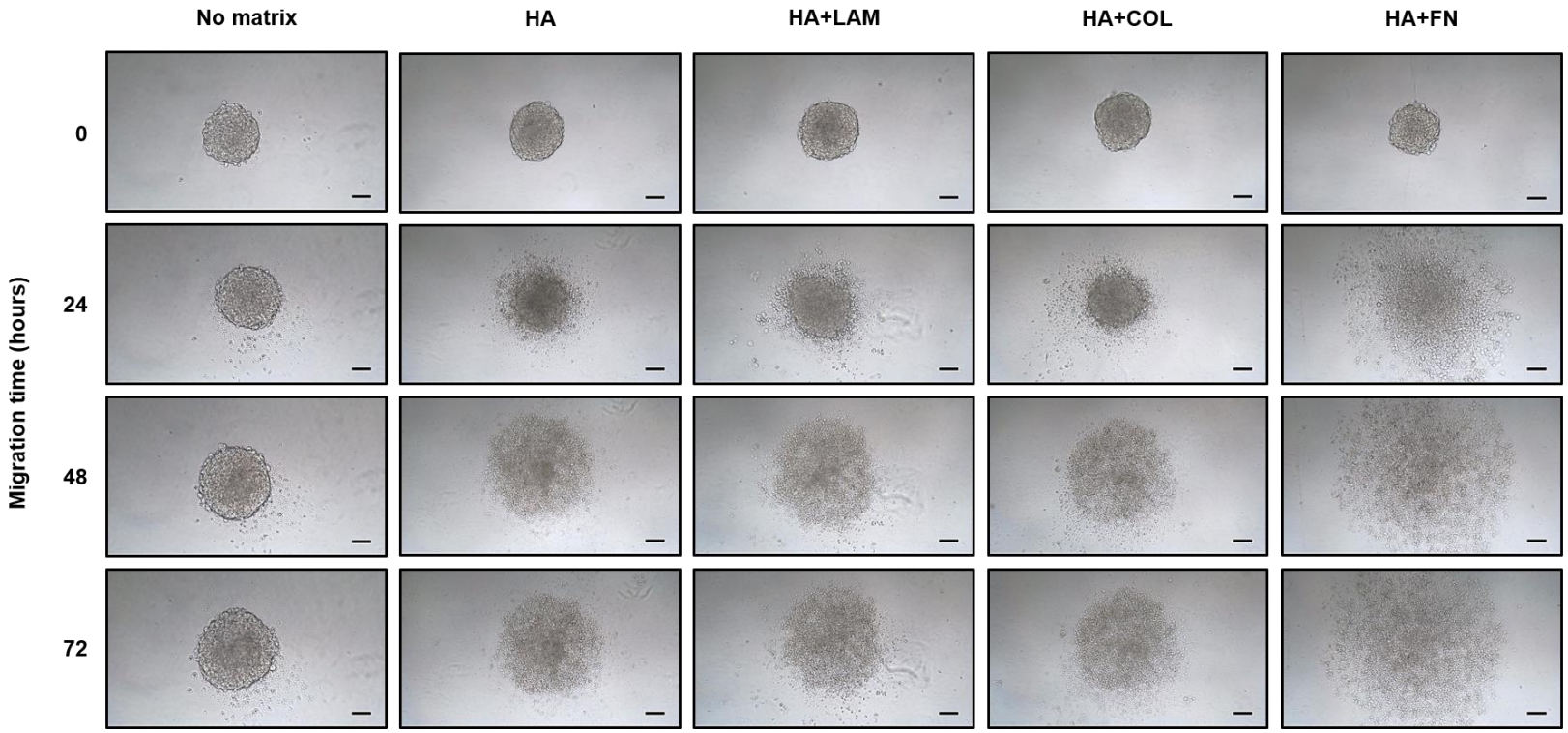


Figure 5.12 ONS76 spheroid migration on hyaluronan hydrogels

ONS76 spheroids were transferred to a 96-well flat-bottom plate coated with hyaluronan (HA) matrices with or without the extracellular matrix components laminin-111 (LAM), collagen I (COL), and fibronectin (FN) on day 4 (0 hours). A no matrix control was included to assess normal spheroid growth. Spheroid migration across the matrices was assessed over a 72 hour period. ONS76 spheroids readily migrated across all matrices. Images of the same spheroid at different time points are shown (scale bar: 100 µm) and are representative of 3 independent experiments each containing 3 replicates.

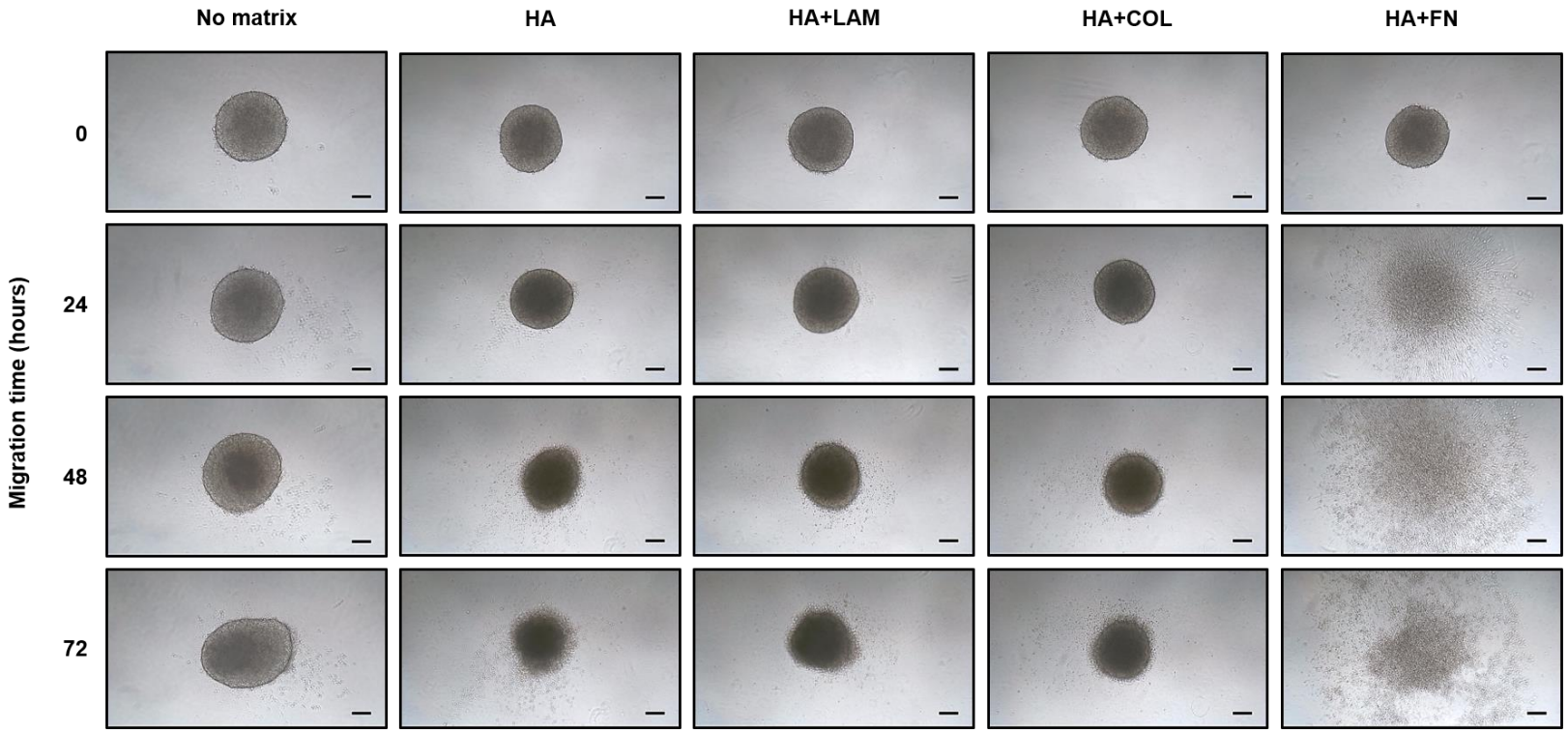


Figure 5.13 UW228-3 spheroid migration on hyaluronan hydrogels

UW228-3 spheroids were transferred to a 96-well flat-bottom plate coated with hyaluronan (HA) matrices with or without the extracellular matrix components laminin-111 (LAM), collagen I (COL), and fibronectin (FN) on day 4 (0 hours). A no matrix control was included to assess normal spheroid growth. Spheroid migration across the matrices was assessed over a 72 hour period. UW228-3 spheroids actively migrated across a HA+FN matrix with very little migration on HA, HA+LAM, and HA+COL matrices. Images of the same spheroid at different time points are shown (scale bar: 100 µm) and are representative of 3 independent experiments each containing 3 replicates.

5.6 Summary

- SHH medulloblastoma spheroids can be utilised in invasion and migration assays.
- Simple and established basement membrane models, including collagen IV coatings and the commercially-available Basement Membrane Extract (BME), were tested:
    - → Collagen IV matrices allowed single cell dissemination for DAOY spheroids and collective cell movement for ONS76 spheroids; however, UW228-3 spheroids failed to migrate
    - → Limited invasion was observed for DAOY and ONS76 spheroids in the higher, gelling concentration of BME. A lower concentration supported spheroid growth but did not promote invasion
    - → DAOY, ONS76, and UW228-3 spheroids displayed some migratory behaviour on BME, the extent of which differed between cell lines. DAOY and ONS76 spheroid migration appeared to be in one direction, with UW228-3 spheroids showing slight protrusions around the spheroid edge.
- Brain-specific models of medulloblastoma metastatic dissemination were established using hyaluronan (HA) hydrogels containing ECM components:
    - → SHH medulloblastoma spheroids expressed the HA receptor, CD44
    - → Laminin, collagen I, and fibronectin gene expression in patient datasets showed higher expression in SHH tumours and there was evidence for elevated expression in the poor prognosis subtype, SHH-β
    - → SHH medulloblastoma spheroids did not effectively invade through HA hydrogels
    - → DAOY and ONS76 spheroids actively migrated across all HA hydrogel compositions; however, UW228-3 only migrated across HA+FN.

Chapter 6

Identifying factors involved in SHH medulloblastoma metastasis using next-generation sequencing technologies

Chapter 6. Identifying factors involved in SHH medulloblastoma metastasis using next-generation sequencing technologies

6.1 Introduction

As discussed in chapter 5, although we now have an increased understanding of medulloblastoma metastasis, including the differential patterns of tumour spread across molecular subgroups, very little is known about the mechanisms involved in tumour spread. In order to understand the processes involved in SHH medulloblastoma metastasis, we chose to apply next-generation sequencing (NGS) technologies to gain an insight into the genes and pathways involved using 3D *in vitro* models.

The aims of this chapter were therefore to:

(1) Adopt an appropriate *in vitro* model for SHH medulloblastoma metastasis

(2) Prepare samples suitable for NGS and compare the techniques adopted

(3) Investigate spheroid-matrix interactions

(4) Understand the processes involved in SHH medulloblastoma metastasis.

6.2 *In vitro* modelling of SHH medulloblastoma metastasis

To understand the mechanisms involved in SHH medulloblastoma metastatic dissemination, our research group have been developing 3D *in vitro* models that recapitulate the metastatic behaviours observed in patient tumours. As discussed previously, SHH medulloblastomas predominantly metastasise through cell dissemination from the primary tumour and the formation of nodular metastases on the leptomeningeal surface. We have modelled these two events *in vitro* by utilising HA hydrogels, used in section 5.5, to mimic the leptomeningeal surface.

A schematic diagram describing the approach taken for modelling SHH medulloblastoma metastasis is shown in Figure 6.1. 96-well flat-bottomed plates were coated with HA hydrogels and spheroids or single cells were used to model the different stages of metastasis. To model cell dissemination from the primary tumour, day 4 spheroids, generated as previously described, were transferred to the HA matrices and cells migrated across the surface. To model the formation of nodular metastases, single cells were seeded on top of the HA matrices and small nodules formed over time.

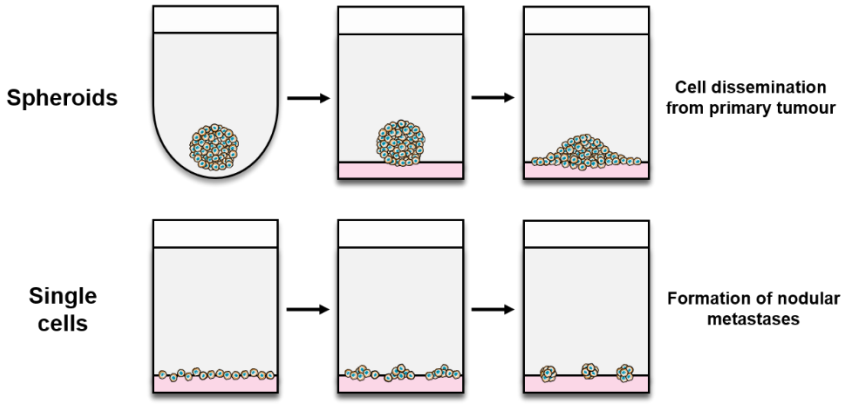


Figure 6.1 Schematic diagram describing the spheroid and single cell models of SHH medulloblastoma metastasis
96-well flat-bottomed plates were coated with hyaluronan (HA) hydrogels. To model cell dissemination from the primary tumour, day 4 spheroids, were transferred to the HA matrices and cells migrated across the surface. To model the formation of nodular metastases, single cells were seeded on top of the HA matrices and small nodules formed over time.

In vitro modelling of SHH medulloblastoma metastasis using the DAOY and ONS76 cell lines is shown in Figures 6.2 and 6.3, respectively. Spheroids in no matrix, modelling the primary tumour, continued to grow throughout the course of the experiment (Figures 6.2A and 6.3A). When transferred to the HA hydrogel matrices, cells actively migrated from DAOY and ONS76 spheroids over a 48 hour period (Figures 6.2B and 6.3B). This cell dissemination from the spheroids was also observed on HA hydrogels containing the ECM component LAM (Figures 6.2C and 6.3C). Dr Franziska Linke used the same matrix compositions and showed different

migratory patterns when single cells were seeded on the matrices. It was observed that DAOY and ONS76 cells formed loosely-attached spheroid-like structures on HA hydrogels over time (Figures 6.2D and 6.3D). However, when single cells were seeded on HA hydrogels containing LAM, it resulted in the growth of multiple nodules on the matrix (Figures 6.2E and 6.3E).

These five conditions were taken forward for NGS as simplified models of the different stages of SHH medulloblastoma metastasis. Spheroid samples were harvested at 48 hours, a time point chosen to capture the cells during active migration. Single cell samples were harvested on day 12, by which point the HA+LAM samples had formed multiple nodules on the matrix surface.

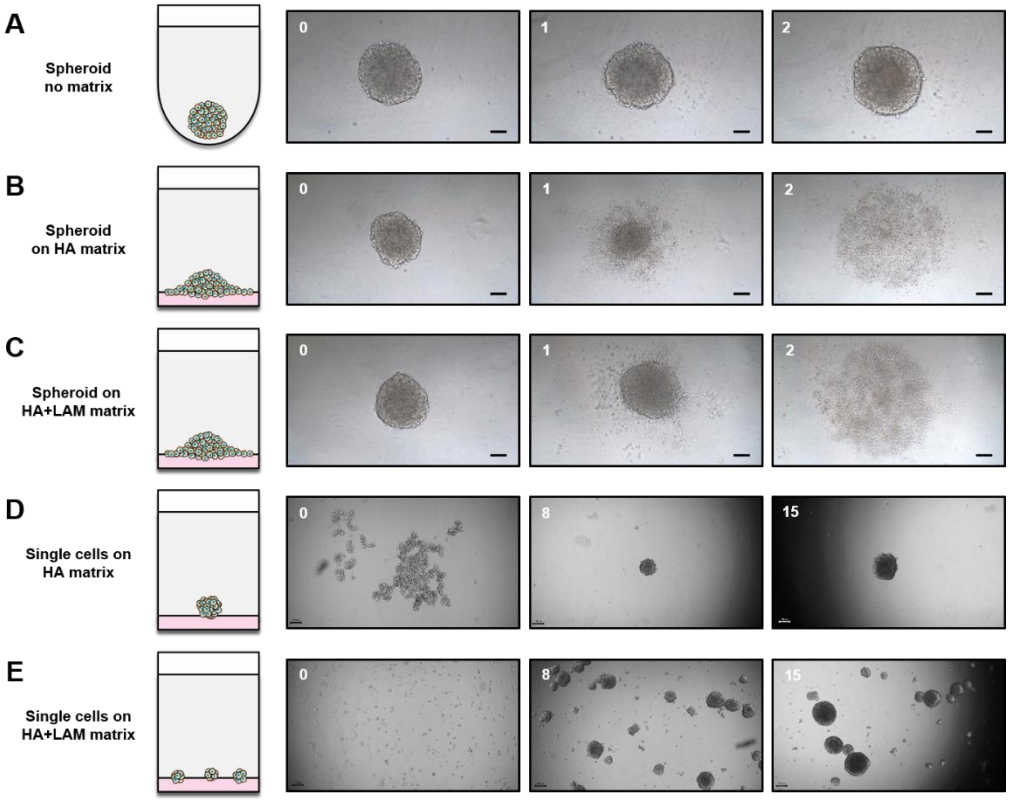


Figure 6.2 ***In vitro*** **modelling of SHH medulloblastoma metastasis using the DAOY cell line**

DAOY spheroids and single cells were used to model SHH medulloblastoma metastasis. (**A**) Spheroids in no matrix grew throughout the experiment. (**B**) Cells actively migrated from the main spheroid body on a hyaluronan (HA) matrix over a 48 hour period. (**C**) Cell dissemination from the spheroid was also observed on a HA hydrogel matrix containing the ECM component laminin-111 (LAM). (**D**) Single cells seeded on HA matrices formed loosely-attached spheroid-like structures. (**E**) When single cells were seeded on HA+LAM hydrogels, it resulted in the growth of multiple nodules on the matrix. The number of days post-transfer onto the matrix is shown in the top left corner of each image. Dr Franziska Linke conducted the single cell experiments. Representative images are shown (scale bar: 100 µm).

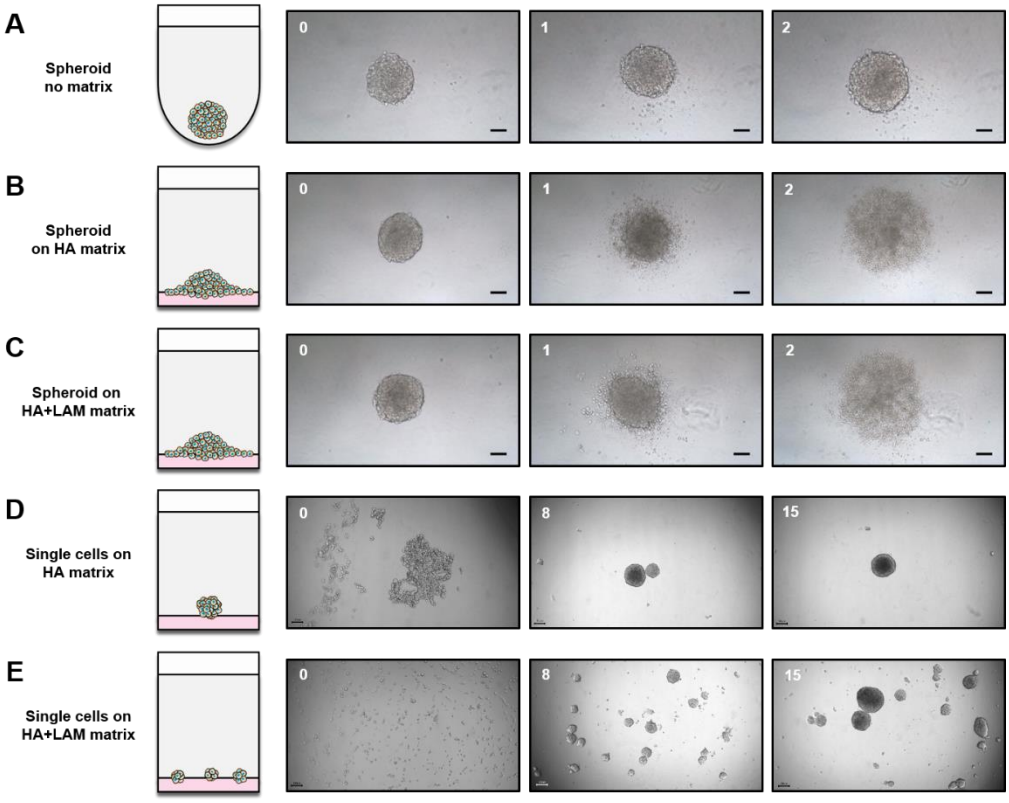


Figure 6.3 ***In vitro*** **modelling of SHH medulloblastoma metastasis using the ONS76 cell line**

ONS76 spheroids and single cells were used to model SHH medulloblastoma metastasis. (**A**) Spheroids in no matrix grew throughout the experiment. (**B**) Cells actively migrated from the main spheroid body on a hyaluronan (HA) matrix over a 48 hour period. (**C**) Cell dissemination from the spheroid was also observed on a HA hydrogel matrix containing the ECM component laminin-111 (LAM). (**D**) Single cells seeded on HA matrices formed loosely-attached spheroid-like structures. (**E**) When single cells were seeded on HA+LAM hydrogels, it resulted in the growth of multiple nodules on the matrix. The number of days post-transfer onto the matrix is shown in the top left corner of each image. Dr Franziska Linke conducted the single cell experiments. Representative images are shown (scale bar: 100 µm).

6.3 NGS of SHH medulloblastoma metastasis models

In order to perform NGS of SHH medulloblastoma metastasis models, it was essential to extract high quality RNA for library preparation and sequencing. However, RNA isolation from hydrogels proved particularly difficult due to the low yields of RNA obtained. To efficiently utilise our samples, we chose to adopt two NGS technologies: traditional mRNA sequencing, which required at least 100 ng of RNA per sample, and 3' UPX sequencing, a method used for low input samples that sequenced the 3' end of RNA near the poly-A tail.

6.3.1 Sample preparation

The workflow for sample preparation for NGS is shown in Figure 6.4. Firstly, RNA was extracted from samples using the NucleoSpin® RNA Plus kit (Macherey-Nagel). Following extraction, samples were shipped to QIAGEN Genomic Services (Hilden, Germany) where the subsequent steps of NGS were performed. Quality control of the RNA was performed using the Qubit RNA high sensitivity assay (Invitrogen™) which quantified the amount of RNA in each sample. Samples with 100 ng or more of RNA in total were suitable for mRNA NGS. Samples with lower RNA yields were lyophilised and resuspended in a smaller volume of RNase-free water. Another quality control step was performed to quantify the RNA. Samples with an RNA concentration above 1.4 ng/mL were appropriate for 3' UPX NGS. However, samples with a lower RNA concentration were unsuitable for either method of NGS.

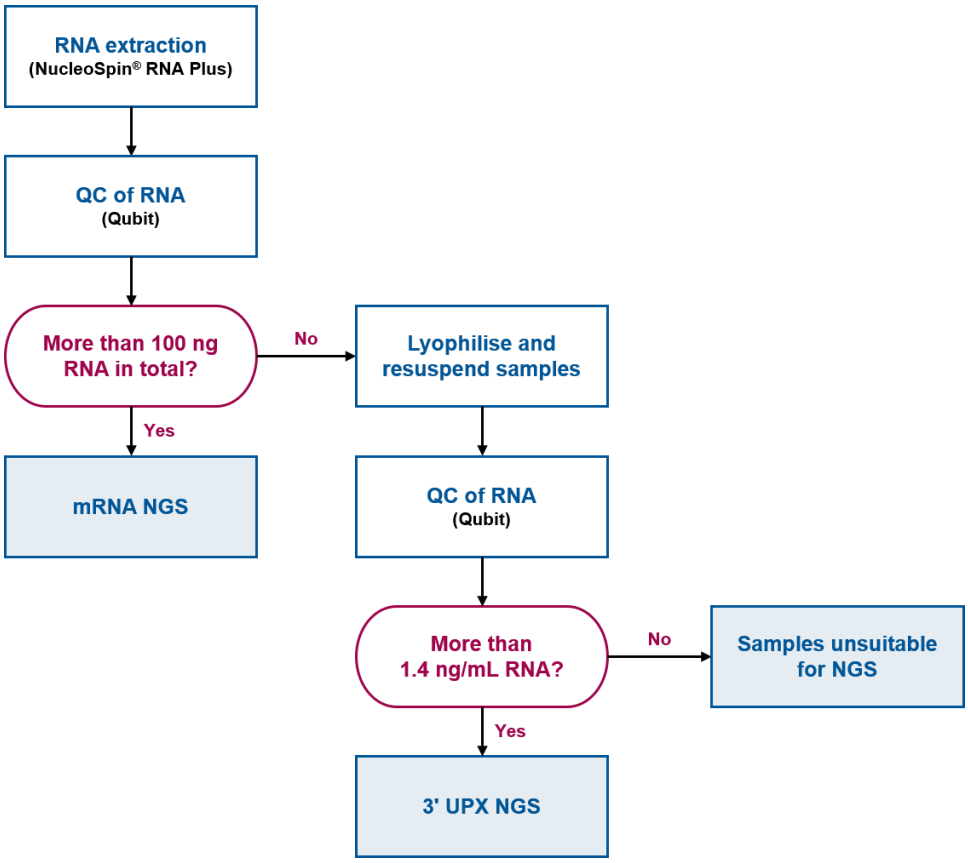


Figure 6.4 Sample preparation for next-generation sequencing
The workflow for the preparation of samples for next-generation sequencing (NGS) is shown as processes (blue) and questions/outputs (red). RNA was extracted using the NucleoSpin® RNA Plus kit. Quality control (QC) of the RNA was performed using the Qubit RNA high sensitivity assay. Samples with 100 ng or more of RNA in total were suitable for mRNA NGS. Samples with lower RNA yields were lyophilised and resuspended in a smaller volume of RNase-free water. Another QC step was performed to quantify the RNA. Samples with more RNA concentration above 1.4 ng/mL, were appropriate for 3' UPX NGS. However, samples with a lower RNA concentration were unsuitable for NGS.

Table 6.1 provides a summary of the samples prepared for NGS. 30 samples were prepared in total (2 cell lines in 5 metastatic models with 3 replicates). 25 samples contained around 100 ng of RNA in total and were therefore suitable for mRNA NGS. The remaining 5 samples were lyophilised and re-quantified, resulting in four samples suitable for 3' UPX NGS. Sample 146 was unsuitable for either method of NGS due to a poor yield and was therefore excluded from further analysis. It is important to note that for some samples with enough RNA, both mRNA and 3' UPX NGS were performed in an attempt to provide complete datasets for analysis.

Table 6.1 Summary of samples prepared for NGS

30 samples were prepared for NGS. RNA concentration (ng/µL) and total yield (ng) were quantified using the Qubit RNA high sensitivity assay. 25 samples contained around 100 ng RNA in total and were suitable for mRNA NGS. The remaining 5 samples were lyophilised and resuspended in a smaller volume, before being quantified. 4 samples had an RNA concentration above 1.4 ng/mL and were suitable for 3' UPX NGS, with one sample (146) excluded from further work.

Sample number	Cell line	Spheroid or single cells?	Matrix	RNA conc. (ng/µL)	RNA yield (ng)	NGS method
135	DAOY	Spheroid	No matrix	21.1	739	mRNA
141	DAOY	Spheroid	No matrix	9	315	mRNA
147	DAOY	Spheroid	No matrix	14	490	mRNA
136	DAOY	Spheroid	HA	5.25	184	mRNA
143	DAOY	Spheroid	HA	44.8	1568	mRNA
148	DAOY	Spheroid	HA	3.06	107	mRNA
137	DAOY	Spheroid	HA+LAM	3.21	112	mRNA
145	DAOY	Spheroid	HA+LAM	4.21	23	3’ UPX
149	DAOY	Spheroid	HA+LAM	3.29	115	mRNA
113	DAOY	Single	HA	49.8	1743	mRNA
117	DAOY	Single	HA	27.9	977	mRNA
121	DAOY	Single	HA	13.7	480	mRNA
114	DAOY	Single	HA+LAM	8.27	289	mRNA
118	DAOY	Single	HA+LAM	12.6	441	mRNA
122	DAOY	Single	HA+LAM	4.45	156	mRNA
138	ONS76	Spheroid	No matrix	22.7	795	Both
142	ONS76	Spheroid	No matrix	10.9	382	Both
150	ONS76	Spheroid	No matrix	9.24	323	Both
139	ONS76	Spheroid	HA	4.12	23	3’ UPX
144	ONS76	Spheroid	HA	2.91	16	3’ UPX
151	ONS76	Spheroid	HA	47.2	1652	Both
140	ONS76	Spheroid	HA+LAM	2.47	14	3’ UPX
152	ONS76	Spheroid	HA+LAM	15.9	557	Both
146	ONS76	Spheroid	HA+LAM	<1.4	n/a	Unsuitable
115	ONS76	Single	HA	2.7	95	mRNA
123	ONS76	Single	HA	124	4340	mRNA
119b	ONS76	Single	HA	4.17	146	mRNA
120	ONS76	Single	HA+LAM	7.23	253	mRNA
124	ONS76	Single	HA+LAM	4.79	168	mRNA
116b	ONS76	Single	HA+LAM	6.4	224	mRNA

Following RNA extraction and quantification, libraries were prepared and sequenced. For mRNA NGS, library preparation was carried out using the TruSeq® Stranded mRNA library preparation kit. All prepared libraries successfully passed QIAGEN's internal quality control checks and were subsequently sequenced on a NextSeq 500 Illumina sequencer. Following sequencing, quality control of the sequencing data was performed using FASTQC analysis. All samples had high quality scores, indicating good technical performance of the sequencing. For 3' UPX NGS, library preparation was performed using the QIAseq® UPX 3' Transcriptome kit. All prepared libraries successfully passed QIAGEN's internal quality control checks and were sequenced on a NextSeq 500 Illumina sequencer. Following sequencing, FASTQC analysis of the sequencing data was performed and all samples were considered suitable for downstream primary and secondary data analysis.

6.3.2 Mapping of sequencing data

Mapping of the sequencing data was performed as an additional control step to evaluate the quality of each sample. A summary of the mapping results for mRNA NGS is shown in Table 6.2. The reads were categorised into the following classes:

(1) Mapped reads: reads aligning to reference genome, including mRNA, pre-mRNA, poly-A tailed lncRNA and pri-miRNA
(2) Outmapped reads: reads that do not map to the reference genome but can be mapped to rRNA, mtRNA, poly-A and poly-C homopolymers
(3) Unmapped reads: no alignment possible.

On average, 33.5 million reads were obtained for each sample. Samples 143, 123, and 116b were excluded from further analysis as they clustered separately to equivalent samples (see Appendix 2).

Table 6.2 Mapping of mRNA NGS sequence data

Mapping of the sequencing data was performed as an additional control step to evaluate the quality of each sample. The number of reads per sample and percentages of mapped, outmapped and unmapped reads are displayed.

Sample number	Cell line	Spheroid or single cells?	Matrix	Mapping results			
				Reads	Mapped	Out-mapped	Un-mapped
135	DAOY	Spheroid	No matrix	34,701,517	88.2%	8.8%	3.0%
141	DAOY	Spheroid	No matrix	36,052,643	88.2%	8.3 %	3.5%
147	DAOY	Spheroid	No matrix	33,856,640	88.0%	8.7%	3.3%
136	DAOY	Spheroid	HA	27,560,802	85.3%	10.4%	4.3%
143	DAOY	Spheroid	HA	32,609,788	69.6%	26.1%	4.2%
148	DAOY	Spheroid	HA	29,927,246	81.0%	14.7%	4.3%
137	DAOY	Spheroid	HA+LAM	28,507,306	84.2%	11.8%	4.1%
149	DAOY	Spheroid	HA+LAM	32,154,621	81.6%	14.3%	4.0%
113	DAOY	Single	HA	31,790,161	70.4%	23.1%	6.4%
117	DAOY	Single	HA	32,409,692	83.4%	13.2%	3.4%
121	DAOY	Single	HA	29,874,972	81.6%	15%	3.4%
114	DAOY	Single	HA+LAM	32,789,443	83.4%	12.6%	4.0%
118	DAOY	Single	HA+LAM	37,981,815	82.8%	13.9%	3.3%
122	DAOY	Single	HA+LAM	35,690,294	80.1%	16.7%	3.2%
138	ONS76	Spheroid	No matrix	39,826,946	88.6%	8.4%	3.0%
142	ONS76	Spheroid	No matrix	32,664,451	89.2%	7.7%	3.1%
150	ONS76	Spheroid	No matrix	37,342,823	89.6%	7.3%	3.2%
151	ONS76	Spheroid	HA	30,074,832	79.7%	16%	4.3%
152	ONS76	Spheroid	HA+LAM	29,324,113	76.5%	18.6%	4.9%
115	ONS76	Single	HA	34,991,683	85.4%	10.8%	3.8%
123	ONS76	Single	HA	30,570,105	77.2%	18.7%	4.1%
119b	ONS76	Single	HA	39,292,664	89.5%	7.5%	3.0%
120	ONS76	Single	HA+LAM	36,187,797	82.8%	14.1%	3.0%
124	ONS76	Single	HA+LAM	39,354,371	78.8%	18.1%	3.1%
116b	ONS76	Single	HA+LAM	30,868,184	88.7%	7.9%	3.4%

A summary of the mapping results for 3' UPX NGS is shown in Table 6.3. The reads were categorised into the following classes:

(1) Total reads: read pairs demultiplexed to each cell identifier

(2) Reads aligned to genome: reads aligned to the reference genome used for UMI counting

(3) Reads aligned to ERCC: Reads aligned to ERCC-spike-ins used for UMI counting

(4) UMIs: Unique Molecular Index tags counted.

On average, 12 million reads were obtained for each sample.

Table 6.3 Mapping of 3' UPX NGS sequence data

Mapping of the sequencing data was performed as an additional control step to evaluate the quality of each sample. The number of reads (total, aligned to genome, aligned to ERCC, and UMIs) per sample are displayed.

Sample number	Cell line	Matrix	Mapping results			
			Total reads	Reads aligned to genome	Reads aligned to ERCC	UMIs
145	DAOY	HA+LAM	15,951,848	4,519,378	1,163,446	1,988,741
138	ONS76	No matrix	5,768,873	1,867,734	381,290	855,038
142	ONS76	No matrix	14,946,025	4,187,416	806,283	1,924,070
150	ONS76	No matrix	5,159,398	1,482,292	288,191	710,987
139	ONS76	HA	14,018,938	4,793,685	707,930	1,986,504
144	ONS76	HA	11,491,915	3,065,209	827,288	1,484,188
151	ONS76	HA	13,768,821	4,341,561	309,609	1,868,633
140	ONS76	HA+LAM	15,610,575	5,210,525	849,791	2,232,182
152	ONS76	HA+LAM	11,236,852	3,874,074	337,410	1,679,303

6.3.3 Comparison of NGS techniques

As mentioned previously, mRNA and 3' UPX NGS technologies were adopted to increase the number of low RNA yield samples included in the analysis. However, these methods of NGS were significantly different, as shown in the workflow comparisons in Figure 6.5. Although sample preparation for both techniques was the same, the subsequent library preparation, mapping, and differential gene expression analysis varied for each method. It was therefore important that we considered how we would compare samples as the results generated for each method could differ.

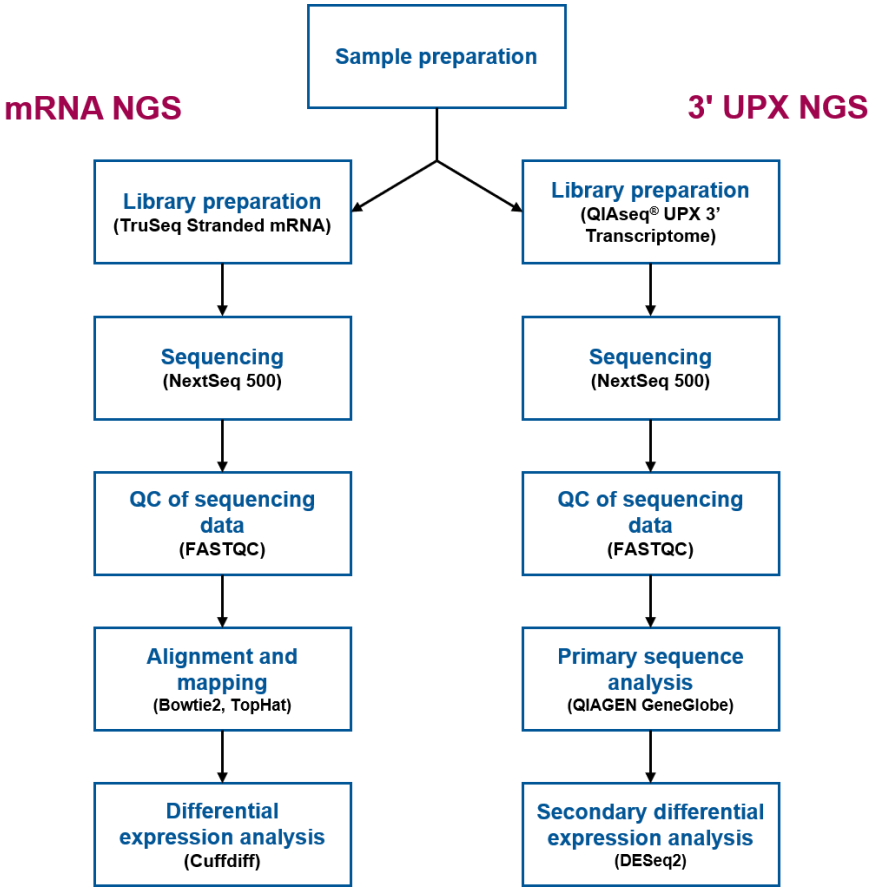


Figure 6.5 Comparison of mRNA and 3' UPX NGS workflows
mRNA and 3' UPX NGS technologies differ in their experimental workflows. Following sample preparation (discussed in detail in Figure 6.4), the subsequent library preparation, mapping, and differential gene expression analysis varied for each method. Steps of the NGS method (with techniques and programmes used) are shown.

As already alluded to in the analysis of the mapping data, the number of reads obtained for samples differed between mRNA and 3' UPX NGS, with an average of 33.5 million and 12 million reads per sample generated for each technique, respectively. This indicated that the outputs from the NGS methods were substantially different. To compare the results of mRNA and 3' UPX analyses, we assessed five samples that were sequenced by both techniques. Firstly, genes were filtered based on FPKM (mRNA) and UMI (3' UPX) values of ≥10 and the number of genes identified for each technique were compared. As shown in Figure 6.6, mRNA sequencing identified around 30-50% more genes than 3' UPX sequencing. This indicated that, as expected, the NGS techniques have different gene quantity outputs and, therefore, analysis based on individual gene levels would be unsuitable.

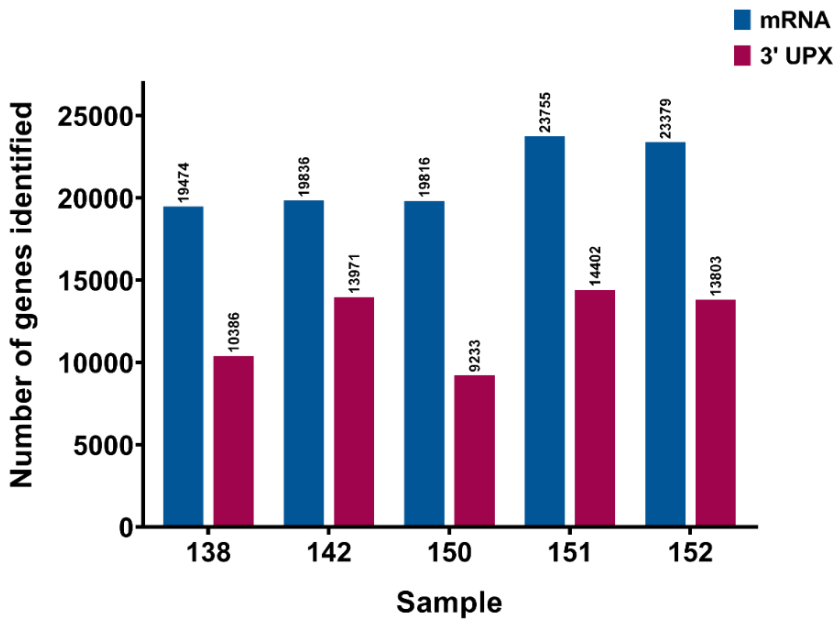


Figure 6.6 Number of genes identified in samples sequenced by both mRNA and 3' UPX NGS methods

Samples 138, 142, 150, 151, and 152 were sequenced by two next-generation sequencing (NGS) methods: mRNA and 3' UPX. Genes were filtered based on FPKM and UMI values of ≥10 and the number of genes identified for each technique were compared. mRNA sequencing identified around 30-50% more genes than 3' UPX sequencing.

To further compare mRNA and 3' UPX results, we chose to compare the differential gene expression analysis results between two sample sets (genes upregulated in spheroids on a HA matrix compared to spheroids on no matrix) to gain a broader overview of the NGS outputs. To do this, significantly differentially expressed genes were filtered based on their fold change (Log2 ≥2) and FPKM or UMI value (≥20). This generated a list of significantly differentially regulated genes between the two comparison groups. Gene Set Enrichment Analysis (GSEA), a computational method used to determine whether a group of genes overlap with defined gene sets on a Molecular Signatures Database (Subramanian *et al.*, 2005; Liberzon *et al.*, 2011), was then performed. Table 6.4 displays the top 20 gene sets that overlapped with the Gene Ontology (GO) biological process gene set for each NGS method through GSEA. Comparison of the gene set lists for mRNA and 3' UPX analysis showed that 75% of gene sets were shared between the two techniques. This indicates that although the results should not be compared on an individual gene level, a broader gene set level could be considered as a relevant and suitable comparison.

Table 6.4 Comparison of top 20 gene sets upregulated in spheroids on a HA matrix identified by mRNA and 3' UPX NGS

Differential gene expression analysis was conducted on samples sequenced by mRNA and 3' UPX NGS methods to generate lists of genes upregulated in spheroids on a HA matrix compared to spheroids on no matrix. Gene Set Enrichment Analysis was performed to identify the top 20 gene sets that overlapped with the Gene Ontology (GO) biological process database. The number of genes in each gene set (# genes) is shown. 75% of identified gene sets were shared by both mRNA and 3' UPX analyses (highlighted).

mRNA		3' UPX	
GO biological processes gene set	**# genes**	**GO biological processes gene set**	**# genes**
Cell projection organisation (GO:0030030)	148	Cell projection organisation (GO:0030030)	120
Neurogenesis (GO:0022008)	128	Neurogenesis (GO:0022008)	102
Neuron differentiation (GO:0030182)	113	Central nervous system development (GO:0007417)	76
Cell projection assembly (GO:0030031)	70	Cilium movement (GO:0003341)	25
Neuron development (GO:0048666)	95	Neuron differentiation (GO:0030182)	86
Microtubule-based process (GO:0007017)	77	Cell projection assembly (GO:0030031)	56
Locomotion (GO:0040011)	127	Locomotion (GO:0040011)	104
Cilium organisation (GO:0044782)	55	Neuron development (GO:0048666)	75
Cytoskeleton organisation (GO:0007010)	98	Cellular component morphogenesis (GO:0032989)	75
Cellular component morphogenesis (GO:0032989)	90	Microtubule-based movement (GO:0007018)	39
Cell motility (GO:0048870)	114	Cell part morphogenesis (GO:0032990)	57
Central nervous system development (GO:0007417)	80	Biological adhesion (GO:0022610)	83
Cell morphogenesis involved in differentiation (GO:0000904)	68	Axoneme assembly (GO:0035082)	22
Cell part morphogenesis (GO:0032990)	64	Microtubule-based process (GO:0007017)	59
Regulation of cell differentiation (GO:0045595)	111	Cilium organisation (GO:0044782)	43
Cell morphogenesis involved in neuron differentiation (GO:0048667)	58	Cell morphogenesis involved in neuron differentiation (GO:0048667)	51
Positive regulation of developmental process (GO:0051094)	93	Microtubule bundle formation (GO:0001578)	24
Microtubule-based movement (GO:0007018)	41	Cytoskeletal organisation (GO:0007010)	76
Circulatory system development (GO:0072359)	83	Cell morphogenesis involved in differentiation (GO:0000904)	56
Cell-cell signalling (GO:0007267)	100	Ion transport (GO:0006811)	87

6.4 Investigating spheroid-matrix interactions

To investigate spheroid-matrix interactions, unsupervised analysis was conducted of the top 500 most significantly differentially expressed genes between spheroids on no matrix versus spheroids on a HA matrix. This generated a heatmap showing the hierarchical clustering of samples where each row represented one gene and individual samples were displayed in columns. The colour scale signified the relative expression level of a transcript across all samples. Expression levels above and below the mean were depicted by the colours red and green, respectively. Hierarchical clustering of the “spheroid no matrix” and “spheroid HA matrix” samples is displayed in Figure 6.7. The heatmap shows that “spheroid no matrix” samples from both cell lines cluster together, but cluster separately and are significantly different to “spheroid HA matrix” samples, indicating that culture conditions have more of an effect on the extent of differential gene expression than the cell line.

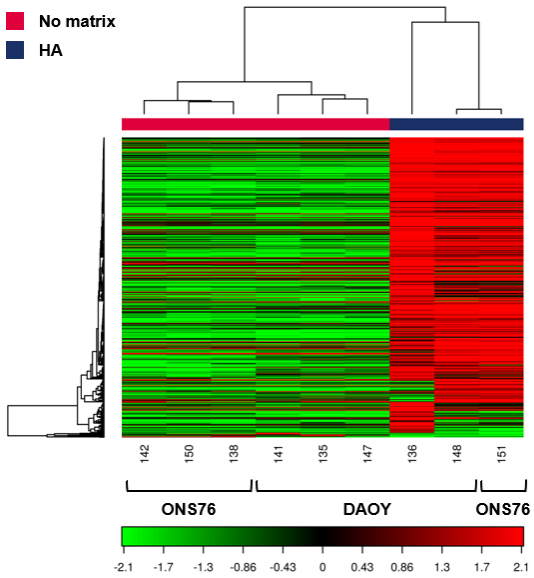


Figure 6.7 Clustering of “spheroid no matrix” and “spheroid HA matrix” samples
Heatmap of the hierarchical clustering of the top 500 most significantly differentially expressed genes between spheroids on no matrix (red) and spheroids on a hyaluronan (HA) matrix (blue) identified by mRNA NGS analyses. Samples for each condition and cell line cluster separately. Each row represented one gene and individual samples were displayed in columns. The colour scale signified the relative expression level of a transcript across all samples. Expression levels above and below the mean were depicted by the colours red and green, respectively.

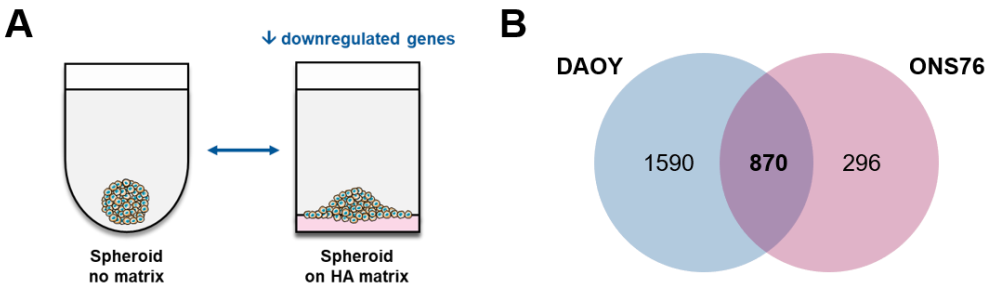
Differential gene expression analysis was conducted to identify significantly up- and down-regulated genes involved in the spheroid-matrix interaction. This involved comparing two groups of samples: (1) “spheroid no matrix” and (2) “spheroid HA matrix”.

Analysis was firstly conducted within cell lines. For DAOY samples, for which only mRNA NGS was performed, significantly differentially expressed genes were filtered based on fold change (Log2 ≥1) and FPKM value (≥20). For ONS76 samples, the analysis was more complex as both mRNA and 3' UPX NGS was performed on samples in this comparison. ONS76 samples sequenced using mRNA NGS were filtered using the same method described for the DAOY samples. For 3' UPX differential gene expression analysis, significantly differentially expressed genes were filtered based on the same fold change threshold (Log2 ≥1) and mean UMI counts of ≥20. This resulted in two lists of differentially regulated genes for ONS76 samples generated for each NGS method. These lists were then compared and only the overlapping genes (i.e. the differentially regulated genes that were shared between the two NGS techniques) were used for further analysis.

The lists of differentially regulated genes for each cell line were then compared with each other. The overlapping genes which were shared between cell lines were further analysed using GSEA and the GO biological process gene set. Significance in overlap with the GO gene set was determined using an uncorrected p-value and a q-value (a p-value adjusted using the Benjamini-Hochberg False Discovery Rate (FDR) approach) to correct for multiple testing.

6.4.1 Cell cycle genes are downregulated in spheroids on a HA matrix

Figure 6.8A summarises the comparison used to identify downregulated genes in the spheroid-matrix interaction. Analysis within cell lines showed that there were 2460 significantly downregulated genes in DAOY samples and 1166 genes for ONS76 samples (overlapping results from the mRNA and 3' UPX analysis). When these cell line-specific gene list were compared, it revealed that were 870 shared significantly downregulated genes (Figure 6.8B). GSEA of these 870 genes was performed to identify associated GO biological process gene sets (Figure 6.8C). Gene sets involved in the cell cycle, including ‘mitotic cell cycle’ (GO: 0000278), ‘cell cycle’ (GO: 0007049), ‘cell cycle process’ (GO: 0022402) and ‘cell cycle transition’ (GO: 0044770), significantly overlapped with the gene list generated from our analyses. This indicated that when spheroids are on a HA matrix, there is downregulation of cell division. Conversely, this could be seen as an upregulation of processes involved in growth and proliferation in the spheroids on no matrix.



C

Gene set name	Number of genes in overlap	p-value	FDR q-value
Mitotic cell cycle (GO:0000278)	137	4.54 e^{-75}	3.34 e^{-71}
Protein containing complex assembly (GO:0065003)	179	1.49 e^{-72}	5.46 e^{-69}
Cell cycle (GO:0007049)	175	1.32 e^{-71}	3.23 e^{-68}
Cell cycle process (GO:0022402)	150	8.68 e^{-69}	1.6 e^{-65}
Interspecies interaction between organisms (GO:0044419)	121	3.84 e^{-64}	5.65 e^{-51}
Cell cycle phase transition (GO:0044770)	98	1.38 e^{-59}	1.69 e^{-56}
Chromosome organisation (GO:0051276)	130	5.5 e^{-59}	5.77 e^{-56}
Cellular macromolecule catabolic process (GO:0044265)	124	2.43 e^{-56}	2.23 e^{-53}
Macromolecule catabolic process (GO:0009057)	134	1.2 e^{-55}	9.77 e^{-53}
Ribonucleoprotein complex biogenesis (GO:0022613)	83	2.78 e^{-53}	2.04 e^{-50}

Figure 6.8 Genes downregulated in the spheroid-matrix interaction
Differential gene expression analysis was conducted to identify downregulated genes in spheroids on a hyaluronan (HA) matrix compared to spheroids on no matrix. (**A**) Schematic diagram showing the spheroid-matrix interaction assessed. (**B**) Venn diagram showing that 870 downregulated genes (Log2 fold change ≥1) were shared between DAOY and ONS76 samples. (**C**) Top 10 Gene Ontology (GO) biological process gene sets significantly associated with these 870 downregulated genes was assessed using Gene Set Enrichment Analysis (GSEA). Significance was determined using an uncorrected p-value and a q-value (a p-value adjusted using the Benjamini-Hochberg False Discovery Rate (FDR) approach to correct for multiple testing).

Following on from this analysis, we wanted to know which genes were most significantly downregulated in the spheroid-matrix interaction. Table 6.5 shows these top 25 genes for both DAOY and ONS76 samples. There were seven genes which overlapped across the cell lines: *HMGA2* (High Mobility Group AT-Hook 2), *KRT8* (Keratin 8), *COL6A3* (Collagen Type IV Alpha 3 chain), *IGF2BP1* (Insulin-Like Growth Factor 2 mRNA Binding Protein 1), *DSP* (Desmoplakin), *DPPA4* (Developmental Pluripotency Associated 4), and *SEMA3A* (Semaphorin 3A).

Table 6.5 Top 25 genes most significantly downregulated in the spheroid-matrix interaction

Differential gene expression analysis of the mRNA NGS datasets was conducted within the DAOY (**A**) and ONS76 (**B**) cell lines. Genes were ordered based on their significance (Log2 fold change). Highlighted genes were shared by both cell lines. Significance was determined using an uncorrected p-value and a q-value (a p-value adjusted using the Benjamini-Hochberg False Discovery Rate (FDR) approach) to correct for multiple testing.

A DAOY

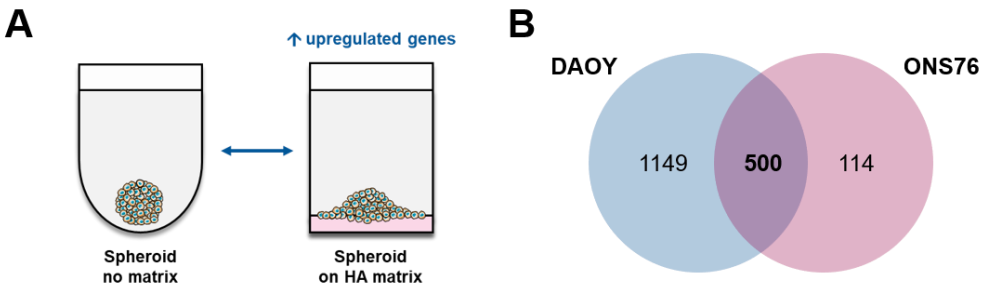
Gene	FPKM value spheroid no matrix	FPKM value spheroid HA matrix	Log2 fold change	p-value	FDR q-value
HOXA-AS2	23.2399	0.026901	9.75474	5.00E-05	0.00042
PAX9	28.6035	0.05401	9.04875	0.00055	0.00326
HMGA2	329.568	0.826231	8.63982	5.00E-05	0.00042
COL2A1	22.2136	0.059968	8.53303	5.00E-05	0.00042
RGS4	199.885	0.602522	8.37394	5.00E-05	0.00042
IGF2BP3	125.5	0.378884	8.37172	5.00E-05	0.00042
KRT8	362.779	1.31981	8.10262	5.00E-05	0.00042
COL6A3	389.552	1.49454	8.02596	5.00E-05	0.00042
FAM27A	222.188	0.90938	7.93268	0.00015	0.001109
NT5E	148.124	0.615512	7.9108	5.00E-05	0.00042
HOXA7	34.2867	0.146522	7.87039	0.0001	0.000779
DSCR8,KCNJ15	52.1674	0.230985	7.8192	5.00E-05	0.00042
AC004540.4	79.8105	0.356157	7.80792	0.0021	0.00999
IGF2BP1	67.1131	0.308601	7.76471	5.00E-05	0.00042
DUSP4	30.4434	0.142433	7.7397	5.00E-05	0.00042
CYP4X1	23.3042	0.114049	7.67479	5.00E-05	0.00042
AC073236.3	337.529	1.79893	7.55173	5.00E-05	0.00042
DSP	67.8914	0.373681	7.50528	5.00E-05	0.00042
HOXD-AS1	24.627	0.144011	7.41792	5.00E-05	0.00042
SIGLEC15	30.3971	0.181561	7.38733	5.00E-05	0.00042
PAGE5	453.942	2.86493	7.30786	5.00E-05	0.00042
SOD3	287.034	1.87874	7.25532	5.00E-05	0.00042
DPPA4	54.9733	0.371371	7.20972	5.00E-05	0.00042
SEMA3A	43.6576	0.350965	6.95876	5.00E-05	0.00042
CMKLR1	40.6068	0.343906	6.88356	5.00E-05	0.00042

B ONS76

Gene	FPKM value spheroid no matrix	FPKM value spheroid HA matrix	Log2 fold change	p-value	FDR q-value
SEMA3A	49.6243	0.00553276	13.1308	0.0038	0.009717
MAGEC1	62.1221	0.0212376	11.5143	0.0147	0.032462
MAGEB2	94.439	0.0921624	10.001	0.00905	0.021046
CHRNA9	154.338	0.164557	9.87328	0.0099	0.022605
POSTN	111.566	0.180801	9.26928	0.00015	0.000488
SPOCK1	143.354	0.233798	9.26011	5.00E-05	0.00017
DMKN	65.3797	0.113565	9.16919	5.00E-05	0.00017
CYP1B1	74.6542	0.146649	8.99171	5.00E-05	0.00017
RP11-169F17.1	32.3771	0.0710788	8.83134	0.00045	0.001354
COL26A1	24.6411	0.0588385	8.71009	0.0009	0.002602
HMGA2	263.151	0.632626	8.70032	5.00E-05	0.00017
MAGEA12	61.915	0.1489	8.6998	0.00035	0.001077
KRT8	279.062	0.680303	8.68019	5.00E-05	0.00017
NAALADL2-AS2	37.6097	0.103488	8.5055	0.01425	0.031557
PCDH7	59.3633	0.177981	8.3817	5.00E-05	0.00017
DPPA4	106.034	0.337556	8.29519	5.00E-05	0.00017
KRT18	231.304	0.749956	8.26877	5.00E-05	0.00017
CACNG8	24.5591	0.0800797	8.26061	5.00E-05	0.00017
GJB2	25.0608	0.105589	7.89083	0.00015	0.000488
HOXB3,HOXB4,HOXB5,HOXB6	33.7443	0.143163	7.88083	5.00E-05	0.00017
COL6A3	565.034	2.51779	7.81003	5.00E-05	0.00017
IGF2BP1	49.1852	0.229306	7.74481	0.0002	0.000641
CHRNA1	21.3582	0.103151	7.69389	0.0055	0.0135
PRSS3	42.6178	0.213143	7.64349	0.00745	0.017586
DSP	51.7173	0.272853	7.56638	5.00E-05	0.00017

6.4.2 Cell movement genes are upregulated in spheroids on a HA matrix

A summary of the comparison used to identify upregulated genes in the spheroid-matrix interaction is shown in Figure 6.9A. Analysis within cell lines showed that there were 1649 significantly upregulated genes in DAOY samples and 614 genes for ONS76 samples (overlapping results from the mRNA and 3' UPX analysis). Comparison of these gene lists showed that were 500 significantly upregulated genes shared between the cell lines (Figure 6.9B). Enrichment analysis of the 500 common genes identified revealed significant overlaps with GO biological process gene sets associated with cell movement (Figure 6.9C), including ‘cell projection organisation’ (GO: 0030030), ‘cytoskeletal organisation’ (GO: 0007010), ‘microtubule-based process’ (GO: 0007017), and ‘cell projection assembly’ (GO: 0030031). These analyses therefore showed that when spheroids are on a HA matrix, there are substantial gene expression changes associated with a migratory phenotype, as shown previously in section 6.2.



C

Gene set name	Number of genes in overlap	p-value	FDR q-value
Cell projection organisation (GO:0030030)	100	$1.39\ e^{-48}$	$1.02\ e^{-44}$
Cellular component morphogenesis (GO:0032989)	71	$3.12\ e^{-33}$	$1.15\ e^{-29}$
Cytoskeleton organisation (GO:0007010)	75	$2.46\ e^{-32}$	$6.03\ e^{-29}$
Neurogenesis (GO:0022008)	82	$9.70\ e^{-32}$	$1.78\ e^{-28}$
Microtubule based process (GO:0007017)	57	$3.65\ e^{-31}$	$5.37\ e^{-28}$
Neuron differentiation (GO:0030182)	74	$1.75\ e^{-30}$	$2.14\ e^{-27}$
Cell projection assembly (GO:0030031)	50	$2.91\ e^{-30}$	$3.05\ e^{-27}$
Neuron development (GO:0048666)	61	$1.73\ e^{-25}$	$1.59\ e^{-22}$
Cilium organisation (GO:0044782)	38	$2.63\ e^{-25}$	$2.15\ e^{-22}$
Cell morphogenesis involved in differentiation (GO:0000904)	49	$3.62\ e^{-24}$	$2.66\ e^{-21}$

Figure 6.9 Genes upregulated in the spheroid-matrix interaction
Differential gene expression analysis was conducted to identify upregulated genes in spheroids on a hyaluronan (HA) matrix compared to spheroids on no matrix. (**A**) Schematic diagram showing the spheroid-matrix interaction assessed. (**B**) Venn diagram showing that 500 upregulated genes (Log2 fold change ≥1) were shared between DAOY and ONS76 samples. (**C**) Top 10 Gene Ontology (GO) biological process gene sets significantly associated with these 500 upregulated genes was assessed using Gene Set Enrichment Analysis (GSEA). Significance was determined using an uncorrected p-value and a q-value (a p-value adjusted using the Benjamini-Hochberg False Discovery Rate (FDR) approach) to correct for multiple testing.

The top 25 significantly upregulated genes in the spheroid-matrix interaction for both DAOY and ONS76 samples are shown in Table 6.6. 13 out of 25 genes were shared across the cell lines. Interestingly, *IGF2* (Insulin-Like Growth Factor 2), *INS* (Insulin), and *INS-IGF2* (INS-IGF2 readthrough) had the highest FPKM values in spheroids on a HA matrix (DAOY: 11454.9; ONS76: 14955.6). This corresponded to Log2 expression fold changes of 12.41 (DAOY) and 12.06 (ONS76). We were therefore interested in the role *IGF2/INS* in SHH medulloblastoma tumours.

Table 6.6 Top 25 genes most significantly upregulated in the spheroid-matrix interaction

Differential gene expression analysis of the mRNA NGS datasets was conducted within the DAOY (**A**) and ONS76 (**B**) cell lines. Genes were ordered based on their significance (Log2 fold change). Highlighted genes were shared by both cell lines. Significance was determined using an uncorrected p-value and a q-value (a p-value adjusted using the Benjamini-Hochberg False Discovery Rate (FDR) approach) to correct for multiple testing.

A DAOY

Gene	FPKM value spheroid no matrix	FPKM value spheroid HA matrix	Log2 fold change	p-value	FDR q-value
RIIAD1	0.007999	58.8304	12.8444	0.0025	0.011571
IGF2,INS,INS-IGF2	2.10241	11454.9	12.4116	5.00E-05	0.00042
PLCH2	0.075939	365.839	12.2341	5.00E-05	0.00042
XIST	0.014302	50.3334	11.7811	5.00E-05	0.00042
MT3	0.531721	1738.33	11.6747	5.00E-05	0.00042
GUCY1B2	0.150969	445.195	11.526	5.00E-05	0.00042
ADAM33	0.103309	276.453	11.3859	5.00E-05	0.00042
ST8SIA3	0.016244	39.9735	11.2649	0.0005	0.003039
HES3	0.046875	82.9744	10.7896	0.0085	0.029939
GPR37L1	0.039631	68.6298	10.758	0.00535	0.02175
MIR135A2,RMST	0.324703	477.075	10.5209	5.00E-05	0.00042
CACNA1I	0.034671	48.9876	10.4645	5.00E-05	0.00042
ADAMTSL2	0.054824	75.6184	10.4297	0.00025	0.001691
CACNA1H	0.558034	705.121	10.3033	5.00E-05	0.00042
PCP4L1	0.180838	201.506	10.1219	0.0001	0.000779
GALNT9	0.058966	61.9472	10.0369	0.00015	0.001109
ZBBX	0.082989	81.9774	9.94809	5.00E-05	0.00042
CELF3	0.084916	73.5686	9.75884	5.00E-05	0.00042
VWA3A	0.191517	158.523	9.69301	5.00E-05	0.00042
WI2-1959D15.1	0.103277	84.1103	9.66962	5.00E-05	0.00042
FOXJ1	0.122219	98.0669	9.64815	0.00795	0.028983
KCNQ2	0.209231	162.181	9.5983	5.00E-05	0.00042
AEBP1	0.142717	108.266	9.56721	5.00E-05	0.00042
CLU	14.3095	10348.9	9.49829	5.00E-05	0.00042
NOTUM	0.348746	243.408	9.44698	5.00E-05	0.00042

B ONS76

Gene	FPKM value spheroid no matrix	FPKM value spheroid HA matrix	Log2 fold change	p-value	FDR q-value
ADAM33	0.034824	295.27	13.0496	0.00065	0.001916
IGF2,INS,INS-IGF2	3.49655	14955.6	12.0625	5.00E-05	0.00017
CACNA1H	0.371129	1296.38	11.7703	5.00E-05	0.00017
LCNL1,PTGDS	0.352569	1193.36	11.7248	5.00E-05	0.00017
PLCH2	0.116447	365.795	11.6171	5.00E-05	0.00017
MT3	0.259505	667.785	11.3294	0.00225	0.006061
ADAMTSL2	0.036962	86.2129	11.1876	0.0096	0.021983
GUCY1B2	0.327787	644.772	10.9418	5.00E-05	0.00017
AEBP1	0.079485	142.43	10.8073	0.0001	0.000332
ATP1A2	0.02105	33.0516	10.6167	0.0013	0.003666
CACNA1I	0.024161	35.4145	10.5175	5.00E-05	0.00017
ACAN	0.040908	54.5073	10.3798	0.0001	0.000332
MEGF6	0.33634	405.046	10.2339	5.00E-05	0.00017
MIR135A2,RMST	0.104127	117.312	10.1378	0.00235	0.006312
STAB1	0.049012	48.2962	9.94455	0.00505	0.012494
VWF	0.086062	77.3393	9.81161	5.00E-05	0.00017
KNDC1	0.143885	126.543	9.78049	0.0041	0.010307
WI2-1959D15.1	0.112828	97.0701	9.74876	5.00E-05	0.00017
SLC6A1	0.047129	35.0882	9.54015	0.00055	0.001636
ADAMTSL4,AL356356.1	0.913221	603.672	9.36859	5.00E-05	0.00017
PCP4L1	0.247201	160.382	9.34161	5.00E-05	0.00017
SOX8	0.14263	91.3918	9.32365	5.00E-05	0.00017
CHD5	0.793316	507.836	9.32225	5.00E-05	0.00017
GFAP	3.71142	2184.68	9.20123	5.00E-05	0.00017
KCNQ2	0.139263	73.6503	9.04674	5.00E-05	0.00017

The R2 Genomics Analysis and Visualization Platform was used to analyse patient datasets for the expression of *IGF2/INS* (Figure 6.10). Significant differences in gene expression compared to the SHH subgroup were calculated using the Kruskal-Wallis test with Dunn's multiple comparisons post-hoc test.

The MegaSampler function assessed *IGF2/INS* gene expression in two datasets: Roth and Pfister. Roth consisted of cerebellum samples (n=9) and served as normal control against the medulloblastoma samples in the Pfister dataset which were categorised into the molecular subgroups (WNT: n=17; SHH: n=59; Group 3: n=56; Group 4: n=91). Expression of *IGF2/INS* was significantly higher in SHH medulloblastoma samples compared to the other three molecular subgroups and higher, but not significantly different, to normal cerebellum (Figure 6.10A; ****p≤0.0001).

Gene expression was also assessed in the Cavalli dataset. *IGF2/INS* expression was significantly higher in the SHH subgroup compared to WNT, Group 3, and Group 4 medulloblastoma samples (Figure 6.10B; ****p≤0.0001), validating the findings in the Pfister dataset. Further analysis in the SHH subgroup showed that there was no difference in *IGF2/INS* expression across the four subtypes (α, β, γ, and δ; Figure 6.10C), indicating that elevated expression is not restricted to particular SHH phenotypes, but is a general characteristic of this subgroup of tumours. We also analysed whether *IGF2/INS* expression differed depending on the metastatic status of SHH tumours. There was no difference in expression level between non-metastatic (M0) and metastatic (M+) tumours, again indicating that high expression is a general feature of SHH tumours (Figure 6.10D).

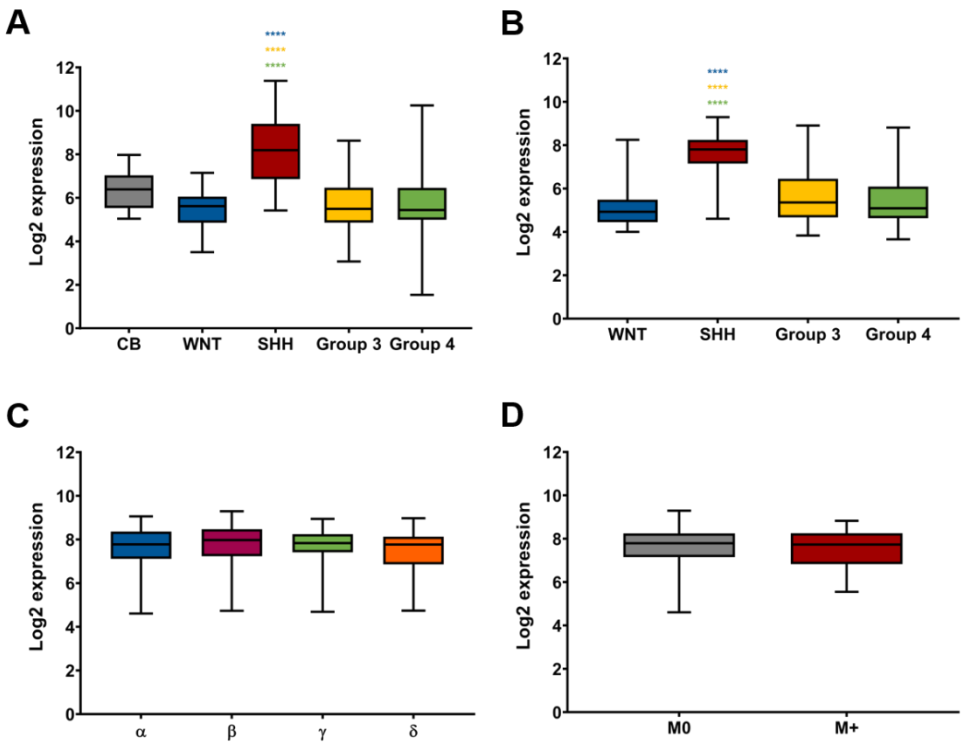


Figure 6.10 ***IGF2/INS*** **gene expression in medulloblastoma patient samples**
Gene expression (Log2) of *IGF2/INS* was assessed on the R2 Genomics Analysis and Visualisation Platform. (**A**) The MegaSampler function was used to assess gene expression in two datasets: Roth (normal cerebellum (CB); n=9) and Pfister (medulloblastoma subgroups; WNT: n=17; SHH: n=59; Group 3: n=56; Group 4: n=91). (**B**) Gene expression across the four medulloblastoma subgroups (WNT: n=70; SHH: n=223; Group 3: n=144; Group 4: n=326) was assessed in the Cavalli dataset. (**C**) Gene expression was also assessed in SHH patients in the Cavalli dataset which were categorised into four subtypes (α: n=65; β: n=35; γ: n=47; δ: n=76). (**D**) Gene expression of non-metastatic (M0: n=134) and metastatic (M+: n=26) SHH tumours was assessed using the Cavalli dataset. Box and whisker plots display the median and interquartile range (25^{th} and 75^{th} percentiles) and the error bars represent the minimum and maximum values in each dataset. Significant differences in gene expression compared to the SHH subgroup were calculated using the Kruskal-Wallis test with Dunn's multiple comparisons post-hoc test. Differences are represented by coloured asterisks of the corresponding subgroup (WNT: blue; Group 3: yellow; Group 4: green; ****p≤0.0001).

6.4.3 Laminin has limited effects on spheroid-matrix interactions

Differential gene expression analysis of the spheroid-matrix interaction established that cell cycle processes were downregulated and migratory behaviours were upregulated in spheroids on HA compared to spheroids on no matrix. Following on from this, we wanted to assess the effect of the ECM component LAM in the spheroids on a HA matrix. To investigate the influence of LAM, unsupervised analysis was conducted of the top 500 most significantly differentially expressed genes between spheroids on a HA matrix versus spheroids on a HA+LAM matrix. Hierarchical clustering of the “spheroid HA matrix” and “spheroid HA+LAM matrix” samples is displayed in Figure 6.11. The heatmap shows that samples from both cell lines and culture conditions clustered randomly.

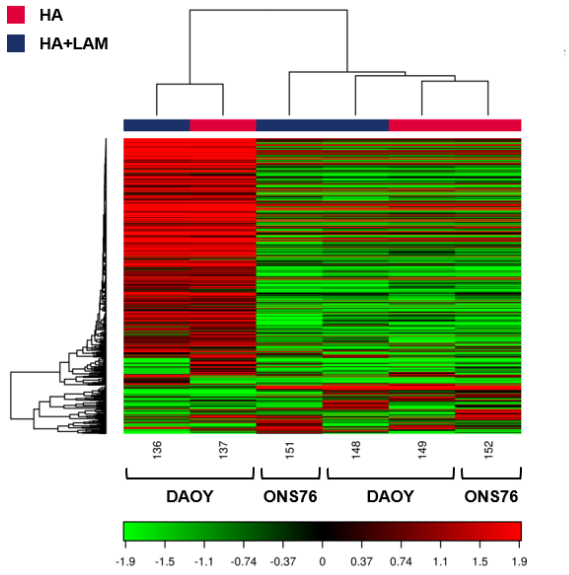
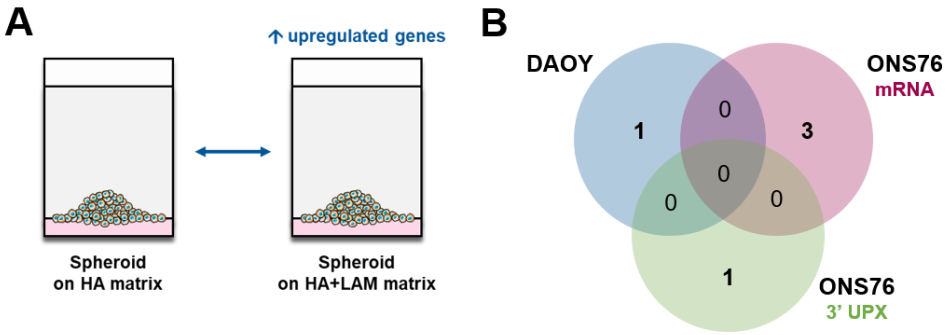


Figure 6.11 Clustering of “spheroid HA matrix” and “spheroid HA+LAM matrix” samples

Heatmap of the hierarchical clustering of the top 500 most significantly differentially expressed genes between spheroids on a hyaluronan (HA) matrix (red) and spheroids on a HA and laminin (LAM) matrix (blue) identified by mRNA NGS analyses. Each row represented one gene and individual samples were displayed in columns. The colour scale signified the relative expression level of a transcript across all samples. Expression levels above and below the mean were depicted by the colours red and green, respectively.

Figure 6.12A summarises the comparison used to identify upregulated genes in spheroids on a HA+LAM matrix, compared to a HA only matrix. Significantly differentially expressed genes were filtered based on their fold change (Log2 ≥2) and FPKM or UMI mean count (≥15). No differentially expressed genes were shared between the DAOY and ONS76 cell lines for either mRNA or 3' UPX NGS methods (Figure 6.12B). The genes identified as being significantly upregulated on HA+LAM in DAOY (*STIM1*), ONS76 mRNA (*TCERG1L*, *TWIST1*, *DLK1*), and ONS76 3' (*SLC1A5*) samples are detailed in Figure 6.12C. GSEA was not performed due to the small gene list.



C **DAOY**

Gene	FPKM value spheroid HA matrix	FPKM value spheroid HA+LAM matrix	Log2 fold change	p-value	FDR q-value
STIM1	33.0487	159.768	2.27332	5.00E-05	0.022575

ONS76 mRNA

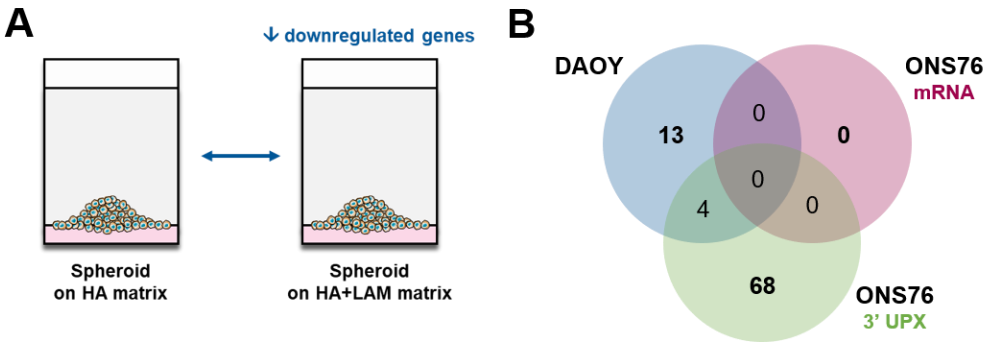
Gene	FPKM value spheroid HA matrix	FPKM value spheroid HA+LAM matrix	Log2 fold change	p-value	FDR q-value
TCERG1L	7.09073	19.7609	1.47864	5.00E-05	0.049142
TWIST1	19.3582	46.0427	1.25003	5.00E-05	0.049142
DLK1	25.0525	50.9374	1.02377	5.00E-05	0.049142

ONS76 3' UPX

Gene	Mean counts	Log2 fold change	p-value
SLC1A5	20.21	1.12	2.66E-02

Figure 6.12 Genes upregulated in spheroids on a HA+LAM matrix
Differential gene expression analysis was conducted to identify upregulated genes in spheroids on a hyaluronan (HA) and laminin (LAM) matrix compared to HA alone. (**A**) Schematic diagram showing the spheroid-matrix interaction assessed. (**B**) Venn diagram showing that no differentially expressed genes were shared between the DAOY and ONS76 cell lines for method of next-generation sequencing (mRNA or 3' UPX). (**C**) *STIM1*, *TCERG1L*, *TWIST1*, *DLK1*, and *SLC1A5* were identified as being significantly upregulated in spheroids on a HA+LAM matrix.

Figure 6.13A summarises the comparison used to identify downregulated genes in spheroids on a HA+LAM matrix, compared to a HA only matrix. There were only a limited number of genes significantly downregulated (Figure 6.13B) in DAOY and ONS76 3' UPX samples. The four genes which overlapped were *CHI3L2*, *LGI4*, *LTF*, and *MECOM* (Figure 6.13C).



C

Gene		Function of encoded protein
CHI3L2 (*YKL-39*)	Chitinase 3 Like 2	Lectin that binds chitooligosaccharides and other glycans with high affinity
LGI4	Leucine-Rich Glioma-Inactivated Protein 4	Promotes the proliferation and differentiation of glial lineage cells
LTF	Lactotransferrin	Regulation of cellular growth and differentiation and protection against cancer development and metastasis
MECOM	MDS1 And EVI1 Complex Locus	Transcriptional regulator and oncoprotein involved in apoptosis, cell differentiation and proliferation

Figure 6.13 Genes downregulated in spheroids on a HA+LAM matrix
Differential gene expression analysis was conducted to identify downregulated genes in spheroids on a hyaluronan (HA) and laminin (LAM) matrix compared to HA alone. (**A**) Schematic diagram showing the spheroid-matrix interaction assessed. (**B**) Venn diagram showing that 4 genes were shared between the DAOY and ONS76 3' UPX lists, but no genes were identified by ONS65 mRNA analysis. (**C**) *CHI3L2*, *LGI4*, *LTF*, and *MECOM* genes were shared between cell lines.

6.5 Understanding processes involved in SHH medulloblastoma metastasis

As previously discussed in section 6.2, the incorporation of LAM into HA hydrogels was required for single cells to form multiple nodules on the matrix surface. We therefore chose to assess this HA+LAM model in particular to understand the processes involved in SHH medulloblastoma metastasis. Unsupervised analysis was conducted of the top 500 most significantly differentially expressed genes between spheroid versus single cell samples spheroids on either a HA matrix (Figure 6.14A) or HA+LAM matrix (Figure 6.14B). Hierarchical clustering showed that spheroid and single cell samples clustered separately for both matrix conditions.

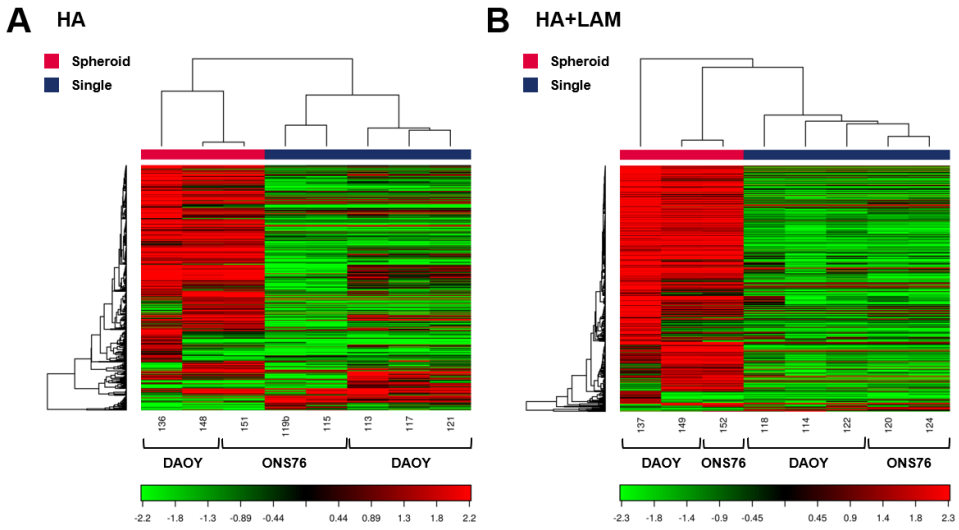


Figure 6.14 Clustering of spheroid and single cell samples on HA and HA+LAM matrices

(**A**) Heatmap of the hierarchical clustering of the top 500 most significantly differentially expressed genes between spheroids (red) and single cells (blue) on a hyaluronan (HA) matrix identified by mRNA NGS analyses. (**B**) Heatmap of the hierarchical clustering of the top 500 most significantly differentially expressed genes between spheroids (red) and single cells (blue) on a HA and laminin (LAM) matrix. Each row represented one gene and individual samples were displayed in columns. The colour scale signified the relative expression level of a transcript across all samples. Expression levels above and below the mean were depicted by the colours red and green, respectively

6.5.1 Cell dissemination is driven by cytoskeletal changes

A summary of the comparison used to identify genes and pathways required for cell dissemination from the primary SHH medulloblastoma tumour is shown in Figure 6.15A. Differential gene expression analysis was conducted to identify significantly upregulated genes in spheroids compared to single cells on either a HA (Figure 6.15A(i)) or HA+LAM matrix (Figure 6.15A(ii)). Significantly differentially expressed genes were filtered based on fold change (Log2 ≥2) and FPKM value (≥20). Analysis within cell lines showed that on a HA matrix, there were 564 significantly upregulated genes in DAOY samples and 934 genes for ONS76 samples. Comparison of these gene lists showed that were 369 significantly upregulated genes shared between the cell lines (Figure 6.15B(i)). On a HA+LAM matrix, there were 962 significantly upregulated genes in DAOY samples and 980 genes for ONS76 samples. When these gene lists were compared, there were 658 overlapping genes shared between the cell lines (Figure 6.15B(ii)).

In order to identify LAM-specific genes that contributed to cell dissemination, we compared the shared lists of genes upregulated in spheroids compared to single cells on both the HA and HA+LAM matrices. As shown in Figure 6.15C, when the HA background was removed, there were 325 LAM-specific genes identified for their involvement in cell dissemination in the SHH medulloblastoma metastasis model. GSEA of these 325 LAM-specific genes was performed and revealed significant overlaps with GO biological process gene sets associated with cell movement (Table 6.7A), including ‘cell projection organisation’ (GO: 0030030), ‘microtubule-based process’ (GO: 0007017), ‘microtubule-based movement’ (GO: 0007018), and ‘cell projection assembly’ (GO: 0030031). Gene sets overlapping with the Pathway Interaction Database (PID; Schaefer *et al.*, 2009) were also assessed. Pathways associated with LAM-specific upregulation of spheroid cell dissemination included the ATF2, IL12 and CXCR4 pathways (Table 6.7B).

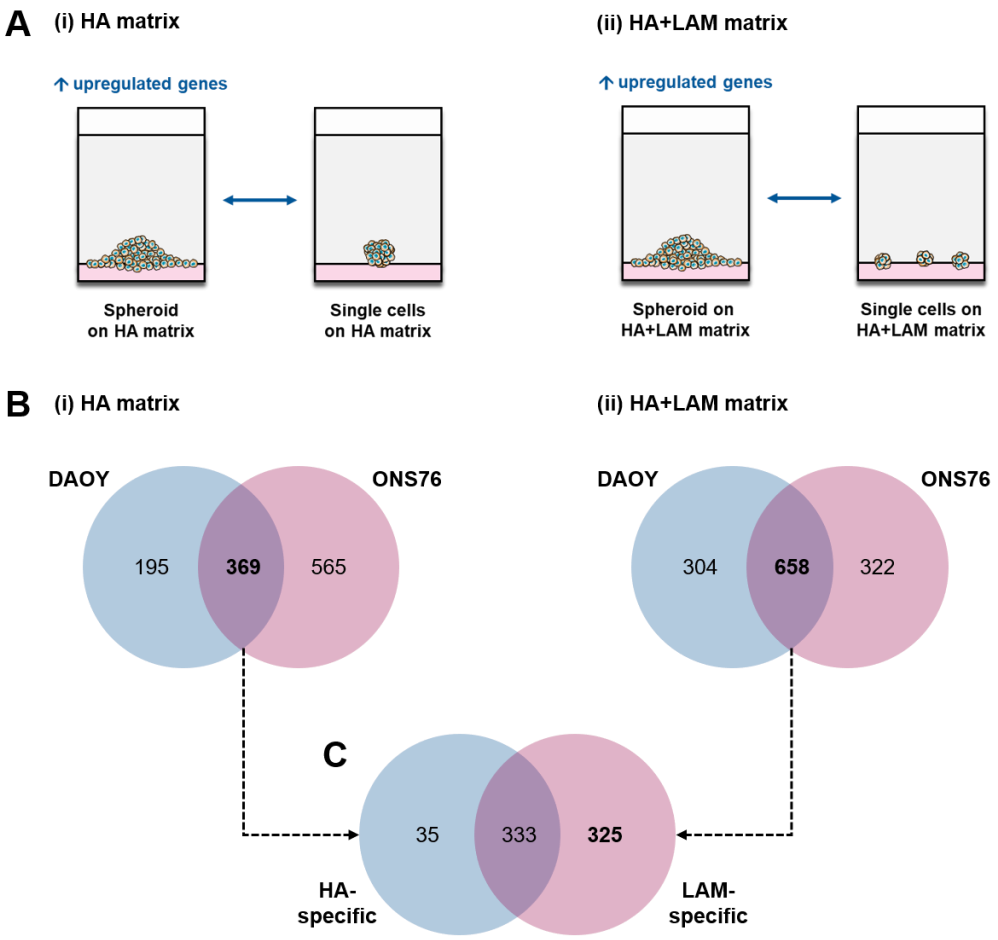


Figure 6.15 Genes upregulated during cell dissemination of SHH medulloblastoma
Differential gene expression analysis was conducted to identify significantly upregulated genes in spheroids compared to single cells on either a hyaluronan (HA) (**i**) or HA and laminin (LAM) (**ii**) matrix. (**A**) Schematic diagram showing the interactions assessed. (**B**) Venn diagrams showing the number of genes shared between cell lines for each comparison (Log2 fold change ≥2). (**C**) The overlapping gene lists were compared. When the HA background was removed, there were 325 LAM-specific genes.

Table 6.7 Gene set enrichment analysis of genes upregulated during cell dissemination of SHH medulloblastoma

Gene set enrichment analysis (GSEA) was used to identify gene sets significantly associated with the 325 laminin (LAM) specific genes identified for their involvement in cell dissemination in the SHH medulloblastoma metastasis model. (**A**) Top 10 Gene Ontology (GO) biological process gene sets associated with the LAM-specific cell dissemination phenotype. (**B**) 6 Pathway Interaction Database (PID) pathways were also identified using GSEA. Significance was determined using an uncorrected p-value and a q-value (a p-value adjusted using the Benjamini-Hochberg False Discovery Rate (FDR) approach) to correct for multiple testing.

A

Gene set name	Number of genes in overlap	p-value	FDR q-value
Cell projection organisation (GO:0030030)	55	$5.25\ e^{-25}$	$3.86\ e^{-21}$
Microtubule-based process (GO:0007017)	35	$9.49\ e^{-20}$	$3.49\ e^{-16}$
Cilium organisation (GO:0044782)	25	$7.44\ e^{-18}$	$1.82\ e^{-14}$
Microtubule-based movement (GO:0007018)	22	$2.21\ e^{-17}$	$4.06\ e^{-14}$
Cell projection assembly (GO:0030031)	28	$1.52\ e^{-16}$	$2.24\ e^{-13}$
Positive regulation of developmental process (GO:0051094)	41	$2.44\ e^{-15}$	$2.99\ e^{-12}$
Positive regulation of cell differentiation (GO:0045597)	34	$5.02\ e^{-15}$	$5.27\ e^{-12}$
Cilium movement (GO:0003341)	12	$1.60\ e^{-14}$	$1.47\ e^{-11}$
Axoneme assembly (GO:0035082)	11	$2.66\ e^{-13}$	$2.17\ e^{-10}$
Microtubule bundle formation (GO:0001578)	12	$8.19\ e^{-13}$	$6.02e^{-10}$

B

Gene set name	Genes in overlap	p-value	FDR q-value
ATF2 pathway	*FOS*, *CCND1*, *DUSP1*, *JUND*, *POU2F1*, *SOCS3*	$2.63\ e^{-6}$	$5.15\ e^{-4}$
IL12 pathway	*FOS*, *HLA-DRA*, *HLA-DRB1*, *RELA*, *GADD45G*	$6.2\ e^{-5}$	$6.07\ e^{-3}$
CXCR4 pathway	*HLA-DRA*, *HLA-DRB1*, *GNAZ*, *CXCR4*, *RGS1*	$5.7\ e^{-4}$	$3.72\ e^{-2}$
AVB3 OPN pathway	*FOS*, *RELA*, *SPP1*	$1.11\ e^{-3}$	$4.37\ e^{-2}$
AP1 pathway	*FOS*, *CCND1*, *DUSP1*, *JUND*	$1.21\ e^{-3}$	$4.37\ e^{-2}$
IL12-STAT4 pathway	*FOS*, *HLA-DRA*, *HLA-DRB1*	$1.34\ e^{-3}$	$4.37\ e^{-2}$

6.5.2 Metastasis-related pathways are upregulated in nodular metastases

In order to identify the genes and pathways required for the formation of nodular metastases during SHH medulloblastoma metastasis, we conducted differential gene expression analysis to identify significantly upregulated genes in single cells compared to spheroids on either a HA (Figure 6.16A(i)) or HA+LAM matrix (Figure 6.16A(ii)). Significantly differentially expressed genes were filtered based on fold change (Log2 ≥2) and FPKM value (≥20). Analysis within cell lines showed that on a HA matrix, there were 478 significantly upregulated genes in DAOY samples and 968 genes for ONS76 samples. When these gene lists were compared, there were 356 overlapping genes shared between the cell lines (Figure 6.16B(i)). On a HA+LAM matrix, there were 741 significantly upregulated genes in DAOY samples and 817 genes for ONS76 samples. Comparison of these gene lists showed that were 488 significantly upregulated genes shared between the cell lines (Figure 6.16B(ii)).

To identify the LAM-specific genes involved in formation of nodular metastases during SHH medulloblastoma metastasis, we compared these shared lists of genes upregulated in single cells compared to spheroids on both the HA and HA+LAM matrices. Following removal of the HA background, we identified 186 LAM-specific genes (Figure 6.16C). GSEA of these LAM-specific genes revealed significant overlaps with a variety of GO biological process gene sets (Table 6.8A). Gene set overlaps with the PID were also assessed. Pathways previously reported as being involved in cancer metastasis, including the HIF1, MAPK and TNF pathways, are associated with LAM-specific formation of nodular metastases (Table 6.8B).

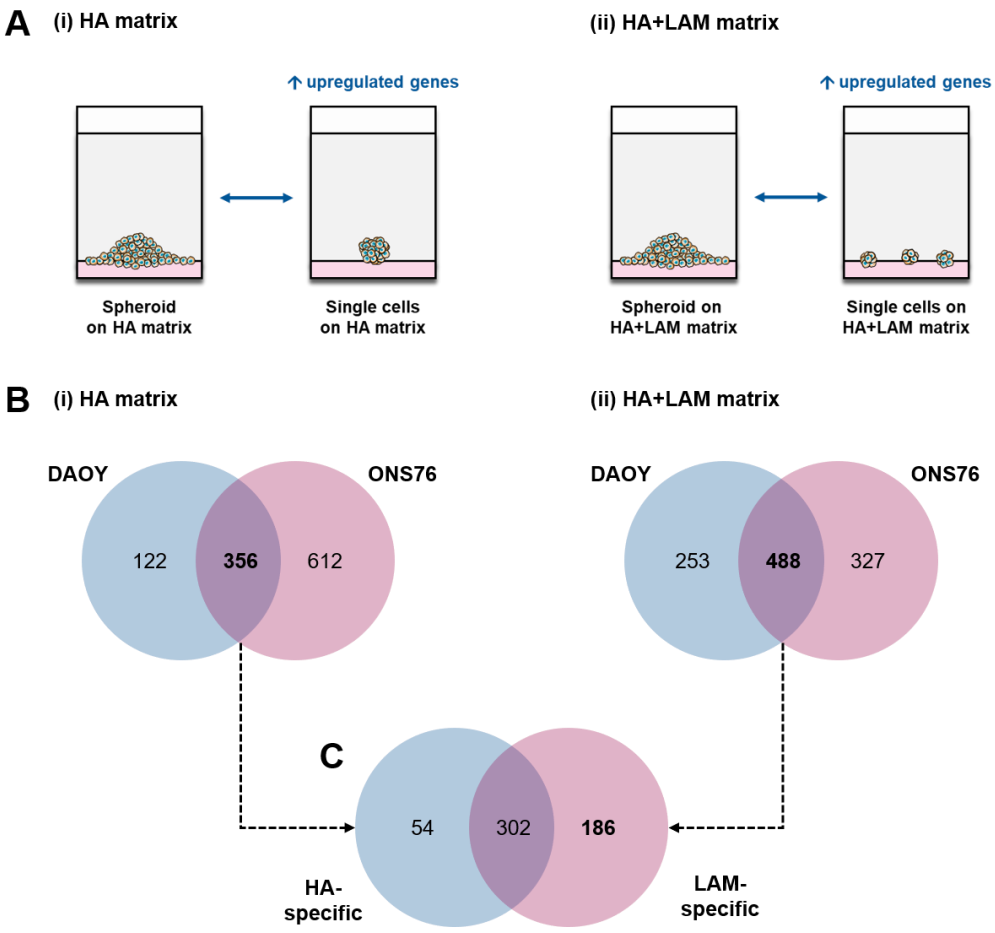


Figure 6.16 Genes upregulated during the formation of SHH medulloblastoma nodular metastases

Differential gene expression analysis was conducted to identify significantly upregulated genes in single cells compared spheroids to on either a hyaluronan (HA) (**i**) or HA and laminin (LAM) (**ii**) matrix. (**A**) Schematic diagram showing the interactions assessed. (**B**) Venn diagrams showing the number of genes shared between cell lines for each comparison (Log2 fold change ≥2). (**C**) The overlapping gene lists were compared. When the HA background was removed, there were 186 LAM-specific genes.

Table 6.8 Gene set enrichment analysis of genes upregulated during the formation of SHH medulloblastoma nodular metastases

Gene set enrichment analysis (GSEA) was used to identify gene sets significantly associated with the 186 laminin (LAM) specific genes identified for their involvement in the formation of nodular metastases in the SHH medulloblastoma metastasis model. (**A**) Top 10 Gene Ontology (GO) biological process gene sets associated with the LAM-specific nodular metastasis phenotype. (**B**) 6 Pathway Interaction Database (PID) pathways were also identified using GSEA. Significance was determined using an uncorrected p-value and a q-value (a p-value adjusted using the Benjamini-Hochberg False Discovery Rate (FDR) approach) to correct for multiple testing.

A

Gene set name	Number of genes in overlap	p-value	FDR q-value
Negative regulation of response to stimulus (GO:0048585)	27	$2.34\ e^{-10}$	$1.72\ e^{-6}$
Response to abiotic stimulus (GO:0009628)	22	$2.41\ e^{-9}$	$8.87\ e^{-6}$
Secretion (GO:0046903)	25	$4.43\ e^{-9}$	$1.08\ e^{-5}$
Defence response (GO:0006952)	25	$1.02\ e^{-8}$	$1.88\ e^{-5}$
Gland development (GO:0048732)	13	$1.70\ e^{-8}$	$2.50\ e^{-5}$
Negative regulation of signalling (GO:0023057)	22	$2.27\ e^{-8}$	$2.78\ e^{-5}$
Response to oxygen containing compound (GO:1901700)	23	$6.89\ e^{-8}$	$7.24\ e^{-5}$
Response to drug (GO:0042493)	18	$8.92\ e^{-8}$	$8.20\ e^{-5}$
Regulation of anatomical structure (GO:0022603)	19	$1.14\ e^{-7}$	$9.31\ e^{-5}$
Negative regulation of apoptotic signalling pathway (GO:2001234)	9	$2.46\ e^{-7}$	$1.81\ e^{-4}$

B

Gene set name	Genes in overlap	p-value	FDR q-value
HIF1-TF pathway	*CREB1*, *HDAC7*, *HIF1A*, *PKM*, *BHLHE41*	$5.76\ e^{-6}$	$1.13\ e^{-3}$
MAPK-TRK pathway	*CREB1*, *ELK1*, *NRAS*	$3.03\ e^{-4}$	$2.41\ e^{-2}$
p38-αβ downstream pathway	*CREB1*, *ELK4*, *ATF6*	$4.22\ e^{-4}$	$2.41\ e^{-2}$
FOXM1 pathway	*ETV5*, *GAS1*, *NEK2*	$4.92\ e^{-4}$	$2.41\ e^{-2}$
ERBB1 downstream pathway	*CREB1*, *ELK1*, *NRAS*	$7.35\ e^{-4}$	$2.43\ e^{-2}$
TNF pathway	*TNFRSF1A*, *CASP8*, *TNFAIP3*	$7.43\ e^{-4}$	$2.43\ e^{-2}$
TCR-RAS pathway	*ELK1*, *NRAS*	$1.29\ e^{-3}$	$3.61\ e^{-2}$
MYC repression pathway	*CREB1*, *WNT5A*, *CSDE1*	$1.85\ e^{-3}$	$4.54\ e^{-2}$
HDAC Class I pathway	*HDAC7*, *TNFRSF1A*, *WDR77*	$2.12\ e^{-3}$	$4.61\ e^{-2}$
HIF1-α pathway	*HIF1A*, *HIF1AN*	$2.39\ e^{-3}$	$4.68\ e^{-2}$

6.5.3 RhoA-associated pathways are involved in both cell dissemination and nodular formation models of SHH medulloblastoma metastasis

Differential gene expression analysis of spheroid and single cell models of SHH medulloblastoma metastasis has allowed us to identify gene sets and pathways related to two stages of metastatic spread: cell dissemination from the primary tumour and the formation of nodular metastases. However, the involvement of LAM in both of these processes prompted us to investigate the broader role of this ECM protein in SHH medulloblastoma metastasis. In order to do this, we aimed to identify the general LAM-related genes and pathways shared between both spheroid and single cell models. Summaries of the comparisons made are shown in Figure 6.17A. Firstly, we filtered genes with FPKM values of ≥20 and selected the genes for which there was no significant difference in expression between both the DAOY and ONS76 samples. This enabled us to identify genes which were commonly expressed in both cell lines. There were 4035 non-significant genes shared between both cell lines on a HA matrix (Figure 6.17B(i)) and 3184 genes shared on a HA+LAM matrix (Figure 6.17B(ii)). When these gene lists were compared, there were 399 genes which were specific for LAM when the HA background was taken away (Figure 6.17C). GSEA of these 399 genes using the PID identified RhoA-associated pathways to be involved in general LAM metastatic processes (Table 6.9).

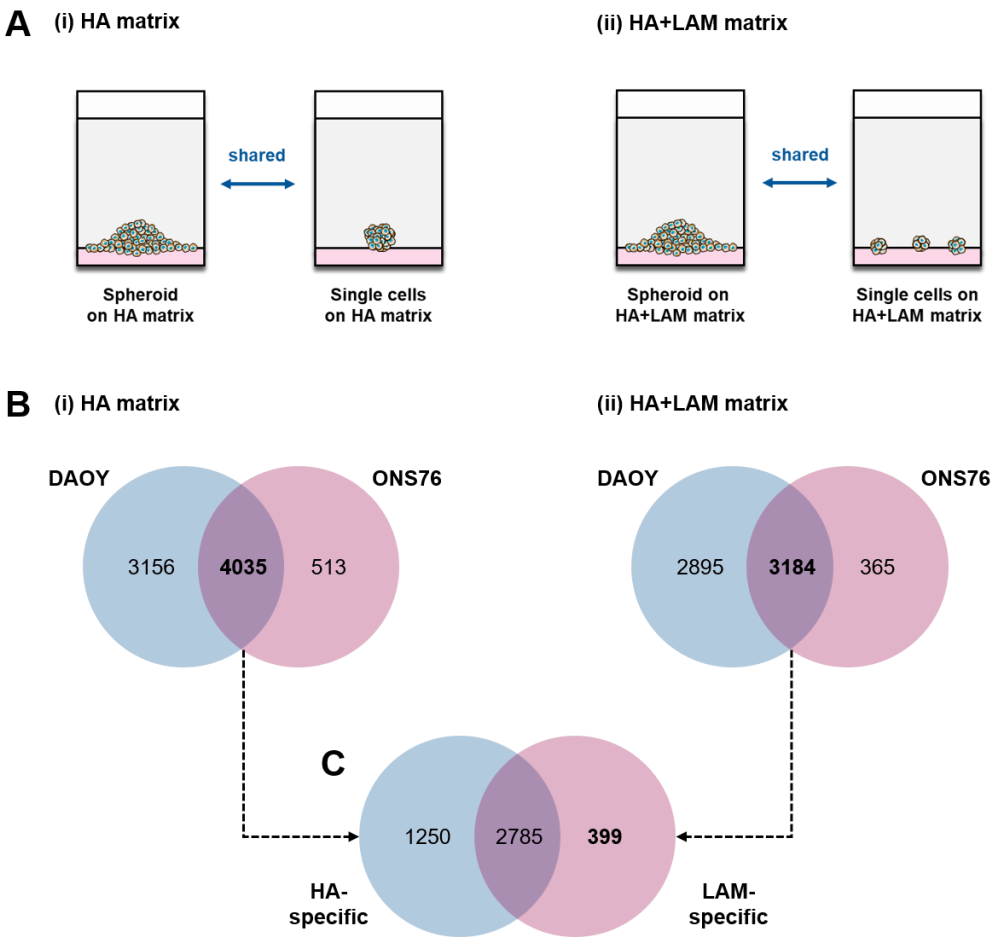


Figure 6.17 LAM-specific genes shared across SHH medulloblastoma metastatic stages

Differential gene expression analysis was conducted to identify genes shared between spheroids and single cells on either a hyaluronan (HA) (**i**) or HA and laminin (LAM) (**ii**) matrix. (**A**) Schematic diagram showing the interactions assessed. (**B**) Venn diagrams showing the number of overlapping shared genes for each comparison. (**C**) The overlapping gene lists were compared. When the HA background was removed, there were 399 LAM-specific genes.

Table 6.9 Gene set enrichment analysis of LAM-specific genes shared across SHH medulloblastoma metastatic stages

Gene set enrichment analysis (GSEA) was used to identify gene sets significantly associated with the 399 laminin (LAM) specific genes identified for their involvement across SHH medulloblastoma metastasis models. The top 10 Pathway Interaction Database (PID) pathways associated with the LAM-specific metastatic phenotype are displayed. (Significance was determined using an uncorrected p-value and a q-value (a p-value adjusted using the Benjamini-Hochberg False Discovery Rate (FDR) approach) to correct for multiple testing.

Gene set name	Genes in overlap	p-value	FDR q-value
FAK pathway	*RHOA*, *BCAR1*, *PTK2*, *PXN*, *MAPK8*, *ARHGEF11*	$5.52\ e^{-6}$	$1.06\ e^{-3}$
RET pathway	*RHOA*, *BCAR1*, *PTK2*, *PXN*, *MAPK8*	$1.08\ e^{-5}$	$1.06\ e^{-3}$
AVB3 integrin pathway	*RHOA*, *BCAR1*, *PTK2*, *PXN*, *MFGE8*, *COL9A2*	$2.07\ e^{-5}$	$1.35\ e^{-3}$
MET pathway	*RHOA*, *BCAR1*, *PTK2*, *PXN*, *MAPK8*, *CDC42*	$3\ e^{-5}$	$1.47\ e^{-3}$
PDGFRB pathway	*RHOA*, *BCAR1*, *MAPK8*, *STAT5B*, *YWHAG*, *YWHAH*, *PPP2CA*	$5.77\ e^{-5}$	$2.26\ e^{-3}$
AVB3 OPN pathway	*RHOA*, *BCAR1*, *MAPK8*, *CDC42*	$8.37\ e^{-5}$	$2.6\ e^{-3}$
Netrin pathway	*RHOA*, *BCAR1*, *PTK2*, *CDC42*	$9.51\ e^{-5}$	$2.6\ e^{-3}$
N-cadherin pathway	*RHOA*, *MAPK8*, *CDC42*	$1.08\ e^{-4}$	$2.6\ e^{-3}$
CXCR4 pathway	*RHOA*, *BCAR1*, *PTK2*, *PXN*, *CDC42*, *STAT5B*	$1.19\ e^{-4}$	$2.6\ e^{-3}$
MTOR pathway	*RHOA*, *PXN*, *YWHAG*, *YWHAH*, *ULK1*	$1.76\ e^{-4}$	$2.92\ e^{-3}$

We then utilised the R2 Genomics Analysis and Visualization Platform to assess the expression of *RHOA* in patient datasets (Figure 6.18). Significant differences in gene expression compared to the SHH subgroup were calculated using the Kruskal-Wallis test with Dunn's multiple comparisons post-hoc test.

RHOA expression was firstly analysed in the Roth and Pfister datasets. We found that *RHOA* expression was significantly higher in SHH tumours compared to normal cerebellum (**p≤0.01) and Group 4 tumours (****p≤0.0001), but similar to WNT and Group 3 medulloblastomas (Figure 6.18A). We also assessed gene expression using the Cavalli dataset, which validated the Pfister analysis, as *RHOA* expression was shown to be higher in the SHH subgroup compared to Group 4 (Figure 6.18B; ****p≤0.0001). We also found that *RHOA* expression was significantly higher in WNT tumours compared to SHH medulloblastomas (Figure 6.18B; ****p≤0.0001). Further analysis within the SHH subgroup in the Cavalli dataset showed that there was no difference in *RHOA* expression across the four subtypes (α, β, γ, and δ; Figure 6.18C). There was also no difference in *RHOA* expression between non-metastatic and metastatic SHH tumours (Figure 6.18D).

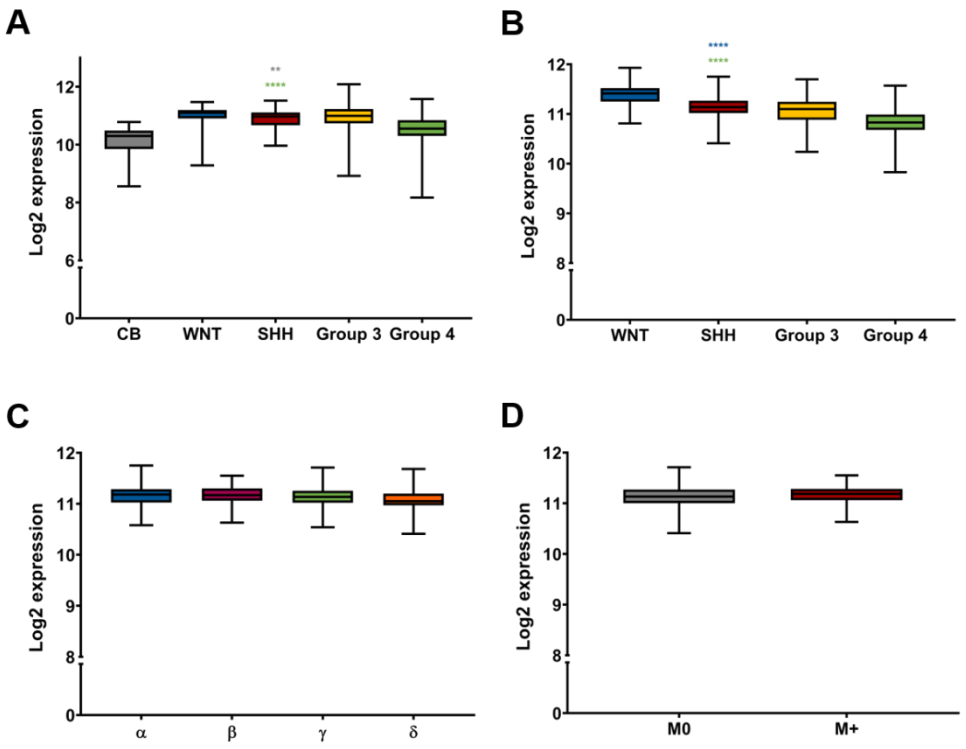


Figure 6.18 *RHOA* gene expression in medulloblastoma patient samples
Gene expression (Log2) of *RHOA* was assessed on the R2 Genomics Analysis and Visualisation Platform. (**A**) The MegaSampler function was used to assess gene expression in two datasets: Roth (normal cerebellum (CB); n=9) and Pfister (medulloblastoma subgroups; WNT: n=17; SHH: n=59; Group 3: n=56; Group 4: n=91). (**B**) Gene expression across the four medulloblastoma subgroups (WNT: n=70; SHH: n=223; Group 3: n=144; Group 4: n=326) was assessed in the Cavalli dataset. (**C**) Gene expression was also assessed in SHH patients in the Cavalli dataset which were categorised into four subtypes (α: n=65; β: n=35; γ: n=47; δ: n=76). (**D**) Gene expression of non-metastatic (M0: n=134) and metastatic (M+: n=26) SHH tumours was assessed using the Cavalli dataset. Box and whisker plots display the median and interquartile range (25th and 75th percentiles) and the error bars represent the minimum and maximum values in each dataset. Significant differences in gene expression compared to the SHH subgroup were calculated using the Kruskal-Wallis test with Dunn's multiple comparisons post-hoc test. Differences are represented by coloured asterisks of the corresponding subgroup (CB: grey; WNT: blue; Group 4: green; **p≤0.01, ****p≤0.0001).

6.6 Summary

- We modelled SHH medulloblastoma metastasis *in vitro* using HA hydrogels containing the ECM component LAM:
    - → Spheroid migration across the hydrogel matrices was used as a model of the initial cell dissemination from the primary tumour
    - → Seeding of single cells on the matrices modelled the formation of nodular metastases on the leptomeningeal surface.
- NGS technologies were used to study our SHH medulloblastoma metastasis models:
    - → Samples were successfully prepared and sequenced using two methods of NGS: mRNA and 3' UPX sequencing
    - → Although the alternative sequencing methods could not be compared on a singular gene level, broader comparisons could be made using gene set enrichment analysis.
- We investigated spheroid-matrix interactions and found that:
    - → Cell cycle genes were downregulated during spheroid migration
    - → Cell movement genes were upregulated during spheroid migration
    - → The addition of LAM to the HA matrix had very little effect on the ability of spheroids to adhere and disseminate.
- We used the HA+LAM model to understand the processes involved in SHH medulloblastoma metastasis:
    - → Cytoskeletal changes were associated with cell dissemination
    - → Metastasis-related pathways were upregulated in laminin-enriched single cell models of nodular formation
    - → RhoA-associated pathways were involved in both cell dissemination and nodular formation models of SHH medulloblastoma metastasis.

Chapter 7

Discussion

Chapter 7. Discussion

7.1 Introduction

Medulloblastoma is the most common malignant paediatric brain tumour, accounting for approximately 10% of cancer-related deaths in children (Pizer and Clifford, 2009). Although once regarded as a single tumour entity, it is now widely accepted that medulloblastoma tumours are heterogeneous. The most recent update to the WHO classification of CNS tumours classified medulloblastomas according to their histological and molecular characteristics (Louis *et al.*, 2016). Following an international consensus on the molecular classification of medulloblastoma, tumours are now categorised into one of four subgroups: WNT, SHH, Group 3, and Group 4 (Taylor *et al.*, 2012). These distinct subgroups are based on transcriptome and methylome profiling and differ in their clinical features, genetic profiles, and pathway signatures (Northcott, Jones, *et al.*, 2012). More recent studies have further stratified these molecular subgroups due to their intertumoral heterogeneity (Cavalli *et al.*, 2017). Risk stratification currently accounts for factors including patient age, metastatic status, and the extent of surgical resection. Risk stratification is important as it is linked to prognosis and outcome, and also designates the treatment regimens that patients receive. Patients with metastatic disease have a particularly poor outcome and currently, very little is known about the process of leptomeningeal dissemination, the most common route of metastasis for these tumours.

7.2 Establishment of a 3D *in vitro* model of medulloblastoma

In order to improve our understanding of medulloblastoma tumour biology and behaviour, it is important to study the disease in a suitable model system. Although *in vivo* models are considered superior models for cancer research, there are limitations to this method. Firstly, animal models are not available for all research groups due to their high costs and the required facilities. In addition, there may not be appropriate *in vivo* models available for some cancer types; for instance, there are a lack of suitable Group 4 medulloblastoma mouse models. Alternatively, studying tumour cells *in vitro* is a well-established technique that is readily accessible. The majority of *in vitro* experiments for medulloblastoma and other tumour types have been performed in 2D monolayer culture. Although reproducible and amenable for high throughput studies, there are many drawbacks to this culture method. For instance, 2D culture fails to recapitulate the multi-dimensional growth, physiological gradients, and cell-cell interactions that exist *in vivo* and in patient tumours. In addition, it has been shown that the genetic profile of a tumour changes *in vitro*, with 2D cultured medulloblastoma cell lines clustering together and not with patient tumours of the same subgroup in genome-wide analyses (Lin *et al.*, 2016).

3D *in vitro* culture techniques have been widely described over the past few decades. These cellular models more accurately reflect the spatial conformation of patient tumours, thus are considered more predictive models of tumour biology than conventional 2D culture methods. Although there are some publications where medulloblastoma has been studied in a 3D model (Zanini *et al.*, 2013; Ivanov *et al.*, 2014; Grotzer, Neve and Baumgartner, 2016), there is no well-established and widely-adopted 3D culture method for this tumour type.

This project aimed to respond to the need for a robust, reliable, and optimised 3D culture technique for the medulloblastoma research community. We hypothesised that medulloblastoma growth, drug response, and metastatic dissemination could

be modelled in 3D culture. In this study, we therefore aimed to optimise, validate, and characterise a 3D *in vitro* model of medulloblastoma that could be applied to study drug response and metastasis. As well as this, we aimed to identify factors involved in SHH medulloblastoma metastasis using the established 3D *in vitro* model through next-generation sequencing technologies.

7.2.1 Determining the appropriate 3D culture method

3D culture models can be broadly categorised into four types: gel/matrix-based models, spheroids, transwell-based models, and tumour-microvessels. When determining which of these 3D culture methods to adopt, we compiled a set of requirements for our *in vitro* medulloblastoma model. The overall aim of this study was to establish a 3D model that could be applied routinely in numerous functional assays, including the evaluation of growth kinetics, drug response analysis, and migration and invasion modelling. We therefore required a high-throughput model with the ability to study each of these processes, as well as standardised growth conditions across cell lines to allow direct comparisons. Spheroid culture, which involves the formation of single, uniform 3D structures, was chosen as the most suitable method for our needs as it has been widely used to study the techniques discussed.

There are numerous methods of spheroid generation, including spontaneous formation, hanging drops, suspension culture, scaffold-based models, and magnetic levitation. The decision regarding which technique to use is typically based on the requirements of the experiment. Suspension culture, either using a spinner flask or bioreactor, was excluded as the method produces aggregates of differing sizes making them not amenable to drug response analysis. Scaffold-based models and the magnetic levitation technique were also dismissed due to their high costs, making them unsuitable for high-throughput analyses. Although the hanging drop method generates single, uniform spheroids in each droplet and are

compatible with higher throughput functional assays, the small volumes used makes spheroid manipulation challenging. The spontaneous formation method, which utilises non-adherent surfaces to allow the formation of spheroids from single cells, was chosen as the ideal model for this study. This technique allows spheroid size to be accurately controlled by adjusting the cell seeding density and the tight regulation of such experimental parameters results in the generation of highly reproducible spheroids.

Although spheroid models have been used in cancer research for almost five decades (Sutherland, McCredie and Rodger, 1971), over that time period there have been vast improvements in the technique. Previously, the coating of cell culture plates with inert substances created a concave surface within the wells, prevented cellular attachment and resulted in the formation of cell aggregates. However, coating plates was a time consuming process and any irregularities in the coatings caused variation in spheroid size. These inconsistencies were problematic both in terms of spheroid imaging and lack of reproducibility. However, the use of ULA round-bottom plates has simplified the spontaneous spheroid formation technique. These plates have a covalently-bound hydrogel layer that effectively inhibits cellular attachment and promotes the formation of a single spheroid in each well. The innovative tumour spheroid modelling study by Vinci *et al.*, 2012 compared spheroids grown in ULA plates to those generated by the traditional agar-coated plate method. They found that spheroids generated by either technique were comparable but those generated in ULA plates were more suitable for imaging analysis due to their central location in each well. Therefore, the ULA plate method with a four day spheroid formation period for the establishment of cell-cell interactions and clear physiological gradients (as recommended by Friedrich *et al.*, 2009) was adopted for our study. This approach is advantageous as it is widely accessible to the medulloblastoma research community, as the only specialised equipment required is an ULA plate.

7.2.2 Cell line differences in the 3D spheroid model

Having determined the appropriate 3D culture technique, we began by testing numerous medulloblastoma cell lines for use in the spheroid model. As previously discussed, less than half of established medulloblastoma cell lines have been characterised based on molecular subgrouping (Ivanov *et al.*, 2016). We chose to use cell lines for which the clinical characteristics and molecular subgroup were known in order to elucidate subgroup-specific spheroid characteristics. In addition, these cell lines are already widely used for *in vitro* research, hence an improved cellular model is urgently required.

For cell lines to be considered optimised and usable in the 3D spheroid model, the spheroids generated needed to satisfy a number of requirements. Firstly, the cells should form spheroids with a suitable morphology for use in functional assays. We adopted a simple, subjective method of assessing spheroid morphology described by Ivascu and Kubbies, 2007, who classified breast cancer spheroids according to the following classes: tight spheroids (compact 3D structures with a clear margin), compact aggregates (slightly irregular 3D structures), and loose aggregates (loose structures with minimal cell-cell contacts). It has previously been shown that invasive or aggressive cell lines are more likely to form looser 3D structures (Gayan, Teli and Dey, 2017). Although the looser morphology reflects the clinical characteristics and behaviour of such tumours, the use of these spheroid models in downstream functional experiments is particularly difficult. For example, spheroid size analysis to assess growth kinetics and drug response is challenging as the 3D structures are diffuse with no clearly defined edges. In addition, loose aggregates typically fall apart when under manipulation; therefore, transferring spheroids between plates to model migration is not possible. Hence, only cell lines which formed a tight spheroid or compact aggregate were deemed suitable for use. Although this resulted in some cell lines with a looser 3D spheroid morphology being

excluded from further analysis, it is apparent that they are still clinically-relevant models in terms of their invasive behaviour.

In addition to morphology, the cell lines should form spheroids with a diameter of 250-350 μm during the initial four day incubation period. Spheroid size is an important consideration as structures which are too small do not have well established physiological gradients, whereas larger spheroids may develop necrotic cores. Spheroid size was easily customised by adjusting cell seeding densities and ensured that different cell lines formed the same size spheroid within the chosen time period. The final requirement was that the spheroids should display continual growth for at least seven days in culture in order to assess functional processes in an actively growing tumour model.

Firstly, we chose to assess spheroid formation and growth in the cell's standard medium compared to serum-free neurosphere medium. Neurosphere medium, consisting of a basal medium (DMEM/F-12) enriched with supplements (including B-27, N2, and heparin) and growth factors (EGF and bFGF), is routinely used for the culture and maintenance of neural stem cells and tumour cells of a neuronal origin. We showed that the SHH medulloblastoma cell lines DAOY, ONS76, and UW228-3 all formed larger spheroids in neurosphere media compared to standard culture media. In addition, spheroid growth over a seven-day period was significantly enhanced in neurosphere medium. This is in contrast to cell lines of other tumour types where their standard culture medium is sufficient for spheroid growth (Friedrich *et al.*, 2009; Vinci *et al.*, 2012), whereas medulloblastoma cell line derived spheroids failed to thrive in this setting. Differences in spheroid growth kinetics between standard and neurosphere medium are likely due to the supplements and growth factors in the neurosphere medium promoting proliferation. Culturing medulloblastoma cell lines in neurosphere medium, rather than standard medium, is advantageous as we are able to mimic an actively proliferating tumour. Therefore, this could be considered a more suitable and

representative model of medulloblastoma growth. An addition benefit of a universal culture medium is that it allows direct comparisons across cell lines which would not have been possible if the cells grew in different media compositions.

Testing of Group 3 medulloblastoma cell lines in the spheroid model revealed substantial differences in the ability to form spheroids across cell lines, highlighting the heterogeneity within subgroups. Unlike SHH subgroup cell lines which formed tight spheroids in neurosphere medium, the four Group 3 cell lines tested did not display the same morphology. Instead, the addition of methyl cellulose to neurosphere medium and the incorporation of a post-seeding centrifugation step, was required for the formation of compact aggregates for the HD-MB03 and D458 cell lines. In addition, we showed that HD-MB03 cells failed to form any 3D structure when seeded in standard culture medium, again highlighting the need for growth factor enriched medium for medulloblastoma cells. The D283 and D425 cell lines failed to form suitable spheroids in the conditions tested and were therefore considered unsuitable for further analysis.

The matched Group 4 cell lines CHLA-01-MED and CHLA-01R-MED failed to form appropriate 3D structures when seeded in neurosphere medium with and without the methyl cellulose supplementation and were deemed unsuitable for this model. In standard culture, these cell lines grow as clusters and single cells in suspension, therefore, it is possible that the dissociation of the cells in preparation for cell seeding for the spheroid assay is unsuitable for these cell lines.

The observed variation in 3D spheroid morphology across cell lines may be a result of the standard culture conditions for each cell type. SHH cell lines grow adherently in standard culture and all three cell lines formed tight spheroids suitable for downstream analysis. HD-MB03 cells, which grow around 80% adherently, also formed a suitable spheroid structure. Although D458 cells, which grow primarily in suspension, formed a spheroid of appropriate morphology, the D283, D425, CHLA-01-MED, and CHLA-01R-MED cell lines, which standardly grow in suspension, all

failed to form suitable spheroids. This suggests that cells which grow predominantly adherently in standard culture are more likely to form suitable spheroids. The adhesive characteristics of these cell lines in standard culture may promote stronger cell-cell interactions in a 3D environment which leads to the formation of a tighter spheroid structure. This observation should be tested across other cell lines in order to conclude whether standard cell culture phenotype is a true indicator of expected spheroid morphology.

Although some of the cell lines tested failed to form spheroids, modifications to the culture medium may promote the formation of a more compact aggregate. Ivascu and Kubbies, 2006 screened a selection of medium additives to induce spheroid formation from loose aggregates. They found that the addition of fibronectin, laminin, or collagen IV did not alter aggregate morphology; however, reconstituted basement membrane supplementation encouraged the formation of a distinct spheroid structure. Alternatively, higher concentrations of methyl cellulose improved spheroid compactness and circularity in the hanging-drop spheroid method (Leung *et al.*, 2015). Additional centrifugation steps during the initial four-day spheroid formation period may also encourage stronger cell-cell interactions and should be tested as an alternative approach.

It is also important to consider that although the ULA plate method was unsuitable for spheroid formation for some cell lines, other generation methods may be compatible; for instance, unlike the ULA plate method which promotes spontaneous spheroid formation, scaffold-based models could provide more support for the cells thus encouraging 3D growth. Alternatively, other 3D *in vitro* models may be more compatible for some medulloblastoma cell lines. It has been shown that the Group 4 cell lines CHLA-01-MED and CHLA-01R-MED are able to grow as ‘mini-tumours’ within HA hydrogels for as long as three months, growing up to 1 mm in diameter (Dr Franziska Linke, unpublished data). Therefore, other approaches to 3D culture should be explored for cell lines in which the spheroid model is not suitable.

7.2.3 Validation of SHH medulloblastoma spheroid reproducibility

Having established the appropriate culture conditions for SHH medulloblastoma cell lines in the spheroid model, we then needed to validate that they were highly reproducible. Verification of spheroid uniformity on day 4 was considered as a quality control step before proceeding with functional analysis. We adopted the coefficient of variation (CV) measurement to determine the consistency in spheroid size both within each plate (intraplate CV) and between plates (interplate CV). Sittampalam *et al.*, 2004 stated that less than 20% variation in spheroid size was acceptable; therefore, we chose the same criteria for our study. UW228-3 spheroids displayed the least variation (<2% variability in diameter) which could be due to their tighter structure compared to DAOY and ONS76 spheroids.

The ONS76 cell line showed the most variation in size, albeit still within the acceptable range. This variability, particularly in the third experimental repeat, could have resulted from seeding later passage cells. Sub-culturing of cell lines over a long period of time can introduce genetic and phenotypic changes that were not present in early passage cells (reviewed by Hughes *et al.*, 2007). Further optimisation of cell lines in spheroid culture could involve tracking whether there is variability in size or morphology in later passages.

Another possibility for the differences in spheroid variation could be due to the clinical characteristics of each cell line. A study by Gayan, Teli and Dey, 2017 examined whether the aggressive characteristics of cancer cell lines was reflected in spheroid culture. They showed that the non-invasive MCF-7 cell line formed a tighter, more compact structure in comparison to the invasive MDA-MB-231 and HT-1080 cell lines, in which the spheroids formed looser aggregates. This is a characteristic that we observe across the SHH medulloblastoma cell lines, with the non-metastatic UW228-3 cell line displaying a clearly defined spheroid periphery compared to the more aggressive metastatic ONS76 cell line which was slightly

looser around the edge, reflected in the increased variation in spheroid size. The aggressive nature of Group 3 and 4 medulloblastoma cell lines were also reflected in a looser spheroid morphology or the inability to form a suitable 3D spheroid structure.

7.2.4 Characterisation of SHH medulloblastoma spheroids

An additional requirement for the 3D spheroid model of medulloblastoma was that it should be applicable to both quantitative and qualitative methods of assessing viability. We aimed to quantify spheroid growth kinetics using both size analysis and a specialised 3D viability assay.

Manual imaging is a simple method of monitoring spheroid growth over time. One of the main advantages of this technique is that the same spheroids can be imaged continuously. Imaging of SHH medulloblastoma spheroids over an 18-21 day period showed a linear increase in volume for the DAOY and ONS76 spheroids. The small error bars from the growth analysis for these cell lines demonstrates the reproducibility and robustness of this method. Volume analysis for the UW228-3 cell line showed that growth plateaued at day 10. However, imaging of UW228-3 spheroids revealed an altered morphology from day 7, which was reflected in the greater variation in volume measurements.

Due to the increased popularity of 3D *in vitro* models, there are now many commercially-available viability assays that are specialised for spheroid culture. Zanoni *et al.*, 2016 tested the performances of three commercial assays and concluded that the best and most reproducible method was the CellTiter-Glo® 3D cell viability assay. This luminescence-based method quantifies spheroid viability by promoting cell lysis and the release of ATP. The enzyme luciferase acts on the substrate luciferin in the presence of ATP to release energy in the form of luminescence. The luminescence signal generated is proportional to the number of

viable cells within the spheroid (Promega, 2015). Although the luminescence readouts followed a similar pattern to the volume measurements, there were differences in linearity between the techniques. Unlike manual imaging, CellTiter-Glo® is an endpoint assay; therefore, the luminescence measurements shown are for a set of replicates at each time point and not the same spheroids measured continuously. This introduces variation that is not present in volume analysis and is particularly observed at later time points. The variation in luminescence readings could also be caused by the larger spheroid sizes in the latter half of the experiment. It was previously shown that the CellTiter-Glo® 3D reagent could completely penetrate spheroids up to 650 µm in diameter; however, a decrease in correlation between spheroid size over 650 µm and luminescence has been reported (Zanoni *et al.*, 2016). Therefore, the variation in luminescence values and deviation from linearity at the later time points could be due to incomplete reagent penetration throughout the spheroid.

These findings suggest that the CellTiter-Glo® 3D cell viability assay is an appropriate method for measuring viability when the spheroid size is below 650 µm in diameter. However, the need to set up replicate wells for each time point is a disadvantage of this method both in terms of the additional costs of resources, as well as the introduction of more variability. Therefore, we concluded that volume analysis is a more suitable measurement of longer term spheroid viability. However, during the course of this project, alternative commercial 3D viability assays have become available, which should be tested for their use and suitability in the medulloblastoma spheroid models.

An alternative, qualitative method of assessing spheroid viability involves the harvesting, processing and sectioning of spheroids for immunohistochemical staining. This technique allows visualisation of protein expression patterns throughout spheroid sections. We chose to assess the expression of Ki67 (a positive marker of proliferation and spheroid growth), and CA9 (a negative marker,

indicative of hypoxia). Staining of SHH medulloblastoma spheroid sections showed Ki67 expression throughout the spheroid on days 7 and 14; however, there was an expression gradient by day 21 where Ki67 was restricted to the spheroid periphery. Expression of CA9, on the other hand, was evident after two weeks of spheroid culture and was more extensive by day 21. This indicates that the spheroids have a hypoxic core at these later time points, making the model amenable to further studies aiming to therapeutically target hypoxic cells (Wilson and Hay, 2011).

As previously discussed, the medulloblastoma cell lines which form suitable spheroids require neurosphere medium, not their standard culture medium, for sustained growth. As neurosphere medium contains supplements and growth factors routinely used in the culture and maintenance of neural stem cells, it was important to assess whether the spheroids produced in this model were enriched for markers of 'stemness'. We chose to assess the expression of the stemness marker SOX2, which is amplified in SHH medulloblastoma (Ahlfeld *et al.*, 2013), in the spheroid sections. SOX2 expression was present throughout the spheroid sections on day 7 and 14; however, expression was limited to cells towards the spheroid edge by day 21. This suggests that stem-like cells are not present within the hypoxic core, consistent with the spheroid physiological gradient model described by Lin and Chang, 2008.

7.3 Assessment of medulloblastoma spheroid drug response

Treatment for medulloblastoma typically consists of a combination of surgery, craniospinal radiotherapy, and adjuvant chemotherapy. Although the currently used standard-of-care chemotherapy agents are somewhat effective, the development of drug resistance and the devastating long-term chemotherapy-associated neurological side effects to the patient are driving the need to establish more suitable treatment options (Fossati, Ricardi and Orecchia, 2009).

Pre-clinical testing of potential therapeutic agents for cancer treatment typically involves initial *in vitro* screening of hundreds of drugs, with only the most successful taken forward for *in vivo* testing. These drug screening approaches still depend on 2D cultures which fail to mimic the complexity and multi-dimensionality of tumours. The development of more appropriate cellular models that recapitulate tumour biology could positively influence pre-clinical testing by providing a more accurate prediction of drug response at the earliest stage. By taking forward only the most promising drug candidates from *in vitro* screening into *in vivo* tests, more therapeutic agents may be successful when progressing to the later trial stages. In turn, this would reduce the number of animals required for testing which would be a considerable benefit and is in line with campaigns to reduce, refine, and replace the use of animals in scientific research.

In chapter 3, we established a highly reproducible 3D spheroid model for SHH medulloblastoma in which cell lines were grown in the same growth-promoting medium, forming the same size by day 4. These identical conditions of growth made this model ideal for drug screening by allowing direct comparisons between cell lines and drugs (Friedrich *et al.*, 2009). In order to assess spheroid drug response, we compared two methods: imaging to determine spheroid volume and the endpoint CellTiter-Glo® 3D cell viability assay. Non-linear regression analyses showed that there were no significant differences between the two methods and they were

comparable both in terms of the drug response curve fit and the IC_{50} values generated. Therefore, we concluded that either of these methods could be used in drug response assays and the decision regarding which method to adopt should be based on the individual requirements of the experiment.

7.3.1 Drug response differences in 2D and 3D *in vitro* culture

As standard 2D culture fails to recapitulate the multi-dimensional growth of tumours, we hypothesised that drug efficacy would differ between 2D monolayers and 3D spheroids. We tested the response of the three SHH medulloblastoma cell lines in both culture conditions to four chemotherapeutic agents. These drugs (etoposide, vincristine, cisplatin, and lomustine) were chosen as they are all currently used standard-of-care treatments for paediatric medulloblastoma and differ in their mechanisms of action. We showed that there was a significant difference in drug response with 3D spheroids being more resistant to treatment compared to 2D monolayer culture in almost all cell lines and drugs tested (11 out of the 12 combinations). This indicated that these shifts in response were unlikely to be drug or cell line specific, but more likely due to the differences in the cellular structures and architecture of the 2D and 3D cultures.

Unlike 2D culture, where cells are exposed to equal levels of nutrients, oxygen, and waste products, the spatial conformation of spheroids generates pathophysiological gradients (Carlsson and Acker, 1988). These gradients mimic patient tumours and can have a substantial effect on drug response. An oxygen gradient is established during spheroid growth, with the oxygen availability decreasing with increasing spheroid depth (Grimes, Fletcher and Partridge, 2014). Some chemotherapy agents, including cisplatin, irinotecan, and 5-fluorouracil, require oxygen to exert their antitumoral effects through the formation of reactive oxygen species (Deavall *et al.*, 2012). Therefore, a low oxygen environment can reduce the cytotoxic effects of some compounds and may account for the shift in response in 3D spheroid

culture. As cells within the spheroid are exposed to differing levels of oxygen, they may undergo alternative processes of energy metabolism. Cells in normal oxygen conditions can obtain their energy through oxidative phosphorylation. However, for those cells where the oxygen concentration is lower, they may instead metabolise anaerobically, resulting in the accumulation of the by-product lactate within the spheroid (Hirschhaeuser *et al.*, 2010). In solid tumours and spheroids, the lactate production results in an acidic environment. For weak basic drugs including vincristine, vinblastine, mitoxantrone, and doxorubicin, this causes protonation (the addition of a proton making the drug positively-charged) (Wojtkowiak *et al.*, 2011). The impact of this is a reduction in uptake as charged drugs are not as effective in bypassing the cellular membrane. Swietach *et al.*, 2012 demonstrated this effect in HCT-116 colon cancer spheroids and showed that the uptake of doxorubicin decreased in acidic regions of the spheroid. This pH gradient within the spheroid could have contributed to the shift in drug response in the SHH medulloblastoma cell lines tested. To elucidate whether this was indeed a mechanism of the observed resistance, combination therapies to stabilise the pH within the spheroid could be tested. McIntyre *et al.*, 2016 demonstrated that this was possible in colon, breast, and glioma spheroids and resulted in increased apoptosis within the spheroid core.

An alternative mechanism of drug resistance in spheroid culture is through cell dormancy, where the lack of oxygen and nutrients and a low pH environment induces quiescence or senescence. DNA damaging agents, for example cisplatin, carboplatin, and doxorubicin, exert their antitumoral effects in actively growing cells (Cheung-Ong, Giaever and Nislow, 2013). Therefore, the non-proliferative state of dormant cells within the spheroid structure may account for shift in response. In addition, we have shown that spheroids in our model express SOX2, which has been linked to quiescence and therapy resistance in SHH medulloblastoma (Vanner *et al.*, 2014).

Another reason drug response may differ in 3D spheroid culture compared to 2D monolayers could be due to the ECM. Cell lines cultured in 3D are capable of producing their own ECM and it has been shown that the gene expression of various ECM factors, including collagen I, fibronectin, and laminin, is higher in 3D cancer spheroid models than 2D monolayer culture (Longati *et al.*, 2013; Bai *et al.*, 2015). It has been hypothesised that a matrix-rich 3D environment may limit drug penetration and therefore, could play a role in chemoresistance (Hazlehurst, Landowski and Dalton, 2003). It has also been suggested that drug penetration in spheroids could be improved by treating in combination with proteases to degrade the ECM (Choi *et al.*, 2013). Assessing the ECM composition of the SHH medulloblastoma spheroids would be interesting, especially when considering that this could be a mode of drug resistance.

Treatment with chemotherapeutic agents in 3D spheroid culture also revealed the presence of a small population of viable cells remaining after high doses of treatment which were not present in 2D monolayer culture. Fluorescent staining of live cells showed that following a high dose of vincristine, CAM-positive cells were present around the spheroid periphery, reinforcing the concept that viable cells remained following treatment. Liau *et al.*, 2017 reported similar findings in their glioblastoma stem cell model and called this population of cells ‘drug tolerant persisters’. However, the CAM/PI data should be interpreted with caution due to the unexpected PI-positive staining in the vehicle-treated spheroid core across all time points. This was particularly surprising as immunohistochemical staining of spheroid sections showed viable, proliferating cells within the centre of the spheroid on day 7. As the CAM/PI staining experiment was only performed once, it should be repeated in order to confirm whether this is a true finding. In addition, an alternative method of analysis should be used to more accurately quantify the CAM/PI staining such as the technique demonstrated by Zanoni *et al.*, 2016 whereby staining intensity profiles are calculated throughout the whole 3D structure.

It would be also be important to distinguish between drug resistance and a lack of drug penetration in future studies. This could be achieved by fluorescently-labelling compounds and visualising their penetration through the spheroid structure using manual imaging at specified time points or monitoring continuously using time lapse microscopy. This technique has been successfully applied within our research group using with spheroids derived from diffuse intrinsic pontine glioma cell lines (Dr Vahid Heravi Shargh, unpublished data). Alternatively, harvesting and sectioning drug-treated spheroids and staining for markers of drug resistance (e.g. ABCB1) could also aid understanding as to whether expression of drug efflux pumps are contributing to therapy resistance.

7.3.2 Assessing spheroid drug response over a longer period

The 2D versus 3D drug treatment study confirmed findings from other cancer types that response does differ between the culture methods. Drug response differed substantially in some conditions and again highlights the need for an improved drug screening approach compared to standard monolayer culture. We next wanted to investigate whether assessing spheroid drug response over a longer period of time would reveal differences typically missed in endpoint experiments. This approach would be a significant advantage over standard 2D monolayer culture, where cell lines need to be passaged every 3-4 days to maintain viability, thus limiting the time frame for chemotherapeutic screening. We adopted a similar drug treatment regimen as Friedrich *et al.*, 2009 and Vinci *et al.*, 2012, whereby day 4 spheroids were drug treated for 72 hours, following which a 50% medium replenishment was performed on days 7 and 10. A complete medium replacement could not be performed as manipulation to the spheroids could result in cell loss or disruption; therefore, the 50% medium replenishment resulted in a 1:2 dilution of the remaining drug and residual drug activity. Images were taken on day 4 (pre-treatment) and day 7 (post-treatment), as well as additional monitoring on days 10 and 13 to

measure changes in spheroid volume. We monitored longer term drug response in the DAOY and ONS76 cell lines as they maintained viability in spheroid culture for at least 3 weeks. Etoposide, vincristine, and cisplatin responses were tested at three concentrations: low dose (similar to the peak CSF concentrations measured in patients), the IC_{50} dose (calculated in initial drug response studies), and high dose (10x the low dose).

Continual monitoring of spheroid volume following drug treatment revealed interesting patterns of response. Low dose etoposide and vincristine treatment allowed continual spheroid growth following treatment, indicating that the drug concentration that is typically achievable in patients would not be enough to cause significant reductions in tumour volume. However, in the clinic, chemotherapies are usually given simultaneously so it would be interesting to mimic the combinations and doses normally administered to patients as a more clinically-relevant model. The IC_{50} doses of all drugs tested resulted in a regression in spheroid volume over time. This highlights how observing drug response over a longer time course is highly beneficial as it can indicate whether the calculated dose is effective over a longer period. We previously showed that treatment at the higher doses of chemotherapy resulted in a subpopulation of viable cells remaining after treatment. However, continual monitoring of the effects of the same dose treatment showed that spheroid volume continued to decrease in size. This shows that in our model, these viable cells do not promote spheroid regrowth; therefore, an alternative approach may be required to model drug resistance. For example, the spheroids could be sequentially treated with lower drug doses over a longer period of time to develop a truly resistant subpopulation (McDermott *et al.*, 2014).

7.3.3 Overcoming ABCB1-mediated drug resistance

We showed that when spheroids were treated at a low dose of either etoposide, vincristine, or cisplatin, they continued to increase in volume following treatment.

We therefore wanted to assess whether we could potentiate the effects of low dose treatments with combination therapy. Previous work within Dr Beth Coyle's research group highlighted the multidrug transporter ABCB1 as a mechanism of drug resistance in medulloblastoma and ependymoma tumours (Othman *et al.*, 2014; Sabnis *et al.*, 2019). They showed that combined treatment with the ABCB1 inhibitor vardenafil potentiated the effects of chemotherapeutics. However, these studies were conducted in 2D monolayer culture; therefore, we aimed to assess whether the effects of vincristine and etoposide (ABCB1 substrates) could be enhanced in combination with vardenafil in 3D spheroid culture.

Spheroid volume significantly decreased following 72 hours of combined low dose vincristine and vardenafil treatment compared to the vincristine treatment alone. This effect was not observed for low dose etoposide or either drug at a higher concentration, indicating that additional drug resistance mechanisms occur. However, continual monitoring of the effects of combination treatment on spheroid volume over a longer time period showed significant differences in volume following combination treatment compared to single chemotherapy. Following etoposide and vardenafil combined treatment, spheroid size remained constant, whereas the vehicle-treated control and etoposide-treated spheroids continued to increase in volume. One of the most surprising results of the ABCB1 dual-inhibition study was the significant increase in spheroid size by day 13 for those treated with cisplatin and vardenafil, compared to cisplatin alone. This is particularly intriguing as cisplatin was included as a negative control as it is not a substrate for ABCB1. These findings could suggest that the combined treatment confers some element of drug resistance. However, the inclusion of a vardenafil-only control would be beneficial to determine whether it is vardenafil itself which is causing this effect. Any future studies based on these experiments should therefore include vardenafil alone as an appropriate control to allow such conclusions to be made.

Vincristine and vardenafil combined treatment caused a significant reduction in tumour size for both cell lines, indicating that the effects of vincristine can be potentiated over a long period of time. Further confirmation that this dual-inhibitor treatment causes synergistic effects is of great clinical importance as it could facilitate the use of lower doses of chemotherapies when treated in combination with vardenafil. This could be hugely beneficial to patient wellbeing, as the use of these chemotherapy drugs can have a devastating effect on quality of life. Vardenafil is a promising candidate as it is approved by the Food and Drug Administration (FDA) for the treatment of paediatric pulmonary hypertension; therefore, repurposing the drug for cancer treatment could be possible.

7.3.4 Further applications of the medulloblastoma drug screening model

We have shown how the 3D spheroid model of SHH medulloblastoma can be applied to study drug response. Having established that drug response differs in 3D culture compared to standard 2D monolayers, we concluded that future *in vitro* drug screening should be conducted in spheroid models which provide a more accurate estimation of drug efficacy. As we focussed on SHH medulloblastoma cell lines in this study, the obvious next step would be to test targeted agents for this pathway. There are numerous SHH pathway inhibitors currently being tested in the preclinical and clinical trials, with some already approved for the treatment of other SHH-driven cancers, such as basal cell carcinoma (Samkari, White and Packer, 2015).

There is also the potential to apply the 3D spheroid model of SHH medulloblastoma to higher throughput drug screening studies. Although this screening approach was beyond the scope of the current study, preliminary results showed that SHH medulloblastoma cell lines were capable of forming spheroids in 384-well plates. We showed that when seeded at the same cell densities determined for 96-well ULA plate culture in a smaller volume of neurosphere medium, cell lines formed tight, highly reproducible spheroids measuring approximately 300 µm in diameter

by day 4 (Figure 7.1). Using this culture system, it would be possible to complete small molecule inhibitor screens, for example using the FDA-approved chemical library containing 1,280 compounds. Drug screening using 384-well plates in conjunction with automated imaging systems could revolutionise the way in which *in vitro* drug assays are conducted for medulloblastoma. It is hoped that adopting such techniques could bridge the gap between *in vitro* studies and animal models, in turn reducing the amount of time it takes for drugs to progress from the bench to the patient's bedside.

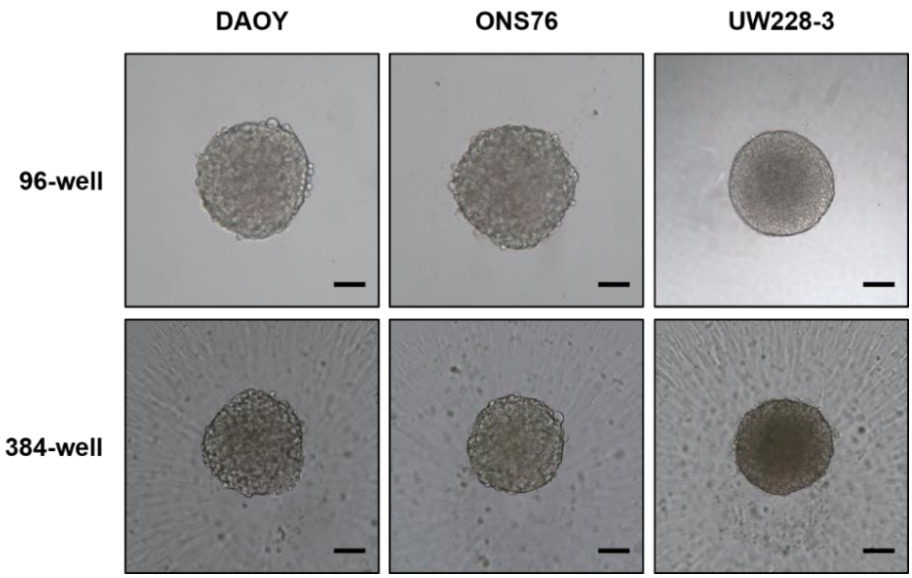


Figure 7.1 Comparison of SHH medulloblastoma spheroids in 96-well and 384-well ultra-low attachment plates
Representative images of day 4 spheroids of the SHH medulloblastoma cell lines (DAOY, ONS76, and UW228-3) generated in 96-well and 384-well ultra-low attachment plates (scale bar: 100 µm).

Future applications could involve assessing the effects of radiotherapy in the medulloblastoma spheroid model. Indeed, the first 3D *in vitro* experiments involved studying radiosensitivity in spheroids generated in spinner flasks (Sutherland *et al.*, 1970). Over recent years, the technique has been developed further with Tesei *et al.*, 2013 describing a novel method of irradiation for spheroids in 96-well plates using plexiglass to mimic human tissue. Using this technique, it would be possible

to incorporate both chemotherapy and radiotherapy dose intensities and schedules utilised in clinical practice to study medulloblastoma spheroid response. Mimicking these patient treatment regimens would provide a more accurate prediction of therapy response.

As mentioned previously, the spheroid model of medulloblastoma could also be used to study drug penetration and delivery. This technique has already been tested within our research group by Dr Vahid Heravi Shargh (Postdoctoral Research Fellow) using fluorescently-labelled drugs encapsulated in nanoparticles in diffuse intrinsic pontine glioma spheroids. The use of Z-stack imaging techniques would allow the visualisation of compounds within the spheroid structure and would be particularly informative for assessing the size-dependent penetration of nanoparticles into the spheroid structure (Tchoryk *et al.*, 2019).

7.4 Modelling medulloblastoma metastasis

Metastasis, the process of tumour spread, is one of the hallmarks of cancer, as described by Hanahan and Weinberg, 2011. Unlike other solid tumours which spread through the vasculature or lymphatic systems, medulloblastomas typically metastasise via the leptomeninges. This occurs through the dissemination of tumour cells to the leptomeningeal space and the circulation of these cells to the rest of the CNS via the CSF. Zapotocky *et al.*, 2018 recently demonstrated that patterns of leptomeningeal metastasis are highly subgroup-specific and showed that SHH medulloblastomas form nodular metastases on the leptomeningeal surface. However, the process by which metastatic dissemination occurs is still poorly understood.

Spheroid migration and invasion assays have been used for many years to study cell movement (Vinci *et al.*, 2013; Vinci, Box and Eccles, 2015). We used the 3D spheroid model of SHH medulloblastoma to study the *in vitro* cell-cell and cell-ECM interactions of spheroids on or within different matrices in order to identify genes and pathways that predict and control tumour spread.

7.4.1 Assessing cell movement on different matrices

Work by Mina Bissell's group has highlighted the importance of the TME in tumour progression and its effects on neighbouring cells (Bissell and Hines, 2011). During the metastatic process, cells migrate and invade into their surrounding TME, which consists of many different cell types including tumour cells, fibroblasts, immune cell, pericytes and ECM (Wang *et al.*, 2017). We initially tested spheroid migration and invasion with models of the basement membrane, a specialised self-assembled ECM that surrounds all tissues (Jayadev and Sherwood, 2017).

We showed different patterns of cell movement across collagen IV, one of the major components of the basement membrane. DAOY spheroids displayed single cell dissemination and ONS76 cells migrated in a collective fashion, whilst UW228-3 spheroids failed to migrate across the collagen IV surface. Although we observed cell line differences, the variations in migratory behaviour for DAOY and ONS76 cell lines, both within and between experimental repeats, means that these results should be treated with caution. The variation could be a result of uneven coatings of collagen IV across the plate surface and the lack of reproducibility indicates that it is not a suitable model for spheroid migration studies. Therefore, it is hard to draw any conclusions of the observed effects.

Instead, we tested the capabilities of SHH medulloblastoma spheroids to migrate across and invade through BME, a commercially-available matrix purified from EHS murine chondrosarcoma tumours (Orkin *et al.*, 1977). BME contains a mixture of ECM components, including laminin, collagen IV, entactin and heparin sulfate proteoglycans. We observed directional, collective cell migration from DAOY and ONS76 spheroids and only slight protrusions from the outer edge of UW228-3 spheroids on a BME matrix. When testing spheroid invasion, two concentrations of BME were used to model different matrix stiffness. The lower BME concentration (3 mg/mL), previously used in 3D spheroid invasion assays (Onion *et al.*, 2016; Sabnis *et al.*, 2019), failed to induce invasion and instead supported DAOY and ONS76 spheroid growth. The higher gelling concentration of BME (10 mg/mL) appeared to only promote growth and some protrusions in DAOY spheroids. The morphology of UW228-3 spheroids remained unchanged in either concentration. Although BME did not cause a substantial invasive or migratory phenotype, the observation that it supports spheroid growth indicates that the addition of the matrix could promote spheroid formation in cell lines which have difficulty forming a 3D structure in culture medium alone. The addition of the lower concentration of BME was previously

shown to promote compaction and improve the structure of D283 and D458 medulloblastoma spheroids (Dr Aishah Nasir, unpublished data).

The observed differences in phenotype could be due to the clinical features of the cell lines. UW228-3 cells were derived from a non-metastatic tumour and although they are *TP53* mutated, which classifies them as higher risk, their behaviour on BME suggests they are not an aggressive cell line (Keles *et al.*, 1995). DAOY cells were also obtained from a non-metastatic tumour; however, in the original publication describing the derivation of the cell line, they showed that following intracerebral inoculation in nude mice, the cells were capable of invading the brain parenchyma as well as spreading over the surface and into the ventricles (Jacobsen, Jenkyn and Papadimitriou, 1985). In addition, the majority of medulloblastoma migration and invasion *in vitro* experiments have been conducted with this cell line, again highlighting its ability to disseminate (reviewed by Grotzer, Neve and Baumgartner, 2016). On the other hand, the ONS76 cell line was derived from a tumour with metastatic disease (M2 stage), indicating that these cells had metastatic potential (Tamura *et al.*, 1989).

Although BME is a well-established and widely-used commercial product, the exact concentration of its components is unknown and the resulting batch-to-batch variability is a significant drawback of the technique. In addition, as it is derived from EHS murine chondrosarcoma tumours, it is not physiologically relevant for medulloblastoma tumours. Hydrogels, water-swollen networks of polymers, are alternative matrices for 3D culture in which cells can be placed on top of or encapsulated within the gels, making them amenable for spheroid migration and invasion modelling. There has been limited research on the use of hydrogels for the culture of medulloblastoma cell lines. Three publications have described the use of the MAX8 β-hairpin self-assembling peptide hydrogels as a suitable scaffold-based model for the culture of the DAOY and ONS76 cell lines (Altunbas *et al.*, 2011; Worthington *et al.*, 2017, 2019). Singh *et al.*, 2014 also described the growth of

DAOY single cells on a cellulose-derived hydrogel. In our study, we aimed to utilise a brain-specific matrix to provide a more tissue-realistic *in vitro* model of medulloblastoma metastatic dissemination. HA, the major constituent and backbone of the brain ECM (Rauch, 2004; Rauch, 2007) was chosen as an appropriate foundation for a brain-specific matrix. HA has been widely used as a bio-scaffold in tissue engineering and regenerative medicine (as reviewed by Hemshekhar *et al.*, 2016) and also possesses many advantageous qualities, for example it is a biocompatible, biodegradable, non-toxic polymer (Burdick and Prestwich, 2011). In this study, we used the HyStem™ hydrogel kit, a semi-synthetic 3D hydrogel platform which consisted of Glycosil® (thiol-modified HA), ExtraLink®-Lite (PEGDA; polyethylene glycol diacrylate), and water. One of the main advantages of the HyStem™ system is the ability to control the hydrogel stiffness. Tumour tissues commonly exhibit increased stiffness compared to their normal tissue counterparts (Levental *et al.*, 2009). This is due to the tumour cells secreting and depositing ECM factors into the surrounding matrix which in turn, increases focal adhesions to promote movement. We chose to make a 1% Glycosil® and 2% ExtraLink®-Lite solution to produce a hydrogel with a stiffness around 1.5-2 kPa (Dr Franziska Linke, personal communication) in order to recapitulate the stiffness of the cerebellum (Vanderhooft *et al.*, 2009). Therefore, our hydrogel model could be considered representative of the stiffness that these tumour cells would typically encounter in patients or *in vivo*. However, the model is limited with regards to the additional effects of other cell types, such as astrocytes and tumour-associated macrophages, on matrix stiffness.

An additional benefit of the HyStem™ model is the ability to customise the HA hydrogel through the incorporation of growth factors and ECM proteins. Fibrous proteins including laminins, collagens, and fibronectin are present in the brain ECM (Novak and Kaye, 2000). Patient dataset analysis showed that gene expression for some subunits of these ECM proteins was significantly higher in SHH tumours,

indicating that they were relevant for incorporation in the HA hydrogel. The finding that *LAMA1*, *LAMB1*, *COLA1*, *COLA2*, and *FN1* gene expression was significantly higher in the SHHβ subtype, defined by Cavalli *et al.*, 2017 as metastatic SHH medulloblastoma patients with a poor outcome, suggests that elevated expression of these ECM components could contribute to metastatic dissemination. The staining of these markers on patient tumour microarrays could provide further support for these ECM proteins as markers of metastasis and should be correlated with patient survival and prognosis.

We established that SHH medulloblastoma spheroids expressed CD44, a receptor which binds to HA, and were therefore capable of interacting with the hydrogel. We first tested the ability of spheroids to invade through HA matrices containing either laminin-111 (LAM), collagen I (COL), or fibronectin (FN). For all three SHH medulloblastoma cell lines, there was no compelling evidence of spheroid invasion in any HA matrix combination. However, assessing behaviour for a longer time period may have shown invasive behaviour. Therefore, in future experiments, spheroid invasion assays should be maintained in longer term culture.

DAOY and ONS76 cells actively migrated from the main spheroid body across the HA hydrogel in a collective manner. Although there appeared to be no substantial difference in migratory behaviour with the addition of LAM or COL compared to HA alone, cells were able to migrate further on HA+FN. Although the non-metastatic UW228-3 cell line showed very little invasive or migratory capacity in the other matrices tested, they actively migrated on a HA+FN matrix. Conversely, there was very little migration on HA, HA+LAM, and HA+COL matrices. This possibly indicates that the addition of FN is inducing a migratory phenotype, despite this not being an innate behaviour of the cell line. This led us to exclude FN from our downstream analyses.

The various migratory phenotypes could potentially be explained by the differential expression of integrin receptors across the cell lines. Integrins, consisting of an α

and β subunit to form a transmembrane heterodimer, are cell adhesion receptors that bind to ECM ligands. Upon ligand binding, integrins activate intracellular signalling pathways regulating cytoskeletal organisation and cell movement (Takada, Ye and Simon, 2007). The ECM components used in this study are all ligands for different integrin heterodimers. The expression of these integrins across the medulloblastoma cell lines may explain the different migration patterns observed. For example, there may be elevated expression of the integrin heterodimers that bind FN, compared to LAM and COL, in the UW228-3 cell line which could explain its altered migratory phenotype. Further work should be carried out to characterise the integrin expression status of medulloblastoma cell lines in order to determine whether this correlates with specific patterns in behaviour.

It would also have been interesting to test different combinations of ECM proteins to elucidate whether this has an additive or inhibitory effect on migration. However, as the stiffness of the HA hydrogel is tightly regulated by the ratio of Glycosil® to ExtraLink®-Lite solution, the incorporation of multiple ECM components in this particular experiment was not feasible. In future studies, higher stock concentrations of ECM components should be made to enable the addition of smaller volumes which would not affect the hydrogel concentration.

Future work should also involve assessing the expression of matrix metalloproteinases (MMPs) in the medulloblastoma migration model. MMPs are enzymes responsible for degrading collagen and other proteins in the ECM and their expression has been correlated to tumour growth and progression (Jabłońska-Trypuć, Matejczyk and Rosochacki, 2016). Research regarding the expression of MMPs in our panel of medulloblastoma cell lines is ongoing by members of Dr Beth Coyle's research group (Hannah Jackson and Christine Mitoko, PhD students). Additional future work should involve using the migration models developed in this study to test MMP inhibitors, with the aim of blocking cell dissemination.

We concluded that the HA hydrogel spheroid migration model was a significant improvement over the collagen IV and BME matrices. There were no issues with assay reproducibility or batch variability and therefore is an ideal brain-specific alternative matrix. As the HyStem^{TM} hydrogel system is commercially-available, the technique could be widely-adopted for modelling SHH medulloblastoma spheroid migration in a physiologically relevant model. There is also the added advantage that researchers can customise the matrix according to their particular interests.

As previously discussed, SHH medulloblastoma tumours predominantly metastasise through cell dissemination from the primary tumour and the formation of nodular metastases on the leptomeningeal surface. In chapter 5, we showed that HA hydrogels can be used as brain-specific matrices to model cell movement. When DAOY and ONS76 spheroids were placed on top of the matrices, cells actively migrated across the surface. Dr Franziska Linke also used the same HA hydrogel compositions and cell lines yet demonstrated different behaviours when single cells were seeded on top of the matrices. It was observed that DAOY and ONS76 single cells formed loosely-attached spheroid-like structures on HA hydrogels; however, on HA+LAM matrices, the single cells formed multiple nodules on the matrix surface. Differences in single cell phenotypes were already observed between HA and HA+LAM matrices on day 0 (images taken 4 hours post-seeding to allow the cells to settle). This suggested, even at this early time point, that there were differences in cell adhesion induced by LAM. Since the different phenotypes of spheroids and single cell on HA hydrogels recapitulated the metastatic behaviours of SHH medulloblastomas, we then applied NGS technologies to these models, our aim being to identify genes and pathways involved in SHH medulloblastoma metastasis.

7.4.2 Optimising sample preparation for NGS

Isolating sufficient RNA from cells within hydrogels was a very difficult process and many attempts were made to improve the technique. Following sample harvesting, we initially used a handheld homogeniser to lyse the cells. However, inconsistencies in timings and overheating of the samples may have resulted in the low RNA yields we were generating. Therefore, we adopted an alternative method, whereby ceramic beads were added to the harvested samples and cells were lysed using a Fast-Prep[24] tissue homogeniser. This technique allowed us to accurately control the homogenisation step, with all samples subjected to the same lysis conditions. In addition, we added a centrifugation step post-homogenisation to pellet the hydrogel in the microcentrifuge tube. This was necessary as the hydrogel blocked the filter columns of the RNA extraction kit in previous attempts. We found that these modifications enhanced RNA yield and this optimised protocol would be highly recommended for any researcher isolating RNA from cells within hydrogels.

Although our modified isolation method improved RNA yield, for some samples there was still too little RNA to perform standard mRNA NGS. For these samples, an alternative NGS approach was adopted: 3' UPX NGS. This method, developed by QIAGEN, is ideal for low input samples and sequences the 3' end of the RNA in short reads near the poly-A tail and therefore aimed to sequence RNA that would be translatable to proteins. For some samples with enough RNA, both mRNA and 3' UPX NGS were performed in an attempt to provide complete datasets for analysis. This also allowed us to compare the results generated from the two NGS techniques. We concluded that the two methods could not be compared on an individual gene level as 3' UPX NGS identified a substantially lower number of genes than mRNA NGS. However, GSEA showed that three quarters of gene sets were shared between mRNA and 3’ UPX analyses, indicating that is it possible to compare the techniques on a broader gene set level. We would advise researchers working with low RNA yield samples to consider 3’ UPX NGS, if mRNA NGS is not

possible, as the results generated are still valid and the technique is a suitable alternative.

7.4.3 Identifying drivers of SHH medulloblastoma metastasis using 3D hydrogel models

We studied spheroid-matrix interactions to elucidate the gene expression changes that occur when spheroids are placed on HA matrices. Differential gene expression analysis revealed that cell cycle genes were downregulated and cell movement genes were upregulated in spheroids on a HA matrix, compared to spheroids in no matrix. We hypothesise that this spheroid-matrix interaction could be a model of the "go or grow" mechanism, whereby there is a trade-off between proliferative and migratory phenotypes (Biddle *et al.*, 2011; Garay *et al.*, 2013). The generation of stably GFP-transfected cell lines would allow us to easily visualise cell movement across the matrix using time-lapse microscopy. This would allow us to understand whether the migrating cells exhibit decreased proliferation rates. When comparing spheroids on HA matrices to those on HA+LAM matrices, we found very few differentially expressed genes. However, this comparison was compromised due to the limited sample size which may account for the few differences observed. This experiment should be repeated again with greater sample numbers in order to study the effects of the incorporation of LAM into the HA hydrogel.

One of the most interesting findings of the spheroid-matrix interaction analysis was the upregulation of *IGF2* (insulin-like growth factor 2) and *INS* (insulin) in spheroids on the HA matrix. It has long been established that IGF2 and INS play a role in cancer development and progression (Macaulay, 1992; Yu, 2000). In addition, a study by Hahn *et al.*, 2000 reported that *Igf2* expression in *Ptch* mutant mice was essential for the formation of medulloblastoma. The binding of IGF2 and insulin to their associated receptors on the cell membrane triggers intracellular signalling via the PI3K/AKT/MTOR pathway (Livingstone, 2013). We showed that *IGF2*/*INS* gene

expression was elevated in SHH medulloblastoma patients in both the Pfister and Cavalli datasets. However, there was no difference in *IGF2*/*INS* gene expression between metastatic and non-metastatic samples. This could be explained by the inaccurate defining of the metastatic status of samples in the R2 Genomics Analysis and Visualization Platform. Samples defined as M+ (metastatic) were likely to be primary tumour samples which had metastasised, not samples taken from the metastatic site. In addition, it does not consider whether patients classified as M0 (non-metastatic) later developed metastatic disease. Therefore, although this dataset showed no significant difference in gene expression between M0 and M+ samples, this may be a false result. More information on the metastatic potential (i.e. whether the tumour subsequently metastasised) could help elucidate any true relationship between gene expression profile and metastatic status. Alternatively, staining of tumour sections, specifically of the invasive edge, would allow direct confirmation of *IGF2*/*INS* expression in disseminating cells.

The synergism between SHH and IGF2 has previously been shown to be important in medulloblastoma (Rao *et al.*, 2004). In 2012, Michael Taylor's group used a *Sleeping Beauty* transposon system in a *Ptch*$^{+/-}$ mouse model to generate medulloblastomas with metastatic dissemination through the CSF pathway (Wu *et al.*, 2012). By studying both the primary tumour and metastases of both mouse and human medulloblastoma, they concluded that only rare cells within a primary tumour have the ability to metastasise. In addition, they identified the PI3K signalling pathway through GSEA as a putative contributor to leptomeningeal dissemination of medulloblastoma. Further pathway analysis comparing mouse and human metastatic genes identified insulin signalling as the only shared pathway. Therefore, the upregulation of *IGF2*/*INS* in our 3D *in vitro* model of SHH medulloblastoma metastasis is of great relevance and provides the confirmation that we are modelling similar pathways that are recognised *in vivo* and in patient tumours.

Although the spheroid-matrix interaction analysis showed upregulation of *IGF2*/*INS* gene expression in spheroids on a HA matrix, we also observed downregulation of IGF2 mRNA-binding proteins (IGF2BPs) 1 and 3 (*IGF2BP1/3*). IGF2BPs regulate the expression of their mRNA targets, which include IGF2, β-actin, and c-Myc (Hüttelmaier *et al.*, 2005; Weidensdorfer *et al.*, 2009). Overexpression of IGF2BPs has been correlated with metastatic progression in many cancer types, including colorectal cancer, melanoma, and lung cancer (Ross, Lemm and Berberet, 2001; Kato *et al.*, 2007; Elcheva *et al.*, 2008). Conversely, loss of function of IGF2BPs is also involved with tumour progression. Gu, Pan and Singer, 2009 demonstrated that a loss of IGF2BP1 function increased the growth ability of metastatic breast cancer cells and also promoted cell migration. In addition, it has been shown that loss of IGF2BP1 promoted a tumorigenic microenvironment in an *in vivo* colorectal cancer model (Hamilton *et al.*, 2015). We hypothesise that the downregulation we observe in our model contributes to the migratory phenotype through the deregulation of IGF2.

Targeting the IGF2/insulin pathway could be an exciting therapeutic approach for medulloblastoma. To date, the majority of studies have focussed on inhibiting the IGF2 and insulin receptor, IGF1R. Monoclonal antibodies targeting IGF-1R, which interfere with ligand binding and the initiation of downstream signalling cascades, have been tested in clinical trials and have showed mixed results (as reviewed by Iams and Lovly, 2015). Testing such inhibitors in our spheroid HA migration model would be an important next step to identify whether this therapeutic approach would be suitable for SHH medulloblastomas. It would be essential to then validate these findings in other metastasis models, both *in vitro* and *in vivo*.

As previously discussed, we utilised spheroids and single cells on HA hydrogels as simplified models of two stages of SHH medulloblastoma metastasis: the initial cell dissemination from the primary tumour (modelled using spheroids) and the formation of nodular metastases (modelled with single cells). Although LAM

appeared to have a very limited effect on the spheroid-matrix interaction, the inclusion of LAM into the HA model was important due to the nodular phenotype it induced for the single cell model. We conducted differential gene expression analysis to identify significantly upregulated genes in spheroids compared to single cells on either a HA or HA+LAM matrix. This enabled us to then identify 325 LAM-specific genes which contributed to cell dissemination. GSEA showed that these genes were involved in cytoskeletal pathways. Wu *et al.*, 2012 also demonstrated enrichment for cytoskeletal genes in metastatic medulloblastomas, again indicating the relevance of our model. We identified upregulation of *CXCR4*, encoding the C-X-C chemokine receptor type 4, in our LAM-specific cell dissemination model. Overexpression of *CXCR4* has been reported in SHH medulloblastoma tumours (Sengupta *et al.*, 2012). In addition, this study demonstrated interactions between the CXCR4 and SHH pathways whereby SHH activation stimulated CXCR4 cell surface localisation and effector signalling activity. Inhibition of these pathways is therefore an exciting prospect for medulloblastoma therapy. Ward *et al.*, 2017 showed that dual inhibition of the SHH and CXCR4 pathways in two SHH medulloblastoma mouse model resulted in potent synergistic antitumor activity. In addition, crosstalk between CXCR4 and the serine/threonine protein phosphatase PPM1D (encoded by the oncogene *WIP1*) was shown to promote progression and invasion of aggressive medulloblastoma variants (Buss *et al.*, 2015). It was shown that *CXCR4* or *WIP1* knockdown inhibited medulloblastoma growth and invasion. Crosstalk between *WIP1* and the SHH pathway has been also demonstrated, with WIP1 inhibition shown to suppress SHH stimulation and potentiate the effects of SHH pathway-inhibiting drugs *in vitro* (Wen *et al.*, 2016). Overexpression of *CXCR4* in our spheroid cell dissemination model will allow the testing of drugs which target this pathway in a relevant medulloblastoma *in vitro* model before proceeding with *in vivo* testing.

The identification of significantly upregulated genes in single cells compared to spheroids on either a HA or HA+LAM matrix enabled us to identify 186 LAM-specific genes involved in the formation of nodular metastases. GSEA highlighted the upregulation of genes associated with metastasis-related pathways in this model, including cAMP responsive element binding protein 1 (*CREB1*; Wang, Cui, *et al.*, 2015), histone deacetylase 7 (*HDAC7*; Guerriero *et al.*, 2017), and hypoxia-inducible factor 1-α (*HIF1α*; Tsai and Wu, 2012). Further analysis should be conducted to assess the relevance of these pathways in medulloblastoma.

Finally, we aimed to identify LAM-specific genes shared across the spheroid and single cell models, as general markers or drivers of SHH medulloblastoma metastasis. To do this, instead of filtering genes based on differential expression, we selected the genes which were not significantly different between spheroids and single cells on either a HA or HA+LAM matrix. GSEA of the 399 LAM-specific genes shared across our *in vitro* SHH metastasis models consistently identified Ras homolog family member A (RhoA)-associated pathways. *RHOA* encodes member A of the Rho family of small GTPases, which have been shown to play essential roles in cell migration and invasion processes (Friedl, 2004). RhoA controls actin cytoskeleton dynamics with its downstream effector Rho-associated serine/threonine kinase (ROCK) (Amano, Nakayama and Kaibuchi, 2010). RhoA-ROCK signalling has been associated with invasion and metastasis in many cancer types (Kamai *et al.*, 2003; Wong *et al.*, 2010; Khalil and El-Sibai, 2012). In addition, another member of the Rho family, cell division cycle 42 (*CDC42*), was also identified in our analysis. Cdc42 regulates the formation of filopodia, finger-like protrusions containing a core of actin filaments, at the cell periphery (Krugmann *et al.*, 2001) and its deregulation has been linked to tumour progression (Qadir, Parveen and Ali, 2015). Our findings suggest that RhoA-associated pathways could also be involved in medulloblastoma metastatic progression. Patient dataset analysis revealed that *RHOA* gene expression was consistently high across all

medulloblastoma samples, indicating that it could be a mechanism shared across molecular subgroups. Future work investigating RhoA-associated pathways should be conducted to confirm its role in medulloblastoma metastasis.

We have shown that our 3D model of SHH medulloblastoma allows us to recapitulate known, and identify novel, mechanisms of metastatic dissemination. In order to validate our findings, future work could involve using single-cell RNA sequencing technologies to capture the migrating cells from the spheroid or nodules. This could enable us to identify additional key genes and pathways driving the metastatic process, whilst validating the findings of our bulk NGS analyses. Alternatively, laser-capture microdissection (LCM) methods could be adopted to isolate actively migrating cells from the hydrogel matrix, followed by transcriptomic and proteomic profiling (Espina *et al.*, 2006). As transcriptional changes do not necessarily correlate to changes in protein levels, for example due to RNA degradation, studying the proteome could be a more informative approach. A recent study by Ezzoukhry *et al.*, 2018 combined LCM and proteomics to study invadosomes, actin-based structures involved in ECM degradation (Di Martino *et al.*, 2016). Application of a similar approach using our 3D model, coupling both transcriptome and proteome profiling, would allow us to more accurately assess the biological processes involved in cell dissemination.

7.5 Future advances to the medulloblastoma spheroid model

In this study, we have optimised and established a 3D *in vitro* culture method for SHH medulloblastoma for the assessment of growth kinetics, drug response, and metastatic dissemination. As previously discussed in section 1.6.1, the currently available models for medulloblastoma consist of cell lines, PDXs, *ex vivo* brain slice cultures, and GEMMs. Our model is a vast improvement over current *in vitro* culture techniques for established cell lines. Although it could still be regarded as a simplistic model compared to more advanced *in vitro* techniques, or indeed *in vivo* models, one of the main advantages of our model is its accessibility to all researchers as the only specialist equipment required is a ULA plate. In addition, there is also the potential to incorporate the spheroids developed in this study into co-cultures with cerebellar brain slices. The coupling of these two established techniques would prove valuable in studying cell dissemination and infiltration.

However, in comparison to PDXs and GEMMs, the 3D spheroid model is limited in its ability to fully recapitulate *in vivo* models or patient tumours with regards to the TME and blood-brain barrier. Although the HA hydrogel that we utilised in this study allowed us to mimic the brain ECM, additional modifications to this assay could be conducted to enhance the physiological relevance. Additional components of the TME that have been shown to be important in medulloblastoma tumorigenesis and progression, could be incorporated into the model, including astrocytes, leptomeningeal cells, macrophages, and other ECM components or growth factors (Margol *et al.*, 2015; Liu *et al.*, 2017; Santhana Kumar *et al.*, 2018). Monitoring changes in the cancer cell's behaviour following the inclusion of these components would be important in understanding the role of the TME in tumour progression and metastasis. By increasing the complexity of the spheroid model through the incorporation of additional elements, it could more accurately reflect the *in vivo* setting and possibly result in a reduction in the mouse models required in future

experimentation. However, the development of a more complex model would be expensive and time-consuming. This would result in a lower throughput technique for studying spheroid growth kinetics and drug screening studies. Therefore, it is important that future studies using the 3D spheroid model consider these advantages and disadvantages when increasing its complexity.

Future work would also involve testing a wider panel of established cell lines in the 3D medulloblastoma spheroid model. It would be particularly interesting to utilise primary cell lines in order to maintain the cellular heterogeneity that exists *in vivo* and in patient tumours. As demonstrated in this study, the spheroid model typically requires between 250-1500 cells per well to generate suitably-sized spheroids for use in downstream analyses. The small number of cells required makes this an ideal model for primary cell lines, for which cell number can be a limitation, especially at early passages. On the other hand, the heterogeneous nature of primary cell lines could make it difficult to standardise the model and therefore, thorough characterisation of spheroid reproducibility and growth would be essential. Optimised primary cell line derived spheroids would be ideal candidates for drug screening approaches and metastasis modelling. It would be interesting to compare the growth and migratory/invasive behaviours of spheroids derived from primary cell lines to the models established in this study to reveal the shared and different characteristics of each model.

7.6 Concluding statement

In conclusion, the 3D spheroid model that we established in this study could be adopted by the medulloblastoma research community as a robust and reliable method of studying tumour growth, drug response and metastatic dissemination. We have demonstrated how drug response differs in 3D spheroids compared to 2D monolayer culture and we consider our model as a more accurate predictor of therapy response and recommend that it is utilised in preclinical drug screening approaches. In addition, we have used 3D spheroids to establish a brain-specific model of SHH medulloblastoma dissemination which mimics the insulin pathway overexpression that is observed *in vivo* and in patients. Overall, our model is a significant improvement over current *in vitro* techniques to study paediatric SHH medulloblastoma.

References

References

Ahlfeld, J. *et al.* (2013) 'Sox2 requirement in Sonic Hedgehog-associated medulloblastoma', *Cancer Research*, 73(12), pp. 3796–3807.

Altunbas, A. *et al.* (2011) 'Encapsulation of curcumin in self-assembling peptide hydrogels as injectable drug delivery vehicles', *Biomaterials*, 32(25), pp. 5906–5914.

Amano, M., Nakayama, M. and Kaibuchi, K. (2010) 'Rho-kinase/ROCK: a key regulator of the cytoskeleton and cell polarity', *Cytoskeleton*, 67(9), pp. 545–554.

Andrews, S. (2010) *FASTQC*, *Babraham Bioinformatics*. Available at: https://www.bioinformatics.babraham.ac.uk/projects/fastqc/.

Bai, C. *et al.* (2015) 'Associations of chemo- and radio-resistant phenotypes with the gap junction, adhesion and extracellular matrix in a three-dimensional culture model of soft sarcoma', *Journal of Experimental and Clinical Cancer Research*, 34, p. 58.

Barnes, J. M., Przybyla, L. and Weaver, V. M. (2017) 'Tissue mechanics regulate brain development, homeostasis and disease', *Journal of Cell Science*, 130, pp. 71–82.

Begicevic, R. R. and Falasca, M. (2017) 'ABC transporters in cancer stem cells: beyond chemoresistance', *International Journal of Molecular Sciences*, 18(11), pp. 2362–2385.

Bellamkonda, S. and Peereboom, D. M. (2018) 'Evaluation and Workup of Leptomeningeal Disease', in *Adult CNS Radiation Oncology*. Springer International Publishing, pp. 191–200.

Biddle, A. *et al.* (2011) 'Cancer stem cells in squamous cell carcinoma switch between two distinct phenotypes that are preferentially migratory or proliferative', *Cancer Research*, 71(15), pp. 5317–5326.

Bissell, M. J. and Hines, W. C. (2011) 'Why don't we get more cancer? A proposed role of the microenvironment in restraining cancer progression', *Nature Medicine*, 17(3), pp. 320–329.

Von Bueren, A. O. *et al.* (2016) 'Treatment of children and adolescents with

metastatic medulloblastoma and prognostic relevance of clinical and biologic parameters', *Journal of Clinical Oncology*, 34(34), pp. 4151–4160.

Bugde, P. *et al.* (2017) 'The therapeutic potential of targeting ABC transporters to combat multi-drug resistance', *Expert Opinion on Therapeutic Targets*, 21(5), pp. 511–530.

Burdick, J. A. and Prestwich, G. D. (2011) 'Hyaluronic acid hydrogels for biomedical applications', *Advanced Materials*, 23(12), pp. 41–56.

Buss, M. C. *et al.* (2015) 'The WIP1 oncogene promotes progression and invasion of aggressive medulloblastoma variants', *Oncogene*, 34(9), pp. 1126–1140.

Caliari, S. R. and Burdick, J. A. (2016) 'A practical guide to hydrogels for cell culture', *Nature Methods*, 13(5), pp. 405–414.

Cancer Research UK (2019) *Children's cancer incidence statistics*. Available at: https://www.cancerresearchuk.org/health-professional/cancer-statistics/childrens-cancers/incidence.

Carlsson, J. and Acker, H. (1988) 'Relations between pH, oxygen partial pressure and growth in cultured cell spheroids', *International Journal of Cancer*, 42(5), pp. 715–720.

Cavalli, F. M. G. *et al.* (2017) 'Intertumoral heterogeneity within medulloblastoma subgroups', *Cancer Cell*, 31(6), pp. 737–754.

Chadwick, E. J. *et al.* (2015) 'A brain tumor/organotypic slice co-culture system for studying tumor microenvironment and targeted drug therapies', *Journal of Visualized Experiments*, 2015(105), p. 53304.

Chang, C. H., Housepian, E. M. and Herbert, C. (1969) 'An operative staging system and a megavoltage radiotherapeutic technic for cerebellar medulloblastomas', *Radiology*, 93(6), pp. 1351–1359.

Cheung-Ong, K., Giaever, G. and Nislow, C. (2013) 'DNA-damaging agents in cancer chemotherapy: serendipity and chemical biology', *Chemistry and Biology*, 20(5), pp. 648–659.

Children with Cancer UK (2019) *Childhood cancer info: types of cancer*. Available at: https://www.childrenwithcancer.org.uk/childhood-cancer-info/types-of-cancer/.

Cho, Y. J. *et al.* (2011) 'Integrative genomic analysis of medulloblastoma identifies

a molecular subgroup that drives poor clinical outcome', *Journal of Clinical Oncology*, 29(11), pp. 1424–1430.

Choi, I. K. *et al.* (2013) 'Strategies to increase drug penetration in solid tumors', *Frontiers in Oncology*, 3(193).

Chou, P. M. *et al.* (1995) 'Multidrug resistance gene expression in childhood medulloblastoma: correlation with clinical outcome and DNA ploidy in 29 patients', *Pediatric Neurosurgery*, 23(6), pp. 283–290.

Clifford, S. C. *et al.* (2006) 'Wnt/Wingless pathway activation and chromosome 6 loss characterize a distinct molecular sub-group of medulloblastomas associated with a favorable prognosis', *Cell Cycle*, 5(22), pp. 2666–2670.

Clifford, S. C. *et al.* (2015) 'Biomarker-driven stratification of disease-risk in non-metastatic medulloblastoma: results from the multi-center HIT-SIOP-PNET4 clinical trial', *Oncotarget*, 6(36), pp. 38827–38839.

Cohen, B. H. *et al.* (2015) 'Pilot study of intensive chemotherapy with peripheral hematopoietic cell support for children less than 3 years of age with malignant brain tumors, the CCG-99703 phase I/II study. A report from the Children's Oncology Group', *Pediatric Neurology*, 53(1), pp. 31–46.

Daneman, R. and Prat, A. (2015) 'The blood-brain barrier', *Cold Spring Harbor Perspectives in Biology*, 7, p. a020412.

Dean, M. (2009) 'ABC transporters, drug resistance, and cancer stem cells', *Journal of Mammary Gland Biology and Neoplasia*, 14(1), pp. 3–9.

Deavall, D. G. *et al.* (2012) 'Drug-induced oxidative stress and toxicity', *Journal of Toxicology*, 2012, p. 645460.

Dimasi, J. A. *et al.* (2010) 'Trends in risks associated with new drug development: Success rates for investigational drugs', *Clinical Pharmacology and Therapeutics*, 87(3), pp. 272–277.

Dobin, A. *et al.* (2013) 'STAR: ultrafast universal RNA-seq aligner', *Bioinformatics*, 29(1), pp. 15–21.

Dufour, C. *et al.* (2012) 'Metastatic medulloblastoma in childhood: Chang's classification revisited', *International Journal of Surgical Oncology*, 2012, p. 245385.

Eberhart, C. G. *et al.* (2002) ‘Histopathologic grading of medulloblastomas: a Pediatric Oncology Group study’, *Cancer*, 94(2), pp. 552–560.

Edmondson, R. *et al.* (2014) ‘Three-dimensional cell culture systems and their applications in drug discovery and cell-based biosensors’, *Assay and Drug Development Technologies*, 12(4), pp. 207–218.

Elcheva, I. *et al.* (2008) ‘Overexpression of mRNA-binding protein CRD-BP in malignant melanomas’, *Oncogene*, 27(37), pp. 5069–5074.

Ellison, D. W. (2002) ‘Classifying the medulloblastoma: insights from morphology and molecular genetics’, *Neuropathology and Applied Neurobiology*, 28(4), pp. 257–282.

Ellison, D. W. *et al.* (2005) ‘β-catenin status predicts a favorable outcome in childhood medulloblastoma: The United Kingdom Children’s Cancer Study Group Brain Tumour Committee’, *Journal of Clinical Oncology*, 23(31), pp. 7951–7957.

Ellison, D. W. (2010) ‘Childhood medulloblastoma: novel approaches to the classification of a heterogeneous disease’, *Acta Neuropathologica*, 120(3), pp. 305–316.

Ellison, D. W., Kocak, M., *et al.* (2011) ‘Definition of disease-risk stratification groups in childhood medulloblastoma using combined clinical, pathologic, and molecular variables’, *Journal of Clinical Oncology*, 29(11), pp. 1400–1407.

Ellison, D. W., Dalton, J., *et al.* (2011) ‘Medulloblastoma: clinicopathological correlates of SHH, WNT, and non-SHH/WNT molecular subgroups’, *Acta Neuropathologica*, 121(3), pp. 381–396.

Englund, C. *et al.* (2006) ‘Unipolar brush cells of the cerebellum are produced in the rhombic lip and migrate through developing white matter’, *Journal of Neuroscience*, 26(36), pp. 9184–9195.

Espina, V. *et al.* (2006) ‘Laser-capture microdissection’, *Nature Protocols*, 1(2), pp. 586–603.

Ezzoukhry, Z. *et al.* (2018) ‘Combining laser capture microdissection and proteomics reveals an active translation machinery controlling invadosome formation’, *Nature Communications*, 9(1), p. 2031.

Falasca, M. and Linton, K. J. (2012) ‘Investigational ABC transporter inhibitors’,

Expert Opinion on Investigational Drugs, 21(5), pp. 657–666.

Fossati, P., Ricardi, U. and Orecchia, R. (2009) 'Pediatric medulloblastoma: toxicity of current treatment and potential role of protontherapy', *Cancer Treatment Reviews*, 35(1), pp. 79–96.

Friedl, P. (2004) 'Prespecification and plasticity: shifting mechanisms of cell migration', *Current Opinion in Cell Biology*, 16(1), pp. 14–23.

Friedman, H. S. *et al.* (1985) 'Establishment and characterization of the human medulloblastoma cell line and transplantable xenograft D283 Med', *Journal of Neuropathology and Experimental Neurology*, 44(6), pp. 592–605.

Friedrich, J. *et al.* (2009) 'Spheroid-based drug screen: considerations and practical approach', *Nature Protocols*, 4(3), pp. 309–324.

Fults, D. W., Taylor, M. D. and Garzia, L. (2019) 'Leptomeningeal dissemination: a sinister pattern of medulloblastoma growth', *Journal of Neurosurgery: Pediatrics*, 23(5), pp. 613–621.

Gajjar, A. J. *et al.* (2013) 'Phase I study of vismodegib in children with recurrent or refractory medulloblastoma: a pediatric brain tumor consortium study', *Clinical Cancer Research*, 19(22), pp. 6305–6312.

Gajjar, A. J. and Robinson, G. W. (2014) 'Medulloblastoma: translating discoveries from the bench to the bedside', *Nature Reviews Clinical Oncology*, 11(12), pp. 714–722.

Garay, T. *et al.* (2013) 'Cell migration or cytokinesis and proliferation? - revisiting the "go or grow" hypothesis in cancer cells in vitro', *Experimental Cell Research*, 319(20), pp. 3094–3103.

Garrè, M. L. *et al.* (2009) 'Medulloblastoma variants: age-dependent occurrence and relation to gorlin syndrome: a new clinical perspective', *Clinical Cancer Research*, 15(7), pp. 2463–2471.

Garzia, L. *et al.* (2018) 'A hematogenous route for medulloblastoma leptomeningeal metastases', *Cell*, 172(5), pp. 1050–1062.

Gayan, S., Teli, A. and Dey, T. (2017) 'Inherent aggressive character of invasive and non-invasive cells dictates the in vitro migration pattern of multicellular spheroid', *Scientific Reports*, 7(1), p. 11527.

Gibson, P. *et al.* (2010) ‘Subtypes of medulloblastoma have distinct developmental origins’, *Nature*, 468(7327), pp. 1095–1099.

Goodrich, L. V *et al.* (1997) ‘Altered neural cell fates and medulloblastoma in mouse patched mutants’, *Science*, 277(5329), pp. 1109–1113.

Goschzik, T. *et al.* (2018) ‘Prognostic effect of whole chromosomal aberration signatures in standard-risk, non-WNT/non-SHH medulloblastoma: a retrospective, molecular analysis of the HIT-SIOP PNET 4 trial’, *The Lancet Oncology*, 19(12), pp. 1602–1616.

Grammel, D. *et al.* (2012) ‘Sonic hedgehog-associated medulloblastoma arising from the cochlear nuclei of the brainstem’, *Acta Neuropathologica*, 123(4), pp. 601–614.

Grimes, D. R., Fletcher, A. G. and Partridge, M. (2014) ‘Oxygen consumption dynamics in steady-state tumour models’, *Royal Society Open Science*, 1(1), p. 140080.

Grotzer, M. A., Neve, A. and Baumgartner, M. (2016) ‘Dissecting brain tumor growth and metastasis in vitro and ex vivo’, *Journal of Cancer Metastasis and Treatment*, 2(5), pp. 149–162.

Gu, W., Pan, F. and Singer, R. H. (2009) ‘Blocking β-catenin binding to the ZBP1 promoter represses ZBP1 expression, leading to increased proliferation and migration of metastatic breast-cancer cells’, *Journal of Cell Science*, 122(11), pp. 1895–1905.

Guerriero, J. L. *et al.* (2017) ‘Class IIa HDAC inhibition reduces breast tumours and metastases through anti-tumour macrophages’, *Nature*, 543(7645), pp. 428–432.

Guerrini-Rousseau, L. *et al.* (2018) ‘Germline SUFU mutation carriers and medulloblastoma: clinical characteristics, cancer risk, and prognosis’, *Neuro-Oncology*, 20(8), pp. 1122–1132.

Hahn, H. *et al.* (2000) ‘Patched target Igf2 is indispensable for the formation of medulloblastoma and rhabdomyosarcoma’, *Journal of Biological Chemistry*, 275(37), pp. 28341–28344.

Hamilton, K. E. *et al.* (2015) ‘Loss of stromal IMP1 promotes a tumorigenic microenvironment in the colon’, *Molecular Cancer Research*, 13(11), pp. 1478–1486.

Hanahan, D. and Weinberg, R. A. (2011) ‘Hallmarks of cancer: the next generation’, *Cell*, pp. 646–674.

Hatton, B. A. *et al.* (2008) ‘The Smo/Smo model: Hedgehog-induced medulloblastoma with 90% incidence and leptomeningeal spread’, *Cancer Research*, 68(6), pp. 1768–1776.

Hazlehurst, L. A., Landowski, T. H. and Dalton, W. S. (2003) ‘Role of the tumor microenvironment in mediating de novo resistance to drugs and physiological mediators of cell death’, *Oncogene*, 22(47), pp. 7396–7402.

He, X. M. *et al.* (1991) ‘Differentiation characteristics of newly established medulloblastoma cell lines (D384 Med, D425 Med, and D458 Med) and their transplantable xenografts.’, *Laboratory investigation; a journal of technical methods and pathology*, 64(6), pp. 833–43.

HeadSmart (2019) *About brain tumours*. Available at: https://www.headsmart.org.uk/symptoms/about-brain-tumours/.

Hemshekhar, M. *et al.* (2016) ‘Emerging roles of hyaluronic acid bioscaffolds in tissue engineering and regenerative medicine’, *International Journal of Biological Macromolecules*, 86, pp. 917–928.

Hirschhaeuser, F. *et al.* (2010) ‘Multicellular tumor spheroids: An underestimated tool is catching up again’, *Journal of Biotechnology*, 148(1), pp. 3–15.

Hoarau-Véchot, J. *et al.* (2018) ‘Halfway between 2D and animal models: are 3D cultures the ideal tool to study cancer-microenvironment interactions?’, *International Journal of Molecular Sciences*, 19, p. 181.

Hoff, K. V. *et al.* (2009) ‘Long-term outcome and clinical prognostic factors in children with medulloblastoma treated in the prospective randomised multicentre trial HIT’91’, *European Journal of Cancer*, 45(7), pp. 1209–1217.

Hovestadt, V. *et al.* (2013) ‘Robust molecular subgrouping and copy-number profiling of medulloblastoma from small amounts of archival tumour material using high-density DNA methylation arrays’, *Acta Neuropathologica*, 125(6), pp. 913–916.

Hovestadt, V. *et al.* (2019) ‘Resolving medulloblastoma cellular architecture by single-cell genomics’, *Nature*, 572(7767), pp. 74–79.

Hughes, P. *et al.* (2007) ‘The costs of using unauthenticated, over-passaged cell

lines: how much more data do we need?', *BioTechniques*, 43(5), pp. 575–586.

Hüttelmaier, S. *et al.* (2005) 'Spatial regulation of β-actin translation by Src-dependent phosphorylation of ZBP1', *Nature*, 438(7067), pp. 512–515.

Iams, W. T. and Lovly, C. M. (2015) 'Molecular pathways: clinical applications and future direction of insulin-like growth factor-1 receptor pathway blockade', *Clinical Cancer Research*, 21(19), pp. 4270–4277.

Illumina (2017a) 'An introduction to next-generation sequencing technology'. Illumina.

Illumina (2017b) 'TruSeq Stranded mRNA Reference Guide'. Illumina.

Ivanov, D. P. *et al.* (2014) 'Multiplexing spheroid volume, resazurin and acid phosphatase viability assays for high-throughput screening of tumour spheroids and stem cell neurospheres', *PLoS ONE*, 9(8), pp. 1–14.

Ivanov, D. P. *et al.* (2016) 'In vitro models of medulloblastoma: choosing the right tool for the job', *Journal of Biotechnology*, 236, pp. 10–25.

Ivascu, A. and Kubbies, M. (2006) 'Rapid generation of single-tumor spheroids for high-throughput cell function and toxicity analysis', *Journal of Biomolecular Screening*, 11(8), pp. 922–932.

Ivascu, A. and Kubbies, M. (2007) 'Diversity of cell-mediated adhesions in breast cancer spheroids', *International Journal of Oncology*, 31(6), pp. 1403–1413.

Jabłońska-Trypuć, A., Matejczyk, M. and Rosochacki, S. (2016) 'Matrix metalloproteinases (MMPs), the main extracellular matrix (ECM) enzymes in collagen degradation, as a target for anticancer drugs', *Journal of Enzyme Inhibition and Medicinal Chemistry*, 31(sup1), pp. 177–183.

Jackson, D. V *et al.* (1981) 'Pharmacokinetics of vincristine in the cerebrospinal fluid of humans', *Cancer Research*, 41(4), pp. 1466–1468.

Jacobsen, P. F., Jenkyn, D. J. and Papadimitriou, J. M. (1985) 'Establishment of a human medulloblastoma cell line and its heterotransplantation into nude mice', *Journal of Neuropathology and Experimental Neurology*, 44(5), pp. 472–485.

Jayadev, R. and Sherwood, D. R. (2017) 'Basement membranes', *Current Biology*, 27(6), pp. 207–211.

Jones, D. T. W. *et al.* (2012) 'Dissecting the genomic complexity underlying medulloblastoma', *Nature*, 488(7409), pp. 100–105.

Kamai, T. *et al.* (2003) 'Significant association of Rho/ROCK pathway with invasion and metastasis of bladder cancer', *Clinical Cancer Research*, 9(7), pp. 2632–2641.

Kato, T. *et al.* (2007) 'Increased expression of insulin-like growth factor-II messenger RNA-binding protein 1 is associated with tumor progression in patients with lung cancer', *Clinical Cancer Research*, 13(2 I), pp. 434–442.

Katt, M. E. *et al.* (2016) 'In vitro tumor models: advantages, disadvantages, variables, and selecting the right platform', *Frontiers in Bioengineering and Biotechnology*, 4(12), pp. 1–14.

Kawauchi, D. *et al.* (2012) 'A mouse model of the most aggressive subgroup of human medulloblastoma', *Cancer Cell*, 21(2), pp. 168–180.

Kawauchi, D. *et al.* (2017) 'Novel MYC-driven medulloblastoma models from multiple embryonic cerebellar cells', *Oncogene*, 36(37), pp. 5231–5242.

Keles, G. E. *et al.* (1995) 'Establishment and characterization of four human medulloblastoma-derived cell lines', *Oncology Research*, 7(10–11), pp. 493–503.

Kelm, J. M. *et al.* (2003) 'Method for generation of homogeneous multicellular tumor spheroids applicable to a wide variety of cell types', *Biotechnology and Bioengineering*, 83(2), pp. 173–180.

Khalil, B. D. and El-Sibai, M. (2012) 'Rho GTPases in primary brain tumor malignancy and invasion', *Journal of Neuro-Oncology*, 108(3), pp. 333–339.

Kieran, M. W. *et al.* (2017) 'Phase I study of oral sonidegib (LDE225) in pediatric brain and solid tumors and a phase II study in children and adults with relapsed medulloblastoma', *Neuro-Oncology*, 19(11), pp. 1542–1552.

Kim, Y. and Kumar, S. (2014) 'CD44-mediated adhesion to hyaluronic acid contributes to mechanosensing and invasive motility', *Molecular Cancer Research*, 12(10), pp. 1416–1429.

Kiya, K. *et al.* (1992) 'Penetration of etoposide into human malignant brain tumors after intravenous and oral administration', *Cancer Chemotherapy and Pharmacology*, 29(5), pp. 339–342.

Kool, M. *et al.* (2008) 'Integrated genomics identifies five medulloblastoma subtypes

with distinct genetic profiles, pathway signatures and clinicopathological features', *PLoS ONE*, 3(8), p. e3088.

Kool, M. *et al.* (2012) 'Molecular subgroups of medulloblastoma: an international meta-analysis of transcriptome, genetic aberrations, and clinical data of WNT, SHH, Group 3, and Group 4 medulloblastomas', *Acta Neuropathologica*, 123(4), pp. 473–484.

Kool, M. *et al.* (2014) 'Genome sequencing of SHH medulloblastoma predicts genotype-related response to smoothened inhibition', *Cancer Cell*, 25(3), pp. 393–405.

Korshunov, A. *et al.* (2017) 'DNA-methylation profiling discloses significant advantages over NanoString method for molecular classification of medulloblastoma', *Acta Neuropathologica*. Springer Verlag, 134(6), pp. 965–967.

Krugmann, S. *et al.* (2001) 'Cdc42 induces filopodia by promoting the formation of an IRSp53:Mena complex', *Current Biology*, 11(21), pp. 1645–1655.

Kumar, V. *et al.* (2017) 'Challenges and Recent Advances in Medulloblastoma Therapy', *Trends in Pharmacological Sciences*, 38(12), pp. 1061–1084.

Künkele, A. *et al.* (2012) 'Pharmacological activation of the p53 pathway by nutlin-3 exerts anti-tumoral effects in medulloblastomas', *Neuro-Oncology*, 14(7), pp. 859–869.

Lafay-Cousin, L. *et al.* (2016) 'Clinical, pathological, and molecular characterization of infant medulloblastomas treated with sequential high-dose chemotherapy', *Pediatric Blood and Cancer*, 63(9), pp. 1527–1534.

Langley, R. R. and Fidler, I. J. (2011) 'The seed and soil hypothesis revisited: the role of tumor-stroma interactions in metastasis to different organs', *International Journal of Cancer*, 128(11), pp. 2527–2535.

Langmead, B. and Salzberg, S. L. (2012) 'Fast gapped-read alignment with Bowtie 2', *Nature Methods*, 9(4), pp. 357–359.

Lannering, B. *et al.* (2012) 'Hyperfractionated versus conventional radiotherapy followed by chemotherapy in standard-risk medulloblastoma: results from the randomized multicenter HIT-SIOP PNET 4 trial', *Journal of Clinical Oncology*, 30(26), pp. 3187–3193.

LeBleu, V. S., MacDonald, B. and Kalluri, R. (2007) ‘Structure and function of basement membranes’, *Experimental Biology and Medicine*, 232(9), pp. 1121–1129.

Lee, Y. *et al.* (2007) ‘Loss of suppressor-of-fused function promotes tumorigenesis’, *Oncogene*, 26(44), pp. 6442–6447.

Leung, B. M. *et al.* (2015) ‘Media additives to promote spheroid circularity and compactness in hanging drop platform’, *Biomaterials Science*, 3(2), pp. 336–344.

Levental, K. R. *et al.* (2009) ‘Matrix crosslinking forces tumor progression by enhancing integrin signaling’, *Cell*, 139(5), pp. 891–906.

Li, Y., Song, Q. and Day, B. W. (2019) ‘Phase I and phase II sonidegib and vismodegib clinical trials for the treatment of paediatric and adult MB patients: a systemic review and meta-analysis’, *Acta Neuropathologica Communications*, 7(1), p. 123.

Liang, Y. *et al.* (2008) ‘Type I collagen is overexpressed in medulloblastoma as a component of tumor microenvironment’, *Journal of Neuro-Oncology*, 86(2), pp. 133–141.

Liau, B. B. *et al.* (2017) ‘Adaptive chromatin remodeling drives glioblastoma stem cell plasticity and drug tolerance’, *Cell Stem Cell*, 20(2), pp. 233–246.

Liberzon, A. *et al.* (2011) ‘Molecular signatures database (MSigDB) 3.0’, *Bioinformatics*, 27(12), pp. 1739–1740.

Lin, C. Y. *et al.* (2016) ‘Active medulloblastoma enhancers reveal subgroup-specific cellular origins’, *Nature*, 530(7588), pp. 57–62.

Lin, R. Z. and Chang, H. Y. (2008) ‘Recent advances in three-dimensional multicellular spheroid culture for biomedical research’, *Biotechnology Journal*, 3(9–10), pp. 1172–1184.

Liu, Y. *et al.* (2017) ‘Astrocytes promote medulloblastoma progression through hedgehog secretion’, *Cancer Research*, 77(23), pp. 6692–6703.

Livingstone, C. (2013) ‘IGF2 and cancer’, *Endocrine-Related Cancer*, 20(6), pp. 321–339.

Longati, P. *et al.* (2013) ‘3D pancreatic carcinoma spheroids induce a matrix-rich, chemoresistant phenotype offering a better model for drug testing’, *BMC Cancer*,

13(1), p. 95.

Louis, D. N. *et al.* (2007) ‘The 2007 WHO classification of tumours of the central nervous system’, *Acta Neuropathologica*, 114(2), pp. 97–109.

Louis, D. N. *et al.* (2016) ‘The 2016 World Health Organization classification of tumors of the central nervous system: a summary’, *Acta Neuropathologica*, 131(6), pp. 803–820.

Love, M. I., Huber, W. and Anders, S. (2014) ‘Moderated estimation of fold change and dispersion for RNA-seq data with DESeq2’, *Genome Biology*, 15, p. 550.

Macaulay, V. M. (1992) ‘Insulin-like growth factors and cancer’, *British Journal of Cancer*, 65(3), pp. 311–20.

Margol, A. S. *et al.* (2015) ‘Tumor-associated macrophages in SHH subgroup of medulloblastomas’, *Clinical Cancer Research*, 21(6), pp. 1457–1465.

Di Martino, J. *et al.* (2016) ‘The microenvironment controls invadosome plasticity’, *Journal of Cell Science*, 129(9), pp. 1759–1768.

McDermott, M. *et al.* (2014) ‘In vitro development of chemotherapy and targeted therapy drug-resistant cancer cell lines: a practical guide with case studies’, *Frontiers in Oncology*, 4, p. 40.

McIntyre, A. *et al.* (2016) ‘Disrupting hypoxia-induced bicarbonate transport acidifies tumor cells and suppresses tumor growth’, *Cancer Research*, 76(13), pp. 3744–3755.

Meng, W. *et al.* (2016) ‘Penetration and intracellular uptake of poly(glycerol-adipate) nanoparticles into three-dimensional brain tumour cell culture models’, *Experimental Biology and Medicine*, 241(5), pp. 466–477.

Milde, T. *et al.* (2012) ‘HD-MB03 is a novel Group 3 medulloblastoma model demonstrating sensitivity to histone deacetylase inhibitor treatment’, *Journal of Neuro-Oncology*, 110(3), pp. 335–348.

Mittler, F. *et al.* (2017) ‘High-content monitoring of drug effects in a 3D spheroid model’, *Frontiers in Oncology*, 7, p. 293.

Mohan, A. L. *et al.* (2012) ‘PI3K/mTOR signaling pathways in medulloblastoma’, *Anticancer research*, 32(8), pp. 3141–3146.

Nakagawa, H. *et al.* (1996) ‘Difference in CDDP penetration into CSF between selective intraarterial chemotherapy in patients with malignant glioma and intravenous or intracarotid administration in patients with metastatic brain tumor’, *Cancer Chemotherapy and Pharmacology*, 37(4), pp. 317–326.

Neumann, J. E., Swartling, F. J. and Schüller, U. (2017) ‘Medulloblastoma: experimental models and reality’, *Acta Neuropathologica*, 134(5), pp. 679–689.

Neve, A. *et al.* (2017) ‘Investigation of brain tissue infiltration by medulloblastoma cells in an ex vivo model’, *Scientific Reports*, 7, p. 5297.

Northcott, P. A., Korshunov, A., *et al.* (2011) ‘Medulloblastoma comprises four distinct molecular variants’, *Journal of Clinical Oncology*, 29(11), pp. 1408–1414.

Northcott, P. A., Hielscher, T., *et al.* (2011) ‘Pediatric and adult sonic hedgehog medulloblastomas are clinically and molecularly distinct’, *Acta Neuropathologica*, 122(2), pp. 231–240.

Northcott, P. A., Jones, D. T. W., *et al.* (2012) ‘Medulloblastomics: the end of the beginning’, *Nature Reviews Cancer*, 12(12), pp. 818–834.

Northcott, P. A., Shih, D. J. H., *et al.* (2012) ‘Subgroup-specific structural variation across 1,000 medulloblastoma genomes’, *Nature*, 488(7409), pp. 49–56.

Northcott, P. A. *et al.* (2017) ‘The whole-genome landscape of medulloblastoma subtypes’, *Nature*, 547(7663), pp. 311–317.

Northcott, P. A. *et al.* (2019) ‘Medulloblastoma’, *Nature Reviews Disease Primers*, 5(1), p. 11.

Novak, U. and Kaye, A. H. (2000) ‘Extracellular matrix and the brain: Components and function’, *Journal of Clinical Neuroscience*, 7(4), pp. 280–290.

Oller-Salvia, B. *et al.* (2016) ‘Blood-brain barrier shuttle peptides: an emerging paradigm for brain delivery’, *Chemical Society Reviews*, 45(17), pp. 4690–4707.

Onion, D. *et al.* (2016) ‘3-dimensional patient-derived lung cancer assays reveal resistance to standards-of-care promoted by stromal cells but sensitivity to histone deacetylase inhibitors’, *Molecular Cancer Therapeutics*, 15(4), pp. 753–763.

Orkin, R. W. *et al.* (1977) ‘A murine tumor producing a matrix of basement membrane’, *The Journal of Experimental Medicine*, 145(1), pp. 204–220.

Orr, B. A. *et al.* (2019) ‘An update on the central nervous system manifestations of Li–Fraumeni syndrome’, *Acta Neuropathologica*, 1, pp. 1–19.

Othman, R. T. *et al.* (2014) ‘Overcoming multiple drug resistance mechanisms in medulloblastoma’, *Acta Neuropathologica Communications*, 2(57), pp. 1–14.

Packer, R. J. *et al.* (2006) ‘Phase III study of craniospinal radiation therapy followed by adjuvant chemotherapy for newly diagnosed average-risk medulloblastoma’, *Journal of Clinical Oncology*, 24(25), pp. 4202–4208.

Packer, R. J. *et al.* (2012) ‘Medulloblastoma and primitive neuroectodermal tumors’, in *Handbook of Clinical Neurology*. Elsevier, pp. 529–548.

Parrish, K. E., Sarkaria, J. N. and Elmquist, W. F. (2015) ‘Improving drug delivery to primary and metastatic brain tumors: strategies to overcome the blood-brain barrier’, *Clinical pharmacology and therapeutics*, 97(4), pp. 336–346.

Pei, Y. *et al.* (2012) ‘An animal model of MYC-driven medulloblastoma’, *Cancer Cell*, 21(2), pp. 155–67.

Phoenix, T. N. *et al.* (2016) ‘Medulloblastoma genotype dictates blood brain barrier phenotype’, *Cancer Cell*, 29(4), pp. 508–522.

Pizer, B. L. and Clifford, S. C. (2009) ‘The potential impact of tumour biology on improved clinical practice for medulloblastoma: progress towards biologically driven clinical trials’, *British Journal of Neurosurgery*, 23(4), pp. 364–375.

Polkinghorn, W. R. and Tarbell, N. J. (2007) ‘Medulloblastoma: tumorigenesis, current clinical paradigm, and efforts to improve risk stratification’, *Nature Clinical Practice Oncology*, 4(5), pp. 295–304.

Pols, S. Y. C. V. *et al.* (2017) ‘Risk factors for development of postoperative cerebellar mutism syndrome in children after medulloblastoma surgery’, *Journal of Neurosurgery: Pediatrics*, 20(1), pp. 35–41.

Promega (2015) ‘CellTiter-Glo(R) 3D Cell Viability Assay’. Promega.

Pugh, T. J. *et al.* (2012) ‘Medulloblastoma exome sequencing uncovers subtype-specific somatic mutations’, *Nature*, 488(7409), pp. 106–110.

Pui, C.-H. *et al.* (2011) ‘Challenging issues in pediatric oncology’, *Nature Reviews Clinical Oncology*, 8(9), pp. 540–549.

Qadir, M. I., Parveen, A. and Ali, M. (2015) ‘Cdc42: role in cancer management’, *Chemical Biology and Drug Design*, 86(4), pp. 432–439.

QIAGEN (2019) ‘QIAseq® UPX 3’ Transcriptome Kit Handbook’. QIAGEN.

Quail, D. F. and Joyce, J. A. (2017) ‘The microenvironmental landscape of brain tumors’, *Cancer Cell*, 31(3), pp. 326–341.

Raffel, C. *et al.* (1993) ‘Absence of p53 mutations in childhood central nervous system primitive neuroectodermal tumors’, *Neurosurgery*, 33(2), pp. 301–306.

Ramaswamy, V. *et al.* (2013) ‘Recurrence patterns across medulloblastoma subgroups: an integrated clinical and molecular analysis’, *The Lancet Oncology*, 14(12), pp. 1200–1207.

Ramaswamy, V. *et al.* (2016) ‘Risk stratification of childhood medulloblastoma in the molecular era: the current consensus’, *Acta Neuropathologica*, 131(6), pp. 821–831.

Ransohoff, K. J., Sarin, K. Y. and Tang, J. Y. (2015) ‘Smoothened inhibitors in sonic hedgehog subgroup medulloblastoma’, *Journal of Clinical Oncology*, 33(24), pp. 2692–2694.

Rao, G. *et al.* (2004) ‘Sonic hedgehog and insulin-like growth factor signaling synergize to induce medulloblastoma formation from nestin-expressing neural progenitors in mice’, *Oncogene*, 23(36), pp. 6156–6162.

Rauch, U. (2004) ‘Extracellular matrix components associated with remodeling processes in brain’, *Cellular and Molecular Life Sciences*, 61(16), pp. 2031–2045.

Rauch, U. (2007) ‘Brain matrix: structure, turnover and necessity’, *Biochemical Society Transactions*, 35(4), pp. 656–660.

Relling, M. V *et al.* (2016) ‘Etoposide achieves potentially cytotoxic concentrations in CSF of children with acute lymphoblastic leukemia’, *Journal of Clinical Oncology*, 14(2), pp. 399–404.

Remke, M. *et al.* (2011) ‘FSTL5 is a marker of poor prognosis in non-WNT/non-SHH medulloblastoma’, *Journal of Clinical Oncology*, 29(29), pp. 3852–3861.

Robertson, P. L. *et al.* (2006) ‘Incidence and severity of postoperative cerebellar mutism syndrome in children with medulloblastoma: a prospective study by the Children’s Oncology Group’, *Journal of Neurosurgery: Pediatrics*, 105(6), pp. 444–

451.

Robinson, G. W. *et al.* (2012) ‘Novel mutations target distinct subgroups of medulloblastoma’, *Nature*, 488(7409), pp. 43–48.

Robinson, G. W. *et al.* (2015) ‘Vismodegib exerts targeted efficacy against recurrent sonic hedgehog subgroup medulloblastoma: results from phase II Pediatric Brain Tumor Consortium studies PBTC-025B and PBTC-032’, *Journal of Clinical Oncology*, 33(24), pp. 2646–2654.

Robinson, G. W. *et al.* (2018) ‘Risk-adapted therapy for young children with medulloblastoma (SJYC07): therapeutic and molecular outcomes from a multicentre, phase 2 trial’, *The Lancet Oncology*, 19(6), pp. 768–784.

Ross, J., Lemm, I. and Berberet, B. (2001) ‘Overexpression of an mRNA-binding protein in human colorectal cancer’, *Oncogene*, 20(45), pp. 6544–6550.

Roth, R. B. *et al.* (2006) ‘Gene expression analyses reveal molecular relationships among 20 regions of the human CNS’, *Neurogenetics*, 7(2), pp. 67–80.

Roussel, M. F. and Stripay, J. L. (2019) ‘Modeling pediatric medulloblastoma’, *Brain Pathology*, 0, pp. 1–10.

Rutkowski, S. *et al.* (2005) ‘Treatment of early childhood medulloblastoma by postoperative chemotherapy alone’, *New England Journal of Medicine*, 352(10), pp. 978–986.

Sabnis, D. H. *et al.* (2019) ‘A role for ABCB1 in prognosis, invasion and drug resistance in ependymoma’, *Scientific Reports*, 9, p. 10290.

Sakka, L., Coll, G. and Chazal, J. (2011) ‘Anatomy and physiology of cerebrospinal fluid’, *European Annals of Otorhinolaryngology, Head and Neck Diseases*, 128(6), pp. 309–316.

Samkari, A., White, J. and Packer, R. (2015) ‘SHH inhibitors for the treatment of medulloblastoma’, *Expert Review of Neurotherapeutics*, 15(7), pp. 763–770.

Sandén, E. *et al.* (2017) ‘Establishment and characterization of an orthotopic patient-derived Group 3 medulloblastoma model for preclinical drug evaluation’, *Scientific Reports*, 7, p. 46366.

Santhana Kumar, K. *et al.* (2018) ‘TGF-β determines the pro-migratory potential of bFGF signaling in medulloblastoma’, *Cell Reports*, 23(13), pp. 3798–3812.

Schaefer, C. F. *et al.* (2009) ‘PID: the Pathway Interaction Database’, *Nucleic Acids Research*, 37, pp. 674–679.

Schüller, U. *et al.* (2008) ‘Acquisition of granule neuron precursor identity is a critical determinant of progenitor cell competence to form Shh-induced medulloblastoma’, *Cancer Cell*, 14(2), pp. 123–134.

Schwalbe, E. C. *et al.* (2013) ‘DNA methylation profiling of medulloblastoma allows robust subclassification and improved outcome prediction using formalin-fixed biopsies’, *Acta Neuropathologica*, 125(3), pp. 359–371.

Schwalbe, E. C. *et al.* (2017) ‘Novel molecular subgroups for clinical classification and outcome prediction in childhood medulloblastoma: a cohort study’, *The Lancet Oncology*, 18(7), pp. 958–971.

Schwarz, R. P., Goodwin, T. J. and Wolf, D. A. (1992) ‘Cell culture for three-dimensional modeling in rotating-wall vessels: an application of simulated microgravity’, *Journal of Tissue Culture Methods*, 14(2), pp. 51–57.

Scotting, P. J., Walker, D. A. and Perilongo, G. (2005) ‘Childhood solid tumours: a developmental disorder’, *Nature Reviews Cancer*, 5(6), pp. 481–488.

Sengupta, R. *et al.* (2012) ‘CXCR4 activation defines a new subgroup of sonic hedgehog-driven medulloblastoma’, *Cancer Research*, 72(1), pp. 122–132.

Shih, D. J. H. *et al.* (2014) ‘Cytogenetic prognostication within medulloblastoma subgroups’, *Journal of Clinical Oncology*, 32(9), pp. 886–896.

Shimizu, K. *et al.* (1991) ‘Biological Characterization of Human Medulloblastoma (ONS-76 and ONS-81) Cell Lines’, in *Biological Aspects of Brain Tumors*. Springer Tokyo, pp. 442–446.

Singh, S. K. *et al.* (2003) ‘Identification of a cancer stem cell in human brain tumors’, *Cancer Research*, 63(18), pp. 5821–5828.

Singh, S. K. *et al.* (2004) ‘Identification of human brain tumour initiating cells’, *Nature*, 432(7015), pp. 396–401.

Singh, T. *et al.* (2014) ‘Carboxymethylcellulose hydrogels support central nervous system-derived tumor-cell chemotactic migration: comparison with conventional extracellular matrix macromolecules’, *Journal of Biomaterials Applications*, 29(3), pp. 433–441.

Sittampalam, G. S. *et al.* (2004) 'HTS assay validation', in *Assay Guidance Manual*. Eli Lilly & Company and the National Center for Advancing Translational Sciences, pp. 945–969.

Smith, M. J. *et al.* (2015) 'Germline mutations in SUFU cause Gorlin syndrome-associated childhood medulloblastoma and redefine the risk associated with PTCH1 mutations', *Journal of Clinical Oncology*, 32(36), pp. 4155–4161.

Smoll, N. R. and Drummond, K. J. (2012) 'The incidence of medulloblastomas and primitive neurectodermal tumours in adults and children', *Journal of Clinical Neuroscience*, 19(11), pp. 1541–1544.

Souza, G. R. *et al.* (2010) 'Three-dimensional tissue culture based on magnetic cell levitation', *Nature Nanotechnology*, 5(4), pp. 291–296.

Subramanian, A. *et al.* (2005) 'Gene set enrichment analysis: a knowledge-based approach for interpreting genome-wide expression profiles', *Proceedings of the National Academy of Sciences of the United States of America*, 102(43), pp. 15545–15550.

Sutherland, R. M. *et al.* (1970) 'A multi-component radiation survival curve using an in vitro tumour model', *International Journal of Radiation Biology*, 18(5), pp. 491–495.

Sutherland, R. M., McCredie, J. A. and Rodger, W. (1971) 'Growth of multicell spheroids in tissue culture as a model of nodular carcinomas', *Journal of the National Cancer Institute*, 46(1), pp. 113–120.

Swartling, F. J. *et al.* (2010) 'Pleiotropic role for MYCN in medulloblastoma', *Genes and Development*, 24(10), pp. 1059–1072.

Swietach, P. *et al.* (2012) 'Importance of intracellular pH in determining the uptake and efficacy of the weakly basic chemotherapeutic drug, doxorubicin', *PLoS ONE*, 7(4), p. e35949.

Szakács, G. *et al.* (2006) 'Targeting multidrug resistance in cancer', *Nature Reviews Drug Discovery*, 5(3), pp. 219–234.

Takada, Y., Ye, X. and Simon, S. (2007) 'The integrins', *Genome Biology*, 8(5), p. 215.

Tamura, K. *et al.* (1989) 'Expression of major histocompatibility complex on human

medulloblastoma cells', *Cancer Research*, 49(19), pp. 5380–5384.

Taylor, M. D. *et al.* (2002) 'Mutations in SUFU predispose to medulloblastoma', *Nature Genetics*, 31(3), pp. 306–310.

Taylor, M. D. *et al.* (2012) 'Molecular subgroups of medulloblastoma: the current consensus', *Acta Neuropathologica*, 123(4), pp. 465–472.

Tchoryk, A. *et al.* (2019) 'Penetration and uptake of nanoparticles in 3D tumor spheroids', *Bioconjugate Chemistry*, 30(5), pp. 1371–1384.

Tesei, A. *et al.* (2013) 'In vitro irradiation system for radiobiological experiments', *Radiation Oncology*, 8(1), p. 257.

The Gene Ontology Consortium (2000) 'Gene Ontology: tool for the unification of biology', *Nature Genetics*, 25(1), pp. 25–29.

The Gene Ontology Consortium (2019) 'The Gene Ontology Resource: 20 years and still GOing strong', *Nucleic Acids Research*, 47(1), pp. 330–338.

Thompson, E. M. *et al.* (2018) 'The clinical importance of medulloblastoma extent of resection: a systematic review', *Journal of Neuro-Oncology*, 139(3), pp. 523–539.

Thompson, M. C. *et al.* (2006) 'Genomics identifies medulloblastoma subgroups that are enriched for specific genetic alterations', *Journal of Clinical Oncology*, 24(12), pp. 1924–1931.

Trapnell, C. *et al.* (2010) 'Transcript assembly and quantification by RNA-Seq reveals unannotated transcripts and isoform switching during cell differentiation', *Nature Biotechnology*, 28(5), pp. 511–515.

Trapnell, C. *et al.* (2012) 'Differential gene and transcript expression analysis of RNA-seq experiments with TopHat and Cufflinks', *Nature Protocols*, 7(3), pp. 562–578.

Trapnell, C. *et al.* (2013) 'Differential analysis of gene regulation at transcript resolution with RNA-seq', *Nature Biotechnology*, 31(1), pp. 46–53.

Trapnell, C., Pachter, L. and Salzberg, S. L. (2009) 'TopHat: discovering splice junctions with RNA-Seq', *Bioinformatics*, 25(9), pp. 1105–1111.

Tsai, Y.-P. and Wu, K.-J. (2012) 'Hypoxia-regulated target genes implicated in tumor metastasis', *Journal of Biomedical Science*, 19(1), p. 102.

Tung, Y.-C. *et al.* (2011) 'High-throughput 3D spheroid culture and drug testing using a 384 hanging drop array', *Analyst*, 136(3), pp. 473–478.

Uchida, Y. *et al.* (2011) 'Quantitative targeted absolute proteomics of human blood-brain barrier transporters and receptors', *Journal of Neurochemistry*, 117(2), pp. 333–345.

Valastyan, S. and Weinberg, R. A. (2011) 'Tumor metastasis: molecular insights and evolving paradigms', *Cell*, 147(2), pp. 275–292.

Vanderhooft, J. L. *et al.* (2009) 'Rheological properties of cross-linked hyaluronan-gelatin hydrogels for tissue engineering', *Macromolecular Bioscience*, 9(1), pp. 20–28.

Vanner, R. J. *et al.* (2014) 'Quiescent Sox2+ cells drive hierarchical growth and relapse in Sonic Hedgehog subgroup medulloblastoma', *Cancer Cell*, 26(1), pp. 33–47.

Vinci, M. *et al.* (2012) 'Advances in establishment and analysis of three-dimensional tumor spheroid-based functional assays for target validation and drug evaluation', *BMC Biology*, 10(29), pp. 1–20.

Vinci, M. *et al.* (2013) 'Tumor spheroid-based migration assays for evaluation of therapeutic agents', in *Target Identification and Validation in Drug Discovery*. Springer Protocols, pp. 253–266.

Vinci, M., Box, C. and Eccles, S. A. (2015) 'Three-dimensional (3D) tumor spheroid invasion assay', *Journal of Visualized Experiments*, 99, pp. 1–9.

Vladoiu, M. C. *et al.* (2019) 'Childhood cerebellar tumours mirror conserved fetal transcriptional programs', *Nature*, 572(7767), pp. 67–73.

Wang, M. *et al.* (2017) 'Role of tumor microenvironment in tumorigenesis', *Journal of Cancer*, 8(5), pp. 761–773.

Wang, X., Dubuc, A. M., *et al.* (2015) 'Medulloblastoma subgroups remain stable across primary and metastatic compartments', *Acta Neuropathologica*, 129(3), pp. 449–457.

Wang, Y. W., Cui, H., *et al.* (2015) 'High expression of cAMP-responsive element-binding protein 1 (CREB1) is associated with metastasis, tumor stage and poor outcome in gastric cancer', *Oncotarget*, 6(12), pp. 10646–10657.

Ward, S. A. *et al.* (2017) ‘Reprogramming medulloblastoma-propagating cells by a combined antagonism of Sonic Hedgehog and CXCR4’, *Cancer Research*, 77(6), pp. 1416–1426.

Waszak, S. M. *et al.* (2018) ‘Spectrum and prevalence of genetic predisposition in medulloblastoma: a retrospective genetic study and prospective validation in a clinical trial cohort’, *The Lancet Oncology*, 19(6), pp. 785–798.

Weidensdorfer, D. *et al.* (2009) ‘Control of c-myc mRNA stability by IGF2BP1-associated cytoplasmic RNPs’, *RNA*, 15(1), pp. 104–115.

Wen, J. *et al.* (2016) ‘WIP1 modulates responsiveness to Sonic Hedgehog signaling in neuronal precursor cells and medulloblastoma’, *Oncogene*, 35(42), pp. 5553–5564.

Wilson, W. R. and Hay, M. P. (2011) ‘Targeting hypoxia in cancer therapy’, *Nature Reviews Cancer*, 11(6), pp. 393–410.

Wojtkowiak, J. W. *et al.* (2011) ‘Drug resistance and cellular adaptation to tumor acidic pH microenvironment’, *Molecular Pharmaceutics*, 8(6), pp. 2032–2038.

Wong, C. C. L. *et al.* (2010) ‘RhoGTPases and Rho-effectors in hepatocellular carcinoma metastasis: ROCK N’ Rho move it’, *Liver International*, 30(5), pp. 642–656.

Worthington, P. *et al.* (2017) ‘Beta-hairpin hydrogels as scaffolds for high-throughput drug discovery in three-dimensional cell culture’, *Analytical Biochemistry*, 535, pp. 25–34.

Worthington, P. *et al.* (2019) ‘Implementation of a high-throughput pilot screen in peptide hydrogel-based three-dimensional cell cultures’, *SLAS Discovery*, 24(7), pp. 714–723.

Wu, X. *et al.* (2012) ‘Clonal selection drives genetic divergence of metastatic medulloblastoma’, *Nature*, 482(7386), pp. 529–533.

Xu, J. *et al.* (2015) ‘Disseminated medulloblastoma in a child with germline BRCA2 6174delT mutation and without Fanconi Anemia’, *Frontiers in Oncology*, 5(191), pp. 1–12.

Yang, Z. J. *et al.* (2008) ‘Medulloblastoma can be initiated by deletion of Patched in lineage-restricted progenitors or stem cells’, *Cancer Cell*, 14(2), pp. 135–145.

Yeom, K. W. *et al.* (2013) ‘Distinctive MRI Features of pediatric medulloblastoma subtypes’, *American Journal of Roentgenology*, 200(4), pp. 895–903.

Yousif, L. F., Di Russo, J. and Sorokin, L. (2013) ‘Laminin isoforms in endothelial and perivascular basement membranes’, *Cell Adhesion and Migration*, 7(1), pp. 101–110.

Yu, H. (2000) ‘Role of the Insulin-like Growth Factor family in cancer development and progression’, *Journal of the National Cancer Institute*, 92(18), pp. 1472–1489.

Zanini, C. *et al.* (2013) ‘Medullospheres from DAOY, UW228 and ONS-76 cells: increased stem cell population and proteomic modifications’, *PLoS ONE*, 8(5), pp. 1–14.

Zanoni, M. *et al.* (2016) ‘3D tumor spheroid models for in vitro therapeutic screening: a systematic approach to enhance the biological relevance of data obtained’, *Scientific Reports*, 6(1), p. 19103.

Zapotocky, M. *et al.* (2018) ‘Differential patterns of metastatic dissemination across medulloblastoma subgroups’, *Journal of Neurosurgery: Pediatrics*, 21, pp. 145–152.

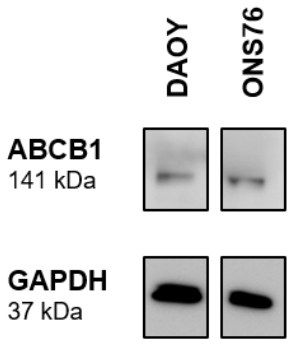
Zhukova, N. *et al.* (2013) ‘Subgroup-specific prognostic implications of TP53 mutation in medulloblastoma’, *Journal of Clinical Oncology*, 31(23), pp. 2927–2935.

Appendices

Appendix 1. ABCB1 protein expression in DAOY and ONS76 spheroids

We aimed to assess the protein expression of ABCB1 in DAOY and ONS76 spheroids. To do this, ten day 7 spheroids per cell line were pooled into 1.5 mL microcentrifuge tubes, snap-frozen in liquid nitrogen and stored at -80°C. Spheroids were lysed using NP-40 lysis buffer and protein concentration was quantified using the Bradford assay. 40 µg of protein was loaded onto SDS-polyacrylamide gels and electrophoresis was performed. Following this, proteins were transferred to polyvinylidene difluoride membranes and blots were subsequently probed with mouse anti-ABCB1 (1:50; GeneTex, GTX23364) and rabbit anti-GAPDH (1:1,000; Cell Signalling Technology, 2118) as a loading control. Enhanced chemiluminescence was performed using SignalFire™ ECL reagent (Cell Signalling Technology, 6889).

Western blot analysis showed that both DAOY and ONS76 spheroids expressed the ABCB1 protein (Appendix Figure 1).

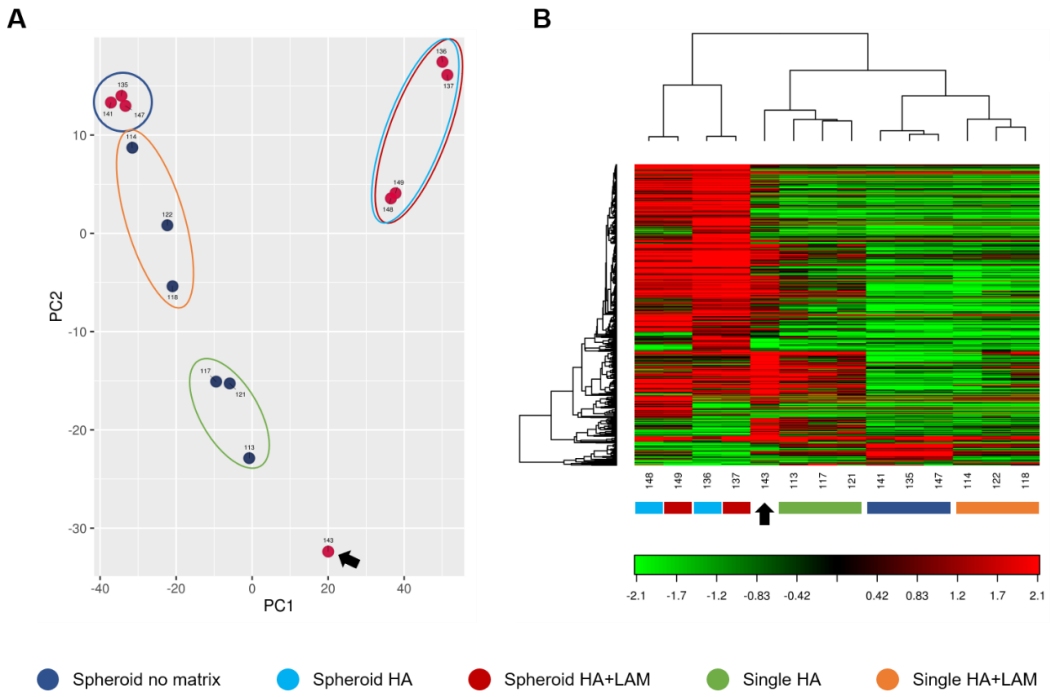


Appendix Figure 1 ABCB1 protein expression in DAOY and ONS76 spheroids
Western blot showing ABCB1 and GAPDH expression in day 7 DAOY and ONS76 spheroids.

Appendix 2. Samples excluded from mRNA NGS analysis

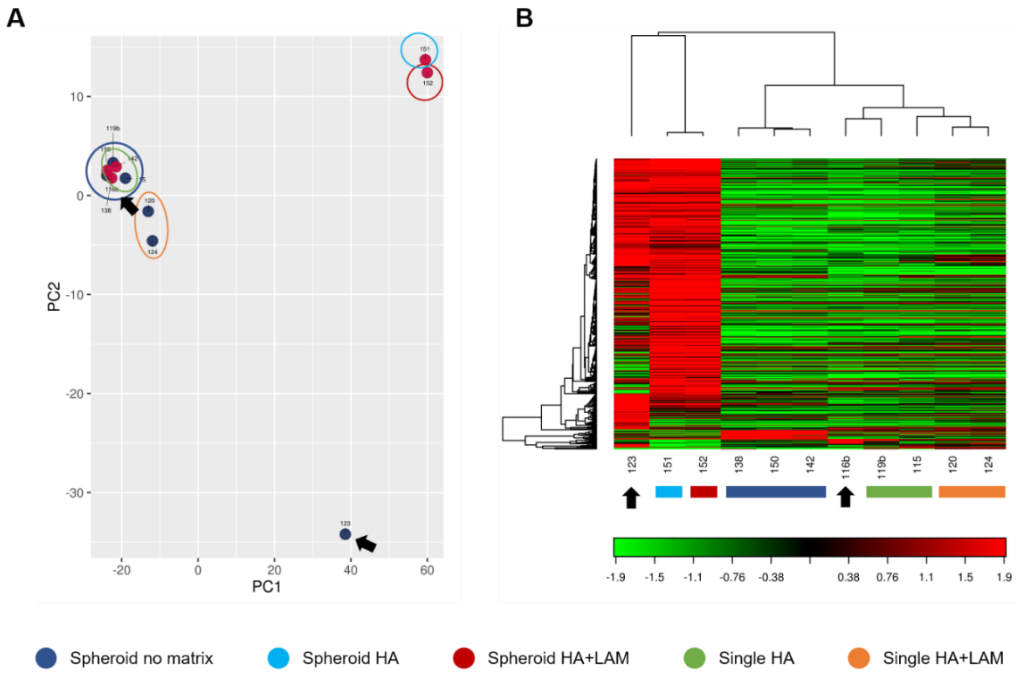
In order to assess variations between samples, we conducted unsupervised analysis. Principle component analysis (PCA) was performed, which clustered samples based on expression profiles. The 500 genes with the largest coefficient of variation (based on FPKM counts) were analysed. The largest component in the variation was plotted along the X-axis (PC1) and the second largest was plotted on the Y-axis (PC2). Pronounced biological differences between the samples lead to their separation in different regions of the PCA plot. Hierarchical clustering was also conducted of the top 500 most significantly differentially expressed genes between spheroid and single cell samples. This generated a heatmap showing the clustering of samples where each row represented one gene and individual samples were displayed in columns. The colour scale signified the relative expression level of a transcript across all samples. Expression levels above and below the mean were depicted by the colours red and green, respectively.

Unsupervised analysis for the DAOY cell line showed that samples for “Spheroid no matrix”, “Single HA”, and “Single HA+LAM” clustered separately on both the PCA plot and the heatmap (Appendix Figure 2). “Spheroid HA” and “Spheroid HA+LAM” samples clustered together; however, sample 143 (DAOY spheroid on a HA matrix) was separate and was therefore excluded from further analysis. The same analysis was conducted for the ONS76 cell line and showed that “Spheroid no matrix”, “Single HA”, and “Single HA+LAM” samples clustered together (Appendix Figure 3). Samples 123 (ONS76 single cells on a HA matrix) and 116b (ONS76 single cells on a HA+LAM matrix) were also excluded from further analysis as they clustered separately to their equivalent samples.



Appendix Figure 2 Unsupervised analysis for all DAOY samples

(**A**) Principle component analysis (PCA) was performed, which clustered samples based on expression profiles. The largest component in the variation was plotted along the X-axis (PC1) and the second largest was plotted on the Y-axis (PC2). (**B**) Heatmap of the hierarchical clustering of the top 500 most significantly differentially expressed genes between DAOY spheroids and single cells across the matrix conditions. Each row represented one gene and individual samples were displayed in columns. The colour scale signified the relative expression level of a transcript across all samples. Expression levels above and below the mean were depicted by the colours red and green, respectively. “Spheroid HA” and “Spheroid HA+LAM” samples clustered together; however, sample 143 (indicated with arrows) was separate and was therefore excluded from further analysis.



Appendix Figure 3 Unsupervised analysis for all ONS76 samples

(**A**) Principle component analysis (PCA) was performed, which clustered samples based on expression profiles. The largest component in the variation was plotted along the X-axis (PC1) and the second largest was plotted on the Y-axis (PC2). (**B**) Heatmap of the hierarchical clustering of the top 500 most significantly differentially expressed genes between ONS76 spheroids and single cells across the matrix conditions. Each row represented one gene and individual samples were displayed in columns. The colour scale signified the relative expression level of a transcript across all samples. Expression levels above and below the mean were depicted by the colours red and green, respectively. “Spheroid no matrix”, “Single HA”, and “Single HA+LAM” samples clustered together. Samples 123 and 116b (indicated with arrows) were excluded from further analysis as they clustered separately to their equivalent samples.

PhD project outputs

PhD project outputs

This PhD project was funded by the Biotechnology and Biological Sciences Research Council (BBSRC) Doctoral Training Partnership (DTP), a four-year PhD programme in which three short research projects are completed in the first seven months, before starting the PhD project. During the programme, a three-month professional internship is also undertaken.

Laboratory rotations

October – December 2015: 'Screening of a delivery peptide for high sensitivity and resolution, dual modality imaging of human tumours in mice' supervised by Professor Anna Grabowska.

January – March 2016: 'Maintenance of methylation and stem-ness in 3D medulloblastoma cultures' supervised by Dr Beth Coyle and Dr Paul Scotting.

March – April 2016: 'Investigating the role of lysine-specific demethylases in prostate cancer' supervised by Professor Nigel Mongan.

Research article in preparation

Sophie J Roper, Franziska Linke, Paul J Scotting, Beth Coyle; "3D-spheroid models of SHH medulloblastoma mimic tumour biology, drug response and metastatic dissemination" – in preparation.

Conference papers

Sophie J Roper, Paul J Scotting, Beth Coyle; MBRS-47. Establishment of a 3D spheroid-based model of medulloblastoma that recapitulates tumour growth, drug

response and migration, *Neuro-Oncology*, Volume 20, Issue suppl_2, 22 June 2018, Pages i138, https://doi.org/10.1093/neuonc/noy059.492

Sophie J Roper, Amy F Lloyd, Paul J Scotting, Tracey D Bradshaw, Beth Coyle; MBRS-46: Jerantinine: a novel tumour-specific alkaloid for the treatment of paediatric medulloblastoma, *Neuro-Oncology*, Volume 20, Issue suppl_2, 22 June 2018, Pages i138, https://doi.org/10.1093/neuonc/noy059.491

Presentations

Oral presentations

- → May 2019: BBSRC DTP Spring Conference 3-minute thesis (2nd place)
- → September 2018: Children's Brain Tumour Research Centre Autumn Research Day
- → March 2018: Division of Cancer and Stem Cells seminar (in collaboration with Celigo®)
- → October 2017: Sue Watson School of Medicine Postgraduate Research Forum
- → April 2017: Children's Brain Tumour Research Centre Spring Research Day
- → April 2016 – 2019: Annual BBSRC DTP Spring School presentations

Poster presentations

- → January 2019: KiTZ Symposium (Heidelberg, Germany)
- → September 2018: Cancer Research Nottingham Symposium (winner)
- → September 2018: Goodbye Flat Biology (Berlin, Germany)
- → July 2018: International Symposium on Paediatric Neuro-Oncology (Denver, United States)
- → April 2017: BBSRC DTP Spring School

Awards and achievements

- → Recipient of the British Association for Cancer Research/Cancer Research UK Student Award (£1000 towards travel to Denver, United States for the International Symposium on Paediatric Neuro-Oncology)
- → Recipient of the University of Nottingham Graduate School Travel Prize (£600 towards travel to Denver, United States for the International Symposium on Paediatric Neuro-Oncology)
- → Recipient of the University of Nottingham School of Medicine Postgraduate Research Development Fund (£345 towards travel to Berlin, Germany for the Goodbye Flat Biology conference)
- → 3rd Year winner of the Cancer Research Nottingham Symposium poster presentation prize
- → 2nd place in the BBSCR DTP Spring Conference 3-Minute thesis competition

Professional Internship

Note to examiners: This statement is included as an appendix to the thesis in order that the thesis accurately captures the PhD training experienced as a BBSRC Doctoral Training Partnership student. The Professional Internship for PhD Students (PIPS) is a compulsory three-month placement which must be undertaken by DTP students. It is usually centred on a specific project and must not be related to the PhD project. This reflective statement is designed to capture the skills development which has taken place during the student's placement and the impact on their career plans it has had.

October 2018 – December 2018: '*Mapping the European cancer research policy landscape*' with the European Association for Cancer Research.

The requirement to undertake a three-month internship during my PhD studies was an exciting and unique opportunity to experience an alternative career path. I decided that I wanted to test out a working environment outside of a laboratory setting, yet still in the field of cancer research. I therefore contacted the European Association for Cancer Research (EACR), Europe's professional membership organisation for those working and studying in cancer research. I have been a student member of the EACR since the start of my PhD and attended one of their scientific conferences. Therefore, I was aware of the important work they carry out for the cancer research community.

The EACR aim to provide a wide variety of services to their community of members, organise scientific conferences, and facilitate communication and collaboration within the scientific community. They also set out to raise the profile of cancer research in Europe and campaign for sustained political and economic support. My project aimed to support the EACR in the development of its cancer policy role. This entailed researching the various organisations and groups active in cancer policy in

Europe and identifying current policy themes and funding streams of particular relevance to cancer researchers. I compiled the information and reported back to the organisation's CEO on a weekly basis. I also provided a detailed report of my findings which was circulated to the EACR management board.

During my internship, I integrated into the small team working within the organisation's Head Office. Interestingly, I was the only scientist in the team which meant that I was able to contribute an alternative opinion in group meetings. One of the main highlights of the internship was when I was asked to write an article for the EACR's online magazine, *The Cancer Researcher*. I decided to gather the opinions of my fellow PhD colleagues to create a blog of PhD survival tips. When I pitched this idea to the EACR team, they loved it and my blog was posted online and had many hits.

Overall, I really enjoyed my time with the EACR but office-life reinforced my love for working on the lab bench! However, I really enjoyed working with people of different backgrounds and it made me appreciate the hard work that goes on behind the scenes to support scientific researchers.